

5. SITE 883¹

Shipboard Scientific Party²

HOLE 883A

Date occupied: 9 August 1992
Date departed: 9 August 1992
Time on hole: 8 hr, 40 min
Position: 51°11.898'N, 167°46.128'E
Bottom felt (rig floor; m, drill-pipe measurement): 2407.0
Distance between rig floor and sea level (m): 10.99
Water depth (drill-pipe measurement from sea level, m): 2396.0
Total depth (rig floor; m): 2445.0
Penetration (m): 38.0
Number of cores (including cores with no recovery): 4
Total length of cored section (m): 38.0
Total core recovered (m): 38.49
Core recovery (%): 101.3
Oldest sediment cored:
Depth (mbsf): 38.0
Nature: clay with quartz and diatoms
Age: Pliocene
Measured velocity (km/s): 1.498

HOLE 883B

Date occupied: 9 August 1992
Date departed: 12 August 1992
Time on hole: 2 days, 23 hr, 20 min
Position: 51°11.908'N, 167°46.128'E
Bottom felt (rig floor; m, drill-pipe measurement): 2395.6
Distance between rig floor and sea level (m): 10.99
Water depth (drill-pipe measurement from sea level, m): 2384.0
Total depth (rig floor; m): 3235.7
Penetration (m): 840.7
Number of cores (including cores with no recovery): 88
Total length of cored section (m): 840.7
Total core recovered (m): 695.41
Core recovery (%): 82.7
Oldest sediment cored:
Depth (mbsf): 840.7
Nature: ashy claystone and basalt chips
Age: middle Campanian
Measured velocity (km/s): 1.62 (at 487 mbsf)

HOLE 883C

Date occupied: 12 August 1992
Date departed: 13 August 1992
Time on hole: 1 day, 6 hr, 15 min
Position: 51°11.919'N, 167°46.123'E
Bottom felt (rig floor; m, drill-pipe measurement): 2396.5
Distance between rig floor and sea level (m): 10.99
Water depth (drill-pipe measurement from sea level, m): 2385.5
Total depth (rig floor; m): 2751.5
Penetration (m): 355.0
Number of cores (including cores with no recovery): 38
Total length of cored section (m): 355.0
Total core recovered (m): 344.3
Core recovery (%): 97
Oldest sediment cored:
Depth (mbsf): 355.0
Nature: calcareous diatom ooze
Age: late Miocene
Measured velocity (km/s): 1.568 (at 355 mbsf)

HOLE 883D

Date occupied: 13 August 1992
Date departed: 13 August 1992
Time on hole: 6 hr, 15 min
Position: 51°11.919'N, 167°46.108'E
Bottom felt (rig floor; m, drill-pipe measurement): 2396.5
Distance between rig floor and sea level (m): 10.99
Water depth (drill-pipe measurement from sea level, m): 2385.5
Total depth (rig floor; m): 2413.5
Penetration (m): 17.0
Number of cores (including cores with no recovery): 2
Total length of cored section (m): 17.0
Total core recovered (m): 17.31
Core recovery (%): 101.8
Oldest sediment cored:
Depth (mbsf): 17.0
Nature: diatom ooze
Age: Quaternary
Measured velocity (km/s): 1.526 (at 17 mbsf)

HOLE 883E

Date occupied: 13 August 1992
Date departed: 16 August 1992

¹ Rea, D.K., Basov, I.A., Janecek, T.R., Palmer-Julson, A., et al., 1993. *Proc. ODP, Init. Repts.*, 145: College Station, TX (Ocean Drilling Program).

² Shipboard Scientific Party is as given in list of participants preceding the contents.

Time on hole: 2 days, 21 hr, 15 min

Position: 51°11.917'N, 167°46.098'E

Bottom felt (rig floor; m, drill-pipe measurement): 2396.5

Distance between rig floor and sea level (m): 10.99

Water depth (drill-pipe measurement from sea level, m): 2385.5

Total depth (rig floor, m): 3253.0

Penetration (m): 856.5

Number of cores (including cores with no recovery): 23

Total length of cored section (m): 226.0

Total core recovered (m): 116.56

Core recovery (%): 51.5

Oldest sediment cored:

Depth (mbsf): 818.72

Nature: ashy claystone

Age: Paleocene

Measured velocity (km/s): 5.692

Hard rock:

Depth (mbsf): 856.5

Nature: basalt

Measured velocity (km/s): 6.2

Basement:

Depth (mbsf): 856.5

Nature: basalt

Measured velocity (km/s): 6.2

Comments: washed: 0–547 mbsf; drilled: 556–640 mbsf (83.5 m).

HOLE 883F

Date occupied: 16 August 1992

Date departed: 20 August 1992

Time on hole: 3 days, 9 hr, 45 min

Position: 51°11.906'N, 167°46.085'E

Bottom felt (rig floor; m, drill-pipe measurement): 2396.5

Distance between rig floor and sea level (m): 10.99

Water depth (drill-pipe measurement from sea level, m): 2385.5

Total depth (rig floor; m): 3245.9

Penetration (m): 849.4

Number of cores (including cores with no recovery): 3

Total length of cored section (m): 29.4

Total core recovered (m): 13.58

Core recovery (%): 46.2

Oldest sediment cored:

Depth (mbsf): 822.65

Nature: claystone with ash and basalt

Age: unknown

Hard rock:

Depth (mbsf): 849.4

Nature: basalt

Basement:

Depth (mbsf): 849.4

Nature: basalt

Comments: washed/drilled from 0 to 820 mbsf.

Principal results: The *JOIDES Resolution* arrived at the start of the site survey for proposed Site DSM-1 (Site 883; Figs. 1 and 2), the shallow site on Detroit Seamount, at 2300 hr on 8 August 1992. Both seismic streamers

were inoperable, so the site was located using the 3.5-kHz profiler, which worked well. A beacon for Site 883 was dropped about 0100 hr on 9 August, and Hole 883A was spudded at 0715 hr. Hole 883A consisted of four APC cores, at a depth of 0 to 38.0 mbsf with 101.3% recovery, taken for detailed physical properties evaluations. Hole 883B was spudded at about 1000 hr on the same morning, and APC/XCB-coring continued there for 71 hr, which extended 88 cores to a depth of 840.5 m with 82.4% recovery. Hole 883B is among the longest APC/XCB holes ever drilled; it was terminated by recovering the sediment/basalt contact atop Detroit Seamount. Hole 883C, an APC/XCB hole intended to duplicate the upper part of the section, was spudded about noon on 12 August. Thirty-eight APC and XCB cores were recovered from Hole 883C, which reached a depth of 355.0 mbsf with 97.0% recovery. Two piston cores were taken when the drill string was pulled back past the mud line. These two cores were taken to permit very high-resolution sampling of the past few hundred thousand years and make up Hole 883D (0–17.0 mbsf) having 101.8% recovery.

On the afternoon of 13 August, we began a pipe trip to change to the RCB bit and bottom-hole assembly (BHA) for rotary drilling of the Paleogene section and basalt. Hole 883E was spudded on 14 August, washed to 547 mbsf, and one core taken to try to recover materials to better constrain a middle Miocene hiatus. Following the retrieval of Core 145-883E-1R, the bit was washed down to 640 mbsf to begin coring the entire Paleogene section for a second time. This coring was accomplished with similar overall recovery as with the XCB bit, and Core 145-883E-20R crossed the sediment/rock interface, with a recovery of mostly basalt. At about 1900 hr on 15 August, the core barrel intended for Core 145-883E-24R could not be disengaged from the drill bit. All efforts to free it came to naught, and at 2100 hr the drillers decided to drop a free-falling funnel, and a pipe trip began that removed the jammed core barrel. Once on the surface, the mechanical fault (which prevented the core barrel from releasing) was repaired, and Core 145-883E-24R was recovered successfully. After routine redressing of the BHA, the bit was run back into the water.

Hole 883E was reentered through the free-falling funnel at about noon on 16 August; this was a smooth operation, considering the 45-kt winds and 5- to 6-m swells. At 1345 hr, the drillers noticed a 50,000 lb weight loss, approximately the weight of the BHA, and began to lower a TV-reentry camera to inspect the lower part of the pipe. The BHA had broken off in Hole 883E, so another round trip was begun with the intent of washing to basement and drilling in basalt until time to begin logging Site 883. Hole 883F was spudded on the morning of 17 August and washed down to basement to provide a logging venue. Three cores were recovered, Core 145-883F-1R, which includes the sediment/basalt contact in a single piece, and two more basalt cores. Thus, Leg 145 became one of the few cruises to double-core the top of a seamount by penetrating into basalt 37.5 m at Hole 883E and 26.75 m at Hole 883F.

Drilling ended, and preparation for logging began at 0300 hr, the morning of 18 August. Successful logging runs were completed by all five tool strings used. The French magnetometer and susceptibility tools were able to define the 221 m of BHA and drill pipe that lodged only 20 m away in the top of Hole 883E. The *JOIDES Resolution* departed Site 883 for the 25-mi-transit to Site 884 at about 0430 hr, 20 August.

The 830 m of sediment encountered at Site 883 can be divided into five major units: clay with diatoms and quartz in the top 86.9 m; diatom ooze between 86.9 and 458 mbsf; calcareous diatom ooze and diatom nannofossil chalk between 458 and 652.2 mbsf; nannofossil chalk and clayey and ashy nannofossil chalk from 652.2 to 814 mbsf; and clay and ash at 814 to 830 mbsf, atop the basalt. At the base of the section, about 37.5 m of basalt was recovered from Hole 883E and about 26.75 m of basalt from Hole 883F. Lithologic Unit I (0–86.9 mbsf), clay with diatoms and quartz, is late Pliocene to Pleistocene in age; the Matuyama/Gauss reversal boundary occurs at 84 mbsf. Accessory dropstones characterize this unit, and ash layers are common. Lithologic Unit II (86.9–458 mbsf) is a nearly pure diatom ooze of late Miocene to late Pliocene age and represents the interval of rapid siliceous sedimentation seen in our nearby drill sites. Calcium carbonate, present in minor amounts above 458 mbsf, becomes an important sedimentary component below that level. Lithologic Unit III

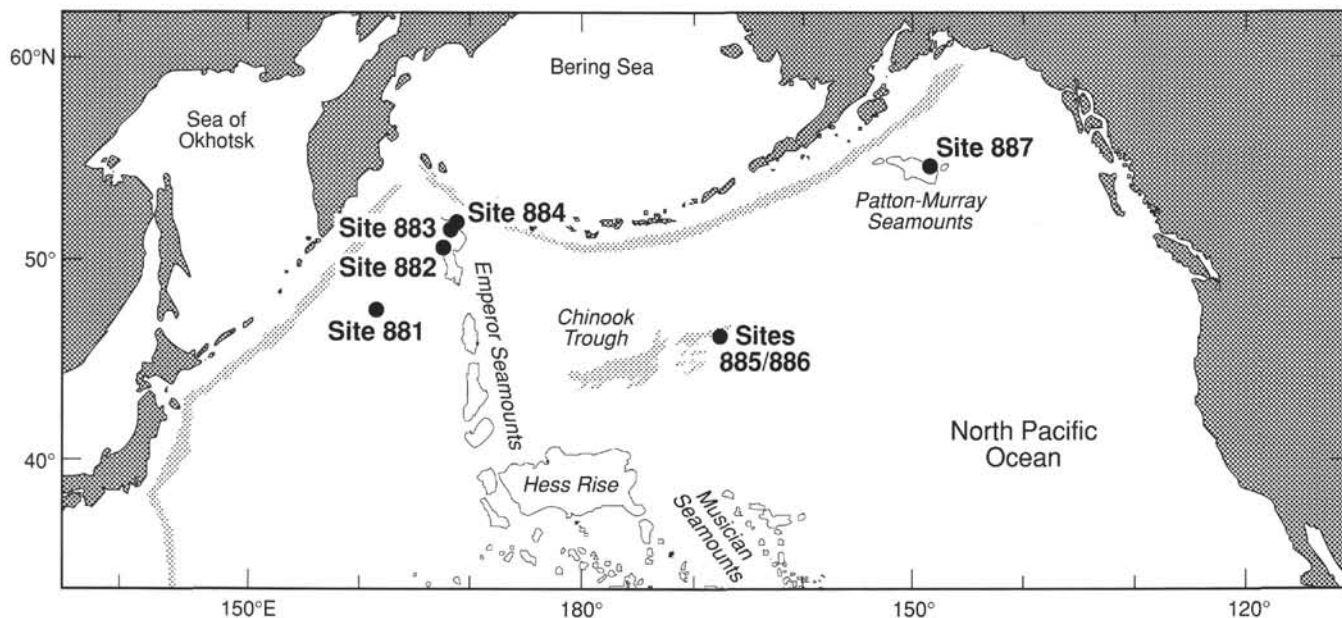


Figure 1. Index map of the North Pacific Ocean showing Leg 145 drill sites.

is a middle to upper Miocene calcareous diatom ooze in its upper portion (Subunit IIIA, 458–597 mbsf) and a lower Miocene diatom nannofossil chalk in its lower portion (Subunit IIIB, 597–652.2 mbsf). Lithologic Unit IV is an upper Eocene to upper Oligocene nannofossil chalk in its upper portion (Subunit IVA, 655–740 mbsf) that grades down to a Paleocene to Eocene clayey and ashy nannofossil chalk in the lower portion (Subunit IVB, 740–814 mbsf). A few chert nodules of Oligocene to Eocene age occur in the chalk. An unconformity occurs where much of the upper Oligocene material is missing; other hiatuses occur in the Eocene and Paleocene parts of the section. The lowermost portion of this section, Subunit IVB (740–814 mbsf) displays evidence of downslope displacement. Laminated layers, small turbidites, scour structures, current ripple marks, soft-sediment deformation structures, and debris flows with matrix-supported clasts of angular ashy chalk all suggest important amounts of reworking low in the section. Partly altered and completely altered ashes, now seen as yellow palagonite and smectite, become important components of the sediments near the bottom of the section, where they make up lithologic Unit V (814–830 mbsf). The age of the sediments immediately overlying the basalt is not well constrained by biostratigraphy; calcareous nannofossils suggest a Campanian age.

About 35 m of basalt was recovered below the sedimentary section in parallel Holes 883E and 883F. These rocks are a series of moderately altered pillow basalts that grade from moderately to highly plagioclase-olivine microphyric basalt to highly olivine-plagioclase microphyric basalt. Initial X-ray fluorescence (XRF) analyses suggest that these basalts are tholeiitic and fairly uniform in composition. Calcite vein and void fillings are common; some interpillow voids are filled with an altered palagonite sediment. One piece of limestone occurs among the pillows. Nannofossils in the palagonites and limestone are severely baked and indicate a general late Mesozoic age.

At Site 883, dropstones occur in Unit I in slightly lower abundances than those encountered at Site 882, 90 km to the south, and in much lower abundances than those at Site 881, about 455 km to the south; again, this is emphasizing the northward decline in ice-rafted debris. In contrast to more southerly locations, no dropstones were found in sediments older than late Pliocene. Ash layers are common to abundant in sediments younger than 2.6 Ma and can be seen again in the Eocene portion of the section. This lower occurrence of ash layers provides one of the first good definitions of a period of Eocene volcanism that has been suggested by

various data from scattered locations. The lower Pliocene and uppermost Miocene sediments at Site 883 are characterized by very high fluxes of biogenic silica, in excess of $3 \text{ g}(\text{cm}^2 \cdot \text{k.y.})^{-1}$. Paleogene carbonates were deposited at lower rates, perhaps 0.5 to $1.0 \text{ g}(\text{cm}^2 \cdot \text{k.y.})^{-1}$. Lower Eocene and Paleocene sediments show striking evidence of redeposition, having been brought into the site by various downslope sedimentation processes.

Magnetic reversal stratigraphy at Site 883 is good in the more clay- and ash-rich Unit I. Reversals associated with the Brunhes/Matuyama boundary, the Jaramillo, Olduvai, and Reunion events, and the Matuyama/Gauss boundary are clear. The more pure siliceous oozes of Unit II are too weakly magnetized to retain the magnetostratigraphy that was determined readily on board the ship. Sedimentation rates at Site 883 average 32 m/m.y. between 0 and 2.6 Ma, are 91 m/m.y. between 2.6 and 6.8 Ma, 23 m/m.y. between 6.8 and 10.8 Ma, and about 10 m/m.y. in the Paleogene carbonates above the zone of downslope redeposition.

BACKGROUND AND SCIENTIFIC OBJECTIVES

Site 883 (proposed Site DSM-1; Fig. 2) is the shallowest of the three-site depth transect down the slopes of Detroit Seamount and the second site to be drilled. Several primary objectives were planned for this site. One was to obtain a high-resolution record of calcium carbonate, and eventually carbon and oxygen isotopic information, so as to define the nature and variability of North Pacific Ocean deep waters. The carbonate record from Site 883 will be compared with those from intermediate-depth Site 882 and deep Site 884 to provide a record of carbonate deposition between 2400 and 3800 m for the northwestern Pacific Ocean. These records can then be compared to records from depth transects in the Atlantic, Indian, and equatorial Pacific oceans. A second important objective was to obtain high-resolution middle to late Neogene records of siliceous sedimentation, terrigenous influx (especially ice-rafted debris) and tephrochronology. Much of the section should be of a suitable lithology for determining a magnetic reversal stratigraphy.

The best chance during Leg 145 for recovering Paleogene and possibly uppermost Cretaceous calcareous sediments was at Site 883. Paleogene and Maastrichtian chalks and limestones, essentially chert-free, had been recovered at Site 192 on Meiji Seamount about 100 miles farther north. Recovery of equivalent sedimentary units, along

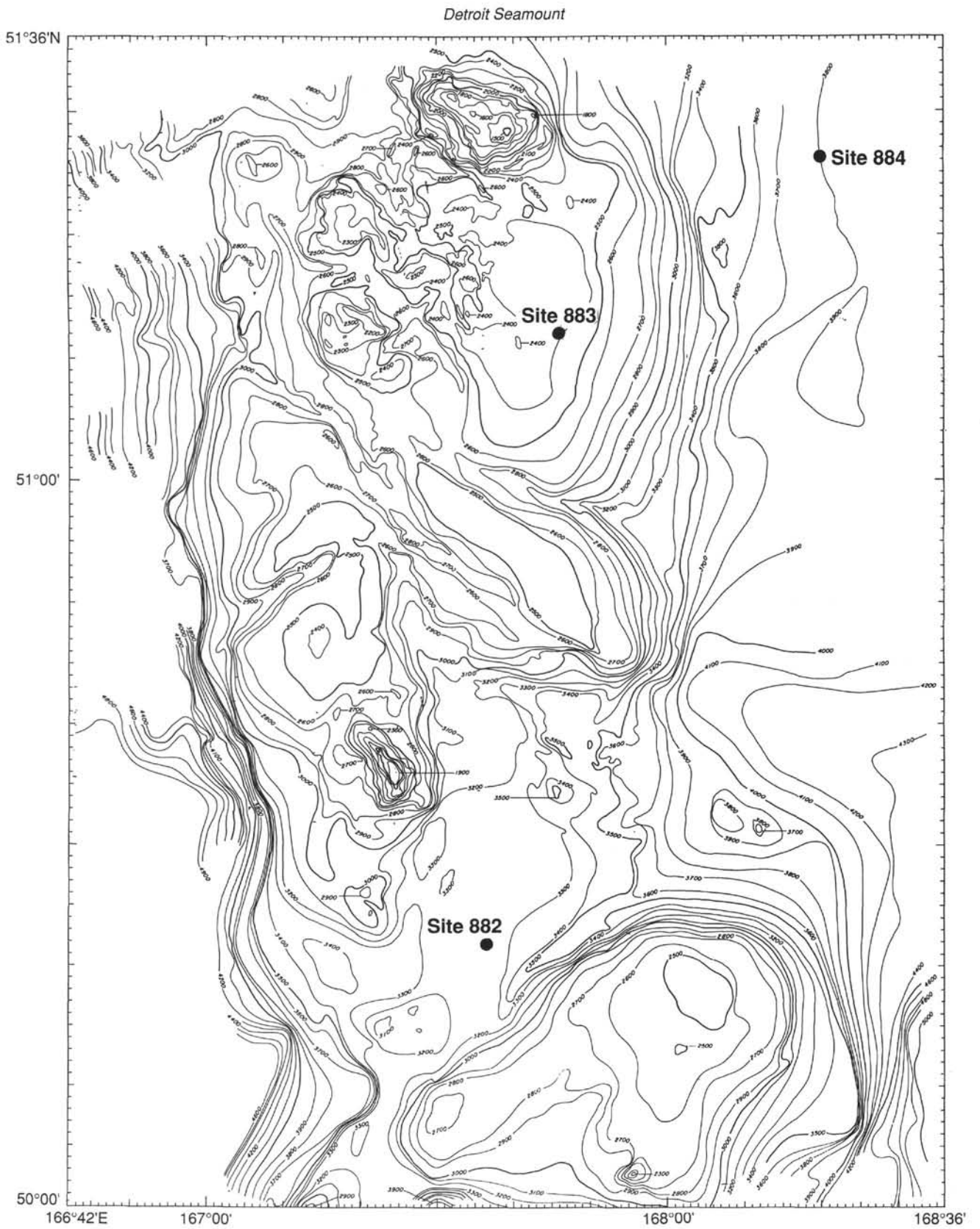


Figure 2. Bathymetry of Detroit Seamount and locations of Leg 145 drill Sites 882, 883, and 884. Contours in meters; map by C. Brenner of Lamont-Doherty Earth Observatory.

with a modest sample of the underlying basalt, was an important objective at Site 883. A complete suite of logs to characterize the entire section was planned for this site.

To achieve these objectives, four holes were planned. The first APC hole was to be short to provide an opportunity for detailed sampling of physical properties. Hole 883B was to be an APC/XCB hole, to be piston-cored until no longer feasible, and then to be continued down with XCB-coring. Hole 883C was to be an APC hole to match that portion of Hole 883B with appropriate vertical offsets. After the completion of piston-coring, the bit was to be changed to an RCB assembly. Hole 883D was to be washed down to the depth of the Hole 883B, where rotary-coring was to begin. Rotary-coring would continue until time to start logging. Logging would consist of the standard three-run suite of tools, plus two runs for the French magnetometer tool.

OPERATIONS

Transit to Proposed Site DSM-1

The 49.0-nmi transit to proposed Site DSM-1 began at 1830 hr (local time), 8 August. At 2330 hr, the ship slowed to 6 kt and began a 13.5-nmi survey. A beacon was launched at 0050 hr at the proposed site location. Upon retrieval of the seismic gear after the beacon was dropped, the ship came about and was on location by 0200 hr, 9 August.

Hole 883A

Hole 883A was spudded at 0715 hr, 9 August, and Core 145-883A-1H was retrieved with 9.5 m of sediment to establish the depth of the mud line at 2407.0 mbrf (see Table 1 for a summary of coring operations at Site 883). Three more APC cores were taken in quick succession at this hole, which was dedicated to physical property studies. The last core (145-883A-4H) was on deck by 0930 hr, after which the bit was pulled out of the hole and cleared the seafloor at 0940 hr. The total cored interval was 38.0 m with 38.49 m recovered (101.3%).

Hole 883B

The ship was offset 20 m north of Hole 883A and at 1100 hr, 9 August, the first piston core was recovered with 7.9 m of sediment to establish the new mud-line depth at 2395.6 mbrf. APC-coring then proceeded to 226.4 mbsf (Core 145-883B-24H), where the first core barrel had to be washed over to recover it from the formation. For the remainder of the APC cores on this hole, procedures were to wash over half the core barrel and then apply up to 120,000 lb of overpull to release the barrel from the sediment. Cores 145-883B-4H through -31H were oriented.

At 292.9 mbsf, the sediment became too stiff for further APC-coring. XCB-coring began with Core 145-883B-32X and proceeded to 448.7 mbsf, where Cores 145-883B-46X (429.0–438.9 mbsf) and -47X (438.9–448.7 mbsf) recovered a total 0.03 m of sediment. In an attempt to increase core recovery, the next core taken was a piston core (145-883B-48H). After washing over this core barrel for 15 min, 9.34 m of sediment was recovered; however, we deemed the sediment too stiff to continue with APC-coring.

XCB-coring resumed to 840.7 mbsf (145-883B-88X), where basalt chips were recovered in the core barrel; the rate of penetration was reduced to 3 m/hr. This depth was considered to be the beginning of basement; thus, the depth objective for the hole had been reached. Overall, 840.5 m of sediment/basement was cored at Hole 883B and 692.9 m was recovered (82.4% recovery). Using the APC system, 302.4 m was cored and 306.36 m was recovered (101.3% recovery). With the XCB system, 538.1 m was cored and 386.54 m was recovered (71.8% recovery).

After Core 145-883B-88X was retrieved, the drill string was pulled out of the hole, and the bit cleared the mud line at 0900 hr, 12 August. While retrieving the pipe, the vessel was offset 20 m north of our previous position.

Hole 883C

Hole 883C was spudded at 1130 hr, with an approximately 4-m vertical offset relative to Hole 883B. Core 145-883C-1H contained 3.13 m of sediment to establish the depth of the mud line at 2396.5 mbrf. APC-coring advanced to 250.0 mbsf (Core 145-883C-27H), at which point we switched over to the XCB-coring system. Cores 145-883C-4H through -27H were oriented.

XCB-coring advanced to 317 mbsf (Core 145-883C-34X), where operations again were switched over to the APC-coring system (Cores 145-883C-35H to -38H) in an attempt to retrieve sediment too soft to be obtained using the XCB in Hole 883B. All these last four APC cores had to be washed-over to be retrieved. The depth objective of the hole was reached after Core 145-883C-38H; the bit was pulled out of the hole and cleared the mud line at 1515 hr, thereby ending Hole 883C. Overall, the APC-coring penetrated 288.0 m of sediment with a 102.8% recovery. With the XCB system, 67.0 m was cored and 48.16 m was recovered (71.9% recovery).

Hole 883D

After offsetting the vessel 20 m west of Hole 883C, Hole 883D was spudded at 1600 hr. After obtaining two cores (17.0 m cored, 17.3 m recovered) to be used for high-resolution sampling, we pulled the bit up to the drill floor to switch over to the RCB-coring system.

Hole 883E

Hole 883E was spudded at 0345 hr, 14 August, and washed down to 300 mbsf, where the first wash barrel was retrieved (empty). After another core barrel was run down the pipe, washing continued to 547.0 mbsf, where the second wash barrel was retrieved. A third core barrel was run down the pipe, and the zone from 547.0 to 556.5 mbsf was cored in an attempt to retrieve an interval that had not been recovered in the other holes at this site. This core contained 6.25 m of sediment, but the interval of interest was not recovered. The bit was washed down farther to 640 mbsf, where continuous RCB-coring began. With RCB-coring, penetration advanced into basement at approximately 820 mbsf and continued to 856.5 mbsf (Core 145-883E-23R), at which point this core barrel became stuck in the pipe. After several attempts to retrieve the core barrel failed, a free-falling funnel (FFF) was deployed and the pipe was pulled out of the hole to retrieve the core barrel.

After retrieval of the core barrel, the pipe was run back to the seafloor. Meanwhile, the weather continued to deteriorate and by the time the bit reached the top of the FFF, winds were near 50 kt, with swells that approached 5 to 6 m, and with ship's heave on the order of 2 to 4 m.

After a 50-min search for the FFF, the bit reentered Hole 883E at 1150 hr, 16 August, and was run in the hole to a depth of 123 mbsf. At this point, the pipe trip stopped while a television camera was brought to the surface. Approximately 40 min later, pipe was again run into the hole. At 1315 hr, while making a pipe connection, the driller observed a 50,000 lb loss of weight. The camera was run back into the hole, where the entire BHA was seen to have had four complete joints and part of a fifth joint of 5-in. drill pipe. The FFF was visible and appeared to be completely intact, as were the three floatation sonar balls. Most likely, the bit packed off while being run in the hole and the 2- to 4-m heave of the vessel caused the pipe to be placed into compression, to flex, and to break at a point 221 m above the bit.

Table I. Coring summary for Site 883.

Core no.	Date (Aug. 1992)	Time (UTC)	Depth (mbsf)	Length cored (m)	Length recovered (m)	Recovery (%)
Hole 883A						
1H	8	2045	0.0-9.5	9.5	9.50	100.0
2H	8	2125	9.5-19.0	9.5	9.58	101.0
3H	8	2155	19.0-28.5	9.5	9.60	101.0
4H	8	2225	28.5-38.0	9.5	9.81	103.0
Coring totals				38.0	38.49	101.3
Hole 883B						
1H	9	0000	0.0-7.9	7.9	7.90	100.0
2H	9	0045	7.9-17.4	9.5	9.90	104.0
3H	9	0120	17.4-26.9	9.5	9.81	103.0
4H	9	0210	26.9-36.4	9.5	7.71	81.1
5H	9	0235	36.4-45.9	9.5	8.86	93.2
6H	9	0310	45.9-55.4	9.5	9.12	96.0
7H	9	0345	55.4-64.9	9.5	9.79	103.0
8H	9	0415	64.9-74.4	9.5	9.94	104.0
9H	9	0450	74.4-83.9	9.5	9.70	102.0
10H	9	0530	83.9-93.4	9.5	8.82	88.2
11H	9	0600	93.4-102.9	9.5	9.77	103.0
12H	9	0630	102.9-112.4	9.5	9.59	101.0
13H	9	0650	112.4-121.9	9.5	9.67	102.0
14H	9	0725	121.9-131.4	9.5	10.12	106.5
15H	9	0800	131.4-140.9	9.5	9.34	98.3
16H	9	0830	140.9-150.4	9.5	9.97	105.0
17H	9	0900	150.4-159.9	9.5	9.77	103.0
18H	9	0930	159.9-169.4	9.5	9.80	103.0
19H	9	1000	169.4-178.9	9.5	9.94	104.0
20H	9	1030	178.9-188.4	9.5	10.01	105.3
21H	9	1100	188.4-197.9	9.5	9.94	104.0
22H	9	1130	197.9-207.4	9.5	9.96	105.0
23H	9	1205	207.4-216.9	9.5	9.83	103.0
24H	9	1250	216.9-226.4	9.5	9.82	103.0
25H	9	1400	226.4-235.9	9.5	9.86	104.0
26H	9	1450	235.9-245.4	9.5	9.46	99.6
27H	9	1535	245.4-254.9	9.5	9.14	96.2
28H	9	1640	254.9-264.4	9.5	9.98	105.0
29H	9	1720	264.4-273.9	9.5	10.02	105.5
30H	9	1750	273.9-283.4	9.5	9.87	104.0
31H	9	1910	283.4-292.9	9.5	9.61	101.0
32X	9	2010	292.9-302.5	9.6	9.68	101.0
33X	9	2050	302.5-312.2	9.7	4.16	42.9
34X	9	2130	312.2-321.9	9.7	7.47	77.0
35X	9	2220	321.9-331.5	9.6	7.83	81.5
36X	9	2255	331.5-341.2	9.7	1.56	16.1
37X	9	2335	341.2-350.9	9.7	4.56	47.0
38X	10	0025	350.9-360.5	9.6	9.48	98.7
39X	10	0110	360.5-370.2	9.7	9.38	96.7
40X	10	0140	370.2-380.0	9.8	9.99	102.0
41X	10	0210	380.0-389.7	9.7	8.81	90.8
42X	10	0245	389.7-399.5	9.8	9.78	99.8
43X	10	0315	399.5-409.3	9.8	9.78	99.8
44X	10	0345	409.3-419.2	9.9	9.21	93.0
45X	10	0415	419.2-429.0	9.8	9.78	99.8
46X	10	0445	429.0-438.9	9.9	0.02	0.2
47X	10	0515	438.9-448.7	9.8	0.01	0.1
48H	10	0635	448.7-458.2	9.5	9.34	98.3
49X	10	0710	458.2-468.1	9.9	9.98	101.0
50X	10	0715	468.1-477.9	9.8	9.55	97.4
51X	10	0820	477.9-487.9	10.0	9.67	96.7
52X	10	0850	487.9-497.7	9.8	0.00	0.0
53X	10	0925	497.7-507.6	9.9	9.99	101.0
54X	10	1000	507.6-517.4	9.8	9.91	101.0
55X	10	1030	517.4-527.2	9.8	9.87	101.0
56X	10	1100	527.2-537.1	9.9	0.00	0.0
57X	10	1135	537.1-547.1	10.0	9.93	99.3
58X	10	1220	547.1-557.0	9.9	0.83	8.4
59X	10	1255	557.0-567.0	10.0	9.96	99.6
60X	10	1335	567.0-577.0	10.0	9.9	90.9
61X	10	1435	577.0-587.0	10.0	9.97	99.7
62X	10	1530	587.0-597.0	10.0	9.88	98.8
63X	10	1610	597.0-607.0	10.0	9.93	99.3
64X	10	1645	607.0-616.7	9.7	2.48	25.5
65X	10	1730	616.7-626.3	9.6	8.02	83.5
66X	10	2015	626.3-636.0	9.7	10.05	103.6
67X	10	2200	636.0-645.1	9.1	10.05	110.4
68X	10	2300	645.1-654.8	9.7	7.39	76.2
69X	10	2330	654.8-664.4	9.6	9.79	102.0
70X	11	0015	664.4-674.1	9.7	10.01	103.2
71X	11	0105	674.1-683.7	9.6	10.05	104.7
72X	11	0120	683.7-693.3	9.6	9.63	100.0
73X	11	0220	693.3-703.0	9.7	9.72	100.0
74X	11	0250	703.0-712.6	9.6	2.99	31.1
75X	11	0355	712.6-720.1	7.5	5.77	76.9
76X	11	0435	720.1-729.9	9.8	8.23	84.0

Table I (continued).

Core no.	Date (Aug. 1992)	Time (UTC)	Depth (mbsf)	Length cored (m)	Length recovered (m)	Recovery (%)
77X	11	0530	729.9-739.7	9.8	7.36	75.1
78X	11	0630	739.7-749.5	9.8	9.8	92.6
79X	11	0710	749.5-759.4	9.9	4.96	50.1
80X	11	800	759.4-769.2	9.8	0.14	1.4
81X	11	900	769.2-779.2	10.0	0.27	2.7
82X	11	1015	779.2-789.2	10.0	10.21	102.1
83X	11	1150	789.2-799.2	10.0	6.07	60.7
84X	11	1310	799.2-808.9	9.7	1.08	11.1
85X	11	1415	808.9-818.5	9.6	5.17	53.8
86X	11	1555	818.5-828.1	9.6	7.04	73.3
87X	11	1735	828.1-837.8	9.7	2.99	30.8
88X	11	2000	837.8-840.7	2.9	0.44	15.2
Coring totals				840.7	695.41	82.7
Hole 883C						
1H	12	0100	0.0-3.0	3.0	3.13	104.0
2H	12	0140	3.0-12.5	9.5	9.85	103.0
3H	12	0215	12.5-22.0	9.5	9.94	104.0
4H	12	0330	22.0-31.5	9.5	8.71	91.7
5H	12	0400	31.5-41.0	9.5	9.64	101.0
6H	12	0430	41.0-50.5	9.5	9.55	100.0
7H	12	0505	50.5-60.0	9.5	9.57	101.0
8H	12	0540	60.0-69.5	9.5	10.08	106.1
9H	12	0620	69.5-79.0	9.5	9.86	104.0
10H	12	0645	79.0-88.5	9.5	9.89	104.0
11H	12	0720	88.5-98.0	9.5	10.8	106.1
12H	12	0750	98.0-107.5	9.5	9.64	101.0
13H	12	0820	107.5-117.0	9.5	10.07	106.0
14H	12	0855	117.0-126.5	9.5	9.43	99.2
15H	12	0930	126.5-136.0	9.5	9.89	104.0
16H	12	1005	136.0-145.5	9.5	9.75	102.0
17H	12	1045	145.5-155.0	9.5	9.84	103.0
18H	12	1120	155.0-164.5	9.5	9.61	101.0
19H	12	1150	164.5-174.0	9.5	8.71	91.7
20H	12	1225	174.0-183.5	9.5	9.76	103.0
21H	12	1320	183.5-193.0	9.5	10.02	105.5
22H	12	1415	193.0-202.5	9.5	10.08	106.1
23H	12	1515	202.5-212.0	9.5	10.13	106.6
24H	12	1630	212.0-221.5	9.5	10.03	105.6
25H	12	1710	221.5-231.0	9.5	10.06	105.9
26H	12	1755	231.0-240.5	9.5	9.88	104.0
27H	12	1915	240.5-250.0	9.5	10.09	106.2
28X	12	2020	250.0-259.6	9.6	0.05	0.5
29X	12	2100	259.6-268.7	9.1	7.91	86.9
30X	12	2140	268.7-278.3	9.6	9.79	102.0
31X	12	2210	278.3-288.0	9.7	9.74	100.0
32X	12	2305	288.0-297.6	9.6	9.74	101.0
33X	13	0000	297.6-307.3	9.7	4.04	41.6
34X	13	0030	307.3-317.0	9.7	6.89	71.0
35H	13	0130	317.0-326.5	9.5	9.58	101.0
36H	13	0205	326.5-336.0	9.5	10.07	106.0
37H	13	0235	336.0-345.5	9.5	9.23	97.1
38H	13	0310	345.5-355.0	9.5	9.97	105.0
Coring totals				355.0	344.30	97.0
Hole 883D						
1H	13	0515	0.0-7.5	7.5	7.53	100.0
2H	13	0555	7.5-17.0	9.5	103.0	9.78
Coring totals				17.0	17.31	101.8
Hole 883E						
***** Washed to 547.0 mbsf *****						
1R	14	0230	547.0-556.5	9.5	6.15	64.7
***** Drilled from 556.5 to 640.0 mbsf (83.5 m) *****						
2R	14	0510	640.0-649.8	9.8	0.56	5.7
3R	14	0630	649.8-659.6	9.8	9.88	101.0
4R	14	0725	659.6-669.5	9.9	3.21	32.4
5R	14	0805	669.5-679.4	9.9	5.45	55.0
6R	14	0850	679.4-689.3	9.9	7.60	76.7
7R	14	0930	689.3-699.2	9.9	9.04	91.3
8R	14	1010	699.2-709.0	9.8	1.79	18.2
9R	14	0110	709.0-718.9	9.9	2.38	24.0
10R	14	1205	718.9-728.8	9.9	0.30	3.0
11R	14	1310	728.8-738.6	9.8	4.46	45.5
12R	14	1405	738.6-748.4	9.8	9.82	100.0
13R	14	1505	748.4-758.3	9.9	7.21	72.8
14R	14	1550				

Table 1 (continued).

Core no.	Date (Aug. 1992)	Time (UTC)	Depth (mbsf)	Length cored (m)	Length recovered (m)	Recovery (%)
18R	14	1930	797.7–807.5	9.8	1.06	10.8
19R	14	2100	807.5–817.4	9.9	9.91	100.0
20R	14	2320	817.4–827.2	9.8	7.07	72.1
21R	14	0500	827.2–837.0	9.8	7.99	81.5
22R	14	0500	837.0–846.9	9.9	7.58	76.5
23R	15	2000	846.9–856.5	9.6	2.61	27.2
Coring totals				226.0	116.56	51.6
Washed 547.0						
Drilled 83.5						
Total 856.5						
Hole 883F						
***** Washed/Drilled from 0 to 820 mbsf *****						
1R	17	1030	820.0–829.5	9.5	4.93	51.9
2R	17	1320	829.5–839.7	10.2	4.67	45.8
3R	17	1600	839.7–849.4	9.7	3.98	41.0
Coring totals				29.4	13.58	46.2

Hole 883F

The pipe was tripped out of the hole and a new RCB and BHA identical to that used at Hole 883E was run to the seafloor. The hole was spudded at 0400 hr, 17 August, and washed down to basement (820 mbsf). During the washing-down operation, empty wash barrels were retrieved at 599.5 and at 820 mbsf. Three RCB cores were taken (820.0–849.4 mbsf) before time constraints forced an end to coring.

In preparation for logging, the hole was flushed with mud. The top drive was set back, and a wiper trip made to 94.5 mbsf and then back down to the base of the hole, where about 3 m of fill was encountered. After flushing the hole again with mud, the bit was released at the bottom and pipe was pulled up to logging depth (119.5 mbsf).

Logging at Hole 883F

Five tool strings were run at Hole 883F: the Schlumberger geochemical, Quad combination, and formation microscanner (FMS) tool strings, and French magnetometer and susceptibility tools. The wireline heave compensator was used on all logging runs. A summary of Hole 883F logging operations is shown in Table 2.

The geochemical combination tool string, consisting of natural gamma-ray (NGT), aluminum activation (AACT) and gamma-ray spectrometry (GST) tools, was calibrated at the sea surface and was run to total depth (3242 mbsf; 846 mbsf). An attempt to re-calibrate the GST at 690 mbsf indicated that the tool would not attain stable re-calibration, possibly owing to very cool bottom-hole temperatures (-3°C). One main up-going log was recorded at 167 m/hr from 846 mbsf to the mud line.

The French magnetometer (NRMT) and susceptibility (SUMT) tools were run next to ensure that both tools would measure a borehole environment unaffected by any electromagnetic induction measurements. Two complete passes of the NRMT were conducted at 548 m/hr from total depth (846 mbsf) to base of pipe at 120 mbsf. The total magnetic field measurements of the NRMT were highly reproducible between the two runs. The quality of these logs was seriously compromised above 220 mbsf because of the presence of several stands of drill pipe that remained in the adjacent Hole 883E, which had been abandoned earlier because of pipe breakage. One main up-going log of the SUMT was recorded at 1097 m/hr from 856 to 120 mbsf; a shorter repeated up-going log was recorded from 380 to 120 mbsf.

The FMS tool string was run next, and three short up-going logs were recorded at 548 m/hr from 846 to 704 mbsf, 846 to 634 mbsf,

Table 2. Summary of logging operations conducted at Site 883.

Local time	Depth (mbsf)	Comments
18 August 1992		
0315		Last core on deck.
1030		Completion of wiper trip; rig up wireline.
1130		Geochemical tool made up and tested.
1330	100	Calibration of geochemical tool.
1500	3242	Tool at T/D; WHC on; begin up-going log. Logging speed, 550 ft/hr.
1515	3190	Tool failed to re-calibrate.
1525	3087	Borehole temperatures at T/D $\sim 3^{\circ}\text{C}$. Several unsuccessful re-calibration attempts at 3062, 3087, and 3063 mbrf.
1610	3242	Tool at T/D, begin second up-going log; GST uncalibrated, AACT and NGT working properly.
2010	2563	WHC turned off, entering pipe.
2200	Surface	Geochemical tool at surface.
2330	Surface	Make up and deploy French magnetometer (NRMT).
19 August 1992		
0200	3242	Begin first up-going log with NRMT. Logging speed, 1800 ft/hr.
0330	3242	Begin second up-going log with NRMT.
0530	Surface	NRMT at surface.
0600		Make up and deploy French susceptibility tool (SUMT).
0730	3242	Begin first up-going log with SUMT, 3600 ft/hr.
0830	2900	Begin second up-going log with SUMT.
0945	Surface	SUMT at surface.
1015	Surface	Make up and deploy FMS tool string.
1125	3242	FMS at T/D, begin first up-going log to 3100 mbrf. Logging speed = 1500 ft/hr.
1200	3231	FMS at T/D, begin second up-going log to 3030 mbrf.
1240	3210	FMS at T/D, begin third up-going log to 3010 mbrf.
1345	3030	Begin fourth up-going log to base of pipe (2497 mbrf).
1425	2529	Pipe raised to 90 mbsf, WHC off.
	2497	FMS in pipe.
1530	Surface	FMS at surface.
1630	Surface	Make up and deploy Quad combination tool string.
1745	2535	Pipe raised to 90 mbsf, begin down-going log; logging speed = 2600 ft/hr.
1845	3226	Quad at T/D, end down-going log.
1845	3226	Density tool (HLDT) caliper will not open. Proceed with up-going log to base of pipe. Logging speed = 1500 ft/hr.
2030	2527	WHC off, Quad enters pipe.
2120	Surface	Quad at surface, rig down, end logging.

Note: WHC = wireline heave compensator.

and 846 to 614 mbsf; the main up-going log was recorded from 846 to 100 mbsf.

The Quad combination tool string, with the Lamont temperature tool, was the final string run into Hole 883F. A down-going log was recorded from 150 mbsf to total depth (840 mbsf). The main up-going log was recorded at 1008 m/hr from 840 mbsf to the mud line. The eccentricizing caliper arm of the lithodensity tool (HLDT) would not open after repeated attempts, so the density and photoelectric effect data recorded during the main up-going log are unreliable because of excessive tool "stand-off."

LITHOSTRATIGRAPHY

Introduction

At Site 883 (Figs. 1 and 2), five major sedimentary units can be identified at (Figs. 3 and 4); these overlie a sixth lithologic unit of tholeiitic olivine basalt. The sedimentary sequence is approximately 830 m thick and ranges in age from Quaternary to Campanian. Unit I (0–86.9 mbsf) contains sparse dropstones ($<0.5\%$) and consists of clay with quartz and clay with diatoms and grades irregularly down-hole to diatom clay and minor diatom ooze with clay. Vitric ashes constitute a minor lithology within Unit I. Unit II (86.9–458 mbsf) consists of diatom ooze that passes downhole irregularly to diatom ooze interbedded with calcareous diatom ooze. Vitric ashes again form a minor lithology. Unit III (458–652.2 mbsf) consists of calcareous diatom oozes interbedded with diatom calcareous oozes or calcareous chalk. Volcanic ashes are absent from Unit III. Unit IV (652.2–814 mbsf) is lithologically diverse, generally being composed

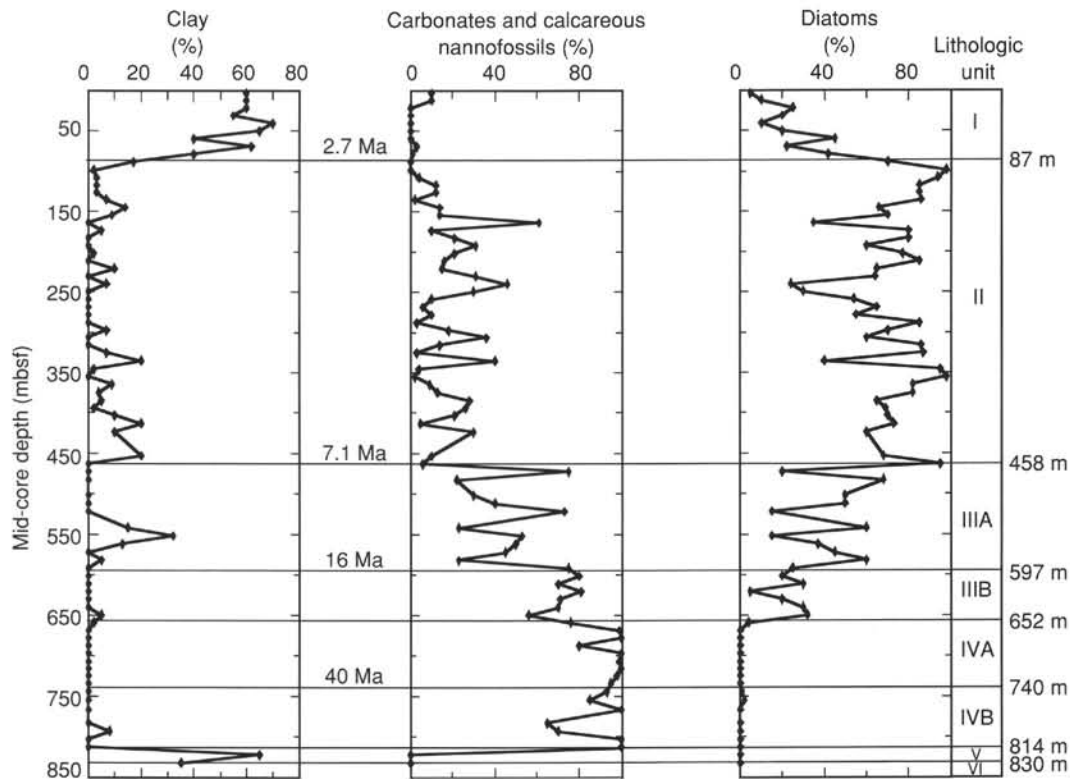


Figure 3. Abundances of clay, total fine-grained carbonate (carbonate particles plus calcareous nannofossils), and diatoms downhole at Site 883, as determined from smear slides. Lithologic units shown at right.

of nannofossil chalk that grades downhole to nannofossil chalk interbedded with increasing amounts of altered ash. Unit V (814–about 830 mbsf) consists of altered ash and claystone.

Both Units III and IV have been divided into two subunits. Subunit IIIA (458–597 mbsf) consists of subequal amounts of interbedded calcareous diatom ooze and diatom nannofossil ooze. Subunit IIIB (597–652.2 mbsf) is similar, but abundances of diatoms are significantly reduced, so that the interbedding in Subunit IIIB is predominantly nannofossil chalk and diatom nannofossil chalk. Subunit IVA (652.2–740 mbsf) consists almost entirely of nannofossil chalk interbedded with minor vitric ashes. Subunit IVB (740–814 mbsf) is characterized by a gradual downhole change from interbedded nannofossil chalk and nannofossil ash to interbedded clayey ash and nannofossil chalk. Evidence of redeposition, hardgrounds, microfaulting, and soft-sediment deformation, including recumbent folding, is widespread in Subunit IVB in Hole 883B. Similar features were noted in Hole 883B, but recovery was poor.

The boundaries between Units I and II and between Subunits IIIA and IIIB at 86.9 and 597 mbsf, respectively (Hole 883B), coincide with major changes in physical properties (see “Physical Properties” section, this chapter). The contact between Units III and IV coincides with the disappearance of diatoms and a color change from green to brown in the nannofossil chalks. The contact between Subunits IVA and IVB is less clear-cut and has been placed somewhat arbitrarily at 740 mbsf, within a gradational interval. This contact is based on the upper limits within Subunit IVB of (1) an overall darkening in color of many chalk intervals and (2) clearly identifiable sedimentary structures, such as laminations, scoured surfaces, and bored hardgrounds.

Because approximately 10% of the sedimentary section was not recovered between successive complete APC cores, an attempt has been made to quantify the size of these gaps by correlating the GRAPE records between Holes 883B and 883C. The coring gaps at these two holes average approximately 1 m (Fig. 5) and are listed in Table 3.

Description of Lithologic Units

Unit I

Interval: Cores 145-883A-1H to -4H
Cores 145-883B-1H to -10H
Cores 145-883C-1H to -10H
Cores 145-883D-1H to -2H

Depth: 0–86.9 mbsf
Age: Quaternary to late Pliocene

Unit I is characterized by an abundance of clay and by the presence of numerous vitric ashes (Figs. 3 and 4). Toward the base of this unit, the clay content decreases rapidly and the abundance of diatoms increases. Consequently, the sediment types change irregularly downhole from dark gray clay with diatoms and quartz to green or green gray diatom ooze with clay and diatom clay. Minor modifying components include spicules, radiolarians, and carbonate particles of undetermined origin. Bioturbation is evident throughout Unit I, with consequent color mottling and scattered large burrows (Fig. 6). Boundaries between the different sediment types contained within Unit I are gradational. Dropstones are rare throughout this unit (Fig. 4), with some core sections containing no dropstones. The largest dropstone, which is approximately 6 cm in diameter, occurs at Section 145-883A-1H-4, 27 cm, and is composed of altered felsic welded tuff. Other dropstone varieties that are present in Unit I include matrix-rich, microfossil-bearing graywacke (re-sedimented ash), andesitic welded tuff, and basic andesitic lavas, similar to the dropstone lithologies recovered at Sites 881 and 882.

Individual vitric ashes within Unit I are up to 18 cm thick (e.g., interval 145-883B-7H-6, 20–38 cm). The vitric ashes are most abundant between approximately 65 and 75 mbsf (Fig. 4). This pyroclastic component is also present as ash pockets and burrow infills. The majority of the ashes are light brown or gray (Fig. 7), but some are black.

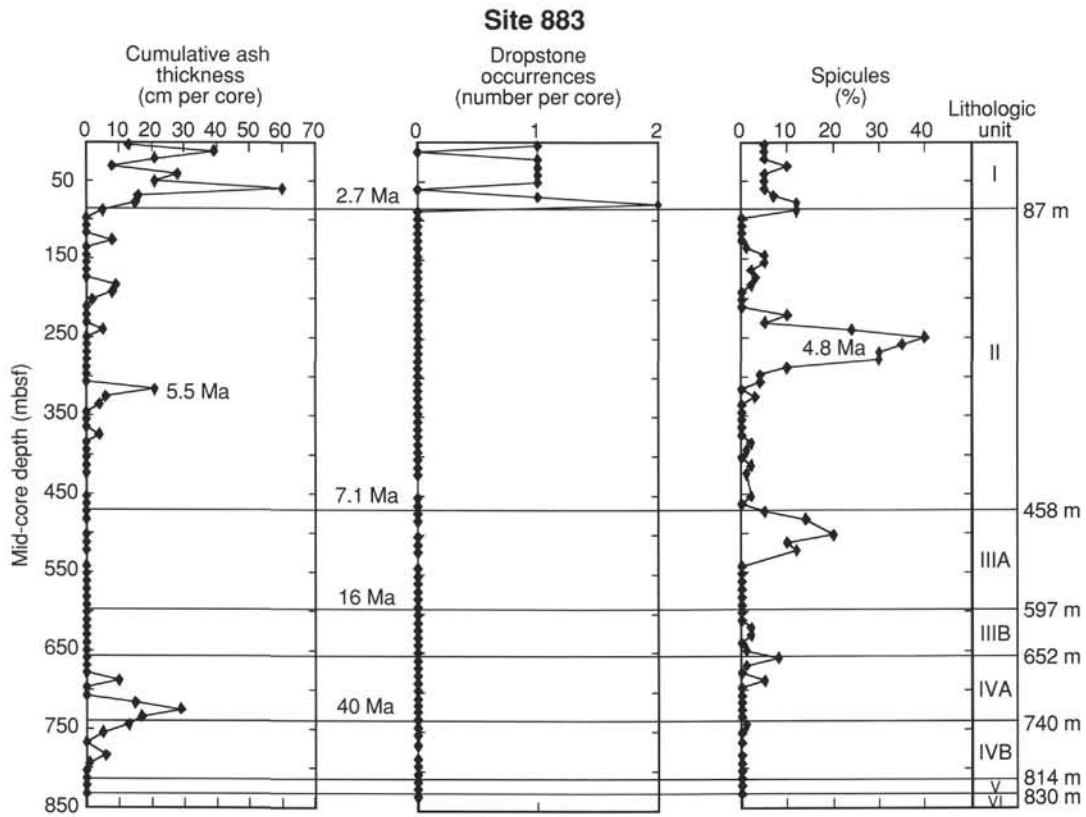


Figure 4. Cumulative ash thickness per core, number of dropstones per core, and spicule abundance (determined from smear slides) downhole at Site 883. Lithologic units shown at right.

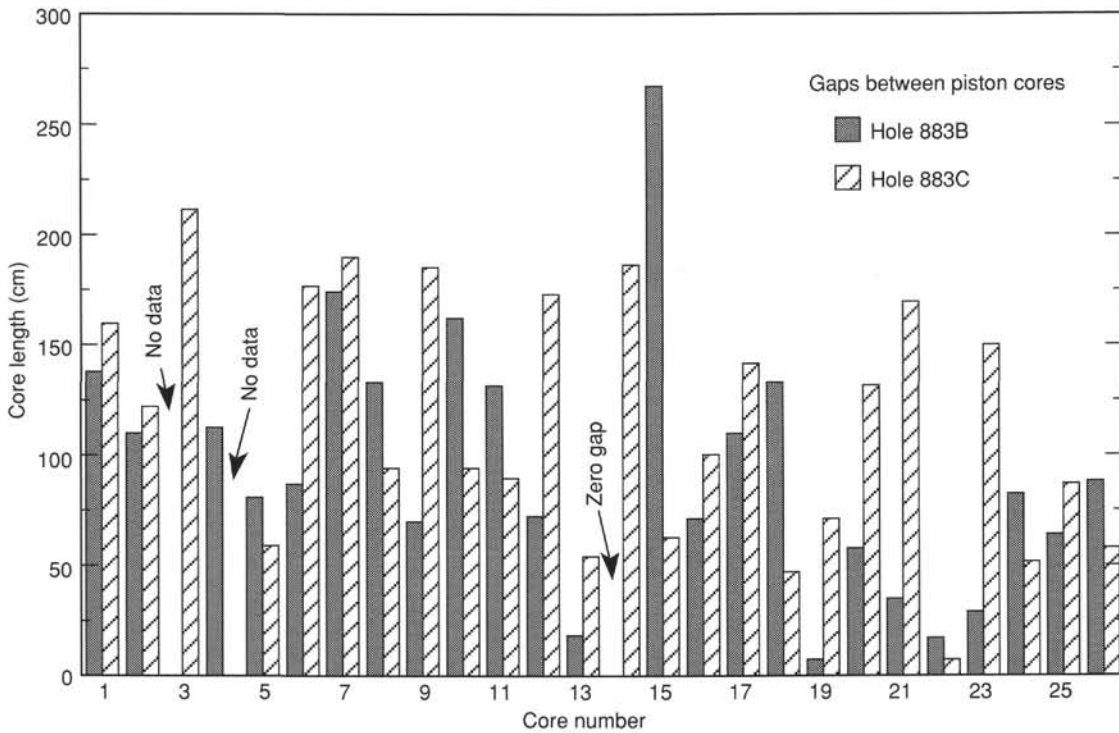


Figure 5. Illustration of recovery gaps between Cores 145-883B-1H to -26H and Cores 145-883C-1H to -26H, as determined from correlation of GRAPE records.

Table 3. Recovery gaps between Cores 145-883B-1H to -26H and Cores 145-883C-1H to -26H, as determined from correlation of GRAPE records.

Hole 883B coring gaps (cm)			Hole 883C coring gaps (cm)			Hole 883D coring gaps (cm)		
Between core and core		is a gap of	Between core and core		is a gap of	Between core and core		is a gap of
1H	2H	13	1H	2H	160	1H	2H	138
2H	3H	111	2H	3H	123			
3H	4H	Flow-in in 883C-4H	3H	4H	212			
4H	5H	113	4H	5H	Flow-in in 883C-4H			
5H	6H	81	5H	6H	60			
6H	7H	87	6H	7H	177			
7H	8H	175	7H	8H	190?			
8H	9H	133	8H	9H	95			
9H	10	71	9H	10H	185			
10H	11	163	10H	11H	95			
11H	12	132	11H	12H	90			
12H	13	73	12H	13H	174			
13H	14	18	13H	14H	55			
14H	15	0	14H	15H	187			
15H	16	268	15H	16H	63			
16H	17	72	16H	17H	101			
17H	18H	111	17H	18H	142			
18H	19H	134	18H	19H	47			
19H	20H	8	19H	20H	72			
20H	21H	58	20H	21H	132			
21H	22H	36	21H	22H	170			
22H	23H	17	22H	23H	8			
23H	24H	30	23H	24H	150			
24H	25H	83	24H	25H	52			
25H	26H	64	25H	26H	88			
26H	27H	89	26H	27H	58			

Many of the thicker ashes show size grading and have sharp bases, but their upper surfaces are often indistinct as a result of bioturbation.

Unit II

Interval: Cores 145-883B-11H to -49X
Cores 145-883C-11H to -38H
Depth: 86.9–458 mbsf
Age: late Pliocene to late Miocene

Unit II consists predominantly of grayish-green or gray diatom ooze. Light brown or brown calcareous diatom ooze and diatom ooze with calcite are subordinate lithologies, and their abundances increase below 160 mbsf. Between 291.6 mbsf (Core 145-883B-31H) and 317.7 mbsf (Core 145-883B-34X), gray diatom calcareous ooze or calcareous diatom ooze is common, alternating with diatom ooze. All of these sediment types within Unit II are moderately bioturbated and exhibit gradational boundaries.

Vitric ashes in Unit II are apparently similar to, but less numerous than, those present in Unit I. These ashes constitute a very minor sediment type that is irregularly distributed to 376 mbsf (Section 145-883B-40X-6). An interval of pumice lonestones, individually up to 1.7 cm in diameter, occurs between 131.26 and 131.40 mbsf (Core 145-883B-14H-7).

Unit III

Interval: Cores 145-883B-49X to -68X
Cores 145-883E-1R to -3R
Depth: 458–652.2 mbsf
Age: late Miocene to early Miocene

Unit III consists of diatom and diatom calcareous oozes interbedded with calcareous or nannofossil oozes, which grade downhole to nannofossil chalk. Vitric ashes are absent in Unit III.

Subunit IIIA

Interval: Cores 145-883B-49X to -62X-CC
Core 145-883E-1R
Depth: 458–597 mbsf
Age: late Miocene to middle Miocene

Subunit IIIA is a lithologically mixed sequence, with gray green and gray brown diatom ooze interbedded with gray white calcareous diatom ooze, and subordinate but appreciable amounts of light gray diatom nannofossil or diatom calcareous ooze. Subunit IIIA forms a transitional sequence between the highly siliceous sediments of Unit II and the dominantly calcareous sediments of Subunit IIIB and Unit IV. A minor modifying component is clay, which increases in abundance between approximately 530 and 557 mbsf. This subunit displays moderate amounts of bioturbation throughout its extent.

Subunit IIIB

Interval: Cores 145-883B-62X to -68X
Cores 145-883E-2R to -3R
Depth: 597–652.2 mbsf
Age: middle Miocene to early Miocene

Subunit IIIB is composed almost entirely of bioturbated stiff nannofossil ooze or nannofossil chalk. The chalks often contain an appreciable diatom component (approximately 20%–25%; Fig. 3) and are light greenish-gray in color. Below 652.2 mbsf, in Unit IV, diatoms are virtually absent and the chalks are brownish-gray or white in color. This sharp boundary between lithologic Units III and IV, which is evidenced by a color change, is seen at 652.2 mbsf (Section 145-883B-68X-CC; Fig. 8).

The bioturbation present throughout Subunit IIIB differs somewhat from that visible in the overlying sediments in that discrete, subhorizontal *Zoophycos* trace fossils are clearly apparent throughout Subunit IIIB (Fig. 9). However, *Zoophycos*-like features may well be present higher in the sedimentary section, but were not observed because of sediment disturbance caused when those cores were split with a wire. Small-scale diagenesis associated with the bioturbation is clearly indicated by a burrow at approximately 619 mbsf (Section 145-883B-65X-2) that contains macroscopic pyrite crystals.

Unit IV

Interval: Cores 145-883B-68X to -85X
Cores 145-883E-3R- to -19R
Depth: 652.2–814 mbsf
Age: late Oligocene to early Eocene

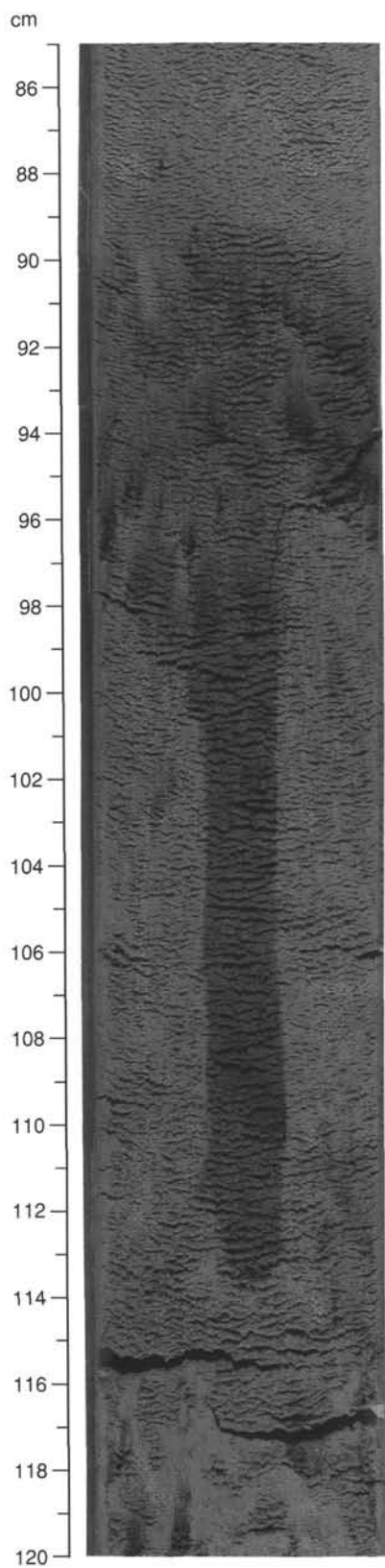


Figure 6. Large vertical burrow in the diatom clay of Unit I (interval 145-883B-7H-4, 85–120 cm).

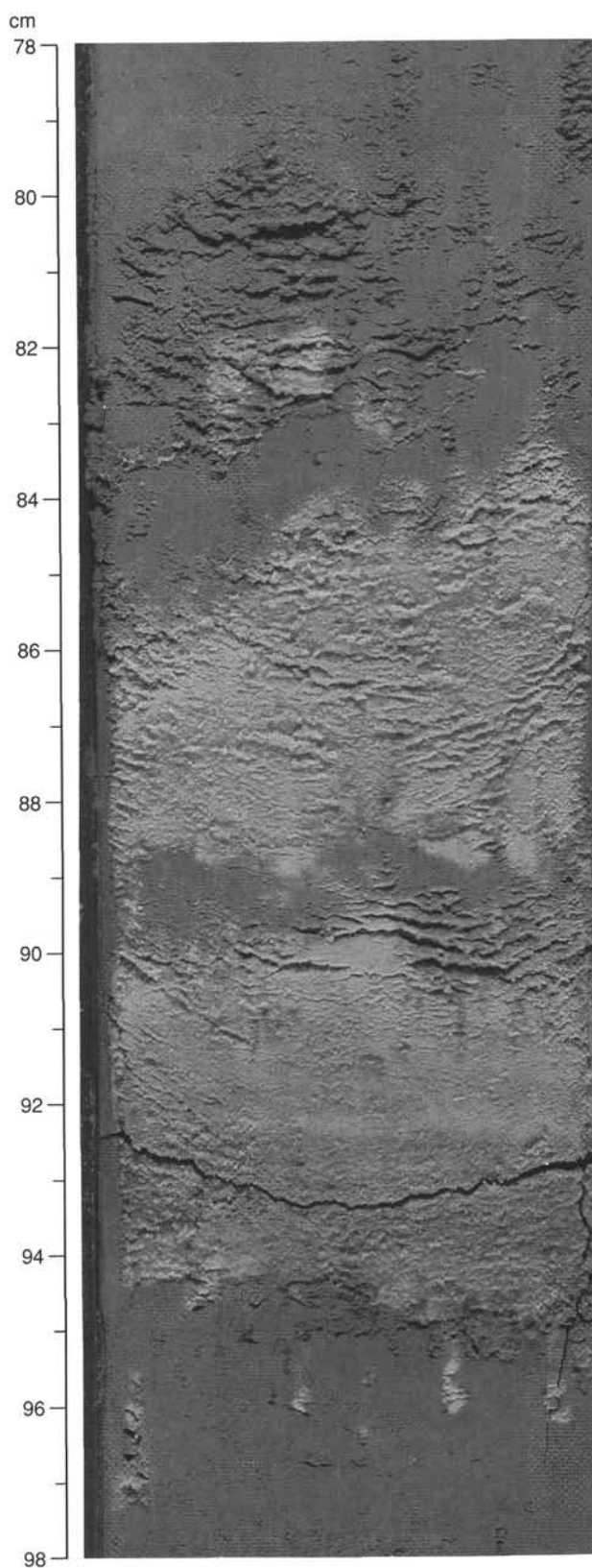


Figure 7. Two slightly bioturbated light gray vitric ashes interbedded with diatom clay in Unit I (interval 145-883B-7H-4, 78–98 cm).

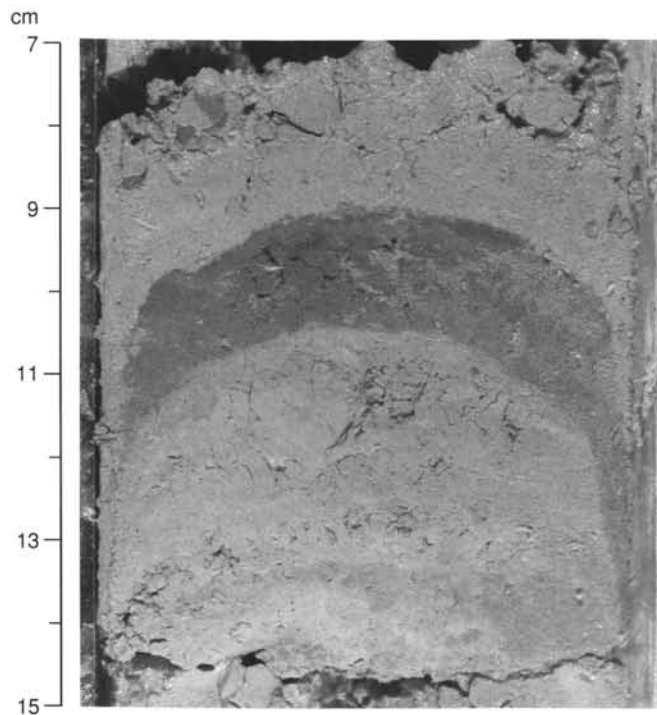


Figure 8. Photograph showing the sharp color boundary between the light gray green, above, and the brown nannofossil chinks, below, at the contact between Subunits IIIB and IVA. The dark band and the chalk below it are brown. The fine-scale brecciation throughout the interval illustrated is the result of drilling disturbance (interval 145-883B-68-CC, 7–15 cm).

Unit IV consists of nannofossil chinks interbedded with vitric ashes, and grades to nannofossil chalk and nannofossil ash with minor vitric ashes below approximately 740 mbsf.

Subunit IVA

Interval: Cores 145-883B-68X to -78X
Cores 145-883E-3R to -12R
Depth: 652.2–740 mbsf
Age: late Oligocene to middle Eocene

Unit IVA consists predominantly of nannofossil chalk. The only other sediment type present is dark vitric ash, forming layers up to 12 cm thick (Fig. 10). Some of these ashes are extensively bioturbated (Fig. 11).

Subunit IVB

Interval: Cores 145-883B-78X to -85X
Cores 145-883E-12R to -19R
Depth: 740–814 mbsf
Age: middle Eocene to early Eocene

Subunit IVB consists predominantly of nannofossil chalk and nannofossil ash, interbedded with altered ash layers that become more abundant downhole. The nannofossil chinks and nannofossil ashes in the upper part of Subunit IVB are bioturbated (including discrete *Zoophycos* trace fossils) and show current-produced sedimentary structures, such as lenticular microlamination and small-scale cross-stratification, as well as deformational structures, such as load casts and convolute laminations. Scoured surfaces and burrowed hardgrounds (Fig. 12) are also present. Microfaulting is widespread and soft-sediment deformational features include rotated bodies and re-

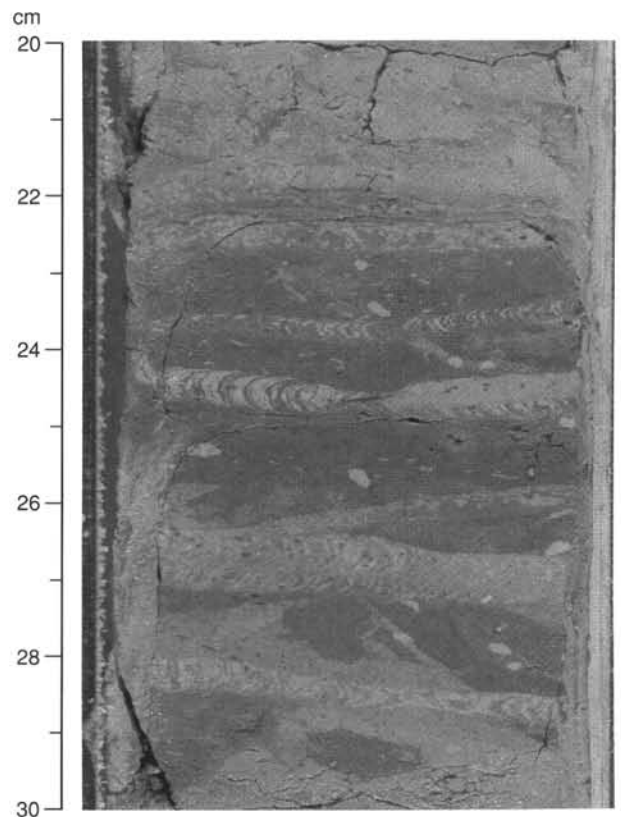


Figure 9. Horizontal *Zoophycos* burrows in gray nannofossil chalk of Subunit IIIB (interval 145-883B-65X-5, 20–30 cm).

cumbent folding on both the micro- (centimeters) and meso- (tens of centimeters) scales (Figs. 13 and 14).

Subunit IVB (at both Holes 883B and 883E) contains much evidence of sediment redeposition in the form of debris or diamicrites (e.g., Cores 145-883B-83X, 145-883E-15R and -16R), which are composed of very angular clasts of altered ash (up to 8 cm in maximum dimension) in a matrix of ashy nannofossil chalk (Figs. 15 and 16). Carbonate mud turbidites approximately 4 cm thick are also present in Core 145-883E-16R. Intervals of undisturbed (nonre-sedimented) strata are relatively minor in both Cores 145-883E-15R and -16R. A 20-cm-thick interval of relatively unaltered laminated vitric ash occurs at approximately 798 mbsf (Core 145-883E-18R).

Unit V

Interval: Cores 145-883B-85X to -87X
Cores 145-883E-19R to -20R
Core 145-883F-1R
Depth: approximately 814–830 mbsf (Hole 883B)
Age: Paleocene–Campanian(?)

Unit V consists of yellow green and yellow brown to reddish-brown altered (palagonitic?) ashes that are speckled with iron and manganese oxides. The ashes are nearly completely reconstituted to assemblages of smectite, some chlorite, and minor illite, as indicated by XRD analyses of two samples. Quartz and feldspar are also present as minor constituents in the altered ashes. A discrete lamina of opaque hydrothermal(?) oxides or sulfides, approximately 5 mm thick, occurs at 818.3 mbsf in Core 145-883E-20R, and similarly in Core 145-883F-1R at 822.5 mbsf. Comparison of Core 145-883E-20R with Core 145-883F-1R (using the thin lamina of hydrothermal sediment

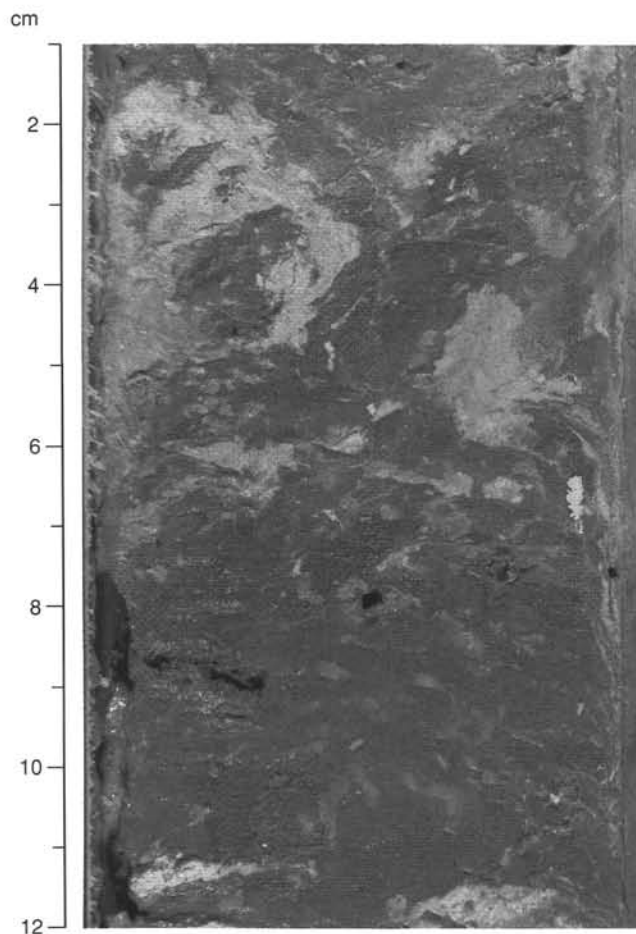


Figure 10. Slightly bioturbated dark vitric ash with Subunit IVA. Bioturbated nannofossil chalk underlies the ash (interval 145-883B-72X-2, 1–12 cm).

as a datum) suggests that at least 20 cm of ash is missing in Hole 883F above the youngest recovered basalt.

Unit VI

Interval: Cores 145-883E-20R to -23R
 Cores 145-883F-1R to -3R
 Depth: approximately 819–856.5 mbsf (Hole 883E)
 approximately 822.6–849.4 mbsf (Hole 883F)
 Age: unknown

Unit VI consists of at least 37.5 m of moderately altered pillow basalts, which grade from moderately and highly plagioclase-olivine microphyric tholeiitic basalt to highly olivine-plagioclase microphyric tholeiitic basalt. These are described in more detail elsewhere in this chapter (see “Igneous Petrology” section, this chapter).

Discussion

The following features of the sequence at Site 883 merit comment.

The remarkable dominance of biogenic silica sedimentation throughout the late Miocene to late Pliocene is represented by the overwhelmingly diatomaceous Unit II. It becomes apparent, however, that this biogenic silica peak was initiated further downhole, in the upper Miocene strata of Subunit IIIA, if due consideration is given to the prominent sponge spicule contribution centered about 250 mbsf (Fig. 4). A similar and possibly correlative spicule contribution peak is apparent at Site 881 at ca. 4.8 Ma (see “Lithostratigraphy” section, “Site 881” chapter, this volume).

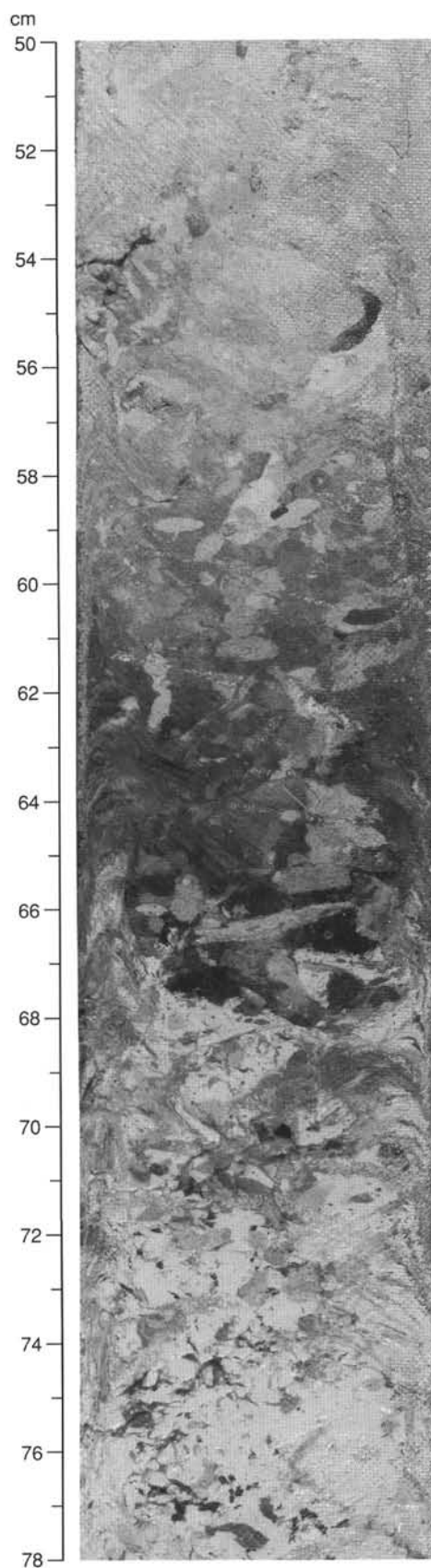


Figure 11. Bioturbated dark vitric ash within moderately bioturbated nannofossil chalk of Subunit IVA (interval 145-883B-72X-5, 50–78 cm).

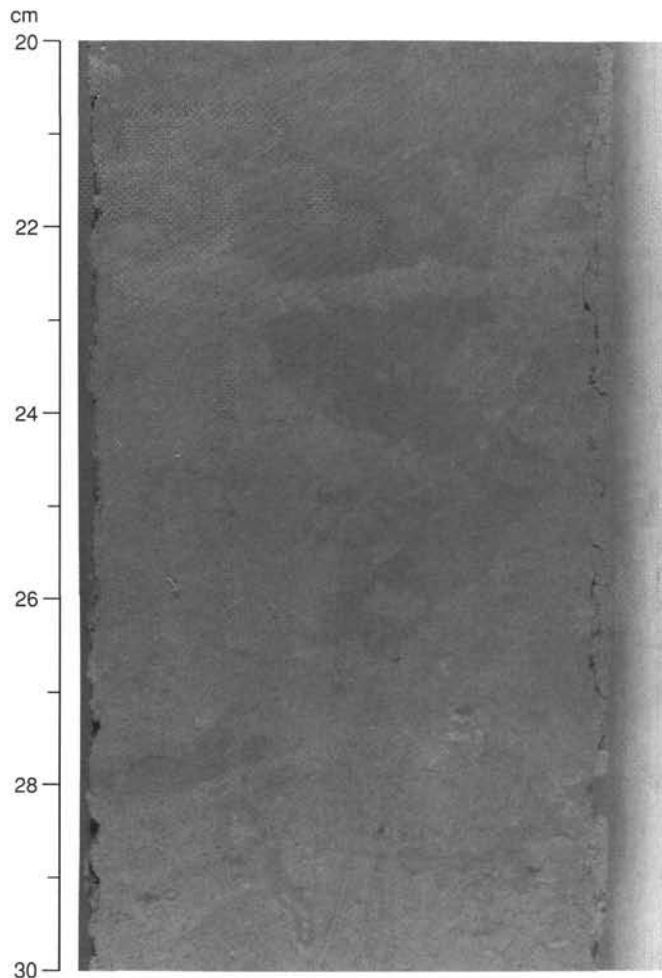


Figure 12. Large, cone-shaped open burrow in light-colored nannofossil chalk, filled in by darker chalk. The size, shape, and nature of the burrow fill suggest that this feature was developed on a subaqueous hardground. The burrow infill and the surrounding hardground were subsequently bored by *Zoophycos* (Subunit IVB, interval 145-883E-12R-3, 20–30 cm).

The clay component in upper Pliocene and Quaternary sediments at the relatively shallow Site 883 is considerably more abundant than the clay component in correlative sediments at the deeper Sites 881 and 882 (see "Lithostratigraphy" section, "Site 881" and "Site 882" chapters, this volume). The apparent decrease in dropstones at Site 83 relative to Sites 881 and 882 is also surprising, particularly the decrease when compared to those found at Site 882. Only an upper Pliocene–Quaternary dropstone interval can be recognized at Site 883. No lower Pliocene and Miocene dropstones were recovered. The Site 883 dropstone distribution is compatible with the incidence of dropstones at DSDP Sites 579 and 580 to the south (Krissek et al., 1985) and Sites 881, 882 (see "Lithostratigraphy" section, "Sites 881 and 882" chapters, this volume), and with the accepted onset of major Northern Hemisphere glaciation at 2.6 Ma (Shackleton et al., 1984; Rea and Schrader, 1985). The much-reduced glaciogenic influx at Site 883 does suggest that this site is more distal with respect to iceberg transport paths, however. Finally, the limited data available suggest no major change in dropstone provenance relative to that observed at Sites 881 and 882. Pyroxene (basic) andesite, andesitic marine volcanoclastic, and metamorphosed felsic volcanic contributions all occur at the three sites.

The abundant clay component of Unit V is altered volcanic ash, rather than being of direct terrigenous origin. In contrast, the vitric

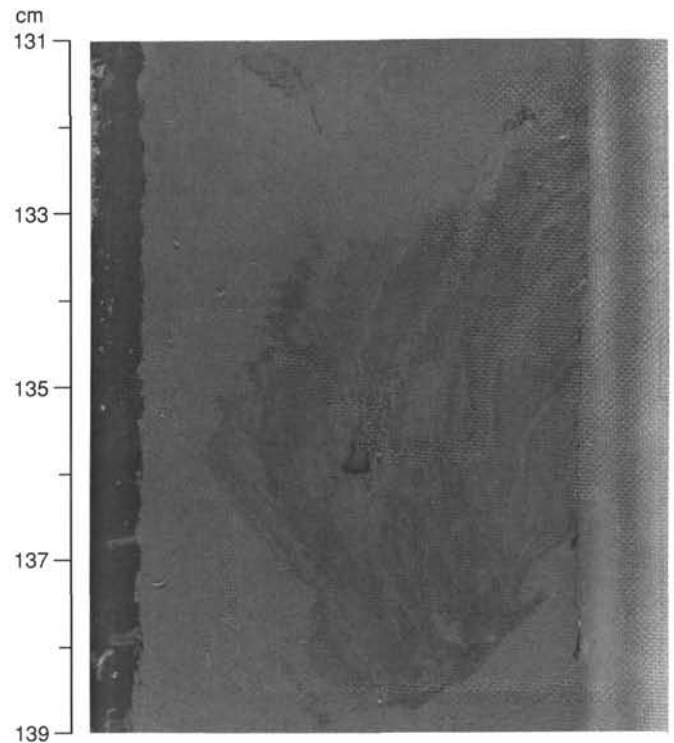


Figure 13. Soft-sediment deformation and microfaulting observed in an intraclast of gray nannofossil chalk that was originally laminated and has subsequently been burrowed. The surrounding matrix is lighter colored nannofossil chalk. Note that the upper boundary of the nannofossil chalk matrix also displays microfaulting (interval 145-883E-12R-4, 131–139 cm).

ashes associated with the abundant clay component in Unit I are still fresh and show little sign of alteration to clay minerals.

When the altered ashes of Unit V are excluded, the simplest interpretation of the record of cumulative ash thickness per core (Fig. 4) indicates (1) an early Eocene-early Oligocene phase of volcanism and (2) a Pliocene-Pleistocene phase of volcanism. The ash frequency within the latter interval, which is presumably a record of parts of the Kurile, Kamchatka, and Aleutian arcs, increases greatly at ca. 2.7 Ma and so is in agreement with the late Pliocene-Pleistocene peak of volcanism identified by Kennett et al. (1977). This distribution of Neogene ashes at Site 883 is similar to that documented nearby at Sites 881 and 882 (see "Lithostratigraphy" section, "Sites 881 and 882" chapters, this volume) and at DSDP Sites 578 and 579 (Heath, Burckle et al., 1985). However, assessing the frequency of volcanism in such a way requires caution, as many thin ashes are doubtlessly obliterated by bioturbation (Fig. 11) and their survival depends considerably upon the sedimentation rate of nonpyroclastic components and the degree of biological activity on the seafloor.

The lower Eocene to lower Oligocene ashes recovered at Site 883 are particularly noteworthy, as their recovery is apparently unique to the region so far. The oldest ashes recovered during DSDP Leg 86 were obtained at Site 581 and are dated at 12 Ma (Heath, Burckle, et al., 1985). No Paleogene ashes were recovered at Site 192 during DSDP Leg 19 (Scholl and Creager, 1973). Thus, the ashes in Unit IV at Site 883 will provide invaluable data about Paleogene volcanism in or adjacent to this portion of the Pacific Ocean.

IGNEOUS PETROLOGY

Introduction

Two of the holes drilled at Site 883 (Figs. 1 and 2) penetrated basaltic basement. Coring in Hole 883E penetrated 37.8 m into base-

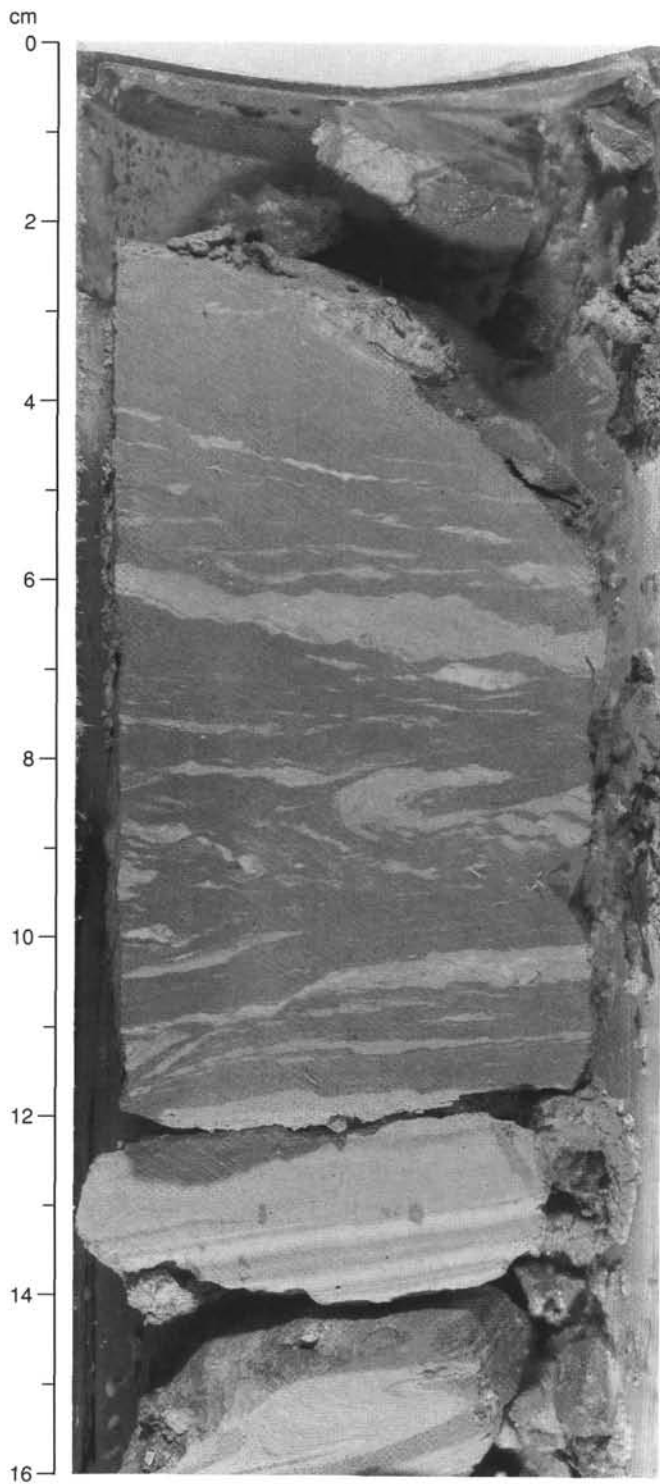


Figure 14. Laminated nannofossil chinks showing soft-sediment folding and subsequent extensional microfaulting (interval 145-883E-13R-3, 0–16 cm).

ment (818.7–856.5 mbsf), and 23.75 m of basalt was recovered (63% recovery). Hole 883F penetrated 26.7 m into basement (822.7–849.4 mbsf) and 10.93 m of basalt was recovered (41% recovery). From both holes, a series of fractured and altered basaltic pillows and massive flows was recovered. Cores from Hole 883E were divided into 27 lithologic units, while 16 units were identified in cores from Hole 883F. Delineation of these units was based almost entirely upon

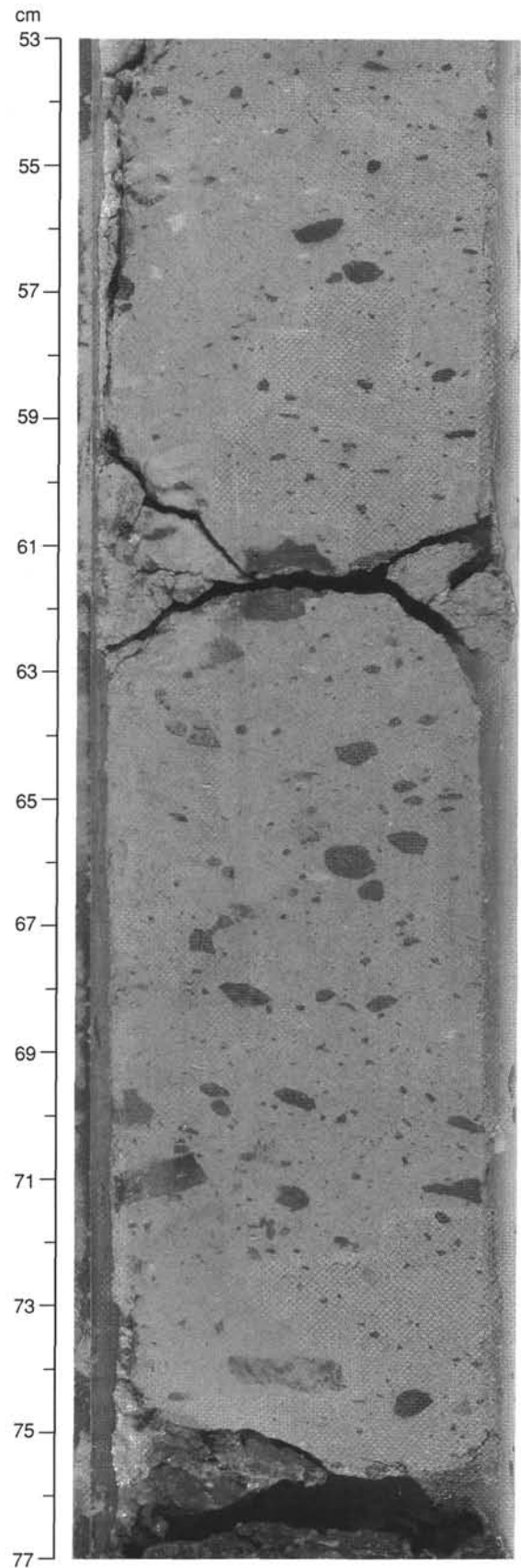


Figure 15. A resedimented diamictite of nannofossil chalk containing well-dispersed dark angular clasts of altered clayey ash (interval 145-883B-83X-1, 53–77 cm).

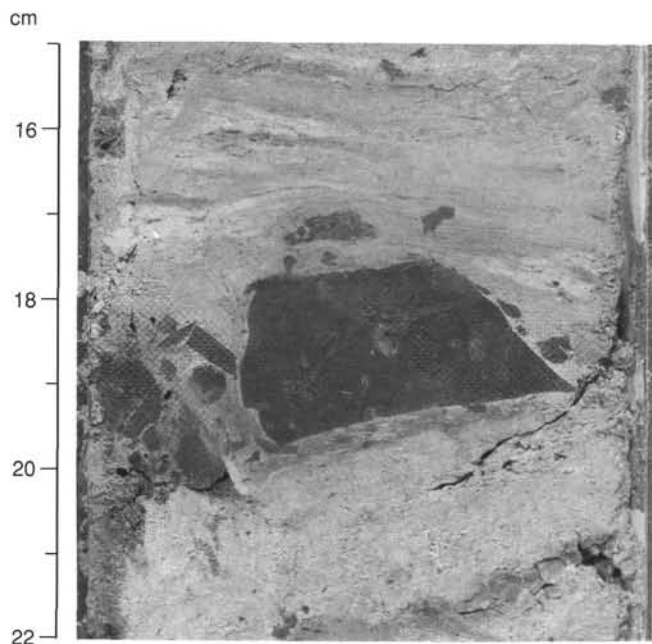


Figure 16. Three-cm-thick interval of resedimented, very angular clayey ash intraclasts, contained within layered nanofossil chalk that exhibits soft-sediment deformational features. Note smaller and well-dispersed intraclasts within the older nanofossil chalk diamictite (matrix-supported debris flow) at the bottom of the interval shown (interval 145-883E-15R-3, 15–22 cm).

the presence of quenched margins, rather than observed changes in lithology. In some cases, as much variation in macroscopic appearance is seen in a single 1-m pillow as in the entire core. The majority of the rocks contain moderate amounts of plagioclase microphenocrysts (0.5–1.5 mm) and reddish-brown alteration products (iddingsite) after olivine microphenocrysts.

Hole 883E

Basalt recovered from Hole 883E consists of a series of highly fractured pillows and flows. Twenty-seven lithologic units were identified, almost always based upon the presence of quenched, usually brown glass, margins. Within a few centimeters of these margins, the basalts are almost aphyric, but otherwise an average of 10%–15% plagioclase microphenocrysts is scattered in a microcrystalline groundmass. Olivine microphenocrysts originally made up 1%–10% of the rock, but are now entirely replaced by clays. Rare clinopyroxene microphenocrysts were noted in a few thin sections. Vesicularity ranges from 0%–20%, but, as with crystallinity, as much variation often occurs in a single unit as within the entire core.

Many vesicles have been filled in with calcite (analyzed by XRD). Narrow (<5 mm) fractures have also been filled in with calcite (Fig. 17), while larger fractures have been filled in with sedimentary rock consisting of calcite with clays, plagioclase, and quartz. These sediments have also filled in gaps between neighboring pillows (Fig. 18), and apparently acted as a cement to hold these pillows together during drilling. A beautifully recovered vertical margin between neighboring pillows (Fig. 19) testifies to the integrity of this sedimentary cement.

No downhole trends are evident in macroscopic or microscopic features of the basalts, although a few large (4–9 mm) plagioclase lathes occur low in the core (in Units 25 and 24).

Hole 883F

Basalt recovered from Hole 883F is lithologically similar to basalt from Hole 883E. Sixteen units were defined in cores from Hole 883F,

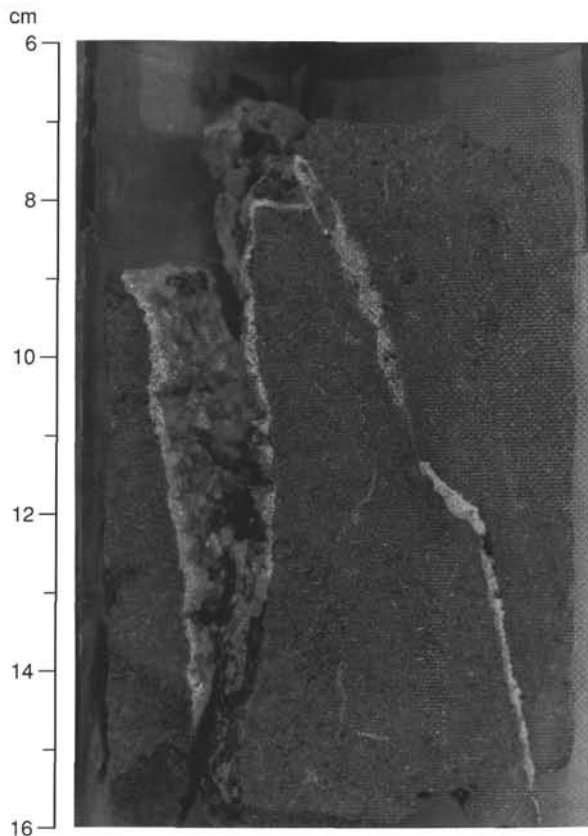


Figure 17. Photograph of Interval 145-883E-23R-2, 6–16 cm, showing calcite fracture infilling.

but, as with cores from Hole 883E, units were almost always identified by the presence of brown glass margins, rather than lithologic changes. The most notable difference among cores from the two holes is the lower frequency of fractures in cores from Hole 883F. Fractures of any kind are fewer, and none wider than 5 mm occur in cores from Hole 883F. In addition, complete sections of pillows, from glassy top margin to radially fractured interior to glassy bottom margin, do not occur in cores from Hole 883F; such complete sections are common in cores from Hole 883E. Whether this lack of nicely sectioned pillows is a result of lower recovery, or the lower recovery of Hole 883F resulted from the lack of well-cemented pillows, is not known.

Geochemical Results

Twenty-two samples from Holes 883E and 883F were analyzed for trace-element concentrations by XRF (Table 4). No systematic downhole chemical variations are evident, nor are significant chemical differences seen between the two holes. Most concentrations of trace elements increase co-linearly with zirconium (Zr is chosen here as the basis for comparison because it is relatively immobile during alteration and can be analyzed well by the XRF technique), suggesting that all of the Site 883 basalts can be related by fractional crystallization. Three obvious deviations from this co-linearity are the compatible elements nickel (Ni) and chromium (Cr), and the incompatible element rubidium. Cr concentrations appear to increase with increasing Zr up to a point (~155 ppm Zr), and then decrease as Zr continues to increase. This suggests that only the more evolved lavas experienced significant fractionation of a Cr-bearing phase (e.g., spinel or diopside). Ni and Rb do not appear to correlate with Zr. In both cases, this is probably an effect of alteration. Ni is compatible in olivine and may have been remobilized when the olivine was altered

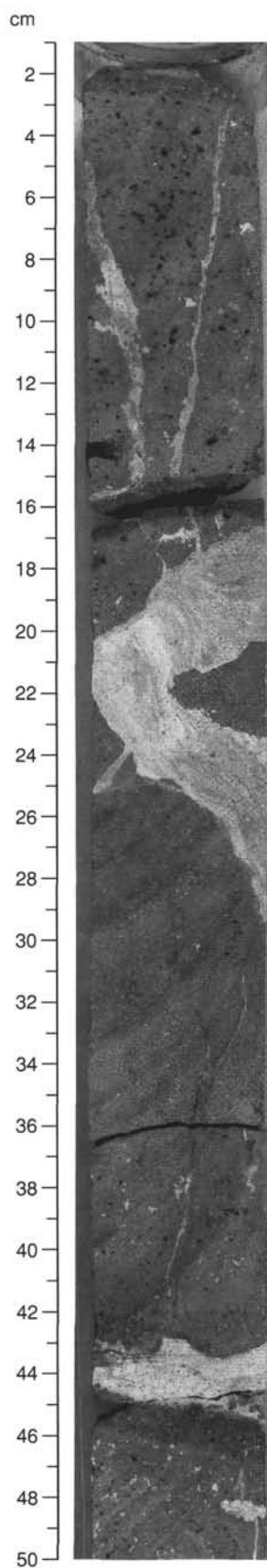


Figure 18. Photograph of Interval 145-883E-20R-5, 0–50 cm, showing bedded sedimentary infilling between basalt pillows.

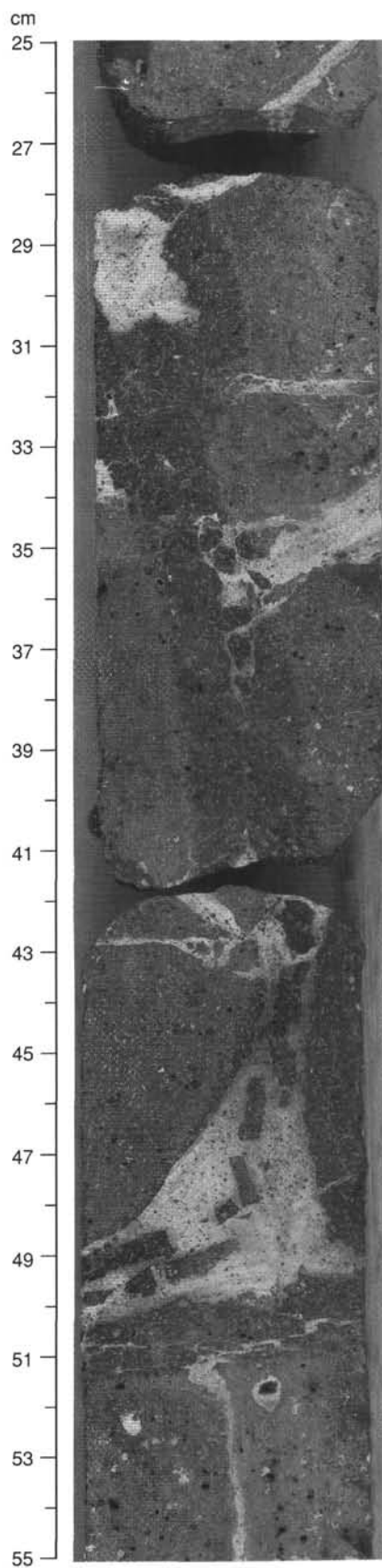


Figure 19. Photograph of Interval 145-883E-20R-6, 25–55 cm, showing palagonite-bearing sedimentary infilling between vertical pillow margins.

Table 4. Results of whole-rock trace-element analyses by XRF.

Core, section, interval (cm)	Igneous unit	Depth (mbsf)	Nb	Zr	Y	Sr	Rb	Zn	Cu	Ni	Cr	V	TiO ₂
145-883E-													
20R-2, 20-24	1	818.93	10.7	164	43	311	24	146	121	59	158	349	2.69
20R-2, 110-115	3	819.83	11.4	169	44	378	23	161	121	46	131	370	2.71
20R-3, 20-23	4	820.36	8.9	139	33	218	38	225	118	157	148	316	2.02
21R-1, 19-23	11	827.39	8.9	136	32	204	48	96	113	84	137	286	2.04
21R-2, 16-20	11	828.82	8.5	139	33	233	18	87	77	62	154	313	2.02
21R-4, 72-76	13	831.86	8.9	140	32	259	11	93	56	83	181	356	2.31
21R-5, 111-115	13	833.49	9.3	140	33	222	8	90	107	86	164	309	2.03
21R-7, 30-34	14	835.56	9.4	150	34	202	3	89	106	97	159	330	2.23
22R-1, 3-6	15	837.03	9.7	149	35	232	14	100	104	88	173	363	2.20
22R-2, 47-51	17	838.43	9.0	134	32	254	16	83	80	58	148	295	1.99
22R-2, 124-128	17	839.20	9.5	145	34	251	33	113	103	70	164	353	2.18
22R-5, 80-83	20	843.06	11.1	163	38	215	37	99	97	61	144	350	2.33
22R-6, 77-81	20	844.42	9.1	145	34	250	24	108	104	59	159	377	2.15
22R-6, 129-133	21	844.94	11.0	166	43	303	28	124	118	82	154	350	2.56
23R-2, 46-49	26	848.86	10.8	159	36	240	49	214	109	76	155	371	2.33
23R-3, 30-34	27	849.97	11.4	166	38	248	40	191	115	73	168	381	2.43
145-883F-													
1R-3, 34-37	1	823.34	10.3	157	37	300	17	154	122	86	180	365	2.45
2R-1, 22-27	6	829.72	9.0	146	33	214	32	194	115	176	149	317	2.08
2R-1, 90-94	7	830.40	10.0	152	35	248	32	146	99	49	164	367	2.26
2R-2, 135-139	9	832.35	9.8	146	34	251	44	240	106	65	156	341	2.20
3R-1, 96-100	14	840.66	9.9	146	34	218	22	152	104	140	157	320	2.11
3R-2, 53-56	15	841.73	9.4	145	33	218	36	133	90	109	162	335	2.15

Note: Concentrations are in parts per million, except TiO₂, which is in weight percent. See "Explanatory Notes" (this volume) for machine conditions and replicate standard analyses.

to iddingsite. The considerable scatter in the Rb data is also undoubtedly a result of alteration. Rb concentrations less than 10 to 15 ppm are typical in oceanic tholeiites, but occur here only in the basalts that appear to be the least altered. When the effects of alteration are taken into account, concentrations of most incompatible trace elements in the Hole 883 basalts are typical of tholeiitic ocean island basalts.

BIOSTRATIGRAPHY

Drilling at Site 883 revealed the presence of a 820-m-thick sequence of Cenozoic sediments overlying a thin sequence of Cretaceous sediments before reaching basement at about 840 mbsf. The Miocene-to-Pleistocene section is 655 m thick expressing high sedimentation rates. The Miocene-to-Pleistocene sediments are rich in usually well-preserved siliceous microfossils, the diatoms being the most abundant. The calcareous microfossil abundance is highly variable. The diversity of the calcareous nannofossils is low, and few stratigraphical data were identified in the Pleistocene sequence. The Miocene to Pleistocene biostratigraphy is essentially based on siliceous microfossils, which are much more diverse than the calcareous microfossils (Fig. 20, Table 5). An apparently continuous, upper Miocene-to-Pleistocene section was recovered that has an exceptionally high sedimentation rate, reaching 120 m/m.y. in the upper Miocene and lower Pliocene sections. A hiatus (or greatly compressed interval) spanning the upper middle Miocene and the lower upper Miocene occurs at about 560 mbsf. The lowermost Miocene section also is missing. Between these two unconformities, a complete sequence has apparently been recovered. The sedimentation rate is lower (about 15 m/m.y.) in this part of the section. The Oligocene/Miocene boundary is not complete.

The Paleogene sediments contain abundant calcareous nannofossil assemblages. Almost no diatoms were observed in this part of the record. Radiolarians are either present in low abundances (rare and very rare) or absent in all but a few pre-Miocene samples. Calcareous foraminifers are common, although preservation deteriorates from moderate to poor throughout the Paleogene section. The stratigraphy is based on the calcareous nannofossil data (Fig. 21, Table 5); however, the Paleogene section is not complete. The upper Oligocene section is either missing or condensed. It is not clear yet whether a complete Eocene/Oligocene boundary has been recorded. The lower/middle Eocene, Paleocene/Eocene, and Cretaceous/Paleocene boundaries ap-

parently are incomplete. Between these unconformities, the sedimentation rate varies from 10 to possibly 30 m/m.y. Zones NP12 (lower Eocene) and NP22 (lower Oligocene) are especially thick.

The upper Cretaceous sediments contain very poor and badly preserved remains of calcareous nannofossils, with no precise age assignment.

Foraminifers

All core-catcher samples from Holes 883B, 883C, and 883E were processed and examined for benthic foraminifers. Foraminiferal abundance ranges from barren to abundant. In general, foraminifers were abundant to common from 0 to 200 mbsf (Cores 145-883B-1H to -23H and Cores 145-883C-1H to -22H), common to rare between 200 and 500 mbsf (Cores 145-883B-24H to -53X, and Cores 145-883C-23H to -38H), and common below 500 mbsf. Preservation was generally good to moderate in the upper few hundred meters of the holes, with little evidence of dissolution or recrystallization. Preservation deteriorated from moderate to poor below Core 145-883B-47X in Hole 883B (448 mbsf) and Core 145-883E-11R in Hole 883E (738 mbsf) as the sediment became more indurated.

Foraminifers were not used for stratigraphy at Site 883. Age assignments have been based on diatom, radiolarian, and nannofossil stratigraphy. Benthic and planktonic foraminifers from Site 883 are used as indicators of paleodepth and paleoenvironment.

Miocene to Pleistocene

Pliocene and Pleistocene sediments were recovered in Cores 145-883B-1H to -32X in Hole 883B and Cores 145-883C-1H to -32X in Hole 883C. Diversity is generally low in these samples. The species composition is dominated by *Melonis barleeanum*, *M. pompilioides*, *Pyrgo murrhina*, *Gyroidinoides* spp., *Pullenia bulloides*, *Hoeglundina elegans*, and *Uvigerina senticosa/probosidea*.

The Miocene section (Cores 145-883B-33X to -68X) contains a more diverse assemblage, dominated by *Planulina wuellerstorfi*, *Cibicides mundulus*, *C. robertsonianus*, *Sphaeroidina bulloides*, *Anomalinoides semicribratus*, *Globocassidulina subglobosa*, and *Epistominella exigua*.

The benthic foraminifer assemblages from several samples (145-883B-7H-CC, -17H-CC, -21H-CC, and -41X-CC) in the upper Mio-

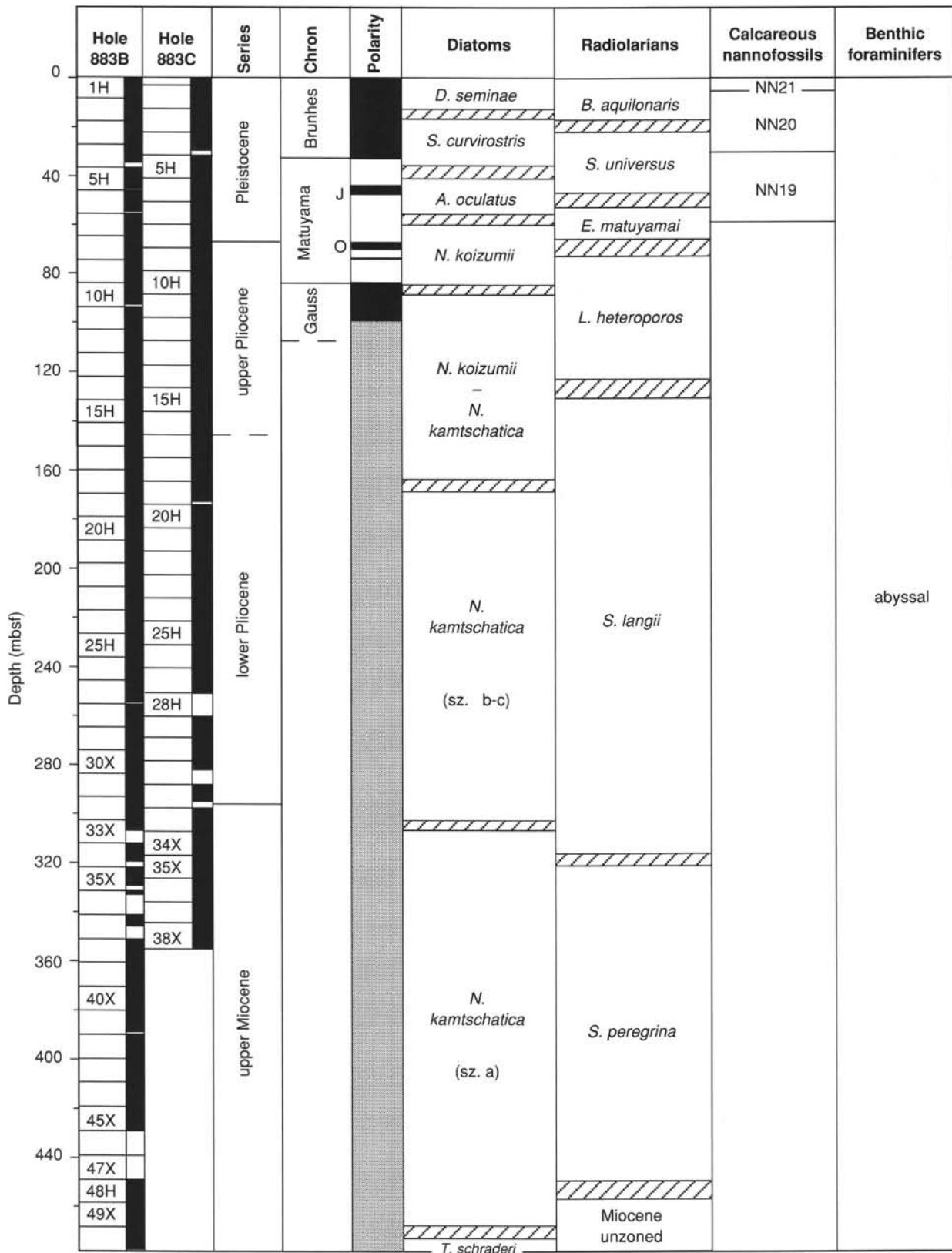


Figure 20. Stratigraphic position of cores, recovery (black), ages, placement of magnetostratigraphic chrons and subchrons, polarity log, and placement of diatom, radiolarian, and calcareous nannofossil zones in Holes 883B and 883C. Intervals filled by slanted lines indicate uncertainty in the placement of biostratigraphic boundaries.

Table 5. Age and stratigraphic position of radiolarian (R), diatom (D) and calcareous nannofossil (N) datum levels in Holes 883B, 883C, and 883E.

Sample no.	Datum	CK 92 (Ma)	Hole 883B		Hole 833C	
			Interval	Depth (mbsf)	Interval	Depth (mbsf)
R1	LO <i>Lychnocanoma grande</i>	0.05	/1H-CC	/7.9	/1H-CC/	3.0
N2	FO <i>Emiliania huxleyi</i>	0.24	1H-5, 13/1H-CC	6.13/7.9		
D2	LO <i>Simonseniella curvirostris</i>	0.30	1H-CC/2H-CC	7.9/17.4	2H-CC/3H-CC	12.5/22.0
R2	LO <i>Drupptractus acquiloni</i>	0.35	1H-CC/2H-CC	7.9/17.4	2H-CC/3H-CC	12.5/22.0
R3	LO <i>Sylatractus universus</i>	0.45	2H-CC/3H-CC	17.4/26.9	2H-CC/3H-CC	12.5/22.0
N3	LO <i>Pseudoemiliania lacunosa</i>	0.49	3H-CC/4H3-28	26.9/30.2		
R5	LO <i>Eucyrtidium matuyamai</i>	1.05	5H-CC/6H-CC	45.9/55.4		
D5	LCO <i>Actinocyclus oculatus</i>	1.00	4H-CC/5H-CC	36.4/45.9	5H-CC/6H-CC	41.0/50.5
D6	FO <i>Simonseniella curvirostris</i>	1.58	6H-CC/7H-CC	55.4/64.9	7H-CC/8H-CC	60.0/69.5
N7	LO <i>Calcidiscus macintyre</i>	1.58	7H-2, 145/7H-CC	58.3/64.9		
N8	FO <i>Gephyrocapsa oceanica</i>	1.67	7H-CC/8H-3-50	64.9/68.4		
D6A	LO <i>Pyxidicula horridus</i>	1.8	6H-CC/7H-CC	55.4/64.9	7H-CC/8H-CC	60.0/69.5
D7	LO <i>Coccolithus pustulatus</i>	1.8	7H-CC/8H-CC	64.9/74.4	7H-CC/8H-CC	60.0/69.5
R7	FO <i>Eucyrtidium matuyamai</i>	1.9	7H-CC/8H-CC	64.9/74.4		
D9	LO <i>Neodenticula koizumii</i>	2.0	6H-CC/7H-CC	55.4/64.9	7H-CC/8H-CC	60.0/69.5
D12	LCO <i>Neodenticula kamschatica</i>	2.63-2.7	9H-CC/10H-CC	83.9/93.4	9H-CC/10H-CC	79.9/88.5
D13	FO <i>Neodenticula seminiae</i>	2.7	9H-CC/10H-CC	83.9/93.4	9H-CC/10H-CC	79.9/88.5
R8	FO <i>Cycladophora davisiana</i>	2.8	11H-CC/12H-CC	102.9/112.4	11H-CC/12H-CC	
R9	LO <i>Stichocorys peregrina</i>	2.9	13H-CC/14H-CC	121.9/131.4		
D14	LO <i>Thalassiosira marujamica</i>	3.2	14H-CC/15H-CC	131.4/140.4	15H-CC/16H-CC	136.0/145.5
D15	LO <i>Thalassiosira jacksonii</i>	3.3	14H-CC/15H-CC	131.4/140.4	15H-CC/16H-CC	136.0/145.5
R10	LO <i>Stichocorys delmontensis</i>	3.55	35H-CC/36H-CC	331.5/341.2	36H-CC/37H-CC	336.0/345.5
N15	LO <i>Reticulofenestra pseudumbilica</i>	3.71	15H-CC/16H-CC	140.9/150.4		
D17	FO <i>Neodenticula koizumii</i>	3.75	18H-CC/19H-CC	159.9/168.4	18H-CC/19H-CC	164.5/174.0
D17A	FO <i>Actinocyclus oculatus</i>	3.8	20H-CC/21H-CC	178.9/188.4	20H-CC/21H-CC	183.5/193.0
R11	LO <i>Theocorys redondoensis</i>		33X-CC/34X-CC	312.2/321.9	34X-CC/35H-CC	317.0/326.5
R12	FO <i>Lamprocyrtis heteroporos</i>	4.6	33X-CC/34X-CC	312.2/321.9	34X-CC/35H-CC	317.0/326.5
D18A	LO <i>Thalassiosira plicata</i>	4.6	30H-CC/31H-CC	283.4/292.9	30X-CC/31X-CC	278.3/288.0
D18B	LO <i>Cosmodiscus insignis</i>	4.6	30H-CC/31H-CC	283.4/292.9		
D19	FO <i>Thalassiosira latimarginata</i>	5.05	31H-CC/32X-CC	292.9/302.5	31X-CC/32X-CC	288.0/297.6
D21	FO <i>Thalassiosira oestrupii</i>	5.4	32X-CC/33X-CC	302.5/312.2	32X-CC/33X-CC	297.6/307.3
D23	LO <i>Thalassiosira miocenica</i>	5.7	34X-CC/35X-CC	321.9/331.5	35H-CC/36H-CC	326.5/336.0
D24	FO <i>Thalassiosira praeoestrupii</i>	5.95	34X-CC/35X-CC	321.9/331.5		
D24A	LO <i>Thalassiosira praeconvexa</i>	6.3	39X-CC/40X-CC	370.2/380.0		
D24B	FO <i>Thalassiosira miocenica</i>	6.3	44X-CC/45X-CC	419.2/429.0		
R	FO <i>Drupptractus acquiloni</i>	6.75	46X-CC/47X-CC	439.3/458.2		
R	FO <i>Stichocorys peregrina</i>	6.75	47X-CC/48H-CC	448.7/458.2		
D24C	FO <i>Thalassiosira jacksonii</i>	6.8	46X-CC/47X-CC	439.3/448.7		
D24D	FO <i>Nitzschia reinholdii</i>	6.9	50X-CC/51X-CC	477.9/487.9		
D25	FO <i>Neodenticula kamschatica</i>	7.25	49X-CC/50X-CC	468.1/477.9		
D26	LO <i>Thalassionema schraderei</i>	7.45	45X-CC/46X-CC	429.0/438.9		
R	LO <i>Lychnocanoma nipponica magnacornuta</i>	8.5	51X-CC/53X-CC	487.9/507.6		
D28A	FO <i>Nitzschia fossilis</i>	8.4	53X-CC/54X-CC	507.6/517.4		
D30	LCO <i>Denticulopsis hustedtii</i>	8.4	53X-CC/54X-2, 104	507.6/510.14		
D32	LO <i>Denticulopsis dimorpha</i>	9.0	57X-4, 104/57X-CC	542.64/547.1		
D34	FO <i>Denticulopsis dimorpha</i>	9.8	57X-CC/58X-CC	547.1/557.0		
R	*FO <i>Lychnocanoma nipponica magnacornuta</i>	12.15	57X-CC/58X-CC	547.1/557.0		
R	LO <i>Cyrtocapsella tetrapera</i>	12.1	58X-CC/59X-CC	557.0/567.0		
R	LO <i>Cyrtocapsella cornuta</i>	11.9	58X-CC/59X-CC	557.0/567.0		
R	*LO <i>Eucyrtidium inflatum</i>	12.2	57X-CC/58X-CC	547.1/557.0		
D42	FO <i>Denticulopsis praedimorpha</i>	12.8	58X-CC/59X-2, 22	557.0/558.72		
D44	FO <i>Denticulopsis hustedtii</i>	13.3	58X-CC/59X-2, 22	557.0/558.72		
D49	FO <i>Denticulopsis hyalina</i>	14.9	60X-CC/61X-2, 104	577.0/579.54		
R	FO <i>Eucyrtidium inflatum</i>	14.8	60X-CC/61X-CC	577.0/587.0		
D52	FO <i>Denticulopsis lauta</i>	15.9	62X-CC/63X-2, 104	597.0/599.54		
D53	FO <i>Denticulopsis praelauta</i>	16.2	63X-2, 104/63X-4, 104	599.54/602.54		
D54	FO <i>Crucidenticula sawamurae</i>	18.4	65X-CC/66X-2, 104	626.3/628.84		
D55	FO <i>Actinocyclus ingens</i>	18.4	65X-CC/66X-2, 104	626.3/628.84		
N	O <i>Sphenolithus heteromorphus</i>	13.5-18.4	63X-CC	607.0		
D57	FO <i>Thalassiosira fraga</i>	20.1	68X-4, 22/68X-CC, 3	649.87/652.13		
D57A	LO <i>Aspeitia oligocenica</i>	20.3	67X-CC/68X-CC, 3	645.1/652.13		
R	FO <i>Stichocorys delmontensis</i>	20.6	64X-CC/65X-CC	616.7/626.3		
R	FO <i>Cyrtocapsella tetrapera</i>	22.6	67X-CC/68X-CC	645.1/654.8		
D	O <i>Lisitzinia ornata</i>	24.3-27.9	68X-CC	654.8		
D66	LO <i>Pyxilla gracilis</i>	30.3	68X-CC/69X-CC	654.8/664.4		
D66A	FO <i>Cavitatus miocenica</i>	30.6	69X-CC/70X-CC	664.4/674.1		
N51	LO <i>Reticulofenestra bisecta</i>	23.81	68X-CC/69X-CC	654.8/664.4	3R-CC/4R-CC	659.6/669.5
N59	LO <i>Reticulofenestra umbilica</i> (>14µm)	31.72	69X-CC/70X-CC	664.4/674.1	4R-CC/5R-CC	669.5/679.4
N58B	LO <i>Isthmolithus recurvus</i>	32.50	70X-CC/71X-CC	674.1/683.7	5R-CC/6R-CC	679.4/689.3
N60	LO <i>Ericsonia formosa</i>	32.70	74X-CC/75X-CC	712.6/720.1	8R-CC/9R-CC	709.0/718.9
N61	LO <i>Discoaster saipanensis</i>	34.98	74X-CC/75X-CC	712.6/720.1	8R-CC/9R-CC	709.0/718.9
N62	LO <i>Discoaster barbadensis</i>	34.98	74X-CC/75X-CC	712.6/720.1	8R-CC/9R-CC	709.0/718.9
N62B	FO <i>Isthmolithus recurvus</i>	35.08	74X-CC/75X-CC	712.6/720.1	8R-CC/9R-CC	709.0/718.9
N65	LO <i>Chiasmolithus solitus</i>	39.72	76X-CC/77X-CC	729.9/739.7	10R-CC/11R-CC	728.8/738.6
N67	LO <i>Nannotetrina spp.</i>	41.85	78X-CC/79X-CC	749.5/759.4	12R-CC/13R-CC	748.4/758.3
N71	LO <i>Nannotetrina fulgens</i>	47.03			12R-CC/13R-CC	748.4/758.3
N72	LO <i>Discoaster subloboensis</i>	47.23	78X-CC/79X-CC	749.5/759.4	12R-CC/13R-CC	748.4/758.3
N73	FO <i>Nannotetrina spp.</i>	47.82	80X-CC/81X-CC	769.2/779.2	14R-CC/15R-CC	768.1/778.0
N74	LO <i>Discoaster lodoensis</i>	47.90	80X-CC/81X-CC	769.2/779.2	14R-CC/15R-CC	768.1/778.0

Table 5 (continued).

Sample no.	Datum	CK 92 (Ma)	Hole 883B		Hole 833C	
			Interval	Depth (mbsf)	Interval	Depth (mbsf)
N75	FO <i>Discoaster subloboensis</i>	49.29	81X-CC/82X-CC	779.2/789.2	14R-CC/15R-CC	768.1/778.0
N76	LO <i>Tribrachiatus orthostylus</i>	50.78	81X-CC/82X-CC	779.2/789.2	14R-CC/15R-CC	768.1/778.0
N77	FO <i>Discoaster lodoensis</i>	52.04	85X-3, 100/85X-CC	813.4/814.7	14R-CC/15R-CC	768.1/778.0
N78	FO <i>Sphenolithus radians</i>	53.12	84X-CC/85X-CC	813.4/814.7	18R-CC/19R-CC	807.5/817.4
N79	FO <i>Tribrachiatus orthostylus</i>	53.32	85X-3, 100/85X-CC	813.4/814.7	18R-CC/19R-CC	807.5/817.4
N84	LO <i>Fasciculithus</i> spp.	54.08	85X-3, 100/85X-CC	813.4/814.7		
N90	LO <i>Heliolithus klempellii</i>	NP8	85X-3, 100/85X-CC	813.4/814.7		
N91	FO <i>Discoaster mohleri</i>	57.79	85X-CC/86X-CC	814.7/828.1		
N92	FO <i>Heliolithus klempellii</i>	58.57	85X-CC/86X-CC	814.7/828.1		
N97	FO <i>Fasciculithus</i> spp.	60.63	85X-CC/86X-CC	814.7/828.1		
N99	FO <i>Sphenolithus</i> spp.	61.36	85X-CC/86X-CC	814.7/828.1		

Notes: First or last occurrence truncated by hiatus. Samples constraining each datum level are separated by a slash (/) as are the depths (mbsf) of these samples. LO = last occurrence; LCO = last common occurrence; FO = first occurrence; FCO = first common occurrence. CK92 refers to the Cande and Kent (1992) geomagnetic polarity time scale.

cene to lower Pliocene section are completely dominated by *Uvigerina senticosa/proboidea* or *Globocassidulina subglobosa*. These species are associated with low-oxygen water in the modern ocean. Increased abundance of these species in the Miocene Pacific Ocean may reflect shoaling of the oxygen minimum zone or an increase in sediment organic carbon (Woodruff, 1985).

Oligocene

Material of Oligocene age was recovered from Cores 145-883B-69X to -74X in Hole 883B and Cores 145-883E-3R to -8R in Hole 883E. The foraminifers in this interval are common to rare in abundance. Assemblages in Hole 883B consist primarily of *Cibicidoides praemundulus*, *Oridorsalis umbonatus*, *Globocassidulina subglobosa*, *Nonion havanense*, *Pullenia* spp., *Stilostomella* spp., and *Gyroidinoides* spp. Minor species include *C. laurissae* and *C. eocaenus*. Oligocene samples from Hole 883E are generally more indurated than those from Hole 883B, hindering identification of foraminifers.

Eocene

A thick Eocene section was recovered from Hole 883B (Cores 145-883B-75X to -84X) and Hole 883E (Cores 145-883E-9R to -18R). The Hole 883B samples contain rare-to-common occurrences of a fauna dominated by *Bulimina semicostata*, *Cibicidoides praemundulus*, *Clinapertina inflata*, and *Nuttallides truempyi*. Additional taxa include *Abyssamina poagi*, *B. grata*, *B. impendens*, *B. bradburytuxpamensis*, *C. osangularis*, *Globocassidulina subglobosa*, *Gyroidinoides quadratus*, *Hanzawaia ammophila*, *Oridorsalis umbonatus*, *Osangularia* sp., and *Turrilina robertsi*. Poor preservation below Core 145-883E-11R in Hole 883E precluded identification of foraminifers.

Paleocene and Cretaceous

One sample contained Paleocene-aged material (Sample 145-883B-85X-CC). This sample contained a rare and poorly preserved assemblage of *Nuttallides truempyi*, *Oridorsalis* sp., and *Clinapertina inflata*.

Cretaceous sediments were recovered in three samples (145-883B-86X-CC, -87X-CC, and -20R-CC). These samples contain an abundant fauna of poorly preserved, recrystallized species of *Rhapydionina*(?), as well as rare specimens of the agglutinated genera *Bathysiphon* and *Reophax*.

Paleoenvironment

Paleobathymetric estimates are based on van Morkhoven et al. (1986). The Paleogene and lower Miocene section share within the lower bathyal zone (1000-2000 mbsl). From the middle Miocene

through the Pleistocene section benthic foraminiferal faunas of Site 883 are dominated by abyssal taxa (>2000 mbsl).

Where planktonic foraminifers occur, preservation is moderate, with little evidence of dissolution. Benthic foraminiferal assemblages are moderately diverse and generally well-preserved above ~500 mbsf. Below this level, recrystallization becomes more prevalent in both benthic and planktonic foraminifers.

Late Neogene planktonic foraminiferal assemblages are dominated by the cold and temperate water species *Globigerina bulloides* and *Neoglobobulimina pachyderma* (sinistral). However, within the Pliocene section, samples frequently contain more diverse assemblages of subtropical-temperate species (*N. pachyderma* (dextral), *N. dutertrei*, *Globorotalia scitula*, *Globigerinita glutinata*, and *Orbulina* spp.), which are indicative of relatively warm surface-water conditions during Pliocene time.

Calcareous Nannofossils

Calcareous nannofossil assemblages were examined in all core catcher samples obtained from Site 883. The calcareous nannofossil abundance fluctuates significantly (from barren to abundant) in the Neogene sediments and is high in the Oligocene and Eocene sediments. Below Sample 145-883B-85X-CC (814.7 mbsf), abundances decrease significantly, and the assemblages are poorly preserved.

Miocene to Pleistocene

As at Site 882, the Miocene-to-Pleistocene calcareous nannofossil assemblages have low diversity at Site 883. The assemblages are dominated by *Coccolithus pelagicus* and *Reticulofenestra* spp. Four Pleistocene markers can be found (Table 5). The virtual absence of discoasters, sphenoliths, and ceratoliths in the Pliocene and Miocene sequences precludes the stratigraphical usefulness of calcareous nannofossils within this interval. Traces of reworked Paleogene species can be observed throughout the Neogene section, especially in Samples 145-883B-32X-CC, -33X-CC, -58X-CC, and -59X-CC.

Paleogene

Paleogene sediments were recovered in Holes 883B and 883E. Good agreement exists among the assemblages observed in these two holes.

The last occurrence (LO) of *Reticulofenestra bisecta* in Samples 145-883B-69X-CC and 145-883E-4R-CC, indicates that the Oligocene/Miocene contact lies within these cores. Although the LO of *Reticulofenestra umbilica* (>14 μ m) in Samples 145-883B-70X-CC and -883E-6R-CC and the LO of *Isthmolithus recurvus* in Samples 145-883B-71X-CC and -883E-5R-CC suggest that the upper Oligocene record was not recovered at Site 883.

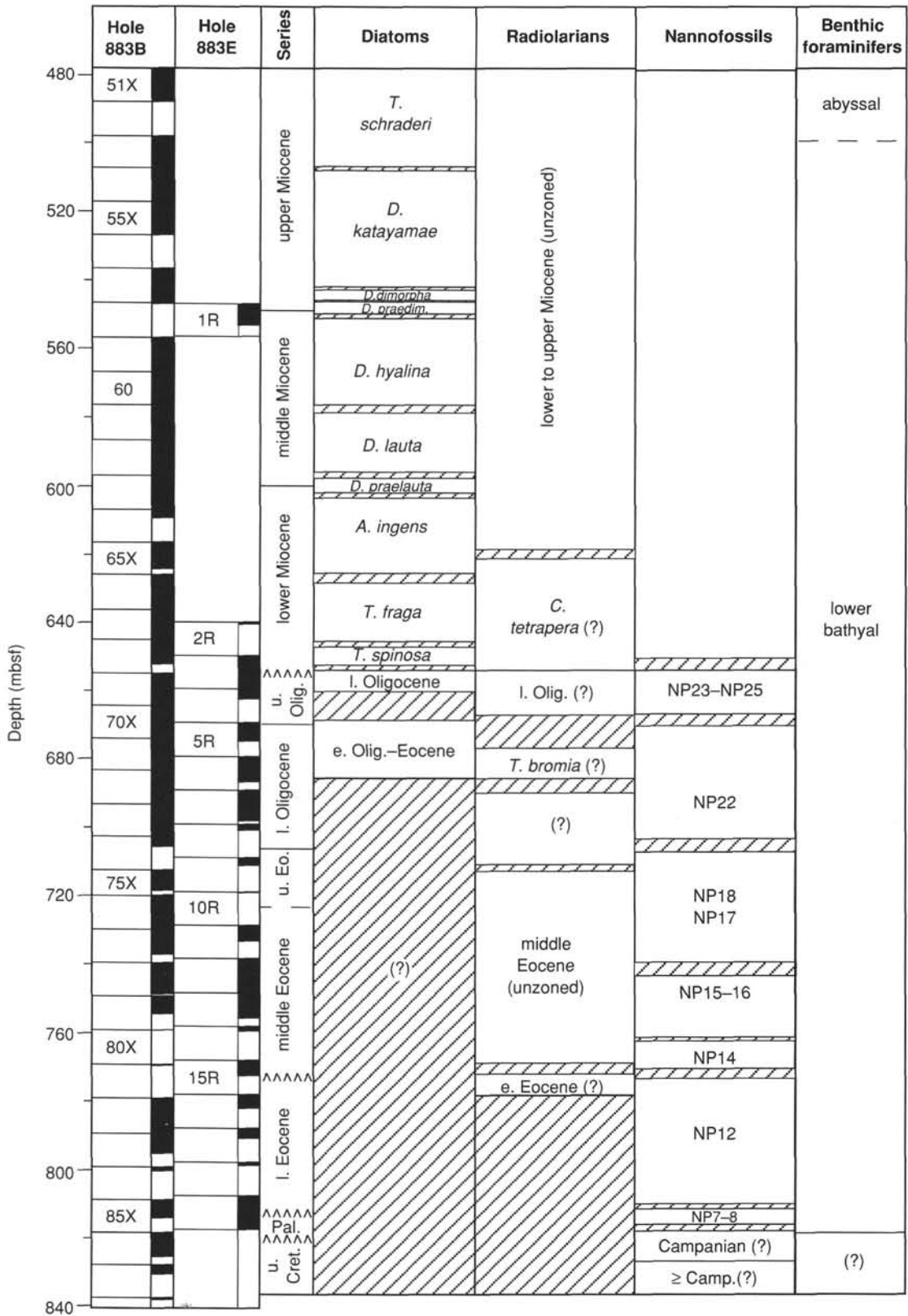


Figure 21. Stratigraphic position of cores, recovery (black), ages, and placement of diatom, radiolarian and calcareous nannofossil, and planktonic foraminifer zones, and the bathymetric range of benthic foraminifers in Holes 883B and 883E. Intervals filled by slanted lines indicate uncertainty in the placement of biostratigraphic boundaries.

Isthmolithus recurvus first occurs in Samples 145-883B-74X-CC and 145-883E-8R-CC, while *Ericsonia formosa*, *Discoaster saipanensis*, and *D. barbadiensis* last occur in Samples 145-883B-75X-CC and 145-883E-9R-CC. Thus, Zones NP19 to NP21 are missing at this site. The LO of *Chiasmolithus solitus*, which defines the top of Zone NP16, is identified in Samples 145-883B-77X-CC and 145-883E-11R-CC. Poor preservation in Samples 145-883B-75X-CC, 145-883B-76X-CC, 145-883E-9R-CC, and 145-883E-11R-CC makes it difficult to identify *Chiasmolithus* specimens at the species level. Therefore, Zones NP17 and NP18 (FO of *C. oamaruensis* defines the base of Zone NP18 and LO of *C. solitus* defines the base of Zone NP17) cannot be recognized. Thus, it is at this time uncertain whether the sedimentation is continuous from the middle Eocene through the lower Oligocene. If the range of *Ericsonia formosa* is not truncated, and if *Chiasmolithus solitus* persists in Samples 145-883B-75X-CC and 145-883E-9R-CC, a long hiatus exists from the lower Eocene (Zone NP16) to the lower Oligocene (Zone NP22). If, however, the range of *E. formosa* is truncated, as in the high-latitude sites of ODP Leg 120 (Aubry, 1992), and if the LO of *C. solitus* was correctly identified, a continuous middle Eocene-lower Oligocene sequence is probably present at Site 883.

The FO of *Discoaster subloboensis* (which defines the top of Zone NP13) and *Nannotetrina* spp. are found in Samples 145-883B-81X-CC and 145-883E-14R-CC. The LOs of *D. lodoensis* and *Tribrachiatus orthostylus* (which defines the base of Zone NP13) can be observed in the same interval; therefore, Zone NP13 was not identified at this site. The presence of a hiatus in the interval of Cores 145-883B-81X and 145-883E-14R is likely, suggesting a discontinuous section across the lower/middle Eocene boundary.

Samples 145-883B-85X-3, 100 cm (813.40 mbsf), and 145-883E-18R-CC yield the first specimen of *D. lodoensis* (which defines the base of Zone NP12) observed in the sections, implying that Zone NP12 is at least 24 m thick. Debris are present in this part of the section, although the samples yield typical calcareous nannofossil assemblages of Zone NP12, without evidence of reworking.

Sample 145-883B-85X-CC (814.17 mbsf) yields rare and poorly preserved upper Paleocene calcareous nannofossils having an age equivalent to Zones NP7 to NP8 (presence of *Heliolithus kleinpellii*). The upper Paleocene to lower Eocene sequence thus is not complete at this site.

Sample 145-883B-87X-CC is almost barren, but one specimen of *Micula decussata*, a poorly preserved specimen of *Watznaueria* spp., and a questionable specimen of *Ceratolithoides aculeus* suggest a Cretaceous age. Also present are questionable remains of specimens that could be assigned to the genus *Nannoconus*. Thus, the sample could be as old as Campanian.

Radiolarians

Radiolarians present in sediments from core-catcher samples from holes drilled at Site 883 range in age from Paleocene(?) early Eocene to Quaternary. Common-to-abundant radiolarians are present in most sediments of late Pliocene through Pleistocene age. Concentrations of radiolarians decrease sharply in upper Miocene through lower upper Pliocene sediments, possibly the result of dilution from the large increase in diatom production. Within the middle and lower Miocene section, radiolarian concentrations increased to Pleistocene levels (common to abundant). Radiolarians are either present in low abundances (rare and very rare) or absent in all but a few pre-Miocene samples.

Although radiolarian preservation is poor in pre-Miocene sequences, radiolarians are moderately well to well preserved in Miocene through Pleistocene sediments. Poor radiolarian preservation in much of the Paleocene(?) through upper Oligocene section and dilution by diatoms in the upper Miocene through lower upper Pliocene sediments from this site make it difficult for one to assign radiolarian fauna in many pre-Pleistocene intervals to specific radiolarian zones.

All of Hole 883D and the first two cores from both Holes 883B and 883C contained radiolarians from the late Quaternary *Botryostrobilus aquilonaris* Zone (Hays, 1970). Radiolarian abundances in these sediments vary between rare and abundant. The LO of *Lychnonoma grande*, having an estimated age of 0.05 Ma, falls within the sediment sequence above core-catcher samples from the first core of Holes 883A, 883B, 883C, and 883D (145-883A-1H-CC, -883B-1H-CC, -883C-1H-CC, and -883D-1H-CC). Sediments from Hole 883B (between Samples 145-883B-1H-CC, and -2H-CC), Hole 883C (between Samples 145-883C-2H-CC and 3H-CC), and Hole 883D (between Samples 145-883D-1H-CC and 2H-CC) contain the LO of *Druppactractus acquiloniensis*.

The boundary between the *B. aquilonaris* and the *Stylatractus universus* zones (Hays, 1970) occurs in sediments between Cores -2H and -3H in both Holes 883B and 883C. The base of the *S. universus* Zone, marked by the LO occurrence of *Eucyrtidium matuyamai*, falls within the sediment sequence between Cores 145-883B-5H and -6H. The faunal assemblage in core-catcher samples from the first three cores from Hole 883A (Samples 145-883A-1H-CC through -3H-CC) is also characteristic of that described for the *S. universus* Zone, with the base of this zone occurring between Cores 145-883A-3H and -4H. *E. matuyamai* was not present in core-catcher samples from Hole 883C. Based upon the position of the base of the *S. universus* Zone in Holes 883A and 883B and comparison with diatom datum levels in Holes 883A, 883B, and 883C, placement of this zonal boundary in Hole 883C has been tentatively set between Cores 145-883C-5H and -6H. Concentrations of radiolarians within the *S. universus* Zone at this site range from common to abundant.

The sediment sequences from the remainder of Hole 883A (Core 145-883A-4H) and in Cores 145-883B-6H and -7H has been assigned to the early Quaternary *E. matuyamai* Zone (Hays, 1970; Foreman, 1975) on the basis of the presence of *E. matuyamai*. Radiolarians are abundant throughout this interval in sediments from these two holes. The base of the *E. matuyamai* Zone occurs in Hole 883B between Samples 145-883B-7H-CC and -8H-CC.

Sediments from Cores 145-883B-8H through -13H do not contain *E. matuyamai* and *Stichocorys peregrina*; however, the species *Lamprocyrtis heteroporos* is present. Based on these faunal associations, this interval in Hole 883B has been placed in the *L. heteroporos* Zone (Hays, 1970; Foreman, 1975). Radiolarian concentrations decrease sharply from abundant in the upper portion of this zone in Hole 883B (Cores 145-883B-8H and -9H) to rare in the middle and lower parts (Cores 145-883B-10H through -13H). Because of the absence of *E. matuyamai* in Hole 883C, no zonation has been allocated to this section of Hole 883C. Radiolarian abundances in Cores 145-883C-9H and -10H are common to abundant; similar to concentrations in the interval in Hole 883B belonging to the upper portion of the late Pliocene *L. heteroporos* Zone. Below this level in Hole 883C, abundances are rare. The FO of *Cycladophora davisiana* var. *davisiana* is recorded in both Holes 883B and 883C (between Cores -11H and -12H), confirming that sediments from this interval are of late Pliocene age.

The LO of *S. peregrina* falls between Samples 145-883B-13H-CC and -14H-CC, marking the boundary between the *L. heteroporos* and the *Sphaeropyle langii* zones (Foreman, 1975) in Hole 883B. Diagnostic species of the *S. langii* Zone do not appear in sediments from Hole 883C until Cores 145-883C-30X through -34X. *L. heteroporos*, *S. langii*, and *S. peregrina* occur in several of core-catcher samples from this interval. Although the radiolarian assemblage in the interval from at least the base of Cores 145-883C-8H through -30X does not contain specific species for defining typical North Pacific Ocean radiolarian zones, the fauna is otherwise indicative of high-latitude North Pacific Pliocene sediments. Radiolarian abundances are rare in all the samples examined from this interval in both Holes 883B and 883C.

The top of the *S. peregrina* Zone (Riedel and Sanfilippo, 1970, 1978) has been tentatively placed in Hole 883B between Cores 145-883B-33X and -34X and in Hole 883C between Cores 145-

883C-34X and -35H, based on the presence of *S. peregrina*, *Stichocorys delmontensis*, and *Theocorys redondoensis* and the absence of *L. heteroporos* and *S. langii* in the sediment sequence below this level. The interval between Cores 145-883B-34X and -47X and from Core 145-883C-35H through the base of Hole 883C contains a fauna characteristic of the *S. peregrina* Zone. Radiolarian concentrations are rare throughout this sediment sequence. The first common occurrence of *S. peregrina*, marking the base of the *S. peregrina* Zone, occurs between Samples 145-883B-47X-CC and -48H-CC.

Throughout the next interval in Hole 883B (Samples 145-883B-48H-CC through -51X-CC) rare, moderately well- to well-preserved radiolarians are present. The radiolarian assemblage consists of *Sphaeropyge robusta*, *S. delmontensis*, and *T. redondoensis*. Although this interval is missing typical radiolarian species that define late Miocene age zones, the occurrence of these species most likely indicates that this interval is of late Miocene age.

The radiolarian assemblage in core-catcher Samples 145-883B-53X through -57X is diagnostic of the middle and upper Miocene section, based on the presence of *Lychnocanoma nipponica* and *Lychnocanoma nipponica magnacornuta*. In addition to both *L. nipponica* and *L. nipponica magnacornuta*, *T. redondoensis* occurs in every core-catcher sample from this level, with *S. delmontensis*, *Cyrtocapsella tetrapera*, and *Cyrtocapsella cornuta* present in at least one sample. Radiolarian concentrations range from rare to abundant and specimens are moderately well to well preserved.

Samples 145-883B-58X-CC through -60X-CC contain abundant moderately well- to well-preserved radiolarians. The faunal assemblage throughout this interval consists of *Eucyrtidium inflatum*, which occurs in every sample, and *S. robusta*, *S. delmontensis*, *T. redondoensis*, *C. tetrapera*, *C. cornuta*, and *Amphymenium* sp. (Ling, 1973), indicative of middle Miocene age sediments. The first core from Hole 883E (Sample 145-883E-1R-CC) contains a similar radiolarian assemblage and is also given a probable age of middle Miocene.

Radiolarians are abundant and moderately well preserved in Samples 145-883B-61X-CC through -64X-CC. Because of the presence of *S. delmontensis*, *T. redondoensis*, *C. tetrapera*, *C. cornuta*, *Acanthodesmid* sp. (Ling, 1973), and *Amphymenium* sp. and the absence of *E. inflatum*, this interval is most likely of late early Miocene to early middle Miocene age. The FO of *S. delmontensis* is recorded between core-catcher Samples 145-883B-64X-CC and -65X-CC.

Moderately well-preserved to poorly preserved and rare radiolarians are present in core-catcher samples from Cores 145-883B-65X through -67X and from Cores 145-883E-2R and -3R. These sediments are probably early Miocene in age (possibly *C. tetrapera* Zone [Riedel and Sanfilippo, 1978]), based on the presence of *C. tetrapera* and *C. cornuta* and the absence of *S. delmontensis*.

Radiolarians are either absent or at low concentrations in Cores 145-883B-68X through -74X and Cores 145-883E-4R through -8R, except for Sample 145-883B-71X-CC. Although radiolarians are rare in this sample, it does contain a diagnostic faunal assemblage with abundant *Dictyoprora mongolfieri*, associated with scattered (rare) *Calocyclus asperum*. This faunal association is indicative of upper Eocene to lower Oligocene sediments (possibly the *Thyrsoyrtis bromia* Zone [Riedel and Sanfilippo, 1970, 1978]).

Radiolarian concentrations increase in Sample 145-883E-9R-CC, with the assemblage containing typical middle Eocene species (*Podocyrtis papalis*, *D. mongolfieri*, *Lophocyrtis biaurita*). Samples 145-883E-75X-CC, -78X-CC, and -81X-CC and Samples 145-883E-10R-CC and -12R-CC also contain rare-to-common middle Eocene age radiolarians, with *D. mongolfieri* and *P. papalis* present in most samples and *S. pachystylus*, *L. biaurita*, and *Theocotyle* sp.(?) present in single samples from each hole. Although radiolarians were poorly preserved in core-catcher Sample 145-883E-15R-CC, tentative identification of the species *Buryella* sp. aff. *B. tetradica*(?) and *Phormocyrtis striata exquisita*(?) was made, indicating a possible late Paleocene to early Eocene age for these sediments. Radiolarians were not

present in sediment samples below this level in Hole 883E and below Core 145-883B-81X in Hole 883B.

Diatoms

Diatoms are generally abundant to common and well preserved to moderately well preserved throughout the lower Miocene through Quaternary section cored above 655 mbsf at Site 883. With the exception of the middle Miocene age *Thalassiosira yabei* and *Crucidentula nicobarica* zones, all of the Neogene North Pacific Ocean diatom zones can be recognized from the lower Miocene *Thalassiosira spinosa* through the upper Quaternary *Neodenticula seminae* zones (Figs. 20 and 21). Standard diatom datum levels were used to recognize these zones (Table 5), and little or no displacement of diatom biostratigraphic horizons is apparent among Holes 883B, 883C, and 883E.

The coincidence of the FO of *Simonseniella curvirostris* (1.58 Ma) and the LO of *Neodenticula koizumii* (2.0 Ma) in the interval between Samples 145-883B-6H-CC and -883B-7H-CC (55.4 to 64.9 mbsf) and between Samples 145-883C-7H-CC and -883C-8H-CC (60.0–69.5 mbsf) suggests the possibility of an unconformity or compressed interval at the Pliocene/Quaternary boundary. Paleomagnetic stratigraphy, however, identifies the Olduvai normal-polarity Subchron (1.76 to 1.98 Ma) at about 67 to 70 mbsf in Hole 883B, suggesting that the last occurrence of *N. koizumii* may be younger at Site 883 than it is at Sites 882 and 881.

At Site 882, the lower Pliocene section was characterized by high sedimentation rates (about 115 m/m.y.) that began near the Miocene/Pliocene boundary (5.1 Ma) and apparently ended at about 3.8 Ma (Site 882, Table 5). A correlative lower Pliocene interval occurs between about 165 to 295 mbsf in Holes 883B and 883C and is also characterized by high (about 100 m/m.y.) sediment accumulation rates (Table 5).

Immediately below the upper Miocene interval of high sediment accumulation rates, an interval of poorly preserved diatoms is present in Cores 145-883B-51X and -53X (about 478–508 mbsf) followed by an interval of improved diatom preservation in Cores 145-883B-54X through -57X (about 508–547 mbsf). Diatom datum levels (Table 5) suggest relatively slow sediment accumulation rates (about 30 m/m.y.) within this poorly preserved interval, which has an estimated age of 7.4 to 8.4 Ma. Deep-sea hiatus NH6 of Keller and Barron (1987), which is widespread in the North Pacific (Barron, 1989), is partly coincident (ca. 7.6–6.5 Ma) with this poorly preserved interval.

The last common occurrence of *Thalassionema schraderi* (7.45 Ma) in Sample 145-883B-46X-CC (438.9 mbsf) is anomalous in Hole 883B, because it falls above normally younger datum levels: the FO of *Thalassiosira jacksonii* (6.8 Ma), -Sample 145-883B-46X-CC; the FO of *Nitzschia reinholdii* (6.9 Ma), -Sample 145-883B-50X-CC; and the FO of *Neodenticula kamtschatica* (7.25 Ma), -Sample 145-883B-49X-CC. It seems likely that *T. schraderi* has been reworked upsection.

The entire upper middle Miocene as well as the lowermost upper Miocene (ca. 13.3 to 9.8 Ma) has been compressed within or removed from the interval between Sample 145-883B-59X-2, 22-23 cm, (558.72 mbsf) and the base of Core 145-883B-57X (547.1 mbsf). Within this interval, Sample 145-883B-58X-CC does contain a *Denticulopsis praedimorpha* Zone assemblage (12.8 to 10.8 Ma), but unfortunately only 0.83 m was recovered in Core 145-883B-58X. An attempt to recover this compressed interval in Core 145-883E-1R (547.0 to 556.5 mbsf) failed, because the top of the 6.15-m-thick section recovered in that core correlates with the *Denticulopsis hyalina* Zone and is older than 13.3 Ma.

Thus, either a greatly compressed interval or two hiatuses—one removing the *Thalassiosira yabei* Zone (10.8 to 9.8 Ma) and the other removing the *Crucidentula nicobarica* Zone (13.37 to 12.8 Ma)—must be present at Site 883. An equivalent interval is missing or greatly compressed at Gulf of Alaska DSDP Site 183 (Barron, 1989).

Sample 145-883B-68X-CC, 3–4 cm, has been assigned to the early Miocene *Thalassiosira spinosa* Zone, based on the presence of *Azpeitia oligocenica* and *Cavatus rectus* (n. sp., Akiba et al., in press) and the absence of *T. fraga* and *Rocella* spp. Below, at the base of the core-catcher sample (interval at about 39 cm), a poorly preserved late Oligocene age assemblage containing *Lisitzinia ornata*, *Cavatus (Synedra) jouseana*, and *Kiesseleviella magnaareolata* can be observed. A sharp lithologic break between greenish-gray, diatom-rich calcareous chalk above and light brownish-gray, diatom-poor calcareous chalk below at the 10-cm level of the core-catcher sample of Core 145-883B-68X possibly represents an unconformity between the middle part of the lower Miocene (*T. spinosa* Zone, ca. 21 Ma) and the upper Oligocene (27.9–24.3 Ma) section.

PALEOMAGNETISM

Procedures

At Site 883, pass-through measurements were performed on all APC cores from Holes 883B and 883C. On XCB cores from Hole 883B, two sections per core were measured as a check on the quality of the magnetization. If good results were obtained, the entire core was measured. Measurements were performed at 10-cm spacings after 15-mT demagnetization, except for the more weakly magnetized zones of the holes (Hole 883B, 389.7–782.2 mbsf), which were demagnetized at 10 mT. Two or three 7-cm³ samples were taken from all sections of Hole 883B and were measured using both the Molspin and Japanese spinner magnetometers. Samples from the first 10 cores were demagnetized in five steps up to 35 mT. Below this depth, one sample per core was demagnetized and measured with the Japanese spinner magnetometer. In addition to the NRM demagnetization, the Japanese instrument also provided anhysteretic remanent magnetization (ARM) data. The multishot orientation devices were deployed in the upper parts of Holes 883B and 883C, and orientations were obtained for Cores 145-883B-4H to -30H and 145-883C-4H to -30X at both holes. Where both the multishot and tensor tools were used, orientations from the two devices agree to within 4° to 5°. Automated susceptibilities were measured at 5-cm (Cores 145-883A-1H to -4H, and 145-883B-1H to -11H), 10-cm (Cores 145-883E-1R to -23R, and 145-883F-2R to -3R), and 15-cm (Cores 145-883B-12H to -87X, and 145-883C-1H to -38H) intervals in whole cores, in conjunction with other measurements performed with the multisensor track.

Results

Pass-through NRM measurements, after 15 mT (0–389.7 mbsf) or 10 mT (389.7–782.2 mbsf) demagnetization, and whole-core susceptibility results are shown in Figure 22 for Hole 883B. These remanence intensities are reasonably high in the upper part of Holes 883B and 883C and decrease gradually with depth to 87 mbsf in Hole 883B and to 90 mbsf in Hole 883C, where intensity abruptly falls off more than an order of magnitude. The intensity does not increase again until below 700 mbsf. Mean intensities after demagnetization are about 60 mA/m from 0 to 87 mbsf (varying between 20 and 200 mA/m) and less than 10 mA/m from 105 to 398 mbsf. A weak, reversed drilling overprint was observed in most cores from Site 883. Discrete sample demagnetizations (Figs. 23 and 24) show that overprints were usually small and were removed by 5- or 10-mT demagnetization fields. In both the whole-core and discrete samples, the remanent intensity decreases by more than an order of magnitude below about 87 mbsf (Figs. 22 and 24). In fact, samples taken below this depth were mostly too weak to measure using the spinner magnetometers. This NRM transition coincides with changes in many of the other physical property measurements and with a decrease in clay content and percentage of ash layers at the boundary between lithologic Units I and II. A significant increase in intensity occurs near the boundary of lithologic Subunits IVA and IVB (740 mbsf) and is coincident with an increase in cumulative ash thickness. XCB drilling disturbance at

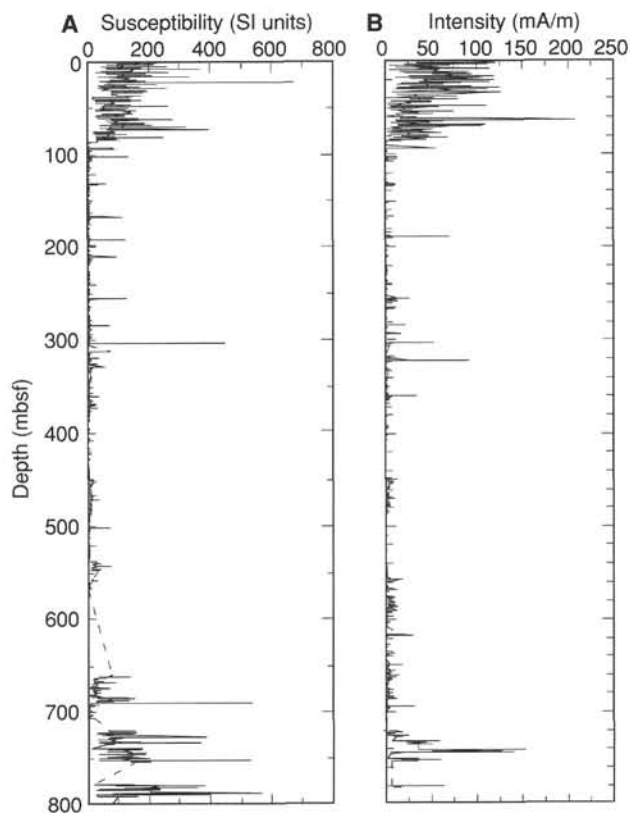


Figure 22. NRM intensities (B), after demagnetization at either 15 (0–389.7 mbsf) or 10 mT (389.7–782.2 mbsf), from Hole 883B compared to whole-core susceptibilities (A).

these depths renders difficult an interpretation of the whole-core magnetization directions.

Whole-core susceptibility measurements vary in a similar fashion to the NRM signal; the background susceptibility signal shows a considerable and abrupt decrease at approximately 87 mbsf. The susceptibility signal also shows numerous discrete peaks between 0 and 87 mbsf that coincide mostly with the many ash layers at these depths (Fig. 22). The frequency and amplitude of peaks decrease dramatically below this depth interval and do not increase again until about 720 mbsf. For many depth intervals, the susceptibility signal is below the detection limit. This can be seen in “Site 881” chapter, Fig. 13, this volume, where susceptibility has been plotted on a log scale; at lower susceptibility values, the steplike nature of the curve indicates low resolution near the detection limit.

Measurements of ARM demagnetization performed with the Japanese spinner magnetometer also indicate an abrupt change in magnetic properties at 87 mbsf (“Site 881” chapter, Fig. 13, this volume). Above 87 mbsf, the ARM values imparted in 40-mT alternating field and 0.03 mT DC field, are in the range of 10^{-4} kA/m (an order of magnitude greater than those of the NRM). In the deeper portions of the hole (87 to 420 mbsf), the ARM values are more than an order of magnitude weaker (10^{-6} kA/m). Sediments in this zone show no stable remanence properties and the demagnetization of ARM shows the sawtoothed pattern typical of spurious ARM values imparted during demagnetization (“Site 881” chapter, Fig. 13, this volume). Deeper in the hole, between 420 and 520 mbsf, the ARM values increase coherently to values between 10^{-4} and 10^{-5} kA/m. In this zone, demagnetization of ARM is comparable to the zone above 87 mbsf (“Site 881” chapter, Fig. 13, this volume). The NRM is also more stable in this deep zone. The comparison between susceptibility and ARM (shown in “Site 881” chapter, Fig. 13, this volume) seems to suggest that magnetic grain size changes in this part of the hole, because the

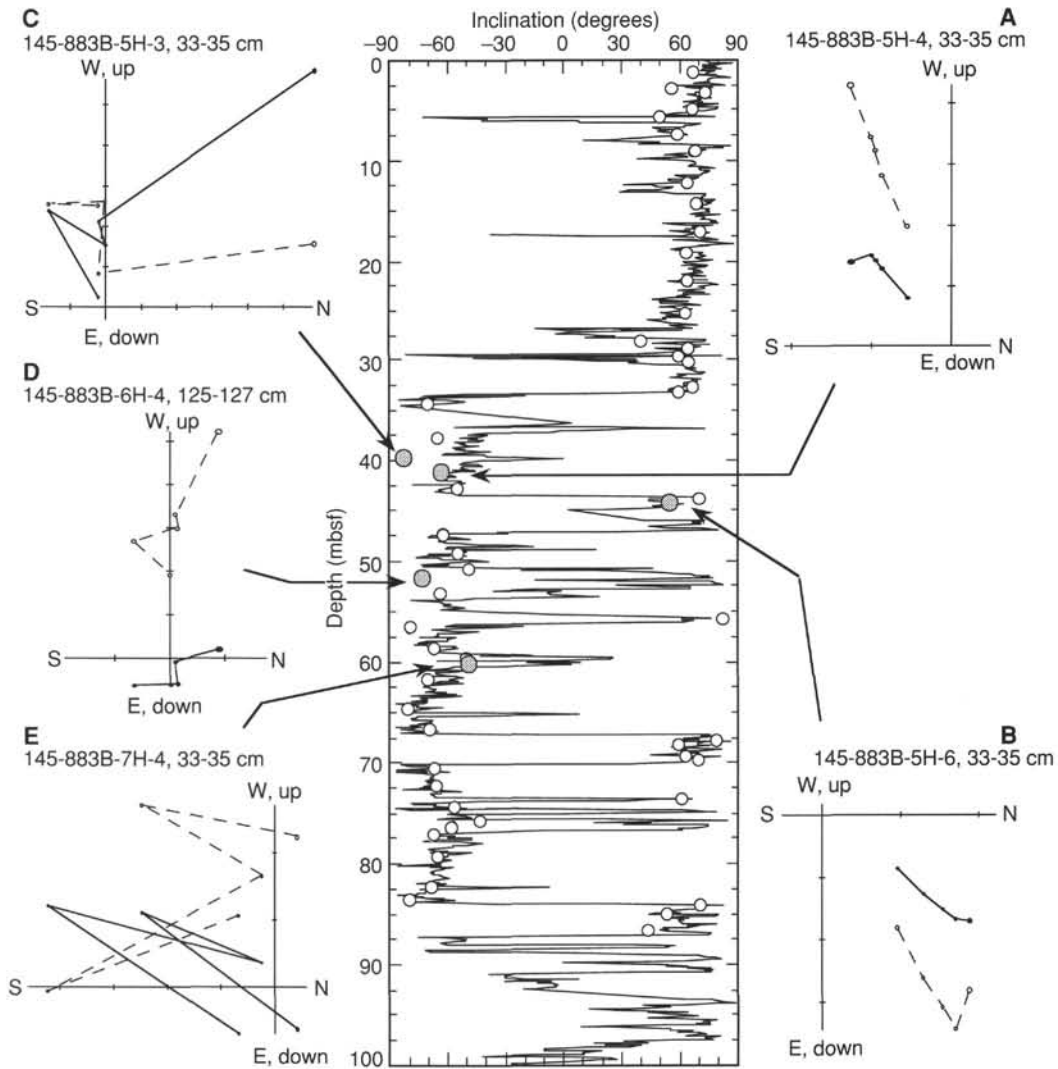


Figure 23. Comparison of results from whole-core measurements of NRM demagnetized at 15 mT (solid line) with results from discrete samples demagnetized at 30 mT (open circles) for Hole 883B. Examples of Zijderveld plots are shown for samples represented as filled circles. **A** and **B** illustrate the stable behavior that predominates between 0 and 90 mbsf, while **C**, **D**, and **E** illustrate unstable behavior thought to be responsible for spurious events in the whole core results.

ratio of ARM to susceptibility is significantly smaller than in the higher parts of the core (0–420 mbsf).

With the exception of disturbed parts of the cores, the sediments appear to record stable normal and reversed field directions in the first 80 to 90 mbsf of Holes 883B and 883C (the axial dipole field inclination is about $\pm 68^\circ$ at a latitude of $51^\circ 33'N$). For the most part, the discrete sample demagnetizations show removal of an overprint between 5 and 10 mT (Figs. 23A, 23B, and 24). Some indications of unstable remanence are seen in localized regions where discrete sample demagnetizations did not support evidence for normal events seen in the whole-core measurements (Figs. 23D and 23E). Samples from these zones proved susceptible to the acquisition of ARM in the demagnetization process. These normal events almost certainly represent a remagnetization of the whole core in the small DC field present in the demagnetization coils of the pass-through system. The individual sample results were again, therefore, useful for helping to discriminate polarity events that are artifacts from those that are more reliable in the whole-core magnetostratigraphy. In this fashion, the whole-core data magnetostratigraphy was interpreted. As usual, data at core breaks and other disturbed parts of the core were removed before making final

interpretations. Aside from the above problematic depth intervals, the discrete sample directions after demagnetization at 30 mT show almost perfect agreement with the whole-core results (Fig. 23).

Hole 883B data show good agreement with those from Hole 883C (Fig. 25) over depths (0–100 mbsf) where demagnetizations were done on both cores. The Brunhes/Matuyama reversal occurs practically at the same depth (33.3 mbsf in Hole 883B, as opposed to 35.0 mbsf in Hole 883C). Table 6 gives the depths to recognizable chrons in Holes 883B and 883C.

Below 87 mbsf in Hole 883B and 90 mbsf in Hole 883C, the NRM decreases by about an order of magnitude, and directional results become noisy and inconsistent. Discrete sample demagnetizations show no stable remanence properties (Fig. 26). The demagnetized NRM intensity and directional records appear to be correlated in such a way that higher intensities are associated more with normal-type directions, while weaker intensities are associated with reversed directions (Fig. 26). This correlation appears to be an overprinting problem, but raises the possibility that the noisy directional polarity record is responding to rock magnetic variability, rather than the geomagnetic field. Unlike results at Site 882, a coherent polarity

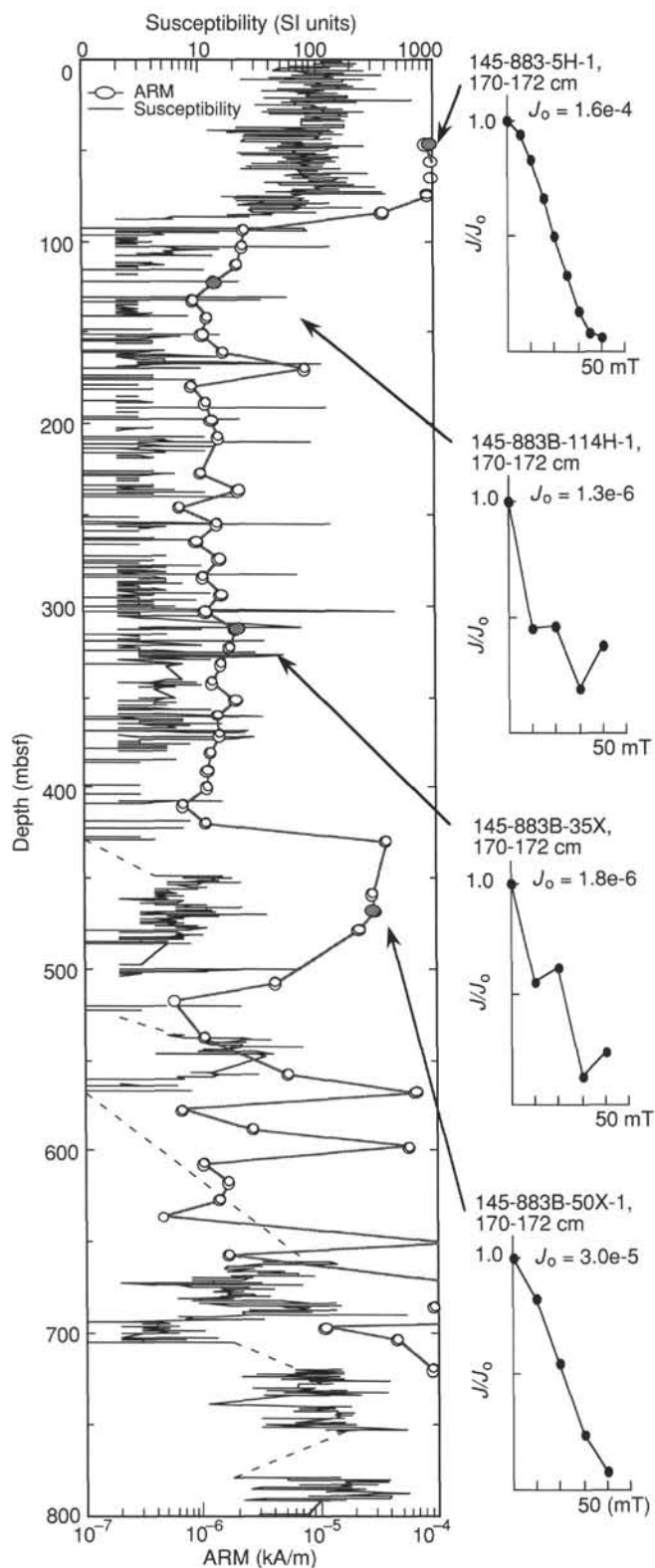


Figure 24. Comparison of whole-core susceptibilities with sample ARMs given in 40 mT AF and 0.03 mT DC fields for Hole 883B. Example J/J_0 plots of ARM demagnetizations from zones of stable and unstable magnetization are presented.

signal does not seem to reappear at depth, although the intensity does recover somewhat below 700 mbsf.

Discussion

A magnetostratigraphic plot of the whole-core inclination records (Fig. 25) was interpreted after the data were edited. The records Holes 883B and 883C showed a simple magnetostratigraphy that could easily be matched to the time scale of Cande and Kent (1992) as far back as the Matuyama/Gauss boundary at approximately 84 mbsf. Between about 90 mbsf and the bottom of Holes 883B and 883C, these data do not warrant magnetostratigraphic interpretation at the present time.

SEDIMENTATION RATES AND FLUXES

Sedimentation Rates

To calculate sedimentation rates and sediment fluxes, we considered the sedimentary section at Site 883 to consist of five time-stratigraphic intervals. The upper two intervals are identical with lithologic Units I and II and have average linear rates of sedimentation of 32 and 91 m/m.y., respectively (Fig. 27). For Unit I, the chronology is based on magnetostratigraphy, whereas biostratigraphy has been used at deeper levels. Below lithologic Unit II, beginning at 458 mbsf and extending to the bottom of the hole, we have defined three additional intervals. The uppermost interval extends to the unconformity or condensed interval within Unit III at ~558 mbsf and has a linear sedimentation rate of 23 m/m.y. The second is bound by condensed intervals or unconformities at about 558 and 650 mbsf, near the lithologic Unit III/Unit IV transition (10 m/m.y.), and the third extends to near the Subunit IVA/Subunit IVB transition, with a rate of 9 m/m.y. Underlying sediments, which are older than ~42 Ma, are marked by both hiatuses and slumps, so it is impossible to estimate a rate of deposition that would be meaningful for flux (mass accumulation rate) purposes.

It is important to stress that the above rates of sedimentation reflect averages for intervals of time lasting millions of years. It is likely that significant fine-scale variability occurs within these intervals, which may have major implications for flux calculations on shorter time scales. For example, although the average linear rate of sedimentation for Subunit IB at Site 883 is high (91 m/m.y.), the ~70-m section between diatom datum levels at ~4.2 and ~4.7 Ma may actually have a rate as much as three times the unit average (Fig. 27). Such rates would compare favorably with the rate calculated in the model for the early Pliocene age interval of Site 882 (~200 m/m.y.), although each is dependent on the accuracy of the 4.2-Ma datum level.

Sediment Fluxes

Sediment fluxes, or mass accumulation rates, were determined in the conventional way, taking the product of the sedimentation rate, the dry bulk density, and the concentration of the sediment component. Average fluxes were calculated for the five time-stratigraphic intervals, results of which are shown as histograms in Figure 27 and keyed to the depth intervals with dashed lines. At the interval boundaries, evidence can be seen of significant changes in rate of sedimentation, dry-bulk density, and sediment composition, each of which can influence flux. Raw data for each of these intervals in Sites 883B and 883C were averaged and are presented in Table 7. Dry-bulk density values were taken from pycnometer measurements, and sedimentary component data come from smear slide estimates, with the exception of percentages carbonate and total organic carbon (TOC), which were measured analytically. Flux results (in $\text{g}[\text{cm}^{-2} \cdot \text{k.y.}]^{-1}$) for diatoms, clay, glass, quartz, and carbonate are listed in Table 7 and are shown in the histograms (TOC fluxes are too close to zero to be visible in these histograms). These results are only semi-quantitative, because of the nature of estimates of smear slide abundances, as well as

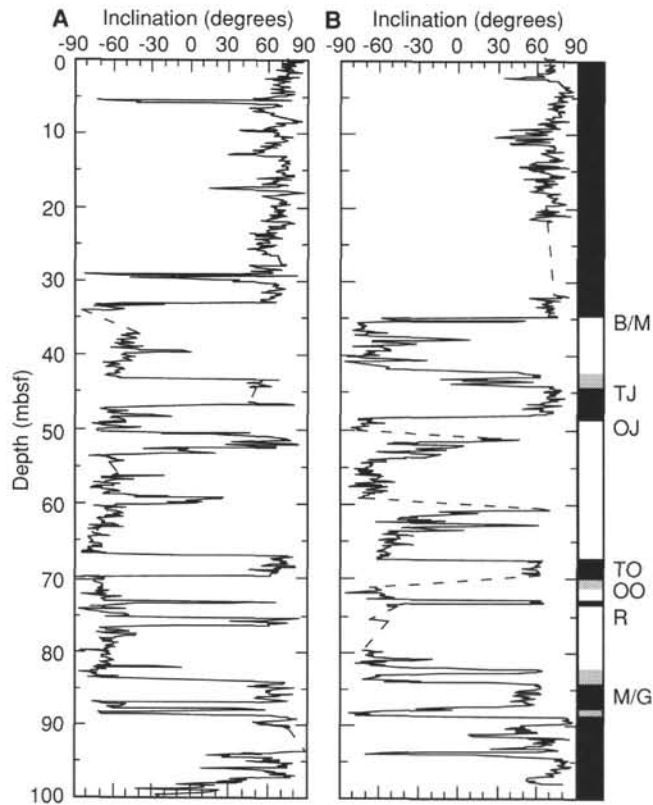


Figure 25. Magnetic inclination records, after 15 mT demagnetization, from Holes 883B (A) and 883C (B). Magnetostratigraphic interpretation is shown on the far right, with gray zones representing more poorly defined polarity events that occurred at weak intensity.

possible errors when calculating deposition rates. For example, Thiede and Rea (1981) noted previously that smear slide results tend to overestimate sedimentary components that were subsequently measured analytically in shore-based studies. Additional errors may stem from the assumption that the estimates of abundance are directly proportional to the weight percentage of each sedimentary component. Thus, taking the 0- to 2.65-Ma interval, for example, we assume that an average of 34% diatoms translates directly to 0.34 g diatoms per gram of bulk sediment.

Average sediment fluxes for the five time-stratigraphic intervals reveal distinctive changes with time (Fig. 27). As at Sites 881 and 882, the base of the uppermost interval at Site 883 is time equivalent with the onset of significant Northern Hemisphere glaciation, and the flux is dominated by clay and diatoms. Unlike nearby Site 882, however, at Site 883, a reversal can be seen in the dominance of diatoms and clay. The diatom flux at Site 883 is about one-third that at Site 882, but the clay flux is about three times greater. These changes are large enough that they are not likely to result from some of the possible errors described above, but at the present time we have no satisfactory explanation for them.

During the second interval, roughly equivalent to latest Miocene and early Pliocene times, sedimentation at Site 883 was completely dominated by diatom flux. This result is similar to our finding at Site 882; however, at the present site we averaged out the brief spike (~4.2–4.8 Ma), where the rate of linear sedimentation may have been significantly higher than the mean for the whole interval.

Moving back in time to the late Miocene interval, the diatom flux is equal to that of the uppermost (glacial) interval, the clay flux is low, and the carbonate flux has increased several-fold. In the next older interval (13.6–20.2 Ma), we find that the carbonate flux is about the

Table 6. Depths of polarity chron boundaries in Holes 883B and 883C.

Polarity chron	Depth (mbsf)		Age (Ma) (CK 92)
	Hole 883B	Hole 883C	
Brunhes/Matuyama	33.30 (4H-5, 50 cm)	35.05 (5H-3, 55 cm)	0.780
Termination Jaramillo	43.50 (5H-5, 120 cm)	41.85-42.25 (6H-1, 85-125 cm)	0.984
Onset Jaramillo	47.00 (6H-1, 100 cm)	48.35 (6H-5, 135 cm)	1.049
Termination Olduvai	67.10 (8H-2, 70 cm)	67.50 (8H-5, 150 cm)	1.757
Onset Olduvai	70.00 (8H-4, 60 cm)	69.70-71.05 (8H-7 to 9H-2)	1.983
Termination Réunion	73.45 (8H-6, 105 cm)	72.90 (9H-3, 40 cm)	2.197
Onset Réunion	73.80 (8H-6, 140 cm)	73.45 (9H-3, 95 cm)	2.229
Matuyama/Gauss	83.70-84.3 (9H-7 to 10H-1)	84.00 (10H-4, 50 cm)	2.600
Termination Kaena			3.054
Onset Kaena			3.127

Note: CK 92 = Cande and Kent, 1992.

same, but that the diatom flux has decreased dramatically. Flux results from the oldest interval, Eocene to Oligocene in age, are dominated by carbonate deposition, with values of about $0.7 \text{ g}(\text{cm}^2 \cdot \text{k.y.})^{-1}$. This value is only about 60% of the modern oceanic average (Broecker and Peng, 1982), but that average contains no data from central or North Pacific Ocean sediments. However, it is consistent with the late Neogene age average carbonate flux from Deep Sea Drilling Project Site 463 located in the subtropical gyre to the west of Hawaii (Thiede and Rea, 1981).

In summary, it is likely that the evolution of flux patterns revealed by our initial results at Site 883 reflects the northwestward migration of this site from relatively shallow depths under oligotrophic surface waters in Paleogene time (carbonate deposition) to greater, more corrosive depths under more productive surface waters during Neogene time (siliceous sediment deposition). Punctuating this general pattern are lithological changes driven by climatic change: the abrupt increase in North Pacific Ocean siliceous deposition, which was apparently associated with increased deep-water production in the North Atlantic Ocean during middle Miocene time (Keller and Barron, 1987) and the increase in clay flux associated with latest Neogene glaciation in the Northern Hemisphere (Shackleton et al., 1984).

INORGANIC GEOCHEMISTRY

Forty-one interstitial-water samples were collected at Site 883 at depths ranging from 1.45 to 802.85 mbsf. Twelve closely spaced samples were taken from Hole 883A between 1.45 and 35.75 mbsf, and 29 broadly spaced samples were collected from Hole 883B at depths ranging from 43.85 to near the bottom of the hole at 802.85 mbsf. Analytical results are listed in Table 8 and have been plotted separately for the two sample sets in all graphs in this section. The pore-water samples span all of the sedimentary lithologic units.

Chloride concentrations in interstitial waters at Site 883 range from near the Pacific Ocean Deep Water value (555 mM) in the shallowest sample (1.45 mbsf) to a maximum of ~568 mM between about 10 and 17 mbsf (Fig. 28A). The relatively shallow but broad maximum probably reflects the ongoing diffusive adjustment of the pore-water Cl^- distribution to the increased mean salinity of seawater during glacially dominated Pleistocene time (see McDuff, 1985). The maximum is 10 to 20 m shallower than is normally encountered in pelagic sections, suggesting that advective displacement upward has occurred at a rate on the order of 1 mm per year. This may reflect dewatering of the high-porosity siliceous oozes that have accumulated rapidly over the last several million years at this location. Chloride concentrations

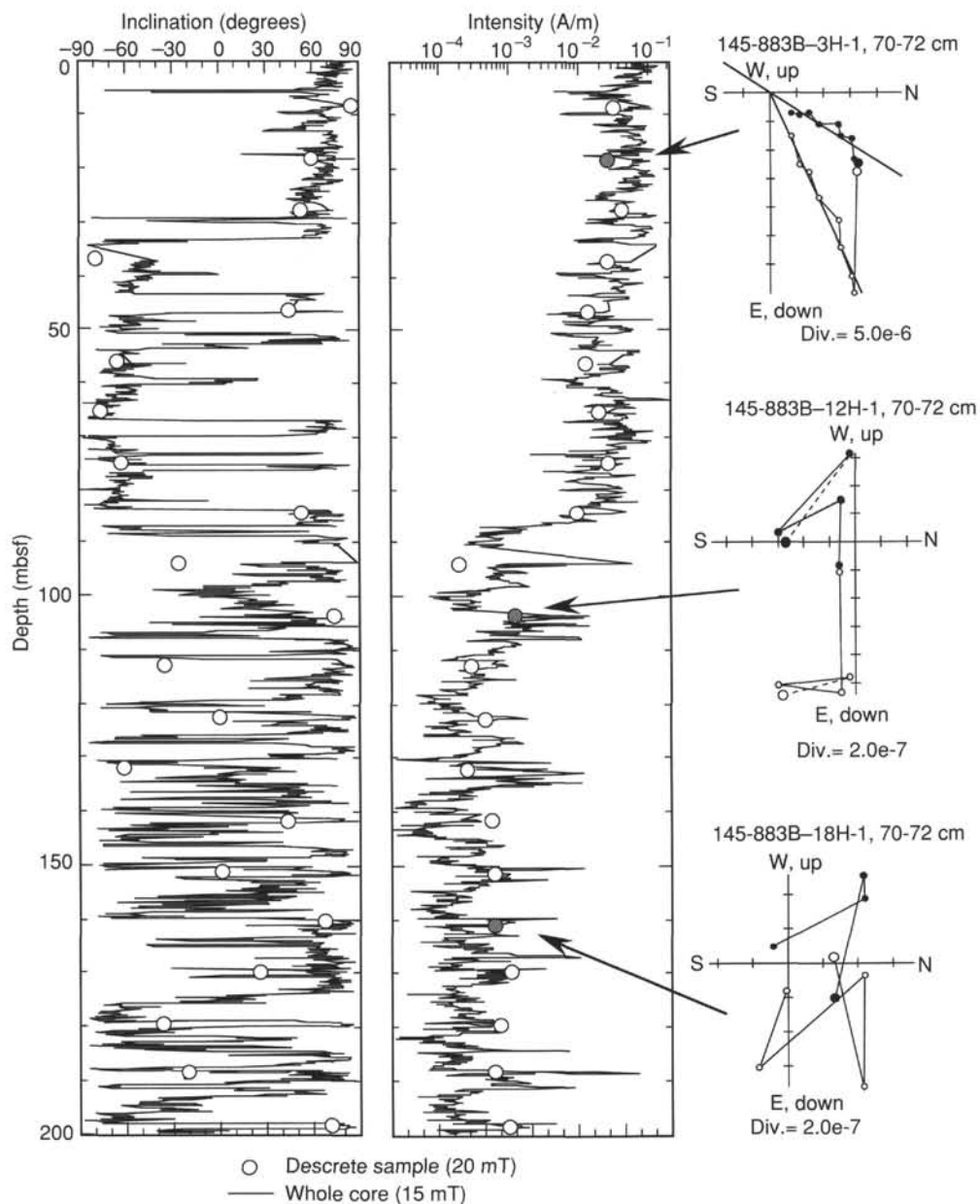


Figure 26. Whole-core measurements of inclination and intensity, after 15 mT demagnetization, from Hole 883B. Sample results, demagnetized at 20 mT, from the Japanese magnetometer are shown as open circles. Example Zijderveld plots are presented for samples shown as filled circles.

progressively decline between 17 and 53 mbsf to about 556 (± 2) mM and remain approximately constant to about 400 mbsf (Fig. 28B). The general increase below this depth can probably be attributed to the uptake of water during hydration of volcanic ash and palagonitization of basalt. Ash was commonly observed below ~ 600 mbsf (see "Lithostratigraphy" section, this chapter), and the basalt basement was intersected at 837 mbsf. The small maximum at 620 mbsf (~ 564 mM) is analytically reproducible, but cannot be readily explained.

The oxidant demand associated with the moderate Quaternary accumulation rates of organic carbon at Site 883 (see "Sedimentation Rates and Fluxes" section, this chapter) is sufficient to deplete oxygen above a depth of 1.5 mbsf, as shown by the presence of significant alkalinity and dissolved manganese and ammonium contents in the shallowest sample (Table 8). Nitrite is measurable only at 4.45 and 5.95 mbsf; NO_2^- concentrations were undetectable at 1.45 mbsf and

in the three samples immediately below 5.95 m depth. This distribution suggests that nitrate reduction is occurring between about 4 and 6 mbsf, but this contention appears to be incompatible with the distributions of alkalinity and sulfate (see below), both of which imply that sulfate reduction commences not deeper than about 2 m at this site. This conundrum should be resolved by nitrate measurements that will be performed in shore-based laboratories.

The dissolved manganese concentrations in the shallowest sample ($\sim 4 \mu\text{M}$) are considerably enriched relative to North Pacific Ocean bottom water ($< 100 \text{ nM}$; Landing and Bruland, 1980) and are similar to the average concentrations seen in the top 30 m (Fig. 28C). This distribution suggests that available MnO_2 is quantitatively dissolved within the top 1.5 m. There is no evidence that the element is participating in authigenesis of carbonate phases in the upper 50 m (Fig. 28D), where the concentration remains relatively constant.

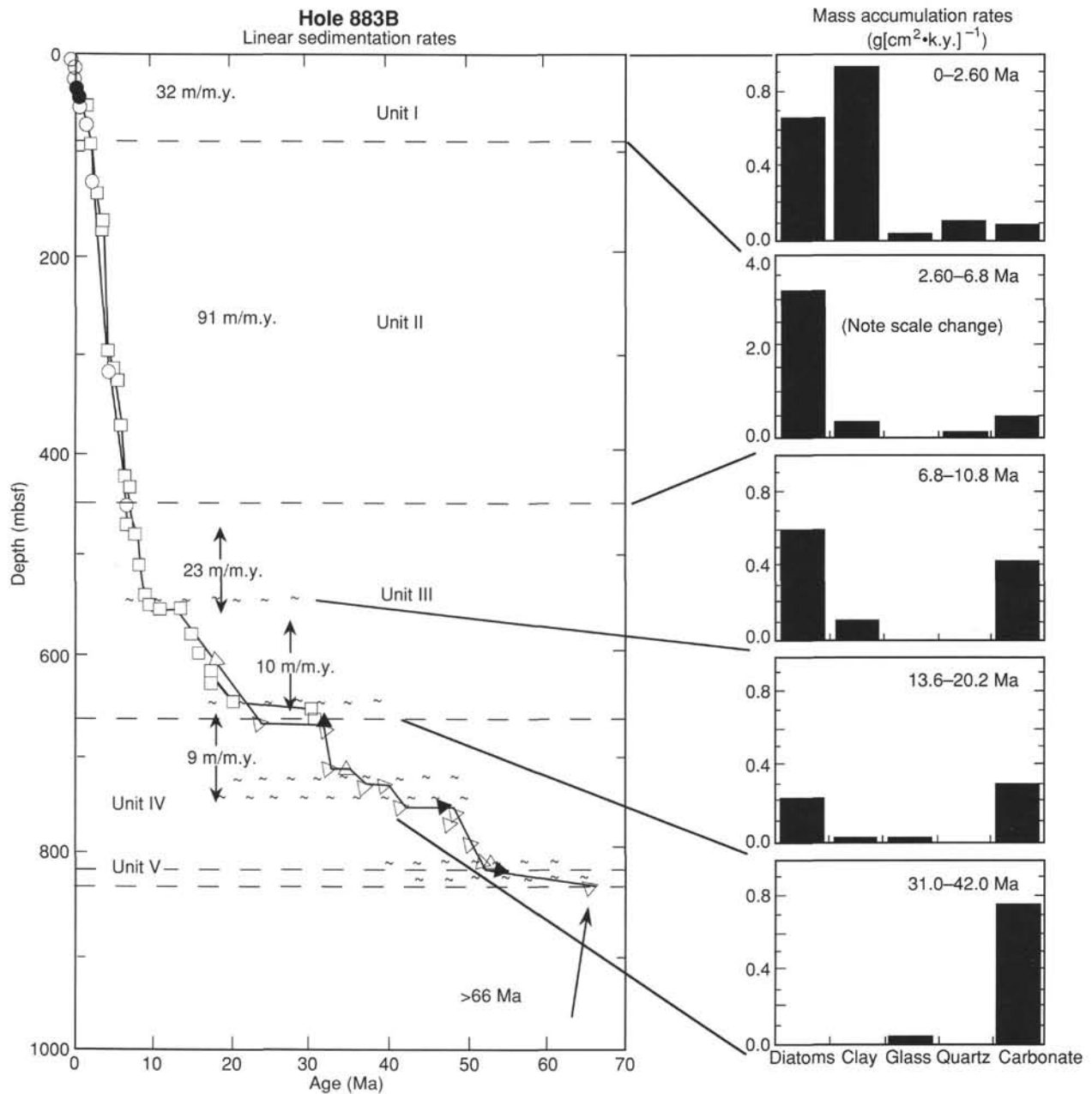


Figure 27. Sedimentation rate plot for Site 883 using magnetostratigraphy (solid symbols) and biostratigraphy (open symbols; squares, circles and triangles = diatoms, radiolarians, and nannofossils, respectively). For flux (mass accumulation rate right panel) calculations, the section has been divided into five intervals where rates of sedimentation are relatively constant. These intervals are identified by lines tying the stratigraphic column to the flux results, and their boundaries coincide with lithological boundaries (dashed lines) or condensed intervals or hiatuses (wavy horizontal lines). The flux results quantify the change from Paleogene carbonate sedimentation to Neogene siliceous sedimentation and the late Neogene onset of terrigenous sedimentation associated with glaciation.

However, the minimum between 100 and 200 mbsf suggests that a manganese-bearing authigenic phase is precipitating in that interval. The peak at ~650 mbsf is analytically reproducible, but enigmatic. There is no indication in the lithologic descriptions (see "Lithostratigraphy" section, this chapter) that a diagenetically labile manganese phase is present at or near this depth.

Titration alkalinity generally decreases throughout the sampled section from ~5.9 mM in the uppermost sample to ~2.7 mM at about 770 mbsf (Figs. 29A and 29B). Slight downward convexity in the profile between 80 and 400 mbsf implies either that consumption of alkalinity (mostly bicarbonate ion at the pH measured in the samples;

Table 8) is occurring in this zone, or that nonsteady-state deposition has altered the distribution of this parameter (Fig. 29B). The latter possibility is supported by sulfate data, as discussed below. The subtle alkalinity maximum centered at about 500 mbsf may reflect addition of carbonate ions to solution as a consequence of calcite dissolution at about this depth. Downward diffusion of alkalinity below the 500 mbsf horizon is implied by the profile and is consistent with the occurrence of abundant carbonate veins in the altered basalts at the base of the hole.

Sulfate at Site 883 decreases from ~28.6 mM in North Pacific Ocean Deep Water to ~24 mM at 1.5 mbsf (Table 8). The shape of the

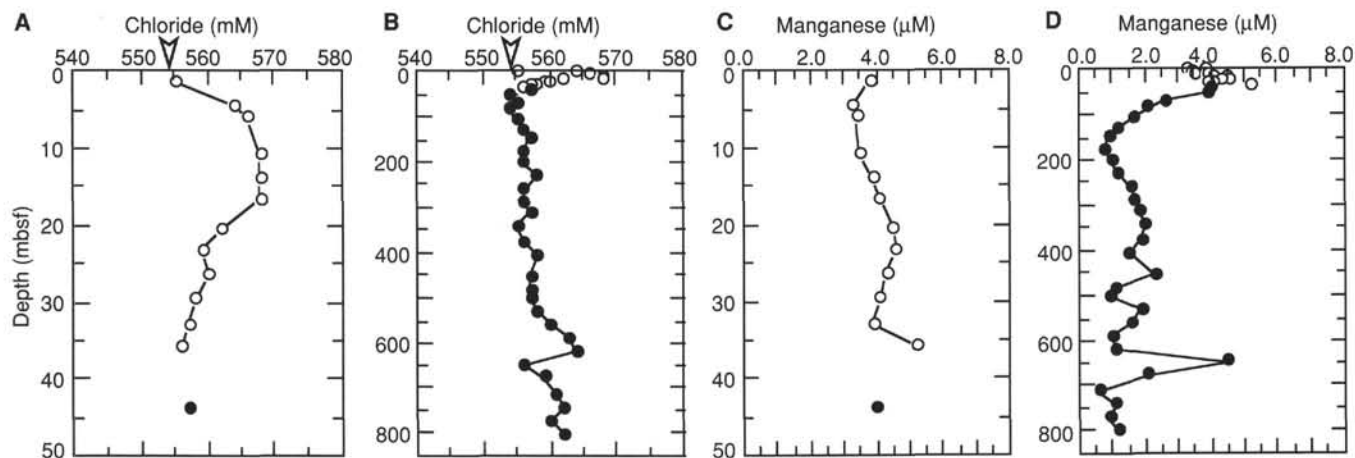


Figure 28. Interstitial-water profiles for Site 883. **A.** Chloride in the top 50 m. **B.** Chloride composite profile for Holes 883A and 883B. **C.** Manganese in the top 50 m. **D.** Manganese composite profile for Holes 883A and 883B. Open and closed circles indicate data from Holes 883A and 883B, respectively. The open arrow head indicates the concentration in modern North Pacific Deep Water.

profile immediately below this depth (Fig. 29A) indicates that active sulfate reduction, rather than molecular diffusion, is probably responsible for the nearly 5 mM decline in the top 1.5 m. Reduction of SO_4^{2-} is not occurring at depths greater than about 15 mbsf. The sulfate content generally increases below about 50 mbsf, reaching ~26 mM toward the base of the hole (Fig. 29C). It is highly unlikely that sulfate is being added to solution in this interval through any diagenetic reaction, and based on the chloride profile, the consumption of water through mineral hydration might account for only a tenth or so of the observed 14% increase. Therefore, the most plausible explanation for the sulfate “addition” at depth is that less SO_4^{2-} was reduced in the past, and diffusion has not yet obscured such a historical change. The hypothesis that the oxidant demand was lower during much of the early to middle Tertiary is consistent with the relatively low organic carbon concentrations and organic carbon accumulation rates observed throughout this time interval (see “Organic Geochemistry” and “Sedimentation Rates and Fluxes” sections, this chapter). The reduction of SO_4^{2-} is normally matched by a charge-equivalent production of alkalinity. Thus, the reduction of ~5 mM of SO_4^{2-} , as seen in the upper 1.5 m at Site 883 should be matched by a 10 mM increase in alkalinity (as HCO_3^-), rather than the ~3 mM increase actually measured. The sink for the “missing” 7 mM of alkalinity can be largely attributed to the precipitation of authigenic carbonate phases, as indicated by the Mg^{2+} and Ca^{2+} profiles, discussed below.

Dissolved ammonium at Site 883 increases with depth from 365 μM at 1.45 mbsf to about 708 μM at 36 mbsf (Fig. 30A). The concentration is essentially constant between ~70 and 300 mbsf and decreases approximately linearly below this interval to a value of 102 μM at 802 mbsf (Fig. 30B). The slight upward convexity in the interval between the sediment/water interface and ~22 mbsf indicates that this is the principal zone of NH_3 release. This is consistent with the sulfate distribution, which indicates that the highest rate of anaerobic decomposition occurs over roughly the same depth range. The generally linear decline of the ammonium content below 290 m is a reflection of downward diffusion from the zone of production in the more organic-rich upper portion of the section toward the organic-lean nannofossil chalks overlying the basement. The profile implies that a sink for ammonium may lie at the base of the hole. Illite, which is forming authigenically in the altering basement basalts (see “Lithostratigraphy” section, this chapter), is known to take up ammonium by isomorphous substitution of NH_4^+ for K^+ , both ions having similar ionic radii. This replacement should be manifested by a small increase in the K^+ concentration in pore waters at the site of reaction; such a minor augmentation is indicated by the potassium data in Table 8.

The composite magnesium and calcium profiles show that the elements are, in general, oppositely distributed at Site 883 (Fig. 30C). Magnesium values show a broad decrease in the upper part of the sampled section and an increase in the lowermost 200 m, while the calcium profile is marked by a long linear increase between ~50 and ~500 mbsf and a subtle decrease below this interval. The “noise” apparent in both data sets in the upper 50 m (Fig. 30C) appears to be inherent to the samples, rather than resulting from analytical artifacts, as shown by the expanded scale in Figure 30D. The variations may reflect “temperature-of-squeezing” effects. Bischoff et al. (1970) and Sayles et al. (1973) noted that warming of shallow-subsurface samples to room temperature before squeezing can lead to an increase of as much as 24% in the dissolved potassium concentrations and up to 7% decreases in the concentrations of dissolved divalent cations, such as Ca^{2+} and Mg^{2+} . Such effects can explain, wholly or in part (1) the near-surface potassium enrichment at Site 883 (see below); (2) the contrast between the calcium and magnesium concentrations in North Pacific Ocean bottom water and those in the uppermost pore-water sample (Fig. 30C); and (3) the rather sharp co-varying changes in Mg and Ca concentrations between, for example, the samples at ~14 and ~17 mbsf, if the whole-round cores from these depths were squeezed at different temperatures. To account for the 7 mM of “missing” alkalinity implied by the sulfate data (see above), about 3.5 mM of alkaline earth elements would need to be consumed from pore waters by precipitation of carbonate minerals in the upper 1.5 m of the section. The calcium and magnesium depletions between the sediment/water interface and the 1.5-m-depth plane total about 6 mM which, notwithstanding the possibility of squeezing artifacts, appears to be sufficient to account for the alkalinity deficiency. Calcium must be released to solution at a depth of about 500 mbsf to maintain the striking linear upward diffusion gradient between that depth and the calcite precipitation zone, which must exist above 50 mbsf. Dissolution of calcite and/or replacement of calcite by dolomite in the vicinity of 500 mbsf can explain the profile and can also provide the sink required to explain the magnesium minimum between ~500 and ~600 mbsf. This scenario also accounts for the addition of strontium to pore waters in the same depth interval, as discussed below.

The presence of chert bands in the lower reaches of the hole will tend to restrict diffusive communication; such inhibition, coupled with consumption of calcium and release of magnesium below the chert horizons, is probably responsible for the sharp changes in the concentrations of these elements in the lowermost pore-water sample from Hole 883B. Note that the anomalous composition of this sample cannot be caused by contamination by seawater because (1) sulfate

Table 7. Listing of average sediment data and flux results for five time-stratigraphic intervals at Site 883.

Depth int. (mbsf)	Age int. (Ma)	Dry-bulk density (g/cm ³)	Linear sed. rate (cm/k.y.)	Diatoms		Clay		Glass		Quartz	
				(%)	(g[cm ⁻² ·k.y.] ⁻¹)	(%)	(g[cm ⁻² ·k.y.] ⁻¹)	(%)	(g[cm ⁻² ·k.y.] ⁻¹)	(%)	(g[cm ⁻² ·k.y.] ⁻¹)
0–86.9	0–2.6	0.59	3.2	34.0	0.64	49.0	0.930	1.10	0.021	4.70	0.089
86.9–458.0	2.6–6.8	0.49	9.1	69.0	3.08	6.0	0.270	0.05	0.002	0.83	0.036
458.0–557.9	6.8–10.8	0.63	2.3	39.7	0.58	6.7	0.097	0.00	0.000	0.00	0.000
557.9–649.8	13.6–20.2	0.78	1.0	30.4	0.23	2.3	0.017	1.00	0.008	0.20	0.002
649.8–749.5	31–42	1.11	0.9	0.5	0.005	0.2	0.002	2.10	0.021	0.40	0.004

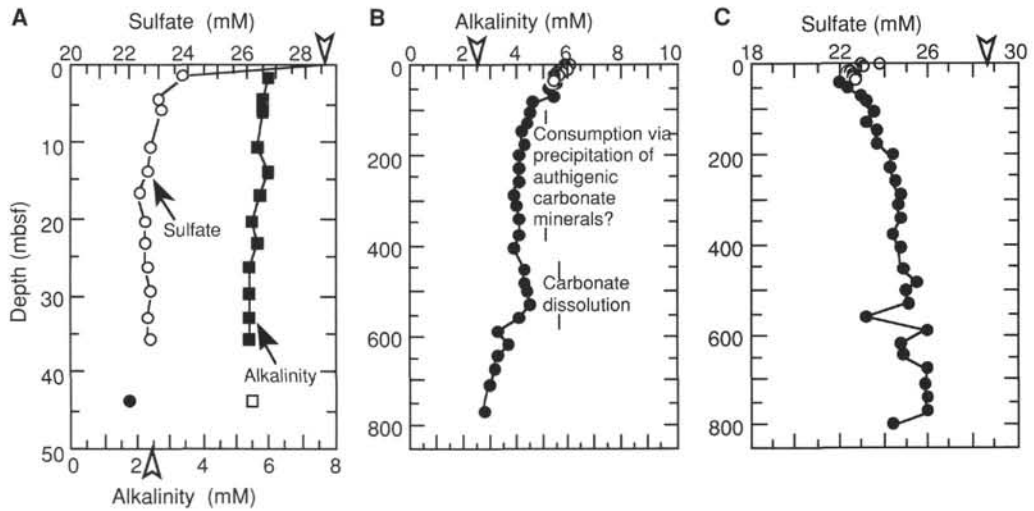


Figure 29. Interstitial-water profiles for Site 883. **A.** Sulfate and alkalinity in the top 50 m. **B.** Alkalinity composite profile for Holes 883A and 883B. **C.** Sulfate composite profile for Holes 883A and 883B. Open circles and closed squares represent data from Hole 883A, while closed circles and open squares mark data from Hole 883B. The open arrowhead indicates the concentration in modern North Pacific Deep Water.

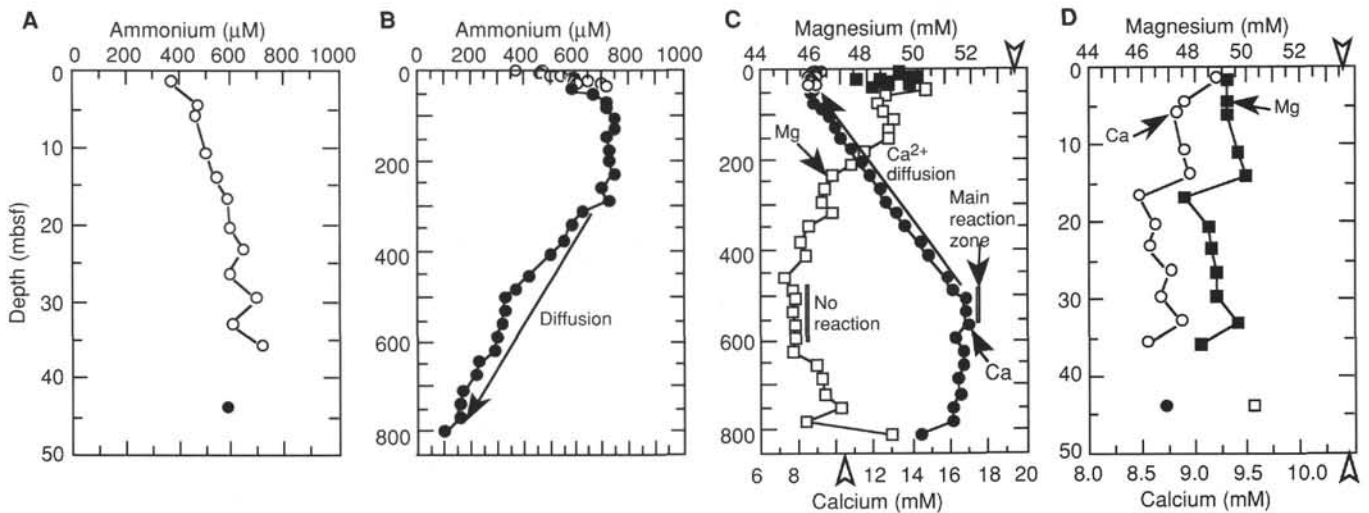


Figure 30. Interstitial-water profiles for Site 883. **A.** Ammonium in the top 50 m. **B.** Ammonium composite profile for Holes 883A and 883B. **C.** Magnesium and calcium composite profiles for Holes 883A and 883B. **D.** Magnesium and calcium in the top 50 m. Open circles and closed squares represent data from Hole 883A, while closed circles and open squares mark data from Hole 883B. The open arrowhead indicates the concentration in modern North Pacific deep water.

concentrations in the sample are sharply lower, rather than higher than seawater; (2) lithium content is significantly higher, rather than lower; and (3) the proportionate change in magnesium (roughly +6%) is notably different from the diminished calcium content (~12%). The opposite variations in Mg and Ca at the base of the core may be attributable to the alteration of olivine to iddingsite, which is perva-

sive in the upper portion of the basalts intersected in Hole 883E (see "Igneous Petrology" section, this chapter). The process of iddingsitization releases Mg, Fe²⁺, and Si and consumes Ca, Al, and Fe³⁺ (Deer et al., 1966).

The dissolved silicate concentrations in the topmost pore-water sample at Site 883 (~826 µM) are sharply higher than those in the

Table 7 (continued).

Carbonate		TOC	
(%)	(g[cm ² ·k.y.] ⁻¹)	(%)	(g[cm ² ·k.y.] ⁻¹)
3.90	0.074	0.15	0.003
8.10	0.361	0.18	0.008
29.0	0.421	0.05	0.001
39.0	0.296	0.06	0.001
72.4	0.724	0.00	0

overlying North Pacific Bottom Water (~160 μM), reflecting pronounced dissolution of opaline skeletons near the sediment/water interface (Fig. 31A). The average silicate concentration generally increases with depth to about 1362 μM at 500 mbsf, with a pronounced decrease between this level and the bottom sample (802 mbsf) to about 364 μM. The lowest values occur below 700 mbsf in the nanofossil chalk and clayey ash interval just above the basalt basement; these probably reflect formation of chert and alteration of ash and basalt to smectite and illite clays.

The concentrations of strontium in the uppermost pore-water sample (114 μM) is significantly greater than that of modern seawater (87 μM; Fig. 31B). The Sr²⁺ content steadily increases with depth, reaching a maximum concentration of 377 μM at 501 mbsf; values progressively decrease between 500 and 800 mbsf to 126 μM. The concentration maximum centered at about 500 mbsf probably reflects dissolution of calcite, as implied by the calcium profile discussed above. This zone contains poorly preserved and reworked calcareous nanofossils, and some intervals are barren of nanofossils due to dissolution (see "Biostratigraphy" section, this chapter). The released strontium supports upward and downward diffusive fluxes, the sinks for which are probably authigenic carbonates are forming at both shallow depths in the section, as implied by the calcium profile, and in the altering basaltic basement.

The lithium concentration (28.2 μM) in the shallowest sample in Hole 883A is slightly above that of modern seawater (27 μM) (Fig. 31B). This profile is similar in form to that of Sr: a concentration maximum at about 400 mbsf supports both an upward diffusive flux, which is clearly supplying Li⁺ to the overlying North Pacific Deep Water, and a downward flux, which signifies an unknown sink near the basement. Available lithologic data do not permit definition of the source of the mid-depth concentration maximum, although it should be noted that clays are relatively abundant between about 390 and 450 mbsf. Could ongoing diagenesis of the clay fraction in the upper Miocene deposits be responsible for the release of lithium to pore waters at this site? Dissolution of opal does not appear to be an important contributor to the lithium maximum, because little resemblance can be seen among the distributions in pore waters of H₄SiO₄ (Fig. 31A) and Li⁺.

Sodium (calculated by charge balance at this site) and potassium show little variation in the pore waters down the core, with concentrations being near those in seawater (Fig. 31B). The high-resolution section of the sodium profile shows a slight enrichment, which is commensurate with the chloride maximum between 10 and 30 mbsf, and reflects the Quaternary salinity effect discussed earlier. The calculated Na⁺ concentrations are invariant throughout the remainder of the profile, indicating that this element is essentially unreactive in the sampled sediments and in the underlying basalts at this location. The potassium data show scatter in excess of the precision of the flame emission method used to determine the concentrations, and the concentrations in the near-surface samples of Hole 883A are as much as 10% higher than that in the overlying seawater. Both the poor precision and the apparently high value may result from the temperature-of-squeezing effect, which is known to be particularly significant for the K⁺; Sayles et al. (1973) observed an increase of up to 24% in the potassium concentration in pore waters as a result of this artifact. A very subtle, approximately linear decline in the K⁺ content over the

course of the sampled section indicates minor diffusion toward greater depths, possibly reflecting exchange with basaltic basement.

ORGANIC GEOCHEMISTRY

Volatile Hydrocarbons

As required by shipboard safety and pollution considerations, the volatile hydrocarbon gases methane (C₁), ethane (C₂), and propane (C₃) were monitored in each core immediately after retrieval on deck. One hundred and twenty-nine samples were collected from sediments of Site 883 using the headspace technique; these were measured in a Carle gas chromatograph. Procedures are described in the "Organic Geochemistry" section of the "Explanatory Notes" chapter (this volume). Methane concentrations measured in the sediments of Site 883 are low, ranging between 2 and 15 ppm (Table 9), and indicate no significant methanogenesis in the sediment column. Ethane and propane concentrations were below the detection limit of the gas chromatograph. These low amounts of volatile hydrocarbons can be ascribed to the low organic matter yield of the analyzed samples (see below).

Carbonate Carbon

Inorganic carbon was measured in 203 samples from Hole 883B using the Coulometrics carbon dioxide coulometer. The results are reported as weight percent calcium carbonate in Table 10.

The CaCO₃ contents of sediments from Site 883 are highly variable with values ranging between 0 and almost 100 wt%. The sedimentary record can be divided into several intervals according to the distribution of calcite. A major change occurs at about 460 mbsf, below which values increase dramatically from <40 wt% up to highest values of 98 wt% (Fig. 32; 40 wt% boundary marked with a line). This change also marks the boundary between lithologic Units II and III at 458 mbsf (see "Lithostratigraphy" section, this chapter.) The transitions from lithologic Units III through V cannot be observed in the carbonate record, because this is based on the change from chalk to altered volcanoclastic material with interbedded chalk layers (see "Lithostratigraphy" section, this chapter).

The carbonate record displays a clear correlation to the relative abundance of nanofossils (Fig. 32; see "Biostratigraphy" section, this chapter). Three intervals of low nanofossil abundance at about 60, 250, and 470 mbsf correspond well to intervals having reduced calcium carbonate contents. This leads to the interpretation that deposition of carbonate at Site 883 is most strongly regulated by sedimentation of calcareous nanofossils, not by other biogenic or detrital calcareous sediment components.

Organic Carbon

Ninety-nine samples gathered from Hole 883B were measured for total carbon by means of a Carlo Erba NCS analyzer; the results are presented in weight percent in Table 10. The concentrations of total organic carbon (TOC) in the sediments of Site 883 were determined by the difference of total carbon (TC) and inorganic carbon (IC) from coulometry.

The organic carbon content of the sediments at Site 883 is very low to low, as shown in Figure 33. Values range from 0 to 0.4 wt%. Two intervals having slightly higher TOC concentrations occur between 0–80 and 200–420 mbsf. These higher values are limited to lithologic Units I and II (see "Lithostratigraphy" section, this chapter) and probably indicate a higher surface-water productivity and/or a better preservation of organic matter in the diatom oozes of Units I and II. However, note that the very low to zero TOC contents within the calcareous oozes and chalks of Units III and IV are possibly subject of analytical error. The higher the carbonate content of the analyzed sediment, the higher the absolute error of the IC analysis; this can have a major effect if the difference in TC and TOC contents is very large. The calculated

Table 8. Interstitial-water data for Site 883.

Interval (cm)	Depth (mbsf)	pH	Alk. (mM)	Sal. (g/kg)	Cl (mM)	Mg (mM)	Ca (mM)	SO ₄ (mM)	NH ₄ (M)	NO ₂ (μM)	H ₄ SiO ₄ (μM)	K (mM)
145-883A-												
1H-1, 145-150	1.45	7.8	5.99	35.0	555	49.3	9.2	23.8	365	0	826	12.9
1H-3, 145-150	4.45	7.9	5.82	35.0	564	49.2	8.9	22.9	471	0.29	834	11.1
1H-4, 145-150	5.95	7.7	5.78	34.5	566	49.2	8.8	23.1	464	1.43	991	12.0
2H-1, 125-130	10.75	7.8	5.62	35.0	568	49.6	8.9	22.7	501	0	804	10.8
2H-3, 145-150	13.95	7.8	5.93	35.0	568	50.0	9.0	22.6	535	0	819	12.9
2H-5, 125-130	16.75	7.9	5.72	34.5	568	47.6	8.5	22.3	585	0	1099	13.1
3H-1, 145-150	20.45	7.8	5.48	35.0	562	48.5	8.6	22.5	595	n.m.	848	11.7
3H-3, 125-130	23.25	7.8	5.64	35.5	559	48.6	8.6	22.5	643	n.m.	856	12.2
3H-5, 145-150	26.45	7.7	5.42	34.5	560	48.9	8.8	22.6	590	n.m.	898	13.3
4H-1, 125-130	29.75	7.9	5.39	35.5	558	48.8	8.7	22.7	695	n.m.	870	12.0
4H-3, 145-150	32.95	7.8	5.39	35.5	557	49.6	8.9	22.6	597	n.m.	809	11.1
4H-5, 125-130	35.75	7.8	5.39	35.0	556	48.3	8.6	22.7	708	n.m.	937	12.1
145-883B-												
5H-4, 145-150	43.85	7.8	5.47	35.0	557	50.2	8.7	22.0	579	n.m.	851	10.1
6H-4, 145-150	53.35	7.8	5.18	34.4	554	48.7	8.6	22.3	663	n.m.	902	11.8
8H-4, 145-150	72.35	8.1	5.36	35.0	555	48.4	8.8	22.9	715	n.m.	701	12.5
10H-3, 0-5	86.90	7.8	4.56	35.0	554	48.7	9.2	23.2	712	n.m.	875	11.6
12H-3, 145-150	106.35	7.7	4.53	35.0	555	49.1	9.6	23.5	743	n.m.	988	11.4
14H-4, 145-150	129.35	7.9	4.39	35.0	556	48.9	9.9	23.2	738	n.m.	976	10.6
16H-4, 145-150	148.35	7.8	4.17	35.0	557	48.8	10.2	23.6	715	n.m.	893	11.8
19H-4, 145-150	176.85	7.8	4.28	35.0	556	47.9	10.8	23.6	725	n.m.	981	10.4
22H-4, 145-150	205.35	7.8	4.13	34.5	556	47.5	11.2	24.3	722	n.m.	1178	12.8
25H-4, 145-150	231.85	7.8	4.13	34.5	558	46.7	11.8	24.3	740	n.m.	1094	10.5
28H-4, 145-150	262.35	7.8	4.06	34.5	556	46.5	12.2	24.5	695	n.m.	1180	13.4
31H-4, 145-150	290.85	7.8	3.88	34.5	556	46.3	12.5	24.7	718	n.m.	1089	11.1
34X-3, 145-150	314.65	7.7	4.00	35.0	557	46.7	13.1	24.6	622	n.m.	1109	10.5
37X-1, 145-150	342.65	7.7	4.12	35.0	555	45.8	13.6	24.8	579	n.m.	1067	10.6
40X-4, 145-150	377.65	7.7	4.14	35.0	556	45.5	14.4	24.4	555	n.m.	944	10.8
43X-6, 145-150	408.45	7.6	3.92	35.0	558	45.7	14.8	24.7	501	n.m.	1205	10.8
48X-4, 145-150	456.15	7.5	4.31	35.0	557	45.0	15.8	24.8	418	n.m.	1141	12.0
51X-4, 145-150	483.85	7.5	4.27	35.0	557	45.3	16.1	25.5	368	n.m.	1301	11.2
54X-4, 145-150	501.55	7.7	4.41	35.0	557	45.3	16.8	25.0	329	n.m.	1362	9.8
57X-4, 145-150	531.05	7.6	4.50	35.0	558	45.2	16.8	25.0	326	n.m.	1249	10.0
60X-4, 145-150	560.95	7.4	4.13	35.0	560	45.3	16.9	23.2	323	n.m.	1343	10.6
63X-4, 145-150	590.95	7.5	3.29	35.0	563	45.3	16.2	25.9	295	n.m.	1257	10.1
66X-4, 145-150	620.25	7.4	3.72	35.0	564	45.2	16.7	24.8	292	n.m.	1129	9.8
69X-4, 145-150	648.75	7.5	3.28	35.0	556	46.2	16.7	24.9	228	n.m.	1043	9.8
72X-4, 145-150	677.75	7.5	3.21	35.0	559	46.3	16.4	26.0	213	n.m.	1217	12.8
76X-4, 145-150	714.01	7.5	2.98	35.0	561	46.4	16.5	25.9	172	n.m.	944	8.9
79X-2, 145-150	743.45	n.m.	n.m.	35.0	562	47.1	16.1	25.9	155	n.m.	961	9.2
82X-4, 145-150	773.15	7.6	2.74	35.0	560	45.8	16.1	25.9	157	n.m.	772	10.4
85X-2, 145-150	802.85	n.m.	n.m.	35.0	562	48.9	14.4	24.3	102	n.m.	364	10.2

Note: n.m. = not measured.

TOC in these circumstances can be significantly in error (see "Explanatory Notes" chapter, this volume). Thus, the shipboard measurements must be verified by shore-based analyses using another analytical method. Total nitrogen concentrations detected in the sediments are near or below the threshold of the NCS analyzer and have not been used to infer the provenance or preservational state of the organic matter.

PHYSICAL PROPERTIES

Introduction

Index property (densities, porosities, water contents, and void ratios), digital sediment velocimeter (DSV), and shear strength measurements were taken at 0.75-m intervals in cores from Hole 883A, 1.5-m intervals from Hole 883B, in Cores 145-883B-1H and -30H through -86X, and in cores from Hole 883C (Table 11). GRAPE bulk density, P-wave velocities, and magnetic susceptibility were continuously measured in all six holes using the multisensor track (MST). Tables containing the compressional wave velocity and shear strength data from Holes 883A, 883B, 883C, and 883E are included, as are tables of index property data from Holes 883A, 883B, 883C and 883E (Tables 12 through 15). GRAPE and P-wave logger data have been smoothed and culled in the same manner as at Sites 881 and 882 (see "Physical Properties" section, "Site 881" chapter, this volume).

Index Properties and Vane Shear Strength

Profiles of sediment wet-bulk density, dry-bulk density, dry water content, and porosity values for Holes 883A, 883B, and 883C (see

Figs. 34 through 36) show good correspondence. Because of the poor recovery in the top part of the XCB-cored section in Hole 883B, shear strength data are limited, and as a result, the profiles do not show good correlation where they overlap between 300 and 350 mbsf (see Fig. 37).

The cored section has been divided into four units (A to D) on the basis of physical properties measurements. In physical properties (PP) Unit A, the wet-bulk density, dry-bulk density, dry water content, shear strength, and wet porosity values in the upper 90 mbsf remain fairly constant, averaging 1.37 and 0.59 g/cm³, 143%, 40–50 kPa, and 76%, respectively. Physical properties Unit B has been divided into two subunits as follows. Subunit B1 extends from 90 to 460 mbsf. Based upon the data from Holes 883B and 883C, Subunit B1 is characterized by a distinct decrease in both wet-bulk density (to an average of 1.30 g/cm³) and shear strength (ranging from 35 to 40 kPa) that corresponds to an increase in wet porosity and dry water content to averages of 78% and 164%, respectively (see Figs. 35 through 37). The slope break of the curve at approximately 90 mbsf corresponds to a change in sediment type from a clayey diatom ooze above 90 mbsf to a diatom ooze below (see "Lithostratigraphy" section, this chapter). The relative increase in opaline silica and decrease in terrigenous clay contents could easily account for the observed changes. A second, less marked change in the baseline value of wet-bulk density occurs at approximately 460 mbsf, marking the start of PP Subunit B2. At this depth, the wet-bulk density increases slightly (to an average of 1.37 g/cm³), corresponding to a slight decrease in the dry water content (averaging 127%). The top of PP Subunit B2 is coincident with an increase in the calcareous component observed from smear slide analysis (see "Lith-

Table 8 (continued).

Li (μM)	Na (mM)	Sr (μM)	Mn (μM)	Mg/Ca (mol ratio)
28.2	478	114	3.8	5.36
27.0	487	126	3.3	5.53
27.7	489	126	3.4	5.58
27.8	490	137	3.5	5.58
28.2	487	137	3.9	5.58
29.9	492	137	4.1	5.62
29.3	485	137	4.5	5.62
29.5	482	137	4.6	5.68
30.4	481	137	4.3	5.57
31.2	481	137	4.1	5.63
30.8	479	148	3.9	5.59
31.5	480	137	5.2	5.64
30.1	478	148	4.0	5.76
30.8	477	148	3.9	5.67
35.5	478	148	2.6	5.51
34.8	477	171	2.1	5.30
35.8	477	183	1.7	5.10
37.4	477	183	1.2	4.92
38.4	477	205	0.9	4.77
41.9	479	240	0.8	4.45
42.4	477	251	1.0	4.22
45.2	478	297	1.2	3.96
45.2	477	297	1.6	3.80
47.3	479	308	1.7	3.69
48.0	479	331	1.8	3.57
48.8	478	342	2.0	3.38
52.4	477	354	1.9	3.17
47.7	478	354	1.5	3.09
46.0	476	377	2.3	2.85
44.0	478	n.m.	1.1	2.81
42.9	476	365	0.9	2.70
42.4	477	365	1.9	2.69
39.6	474	354	1.6	2.68
39.0	484	320	1.0	2.79
35.6	483	285	1.1	2.71
36.2	473	274	4.5	2.77
31.1	475	240	2.1	2.82
30.8	480	217	0.6	2.82
32.6	477	194	1.1	2.92
28.1	480	148	0.9	2.84
31.4	473	126	1.2	3.40

ostratigraphy" section, this chapter). In PP Unit C, which begins at 600 mbsf, an increase is seen in the values of wet-bulk and dry bulk densities to average values of 1.71 g/cm³ and 1.10 g/cm³, respectively. These changes are mirrored in the form of decreases in the values of dry water content (averaging 58%) and wet porosity (65%). The sharp deviations in the profiles at the top of PP Unit C occur at the onset of nanofossil chalk and may be the result of cementation and diagenesis of the carbonate component of this lithology (see "Lithostratigraphy" section, this chapter). Basalt, PP Unit D, was cored in the base of Holes 883E and 883F, 819 to 856.5 mbsf (see "Igneous Petrology" section, this chapter); the bulk densities of this basalt range from 2.15 to 3.56 g/cm³.

The grain density profiles (Fig. 38) display trends similar to those seen in the wet-bulk density profiles. Within PP Unit A, the grain density is fairly constant at 2.50 g/cm³, while in Subunit B1, below 90 mbsf, grain density decreases to approximately 2.26 g/cm³, probably the result of the previously mentioned relative decrease in terrigenous clay and increase in biogenic opal content. The grain density values then increase to values of approximately 2.33 g/cm³ in Subunit B2, at 460 mbsf, and again in Unit C, at 600 mbsf, to an average of 2.67 g/cm³, most likely because of the appearance of nanofossil ooze. Within the basalts at the base of Hole 883E, grain densities range from 2.67 to 4.5 g/cm³. The units discussed above coincide with some of the lithostratigraphic units delimited by the sedimentology (see "Lithostratigraphy" section, this chapter): PP Unit A is equivalent to lithologic Unit I (0–87 mbsf, base \approx 2.7 Ma), Subunit B1 to lithologic Unit II (87–458 mbsf, base \approx 7.3 Ma), Subunit B2 to lithologic Subunit IIIA (464–597 mbsf, base \approx 16 Ma), PP Unit C to lithologic Subunit IIIB (597–652 mbsf, base \approx 25 Ma)

and lithologic Unit IV (652–814 mbsf, base \approx 70 Ma), and PP Unit D to lithologic Unit V (814–856.5 mbsf).

GRAPE Data

Figure 39 shows each profile of the GRAPE bulk density values in Holes 883A, 883B, 883C, and 883D. Although in all four cases the GRAPE bulk density profiles parallel the trends of those obtained with the pycnometer, the GRAPE data were consistently higher valued by approximately 0.1 g/cm³ than those data produced by pycnometer analysis (see "Physical Properties" section, "Site 881" chapter, this volume). Special 2-min counts were used when testing the basalt from Hole 883E.

Compressional Wave Velocities

Figure 40 shows profiles of compressional wave velocity data. The P-wave profiles include data from both the P-wave logger (PWL), Hamilton Frame, and the DSV. Below 490 mbsf, data from the PWL are not available because of the nature of the XCB cores. Compressional wave velocities from the PWL average 1545 m/s (1546 m/s in Hole 883B and 1544 m/s in Hole 883C) throughout the section logged, but increase downhole (see Fig. 40A), following the general trend of the data from the DSV and Hamilton Frame. The spiky nature of the PWL data may be attributed to the presence of ash layers and ice-rafted debris (IRD) in the form of igneous pebbles (see "Lithostratigraphy" section, this chapter). The DSV and Hamilton Frame profiles do not reflect the presence of all of the ash layers and IRD owing to the bias inherent in the discontinuous sampling for DSV data. The basalts tested from the base of Hole 883E gave velocity values of between 2937 and 4874 m/s and averaged 4037 m/s; these data are shown in Figure 40B.

DOWNHOLE MEASUREMENTS

Logging Operations and Quality of Logs

A total of five tool strings were run at Hole 833F: the Schlumberger geochemical, Quad combination, and formation microscanner (FMS) tool strings, and the French magnetometer and susceptibility tools. A summary of the logging tool strings, the basis of their measurement principles, and logging operations is provided in the "Explanatory Notes" chapter (this volume). The wireline heave compensator was used for all logging runs, although sea-state conditions were mild. Base of pipe was set at 120 mbsf. Log data presented in this section have not been corrected for environmental factors, nor have these data been depth-shifted to match drilling depths exactly.

The geochemical combination tool string, consisting of natural gamma-ray (NGT), aluminum activation (AACT), and gamma-ray spectrometry (GST) tools, was calibrated at the sea surface and was run to total depth (3242 mbsf; 846 mbsf). An attempt to re-calibrate the GST at 690 mbsf indicated that the tool would not attain stable re-calibration possibly due to very cool bottom-hole temperatures (\sim 3°C). As a result, all elemental yield logs from this tool are of uncertain quality and are not presented here. Post-cruise processing will determine whether these data contain any valid information. The aluminum yield from the AACT, and potassium, uranium, and thorium from the NGT were not similarly affected and are reliable. One main up-going log was recorded at 550 ft/hr from 846 mbsf to the mud line.

The French CEA-LETI/TOTAL/CNRS-ENS magnetometer (NRMT) and susceptibility (SUMT) tools were run next to ensure that both tools would measure a borehole environment unaffected by any electromagnetic induction measurements. Two complete passes of the NRMT were conducted at 1800 ft/hr from total depth (846 mbsf) to base of pipe, raised at 100 mbsf. The total magnetic field measurements of the NRMT were highly reproducible between the two runs. NRMT Log quality was seriously compromised above 220 mbsf

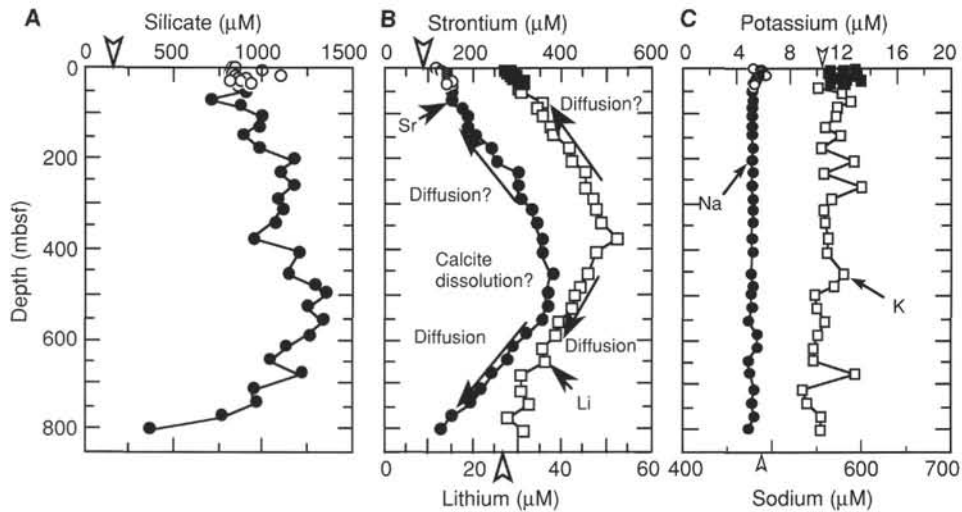


Figure 31. Interstitial-water profiles for Site 883. **A.** Silicate composite profile for Holes 883A and 883B. **B.** Strontium and lithium composite profiles for Holes 883A and 883B. **C.** Potassium and sodium composite profiles for Holes 883A and 883B. Open circles and closed squares represent data from Hole 883A, while closed circles and open squares mark data from Hole 883B. The open arrowhead indicates the concentration in modern North Pacific Deep Water.

because of the presence of the BHA and several stands of drill pipe remaining in the adjacent Hole 883E. One main up-going log of the SUMT was recorded at 3600 ft/hr from 856 to 120 mbsf; a shorter repeat up-going log was recorded from 380 to 120 mbsf. Susceptibility data were not calibrated in absolute terms. Data were collected at 5-cm intervals for both tools.

The FMS tool string was run next, and three short up-going logs were recorded at 1800 ft/hr from 846 to 704, 846 to 634, and 846 to 614 mbsf; the main up-going log was recorded from 846 to 100 mbsf. Hole 883F had been drilled with a 9-7/8 in. rotary bit, and a roughly circular 10 to 12 in. diameter hole was maintained throughout the lower section of the hole (850–400 mbsf). Above 400 mbsf, however, the hole gradually developed an elliptical shape with a maximum diameter above 225 mbsf, exceeding the 15 in. limit of the FMS caliper arm measurement. The minimum diameter was consistently between 10 to 12 in. Poor contact of two of the four FMS pads with the borehole wall was noted in the FMS monitor log for the uppermost 225 mbsf of this main up-going log. The maximum diameter of the borehole ellipse was consistently oriented at about 310°. The origin of an elliptical borehole geometry in these unconsolidated sediments remains unknown; the ship's heading was consistently due north throughout the drilling and logging operations of Hole 883F.

The Quad combination tool string, with the Lamont temperature tool, was the final string run into Hole 883F. A down-going log was recorded from 150 mbsf to total depth (840 mbsf). The main up-going log was recorded at 2600 ft/hr from 840 mbsf to the mud line. The eccentricizing caliper arm of the lithodensity tool (HLDT) would not open after repeated attempts, so the density and photoelectric effect data recorded during the main up-going log are unreliable because of excessive tool "stand-off." The natural gamma-ray, sonic, porosity, and resistivity logs are reliable throughout the entire logged interval.

Results

Borehole Temperature

Borehole temperatures measured by the Lamont temperature tool reflect the temperature of seawater in the borehole, not the true formation temperature itself. The formation cools during drilling because of fluid circulation, and it is only after drilling has ceased that the temperatures can begin to rebound. The geochemical tool string

was the first to be run into Hole 883F, and bottom-hole temperatures measured with this tool were 3.1°C, or about 2°C above the ambient deep seawater temperatures. The borehole temperature profile measured by the Lamont temperature tool during the final run with the Quad tool string indicated that bottom-hole temperatures had warmed to a maximum of 8.2°C over the intervening 27 hrs. (Fig. 41). In addition, the borehole had warmed by 0.7°C between the beginning of the down-going log and the end of the up-going log (~2.5 h).

Lithology

Inflections in the log data reflect major lithological boundaries identified from core smear slide data (see "Lithostratigraphy" section, this chapter). The geochemical and geophysical log data are presented in Figures 42, 43, and 44. The natural gamma-ray logs shown in Figure 42 were taken from the geochemical tool string; the slow logging speed employed for this tool string provides the most reliable spectral gamma-ray logs. The elemental yield logs from the geochemical tool are not presented because these data were not considered unreliable.

The natural gamma-ray, neutron porosity, and aluminum logs can be used to define the boundary between lithologic Units I and II, which occurs at 87 mbsf (Figs. 42, 43, and 44). The nuclear basis of these log measurements permits the delineation of this lithologic boundary through the drill pipe. From smear slide descriptions, lithologic Unit I is a clay containing diatoms, abundant ash, dropstones, and quartz, whereas the underlying Unit II is a more porous diatom clay having less abundant ash and fewer dropstones (see "Lithostratigraphy" section, this chapter). The boundary corresponds to the onset of Northern Hemisphere glaciation near 2.6 Ma. The increased abundances of both clay and ash in Unit I are reflected by increased K, Th, and Al log values.

The thick accumulations of diatom ooze that characterize lithologic Unit II are represented by relatively low sonic velocities (1.6–1.7 km/s), low resistivity values, and variable gamma-ray values. The intrinsically high porosity and low density of diatomaceous sediment contribute to the low P-wave velocities and increased neutron porosities. The spectral gamma-ray logs demonstrate that significant variability is evident in the concentration of terrigenous material, however. The increased K and Th log values reflect an increase in clay content

Table 9. Results of headspace gas analyses from Holes 883A, 883B, 883C, 883D, and 883E.

Core, section, interval (cm)	Depth (mbsf)	C ₁ (ppm)
145-883A-		
1H-5, 0-3	6.00	5
2H-5, 0-3	15.50	4
3H-5, 0-3	25.00	4
4H-5, 0-3	34.50	3
145-883B-		
1H-4, 0-3	4.50	3
2H-5, 0-3	13.90	5
3H-5, 0-3	23.40	8
4H-4, 0-3	31.40	10
5H-5, 0-3	42.40	11
6H-5, 0-3	51.90	10
7H-5, 0-3	61.40	8
8H-5, 0-3	70.90	7
9H-5, 0-3	80.40	11
10H-3, 5-8	86.95	5
11H-5, 0-3	99.40	10
12H-4, 0-3	107.40	11
13H-5, 0-3	118.40	8
14H-5, 0-3	127.90	7
15H-5, 0-3	137.40	7
16H-5, 0-3	146.90	7
17H-5, 0-3	156.40	6
18H-5, 0-3	165.70	8
19H-5, 0-3	175.40	7
20H-5, 0-3	184.90	8
21H-5, 0-3	194.40	3
22H-5, 0-3	203.90	6
23H-5, 0-3	213.40	9
25H-5, 0-3	232.40	7
26H-5, 0-3	241.90	8
27H-5, 0-3	251.40	5
28H-5, 0-3	260.90	5
29H-5, 0-3	270.40	4
30H-5, 0-3	279.90	5
31H-5, 0-3	289.40	5
32X-5, 0-3	298.90	4
33X-2, 0-3	304.00	4
34X-4, 0-3	316.70	5
35X-4, 0-3	326.40	4
37X-2, 0-3	342.70	3
38X-5, 0-3	356.90	4
39X-4, 0-3	365.00	3
40X-5, 0-3	376.20	3
41X-4, 0-3	384.50	3
42X-5, 0-3	395.70	3
43X-6, 0-3	407.00	3
44X-5, 0-3	415.30	2
45X-5, 0-3	425.20	3
48H-5, 0-3	454.70	8
49X-5, 0-3	464.20	12
50X-5, 0-3	474.10	8
51X-5, 0-3	483.90	10
53X-5, 0-3	503.70	13
54X-5, 0-3	513.60	10
55X-5, 0-3	523.40	15
57X-5, 0-3	543.10	12
59X-5, 0-3	563.00	6
60X-5, 0-3	573.00	8
61X-5, 0-3	583.00	12
62X-5, 0-3	593.00	14
63X-5, 0-3	603.00	8
64X-2, 0-3	608.50	10
65X-4, 0-3	621.20	6
66X-5, 0-3	632.30	7
67X-5, 0-3	642.00	8
68X-3, 0-3	648.10	7
69X-5, 0-3	660.80	8
70X-5, 0-3	670.40	4
71X-5, 0-3	680.10	5
72X-5, 0-3	689.70	6
73X-5, 0-3	699.30	7
74X-2, 0-3	704.50	8
76X-5, 0-3	726.10	5
77X-5, 0-3	735.90	5
78X-5, 0-3	745.70	6
79X-3, 0-3	752.50	3
82X-5, 0-3	785.20	4
83X-3, 0-3	792.20	3
85X-3, 0-3	811.90	2
86X-3, 0-3	821.50	2
87X-2, 0-3	829.50	2

Table 9 (continued).

Core, section, interval (cm)	Depth (mbsf)	C ₁ (ppm)
145-883C-		
1H-2, 0-3	1.50	3
2H-5, 0-3	9.00	4
3H-5, 0-3	18.50	8
4H-5, 0-3	28.00	8
5H-5, 0-3	37.50	9
6H-5, 0-3	47.00	7
7H-5, 0-3	56.50	5
8H-5, 0-3	66.00	8
9H-5, 0-3	75.50	8
10H-6, 0-3	86.50	12
11H-5, 0-3	94.50	10
12H-5, 0-3	104.00	11
13H-5, 0-3	112.14	10
14H-5, 0-3	123.00	8
15H-5, 0-3	132.50	12
16H-5, 0-3	142.00	9
17H-5, 0-3	151.50	7
18H-5, 0-3	161.00	7
19H-5, 0-3	170.50	7
20H-4, 0-3	178.50	5
21H-5, 0-3	189.50	7
22H-5, 0-3	199.00	8
23H-5, 0-3	208.50	8
24H-5, 0-3	218.00	5
25H-5, 0-3	227.50	3
26H-5, 0-3	237.00	5
27H-5, 0-3	246.50	7
29X-5, 0-3	265.60	5
31X-5, 0-3	284.30	6
32X-5, 0-3	294.00	4
33X-2, 0-3	299.10	4
34X-4, 0-3	311.80	3
35H-5, 0-3	323.00	3
36H-5, 0-3	332.50	3
37H-5, 0-3	342.00	3
38H-5, 0-3	351.50	4
145-883D-		
1H-2, 0-3	1.50	4
2H-5, 0-3	13.50	5
145-883E-		
1R-4, 0-3	551.50	8
3R-2, 0-3	651.30	9
4R-2, 0-3	661.10	6
5R-3, 0-3	672.50	7
6R-3, 0-3	682.40	8
7R-4, 0-3	693.80	5
11R-3, 0-3	731.80	6
12R-4, 0-3	743.10	4
13R-3, 10-13	751.50	4
15R-2, 0-3	769.60	4
16R-2, 0-3	779.50	5

Note: C₁ = methane. All samples are headspace samples.

between 275 and 375 mbsf, as also is noted in the smear slide analyses. This interval is also represented by relatively high-amplitude periodic variations in several log properties (discussed later), whereas the remainder of Unit II is more homogeneous and less variable in comparison.

The gradual transition to a carbonate-rich ooze occurs within lithologic Subunit IIIA from 458 to 597 mbsf. This transition is clearly reflected in the sonic and porosity logs with gradual, but distinct increases in sonic velocity and decreases in neutron porosity. Several small-scale changes in lithology that were observed in the smear slide descriptions are more clearly defined by the logs. The spectral gamma-ray (K and Th) and Al logs identify a short clay-rich interval between 525 and 550 mbsf (Figs. 42 and 44). Below this, an increase in diatom concentration between 570 and 597 mbsf is reflected by sharply lower sonic velocities and resistivity values.

The nannofossil chalk lithology of lithologic Subunit IIIB (597–652.2 mbsf) is indicated by a sharp and persistent increase in sonic velocity and resistivity (Fig. 43). In agreement with core-based physical-property measurements (see "Physical Properties" section, this chapter), the logs reflect a sharp increase in sediment density and

Table 10. Results of geochemical analyses from Hole 883B.

Core, section, interval (cm)	Depth (mbsf)	TC (wt%)	ICF (wt%)	TOC (wt%)	CaCO ₃ (wt%)	TN (wt%)
145-883B-						
1H-1, 112-113	1.12	0.88	0.55	0.33	4.60	0.10
1H-3, 112-113	4.12	0.33	0.20	0.13	1.70	0.00
1H-5, 112-113	7.12	2.41	2.24	0.17	18.70	0.02
2H-1, 112-113	9.02	0.99	0.83	0.16	6.90	0.04
2H-3, 112-113	12.02	0.39	0.22	0.17	1.80	0.05
2H-5, 112-113	15.02	0.17	0.17	0.00	1.40	0.00
3H-1, 112-113	18.52	0.30	0.17	0.12	1.40	0.00
3H-3, 112-113	21.52	0.60	0.37	0.23	3.10	0.00
3H-5, 112-113	24.52	1.26	1.15	0.11	9.60	0.00
4H-1, 112-113	28.02	0.59	0.50	0.09	4.20	0.14
4H-3, 112-113	31.02	0.43	0.22	0.21	1.80	0.06
5H-1, 112-113	37.52	0.32	0.00	0.32	0.00	0.00
5H-3, 112-113	40.52	0.38	0.00	0.38	0.00	0.05
5H-5, 112-113	43.52	0.26	0.19	0.07	1.60	0.00
6H-1, 111-112	47.01	4.71	4.64	0.07	38.70	0.00
6H-3, 111-112	50.01	0.37	0.12	0.25	1.00	0.00
6H-6, 112-113	54.52	0.12	0.11	0.01	0.90	0.00
7H-1, 113-114	56.53	0.07	0.00	0.07	0.00	0.00
7H-3, 113-114	59.53	0.18	0.00	0.18	0.00	0.04
7H-5, 113-114	62.53	0.31	0.00	0.31	0.00	0.00
8H-1, 112-113	66.02	0.11	0.00	0.11	0.00	0.00
8H-3, 112-113	69.02	0.00	0.00	0.00	0.00	0.00
8H-5, 112-113	72.02	0.00	0.00	0.00	0.00	0.00
9H-1, 112-113	75.52	0.18	0.00	0.18	0.00	0.00
9H-3, 112-113	78.52	1.22	1.11	0.11	9.20	0.00
9H-5, 112-113	81.52	0.10	0.00	0.10	0.00	0.00
10H-1, 112-113	85.02	0.12	0.00	0.12	0.00	0.00
10H-3, 112-113	88.02	0.13	0.00	0.13	0.00	0.00
11H-1, 112-113	94.52	0.21	0.28	0.00	2.30	0.00
11H-3, 112-113	97.52	0.49	0.37	0.12	3.10	0.00
11H-5, 112-113	100.52	0.00	0.14	0.00	1.20	0.00
13H-1, 112-113	113.52	0.14	0.13	0.01	1.10	0.00
13H-3, 112-113	116.52	3.20	3.02	0.18	25.20	0.00
13H-5, 112-113	119.52	1.55	1.46	0.09	12.20	0.00
14H-1, 112-113	123.02	0.39	0.36	0.03	3.00	0.00
14H-3, 112-113	126.02	1.06	0.96	0.10	8.00	0.00
14H-5, 112-113	129.02	0.98	0.90	0.08	7.50	0.00
15H-1, 112-113	132.52	2.70	2.69	0.01	22.40	0.00
15H-3, 112-113	135.52	1.48	1.46	0.02	12.20	0.00
15H-5, 112-113	138.52	2.89	2.70	0.19	22.50	0.00
16H-1, 113-114	142.03	1.90	1.75	0.15	14.60	0.00
16H-3, 113-114	145.03	2.76	2.60	0.16	21.70	0.00
16H-5, 113-114	148.03	1.78	1.60	0.18	13.30	0.00
17H-1, 112-113	151.52	0.47	0.32	0.15	2.70	0.00
17H-3, 112-113	154.52	1.95	1.95	0.00	16.20	0.00
17H-5, 112-113	157.52	2.29	2.10	0.19	17.50	0.00
18H-1, 112-113	161.02		3.03		25.20	
18H-3, 112-113	163.82		4.36		36.30	
18H-5, 112-113	166.82		1.84		15.30	
19H-1, 112-113	170.52		0.00		0.00	
19H-3, 112-113	173.52		0.62		5.20	
19H-5, 112-113	176.52		0.00		0.00	
20H-1, 112-113	180.02		0.00		0.00	
20H-3, 112-113	183.02		0.47		3.90	
20H-5, 112-113	186.02		0.42		3.50	
21H-1, 112-113	189.52		0.23		1.90	
21H-3, 112-113	192.52		0.55		4.60	
21H-5, 112-113	195.52	1.38	1.17	0.21	9.70	0.03
22H-1, 111-112	199.01	1.12	0.72	0.40	6.00	0.12
22H-3, 111-112	202.01	0.57	0.26	0.31	2.20	0.04
22H-5, 111-112	205.01	0.26	0.00	0.26	0.00	0.04
23H-1, 112-113	208.52	0.41	0.26	0.15	2.20	0.04
23H-3, 112-113	211.52	1.29	1.00	0.29	8.30	0.05
23H-5, 112-113	214.52	0.76	0.40	0.36	3.30	0.05
25H-1, 112-113	227.52		0.23		1.90	
25H-3, 112-113	230.52		0.43		3.60	
25H-5, 112-113	233.52		1.20		10.00	
26H-1, 112-113	237.02		1.24		10.30	
26H-3, 112-113	240.02		0.89		7.40	
26H-5, 112-113	243.02		1.41		11.70	
27H-1, 112-113	246.52		0.37		3.10	
27H-3, 112-113	249.52	0.71	0.38	0.32	3.20	0.05
27H-5, 112-113	252.52		0.85		7.10	
28H-1, 112-113	256.02		0.26		2.20	
28H-3, 112-113	259.02	0.57	0.19	0.38	1.60	0.04
28H-5, 112-113	262.02		0.40		3.30	
29H-1, 112-113	265.52		0.00		0.00	
29H-3, 112-113	268.52	0.36	0.00	0.36	0.00	0.04
29H-5, 112-113	271.52		0.00		0.00	
30H-1, 112-113	275.02		0.00		0.00	
30H-3, 112-113	278.02	0.55	0.32	0.23	2.70	0.04
30H-5, 112-113	281.02		0.00		0.00	
31H-1, 112-113	284.52		0.00		0.00	
31H-3, 112-113	287.52	0.50	0.32	0.18	2.70	0.03
31H-5, 112-113	290.52		4.07		33.90	

Table 10 (continued).

Core, section, interval (cm)	Depth (mbsf)	TC (wt%)	ICF (wt%)	TOC (wt%)	CaCO ₃ (wt%)	TN (wt%)
32X-1, 37-38	293.27		0.52		4.30	
32X-3, 37-38	296.27	1.56	1.35	0.21	11.20	0.05
32X-5, 37-38	299.27		0.00		0.00	
33X-1, 37-38	302.87		2.85		23.70	
33X-3, 37-38	305.87		4.82		40.20	
35X-1, 37-38	322.27		0.29		2.40	
35X-3, 37-38	325.27	0.51	0.29	0.22	2.40	0.04
35X-5, 37-38	328.27		0.24		2.00	
37X-1, 37-38	341.57		0.17		1.40	
37X-3, 37-38	344.57	0.32	0.00	0.32	0.00	0.05
38X-1, 108-109	351.98		0.00		0.00	
38X-3, 108-109	354.98	0.25	0.00	0.25	0.00	0.03
38X-5, 108-109	357.98		0.00		0.00	
39X-1, 112-113	361.62		0.62		5.20	
39X-3, 112-113	364.62	1.34	1.06	0.28	8.80	0.03
39X-5, 112-113	367.62		2.49		20.70	
40X-1, 111-112	371.31		4.65		38.70	
40X-3, 111-112	374.31	2.36	2.18	0.18	18.20	0.03
40X-5, 111-112	377.31		0.23		1.90	
41X-1, 112-113	381.12		1.90		15.80	
41X-3, 112-113	384.12	1.60	1.33	0.27	11.10	0.03
41X-5, 112-113	387.12		2.33		19.40	
42X-1, 112-113	390.82		1.22		10.20	
42X-3, 112-113	393.82	2.09	1.88	0.21	15.70	0.03
42X-5, 112-113	396.82		3.40		28.30	
43X-1, 107-108	400.57		1.29		10.70	
43X-3, 107-108	403.57	1.51	1.35	0.16	11.20	0.03
43X-5, 107-108	406.57		1.40		11.70	
44X-1, 112-113	410.42		0.54		4.50	
44X-3, 112-113	413.42	0.57	0.34	0.23	2.80	0.00
44X-5, 112-113	416.42		0.00		0.00	
45X-1, 112-113	420.32		0.00		0.00	
45X-3, 112-113	423.32	0.77	0.54	0.23	4.50	0.00
45X-5, 112-113	426.32		1.59		13.20	
48H-1, 111-112	449.81		1.06		8.80	
48H-3, 112-113	452.82	0.16	0.00	0.16	0.00	0.03
48H-5, 113-114	455.83		0.00		0.00	
49X-1, 111-112	459.31		0.21		1.70	
49X-3, 111-112	462.31	0.27	0.15	0.12	1.20	0.02
49X-5, 111-112	465.31		2.57		21.40	
50X-1, 112-113	469.22		4.45		37.10	
50X-3, 112-113	472.22	2.70	2.67	0.03	22.20	0.01
50X-5, 112-113	475.22		1.94		16.20	
51X-1, 112-113	479.02		2.16		18.00	
51X-3, 112-113	482.02	5.22	5.24	0.00	43.60	0.02
51X-5, 112-113	485.02		4.35		36.20	
53X-1, 111-112	498.81		4.27		35.60	
53X-3, 111-112	501.81	2.93	2.81	0.12	23.40	0.03
53X-5, 111-112	504.81		2.07		17.20	
54X-1, 111-112	508.71		3.26		27.20	
54X-3, 111-112	511.71	6.02	6.08	0.00	50.60	0.02
54X-5, 111-112	514.71		5.00		41.70	
55X-1, 111-112	518.51		2.38		19.80	
55X-3, 111-112	521.51	7.90	7.80	0.10	65.00	0.02
55X-5, 111-112	524.51		5.04		42.00	
57X-1, 112-113	538.22		0.92		7.70	
57X-3, 112-113	541.22	0.04	0.00	0.04	0.00	0.02
57X-5, 112-113	544.22		0.00		0.00	
58X-1, 46-47	547.56		6.77		56.40	
59X-1, 112-113	558.12		5.69		47.40	
59X-3, 112-113	561.12	6.87	6.73	0.14	56.10	0.01
59X-5, 112-113	564.12		4.70		39.20	
60X-1, 112-113	568.12		5.74		47.80	
60X-3, 112-113	571.12	0.28	0.19	0.09	1.60	0.02
60X-5, 112-113	574.12		0.00		0.00	
61X-1, 107-108	578.07		0.00		0.00	
61X-3, 107-108	581.07	0.05	0.00	0.05	0.00	0.02
61X-5, 107-108	584.07		0.00		0.00	
62X-1, 111-112	588.11		0.00		0.00	
62X-3, 111-112	591.11	0.54	0.43	0.11	3.60	0.02
62X-5, 111-112	594.11		2.49		20.70	
63X-1, 112-113	598.12		3.67		30.60	
63X-3, 112-113	601.12	9.52	9.63	0.00	80.20	0.01
63X-5, 112-113	604.12		1.87		15.60	
64X-1, 104-105	608.04		3.56		29.70	
65X-1, 112-113	617.82		9.83		81.90	
65X-3, 111-112	620.81	7.64	7.72	0.00	64.30	0.02
65X-5, 111-112	623.81		5.55		46.20	
66X-1, 111-112	627.41		6.59		54.90	
66X-3, 111-112	630.41	8.17	8.27	0.00	68.90	0.02
66X-5, 109-110	633.39		9.40		78.30	
67X-1, 112-113	637.12		3.34		27.80	
67X-3, 115-116	640.15	7.60	7.67	0.00	63.90	0.01
67X-5, 115-116	643.15		9.98		83.10	
68X-3, 106-107	649.16	8.83	8.68	0.15	72.30	0.01
69X-1, 109-110	655.89		6.04		50.30	

Table 10 (continued).

Core, section, interval (cm)	Depth (mbsf)	TC (wt%)	ICF (wt%)	TOC (wt%)	CaCO ₃ (wt%)	TN (wt%)
69X-3, 109–110	658.89	6.58	6.77	0.00	56.40	0.02
69X-5, 111–112	661.91		4.66		38.80	
70X-1, 108–109	665.48		8.71		72.60	
70X-3, 113–114	668.53	6.11	6.31	0.00	52.60	0.02
70X-5, 112–113	671.52		10.86		90.50	
71X-1, 110–111	675.20		9.78		81.50	
71X-3, 106–107	678.16	10.23	10.45	0.00	87.00	0.01
71X-5, 106–107	681.16		11.32		94.30	
72X-1, 107–108	684.77		8.73		72.70	
72X-3, 107–108	687.77	9.04	9.05	0.00	75.40	0.01
72X-5, 107–108	690.77		11.32		94.30	
73X-1, 107–108	694.37		11.24		93.60	
73X-3, 107–108	697.37	11.28	11.46	0.00	95.50	0.02
73X-5, 107–108	700.37		11.50		95.80	
74X-1, 111–112	704.11		11.52		96.00	
77X-2, 26–27	731.66		6.79		56.60	
77X-3, 56–57	733.46	6.57	6.70	0.00	55.80	0.01
78X-1, 104–105	740.74		7.07		58.90	
78X-3, 128–129	743.98	6.55	6.73	0.00	56.10	0.01
78X-5, 128–129	746.98		5.42		45.10	
79X-1, 76–77	750.26		7.89		65.70	
79X-2, 26–27	751.26		2.71		22.60	
79X-3, 91–92	753.41	3.24	3.33	0.00	27.70	0.01
82X-1, 109–110	780.29		9.81		81.70	
82X-3, 81–82	783.01	9.46	9.73	0.00	81.10	0.01
82X-5, 74–75	785.94		10.05		83.70	
83X-3, 52–53	792.72	0.31	0.34	0.00	2.80	0.01
83X-4, 68–69	794.38		10.43		86.90	
84X-1, 38–39	799.58	9.07	9.16	0.00	76.30	0.01
86X-2, 99–100	820.99	0.03	0.00	0.03	0.00	0.00
86X-4, 50–51	823.50	6.85	7.01	0.00	58.40	0.00

Notes: TC = total carbon, IC = inorganic carbon, TOC = total organic carbon, and TN = total nitrogen. All results are given in weight per cent of bulk dry sediment. All samples are carbonate [analyses] samples.

rigidity that corresponds to increased sediment lithification and increased carbonate concentration.

Lithologic Subunit IVA (652.2–740 mbsf) is a nanofossil chalk having interbeds, and the logs show a trend toward increasing lithification. The sonic log attains peak values near 710 mbsf, whereas the resistivity logs increase gradually toward the base of this subunit. The peak sonic velocities and very low gamma-ray and Al log values between 700 and 725 mbsf correspond to the presence of a nearly pure nanofossil chalk lithology. The Al and capture cross-section logs demonstrate that the altered ash interbeds become more prevalent between 725 and 740 mbsf.

This altered ash layer can be recognized as a thick and distinct subunit from 725 to 760 mbsf, based on the Al/K ratio log (Fig. 45). The ash is characterized by elevated Al concentrations relative to K; Th and U concentrations are also low. The high Al/K ratio suggests that the ash was derived from a geochemically primitive volcanic source of ocean island affinity, as opposed to more calc-alkaline Pacific rim volcanism or terrigenous material, both of which have lower Al/K ratios. This ash interval is also characterized by lower sonic velocities, higher porosity (clay) and a higher than average capture cross section.

The dominant nanofossil chalk lithology, with an increased altered ash component, characterizes lithologic Subunit IVB (740–814 mbsf). Slump structures are also common in this subunit. Logs identify this subunit in terms of continued increases in sonic velocity and resistivity and decreases in neutron porosity. A gradual increase in terrigenous content can be seen toward the base of this subunit, as suggested by the increased gamma-ray (K and Th) and Al log values.

The altered ash lithology of Unit V (814–830 mbsf in Hole 883B, thinner in logged Hole 883F) is represented by high, but uniform, resistivity, gamma-ray (K and Th), and Al log values. The capture cross section, derived from the GST, is much higher than that in the calcareous material above, principally reflecting an increase in the ferro-magnesian component of the ash of Unit V and the basalts of Unit VI below. The thin lithologic Unit V is apparent as a distinct physical entity in the logs and occupies a transitional lithology

between the nanofossil lithology of Subunit IVB and the basement lithology (basalt) of Unit VI. Only the resistivity, gamma-ray, and Al logs were sufficiently deep in the hole to measure the basalt unit, but these logs show dramatic shifts to a denser and less porous lithology. All three components of the gamma-ray log (K, U, and Th) exhibit maxima within this basalt unit; the U log is essentially featureless throughout the other units of Site 883.

The diatom ooze lithology of Unit II represents an interval between 2.7 and 7.1 Ma of extremely high accumulation rates of biogenic opal (see "Sedimentation Rates and Fluxes" section, this chapter). The logs are monotonous and relatively invariant throughout this entire interval, suggesting little lithological variability. Closer inspection of the spectral gamma-ray log data within this unit demonstrates that cyclic lithologic variations occurring within this unit begin near 380 mbsf and maintain relatively high amplitudes until 280 mbsf. Figure 46 shows the total gamma-ray, Al, and resistivity logs for this interval, with two biostratigraphic datums at ~295 ± 5 mbsf (5.1 Ma; D19) and ~375 ± 5 mbsf (6.3 Ma; D24a) (see "Biostratigraphy" section, this chapter).

Although chronostratigraphic control is too poor to constrain the logs as a time-series, the estimated age of onset for these variations (ca. 6.3 Ma) is roughly coincident with the first abundant appearance of IRD in subantarctic sediments. Stable isotopic, sedimentologic, and microfossil results from Leg 114 Hole 704B in the subantarctic sector of the South Atlantic suggest a rapid and prolonged northward migration of the Antarctic Ocean polar front during the latest Miocene (within Chron C3AR, ca. 6.3 Ma; Müller et al., 1991). A similar shift toward a cooler and more variable climate between 6.3 and 5.1 Ma has also been suggested for the North Atlantic Ocean, based on nanofossil abundance records (Beaufort and Aubry, 1990). The timing of this increase in terrigenous-biogenic opal deposition variability at this North Pacific site may be reflecting a similar change in high-latitude climate.

Processed images from the formation microscanner (FMS) in Hole 883F provide a multitude of lithological and structural information. The processed images available at present, in the basal portion of the

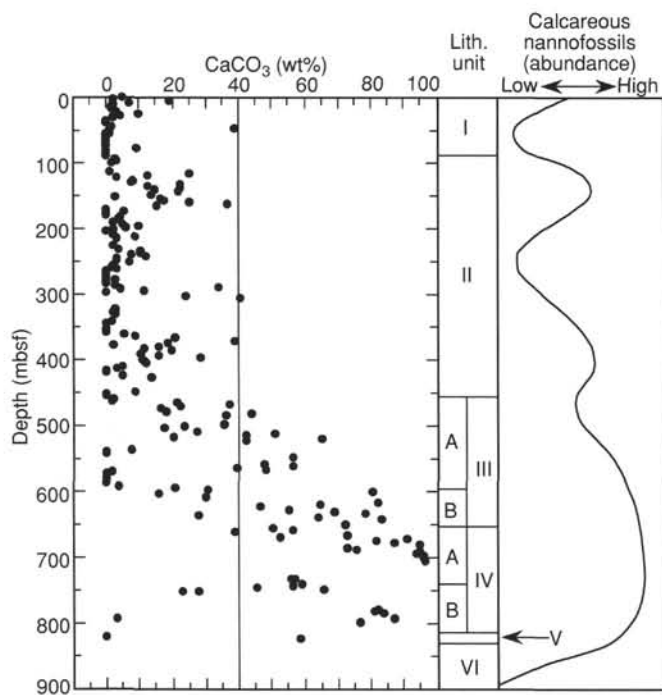


Figure 32. Carbonate contents vs. depth below the seafloor in sediments from Hole 883B and schematic plot of relative abundance of calcareous nannofossils (as described in the "Biostratigraphy" section, this chapter). Lithologic units are shown in center of plot.

hole, show the orientation and degree of bed dips, image and oriented slump structures, and debris flows in Unit IV and outline pillow basalts and fractures in the basement section of Unit VI.

From a preliminary assessment of the microresistivity images, deformation and slump structures in Unit IV are apparent at 750, 756, 776–778, 790, and 794–796 mbsf; these are in good general agreement with available lithologic core descriptions at these levels. Figure 47 is a merged image from two repeat passes of the FMS tool and shows part of a slump structure at 794 mbsf. Figure 48 shows the pillow basalts of Unit VI at 828 mbsf with clear images not of pillow basalts (dark) and of the more resistive secondary calcite (white) filling the voids and fractures.

Magnetic Induction and Magnetic Susceptibility Logging Results

Two passes each of the French total magnetic induction (NRMT) and magnetic susceptibility (SUMT) logging tools were conducted at Hole 883F. The repeat logs for each tool permit a quantitative evaluation of tool sensitivity and the separate components of the borehole magnetic environment. A review of these tools and magnetic logging measurement principles is provided in the "Explanatory Notes" chapter (this volume). Over the several-hour logging interval, the magnetometer and the susceptibility logs reflect both time-dependent (transient variations in Earth's field, temperature drift) and time-invariant (magnetic mineral concentration, remanent magnetization) factors. These factors have been quantified and isolated following post-cruise data processing. In this section, we discuss the quality of magnetometer and susceptibility logging data and then show some examples of correlations with the lithology and the whole-core susceptibility data.

Total Induction Log

The magnetometer measures the total induction $B = \mu_0(H + [J_i + J_r])$ (SI units), which is commonly and incorrectly referred to as

Table 11. Summary of physical properties values measured at Site 883.

Physical properties measurement	Hole 883A	Hole 883B	Hole 883C	Hole 883D	Hole 883E	Hole 883F
Index properties	X	^a X	X		X	
Vane shear strength	X	^c X	X			
DSV or Hamilton		^c X	X		X	
Frame						
GRAPE	X	^a X	X	^b X	X	X
P-wave logger		X	X		X	

^aCores 145-883B-1H and -30H through -86X.

^bCores 145-883C-1H through -52X.

^cCores 145-883B-1H and -30H through -62X.

"Earth's magnetic field." B (Earth's total induction) is expressed in nanoteslas (nT) and is the induction that results either from a magnetic field H (Earth's field, in that case) and/or from an induced magnetization J_i or remanent magnetization J_r , both of which are expressed in amperes per meter (A/m), with μ_0 being the permeability of vacuum. To avoid confusion between the mathematically defined total induction B and the induced magnetization J_i , we refer to induction as the "B field," which is expressed in nT.

In a borehole, B is the sum of several components:

$$B(z, t) = B_r(z) + B_{va}(z) + B_f(z) + B_l(z, t), \text{ from}$$

B_r being the inner regular induction, B_a the induction from nearby highly magnetized rocks (anomaly field), B_f the induction produced by the geological formations surrounding the hole (what we finally want to measure), and B_l the induction caused by transient variations of earth's field H . To isolate B_f , the desired component, one must first evaluate and remove B_r , B_a , and B_l .

To a first approximation (see "Explanatory Notes" chapter, this volume), B_r can be estimated by assuming it is dipolar, axial, and centered. Thus, one can easily remove its contribution to the field B , measured by the magnetometer using the local value (48,603 nT) and its gradient as a linear function of depth (~ 22 nT/km). Figure 49 shows the remaining "local" field $B_L(z)$ for the only two runs that contain local effects [i.e.: $B_{L1}(z) = B_f(z) + B_a(z) + B_l(z, t)$ and $B_{L2}(z) = B_f(z) + B_a(z) + B_{l2}(z, t)$].

Main Magnetic Anomalies

Five different magnetic signatures can be recognized throughout the logged sequence. Above 100 mbsf, the remaining "local" B_L field shows large variations, with values exceeding 1000 nT, followed by a sharp decrease at 100 mbsf. This results from the highly magnetic BHA and drill pipes, which were set at 100 mbsf. One of the most prominent features in these logs is the large variation between 100 and 220 mbsf, with an amplitude of more than 1000 nT. These variations cannot be explained by the presence of the drill-pipe sections above 100 mbsf. The similarity between the two passes and their high amplitude suggests that these anomalies are not related to transient variations of Earth's field and are likely related to the presence of nearby highly magnetized materials. To produce such an effect, magnetizations in excess of 1 A/m are needed, which would not be compatible with a sedimentary source. More than 170 m of the BHA was lost in Hole 883E about 20 m away; thus, these anomalies can be related to the proximity of this highly magnetic source. The shape of the signal shows that these are not seen as simple dipoles by the magnetometer, probably because of their length/distance ratio. A broad zone, free of any large magnetic variations, occurs between 220 and 720 mbsf that corresponds to a broad zone of sedimentary rocks. Between 720 and 823 mbsf, the signal shows strong, mostly negative peaks having average amplitudes in excess of 2000 nT; many of these peaks can be seen in both runs, as well as: in a partial downward recording. Below 823 to 824 mbsf, the remaining B_L signal becomes

Table 12. Index properties and shear strength data from Hole 883A.

Core, section, interval (cm)	Depth (mbsf)	Wet-bulk density (g/cm ³)	Dry-bulk density (g/cm ³)	Grain density (g/cm ³)	Wet porosity content (g/cm ³)	Dry water (g/cm ³)	Void ratio	Shear strength (kPa)
145-883A-								
1H-1, 44	0.44	1.37	0.58	2.64	77.7	137.7	3.55	
1H-1, 109	1.09	1.46	0.72	2.67	72.9	104.4	2.72	
1H-1, 110	1.10							11.26
1H-2, 39	1.89	1.24	0.39	2.37	83.3	220.2	5.09	
1H-2, 109	2.59	1.37	0.59	2.56	76.7	133.7	3.34	
1H-2, 110	2.60							10.51
1H-3, 39	3.39	1.42	0.66	2.61	74.4	115.5	2.94	
1H-3, 109	4.09	1.29	0.46	2.49	81.0	178.6	4.34	
1H-3, 115	4.15							19.94
1H-4, 39	4.89	1.37	0.59	2.49	76.0	132.4	3.22	
1H-4, 109	5.59	1.42	0.65	2.65	75.1	118.5	3.06	
1H-4, 110	5.60							22.26
1H-5, 44	6.44	1.36	0.57	2.56	77.4	138.9	3.48	
1H-5, 109	7.09	1.31	0.50	2.40	78.8	161.5	3.79	
1H-5, 110	7.10							28.75
1H-6, 19	7.69	1.49	0.79	2.48	67.9	87.9	2.13	
1H-6, 119	8.69	1.42	0.66	2.57	74.0	114.5	2.88	
1H-6, 120	8.70							23.65
1H-7, 19	9.19	1.22	0.37	2.21	82.7	226.3	4.87	
2H-1, 49	9.99	1.33	0.52	2.45	78.3	153.2	3.67	
2H-1, 109	10.59	1.45	0.70	2.63	72.9	106.2	2.73	
2H-1, 110	10.60							19.94
2H-2, 39	11.39	1.48	0.78	2.44	67.6	88.3	2.10	
2H-2, 109	12.09	1.33	0.51	2.61	80.1	160.7	4.09	
2H-2, 110	12.10							23.19
2H-3, 39	12.89	1.42	0.64	2.67	75.7	121.0	3.16	
2H-3, 109	13.59	1.30	0.47	2.56	81.3	176.8	4.42	
2H-3, 110	13.60							31.54
2H-4, 39	14.39	1.31	0.53	2.31	76.9	149.7	3.37	
2H-4, 109	15.09	1.43	0.68	2.60	73.5	110.8	2.81	
2H-4, 110	15.10							28.29
2H-5, 39	15.89	1.40	0.63	2.60	75.4	122.2	3.10	
2H-5, 109	16.59	1.33	0.52	2.53	79.0	155.4	3.83	
2H-5, 110	16.60							30.61
2H-6, 39	17.39	1.22	0.37	2.32	83.9	235.4	5.32	
2H-6, 109	18.09	1.27	0.41	2.50	83.0	205.0	5.00	
2H-6, 110	18.10							25.97
2H-7, 19	18.69	1.39	0.62	2.50	74.8	122.9	3.00	
3H-1, 49	19.49	1.31	0.49	2.52	80.1	167.0	4.11	
3H-1, 109	20.09	1.42	0.69	2.43	71.2	105.5	2.50	
3H-1, 110	20.10							28.75
3H-2, 39	20.89	1.27	0.42	2.46	82.4	200.0	4.80	
3H-2, 109	21.59	1.31	0.50	2.46	79.4	163.5	3.92	
3H-2, 110	21.60							28.75
3H-3, 39	22.39	1.44	0.68	2.65	74.0	111.4	2.88	
3H-3, 99	22.99	1.37	0.59	2.49	75.9	131.5	3.20	
3H-3, 100	23.00							27.36
3H-4, 39	23.89	1.40	0.63	2.60	75.5	123.5	3.13	
3H-4, 99	24.49	1.46	0.75	2.47	69.5	95.3	2.30	
3H-4, 100	24.50							27.83
3H-5, 39	25.39	1.44	0.70	2.60	72.8	106.8	2.71	
3H-5, 109	26.09	1.48	0.77	2.58	70.0	93.7	2.36	
3H-5, 110	26.10							27.83
3H-6, 39	26.89	1.20	0.30	2.48	87.3	293.5	7.11	
3H-6, 109	27.59	1.29	0.47	2.41	80.1	173.6	4.09	
3H-6, 110	27.60							45.45
3H-7, 39	28.39	1.19	0.29	2.37	87.2	303.7	7.03	
4H-1, 49	28.99	1.26	0.40	2.46	83.3	212.1	5.09	
4H-1, 109	29.59	1.21	0.34	2.30	85.0	259.7	5.83	
4H-1, 110	29.60							30.15
4H-2, 39	30.39	1.18	0.30	2.24	86.2	293.4	6.41	
4H-2, 109	31.09	1.35	0.55	2.49	77.4	143.3	3.48	
4H-2, 110	31.10							31.07
4H-3, 39	31.89	1.38	0.58	2.65	77.7	136.8	3.54	
4H-3, 109	32.59	1.26	0.41	2.41	82.5	205.3	4.82	
4H-3, 110	32.60							38.03
4H-4, 34	33.34	1.25	0.41	2.32	81.9	203.0	4.60	
4H-4, 109	34.09	1.50	0.77	2.72	71.4	95.0	2.52	
4H-4, 110	34.10							44.52
4H-5, 39	34.89	1.47	0.73	2.64	72.2	102.1	2.63	
4H-5, 109	35.59	1.23	0.37	2.29	83.3	228.1	5.11	
4H-5, 110	35.60							44.06
4H-6, 39	36.39	1.44	0.68	2.70	74.4	111.9	2.95	
4H-6, 99	36.99	1.19	0.30	2.29	86.3	291.4	6.50	
4H-6, 100	37.00							33.39
4H-7, 49	37.99	1.36	0.57	2.49	76.7	137.5	3.35	

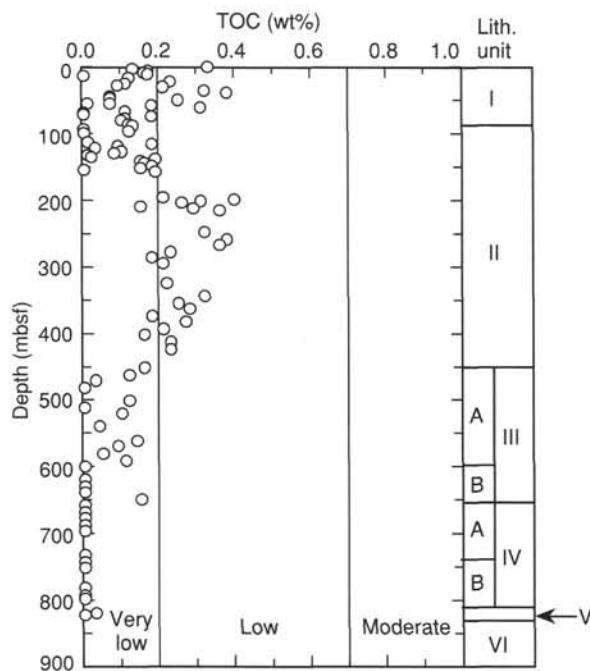


Figure 33. Total organic carbon contents vs. depth below the seafloor in sediments from Hole 883B. Lithologic units also are shown (right).

more variable and has a high average value of more than 1000 nT. This results from the high magnetizations of the basalt basement.

The average values of the "local" fields B_{L1} and B_{L2} in the central sedimentary zone are slightly higher than zero. To get the true value of B_f , the component related to the magnetization of the surrounding rocks (which should be the same for the two runs), one must evaluate the anomaly field B_a and the transient fields B_{t1} and B_{t2} .

Analysis of the Components of the Magnetic Induction

Figure 50 shows the "local" B_L field for the two runs between 220 and 670 mbsf, which is in the central sedimentary zone of Figure 49. This illustrates two significant results: the effect of the lost drill pipe in adjacent Hole 883E is dominant when compared to variations produced by the sediment magnetizations down to 350 mbsf and, at this scale, the two runs are similar, indicating that no high disturbance of the external Earth's field occurred during log acquisition.

Figure 51 shows the two runs between 350 and 650 mbsf. Again, good agreement is seen between the two runs. A slight overall increase in values for the remaining "local" fields B_{L1} and B_{L2} occur with depth for both runs, which is consistent with their overall positive value. Indeed, if the average value of B_f , the field attributable to the sedimentary formation, must be slightly positive when assuming an average Koenigsberger ratio of 1, a 170 to 180-nT value should imply rock magnetizations [B_r (nT) = $\mu_0(J_r + J_r')$] (A/m) in excess of 0.2 A/m. These magnetizations would be equivalent to susceptibilities of about 5×10^{-3} SI, which are much higher than the values measured in rock samples (see "Paleomagnetism" section, this chapter). Thus, one must consider that Site 883 is located in a positive anomaly field ($B_a \leq 150$ nT). However, because of perturbation from the lost pipe in adjacent Hole 883E, a precise estimation of B_a will require further analysis.

To isolate the true field from the sedimentary formation, B_{L1} the local time-dependent (transient) field was first be quantified and reviewed from the total field $B_{L1} - B_{L2}$ measurements. Figure 52 shows $B_{L1} - B_{L2}$, the difference between the "local fields" obtained from the two passes with respect to depth and to B_{L1-51} , the local field obtained from Pass 1. Because these measurements were performed under more than 2000 m of conductive salt water, only low frequency

variations ($\leq 10^{-2}$ Hz, or ≥ 16 m in the logs) affects the recorded values (skin effect). During a magnetic storm, the difference between the two logs should show uncorrelated variations on a scale of 10 m or more. This was not observed, and only two types of variations can be seen in Figure 52: a smooth, slow variation of the average value of $B_{L1}(z) - B_{L2}(z)$ (1.5 nT between 650 and 500 mbsf) and discrete sharp variations that occur near zones of observed high gradient of local B field, which correspond to small errors in depth. Thus, both runs were recorded during a magnetically quiet period with only a smooth, slow variation of the external field.

Analysis of the total induction logs obtained from the magnetometer shows that only a central part of the logs (350–700 mbsf) is free of environmental (<350 mbsf) or geological disturbances (>700 mbsf). This part of the logs shows that the drill site is characterized by a positive value of the anomaly field and that the data were recorded during a magnetically quiet period. The total induction signals appear to be of good quality and should permit future interpretation in terms of magnetostratigraphy despite the overall low magnetization of most of the surrounding sediments.

Susceptibility Results

The susceptibility tool is based on two coils that are balanced in the absence of any magnetic material. During logging, the variation of a secondary flux induced by the surrounding rocks between the two coils is measured in parts per million (ppm) of the main flux, 1 ppm being roughly equivalent to 10^{-6} SI. One of the problems is the absence of true zero, so that the baseline must be estimated from the logs and, when available, from parallel core measurements. Possible errors can be estimated by comparing the main log with the repeat section. Measurements can be in error, and depth errors or discrepancies can result from thermal drift of the measurement coils.

Main Susceptibility Zones

Figure 53 shows the main susceptibility log and the repeat section expressed in parts per million (ppm). To conserve time during logging, Run 1 was recorded at the fastest possible speed (3600 ft/hr) and only to 150 mbsf, whereas Run 2 is only a partial repeat section that starts at 380 mbsf and ends at 114 mbsf within the drill pipe. Most of the values are negative, because the susceptibility tool has no fixed zero reference. Four different zones can be deduced from these logs. From 120 to about 440 mbsf, susceptibility values are low, with discrete narrow peaks. From 440 to about 650 mbsf, the average susceptibility is slightly higher with broader and more pronounced anomalies. Below 650, high susceptibility variations are recorded, and a higher background level is seen. Basement is reached in the logs at 823 mbsf. High values above 120 mbsf correspond to the base of pipe, which was not raised during the susceptibility logging runs.

Analysis of the Susceptibility Records

Figure 54 shows a close-up of the susceptibility records for the 200 to 650 mbsf interval; these data have been corrected for a -2450 offset of the zero value. The lowermost values are slightly below 50 ppm and occur within high anomaly zones. This result is characteristic of the tool's response function, which is composed of two peaks (a "saddle") that result from the two-coil design of the sonde. Thus, the signal must be treated (according to the tool response) with a low-pass filter before the exact baseline can be determined. The correlation between the main log and the repeat section (Run 2) is very good. No broad discrepancies exist between the two runs, indicating few local measurement errors or thermal drift.

Figure 55 shows a plot of the first run between 150 and 380 mbsf, as well as the difference in susceptibility between the two runs ($k_1 - k_2$). The difference is small and relatively constant at around 20 ppm for the entire repeat section. The few difference peaks are always

Table 13. Index properties, compressional wave velocity, and shear strength data from Hole 883B.

Core, section, interval (cm)	Depth (mbsf)	Wet-bulk density (g/cm ³)	Dry-bulk density (g/cm ³)	Grain density (g/cm ³)	Wet porosity (%)	Dry water content (%)	Void ratio	Shear strength (kPa)	Compressional wave velocity (m/s)
145-883B-									
IH-1, 39	0.39	1.38	0.57	2.84	79.6	143.2	3.97		
IH-1, 109	1.09	1.40	0.62	2.57	75.4	123.8	3.11		
IH-1, 110	1.10							1.86	
IH-2, 39	1.89	1.34	0.51	2.71	80.8	162.8	4.30		
IH-2, 114	2.64	1.39	0.61	2.58	76.0	127.5	3.21		
IH-2, 115	2.65							8.35	
IH-3, 39	3.39	1.39	0.60	2.66	77.0	130.9	3.40		
IH-3, 109	4.09	1.33	0.52	2.48	78.5	153.4	3.71		
IH-3, 110	4.10							21.80	
IH-4, 109	5.59	1.25	0.41	2.34	82.1	205.5	4.69		
IH-4, 110	5.60							22.73	
IH-5, 39	6.39	1.35	0.54	2.63	79.1	150.1	3.85		
IH-5, 109	7.09	1.37	0.58	2.58	77.2	136.5	3.44		
IH-5, 110	7.10							27.36	
IH-6, 14	7.64	1.39	0.60	2.63	76.7	130.2	3.34		
30H-1, 39	274.29	1.27	0.47	2.16	78.1	171.3	3.62		
30H-1, 110	275.00							47.28	
30H-2, 39	275.79	1.29	0.48	2.29	78.6	167.5	3.74		
30H-2, 110	276.50							64.54	
30H-3, 39	277.29	1.30	0.50	2.28	77.6	158.1	3.52		
30H-3, 40	277.30							1425.1	
30H-3, 110	278.00							48.78	
30H-4, 39	278.79	1.30	0.51	2.27	77.2	155.4	3.44		
30H-4, 110	279.50							63.04	
30H-5, 39	280.29	1.29	0.49	2.29	78.3	164.3	3.68		
30H-5, 110	281.00							63.79	
30H-6, 39	281.79	1.30	0.50	2.29	77.8	159.3	3.55		
30H-6, 110	282.50							75.05	
30H-7, 39	283.29	1.29	0.49	2.25	77.8	161.9	3.56		
31H-1, 39	283.79	1.25	0.44	2.12	78.7	181.3	3.75		
31H-1, 110	284.50							48.78	
31H-2, 39	285.29	1.29	0.48	2.32	79.0	169.4	3.84		
31H-2, 110	286.00							61.54	
31H-3, 39	286.79	1.29	0.49	2.26	78.1	164.3	3.63		
31H-3, 75	287.15							1469.2	
31H-3, 110	287.50							38.27	
31H-4, 39	288.29	1.29	0.49	2.22	77.5	161.2	3.50		
31H-4, 110	289.00							57.04	
31H-5, 39	289.79	1.36	0.59	2.4	75.3	131.7	3.09		
31H-5, 110	290.50							62.29	
31H-6, 39	291.29	1.32	0.53	2.41	77.7	150.4	3.53		
31H-6, 110	292.00							94.56	
31H-7, 24	292.64	1.32	0.54	2.26	75.8	144	3.18		
32X-1, 39	293.29	1.36	0.60	2.41	74.9	128.4	3.02		
32X-1, 110	294.00							56.29	
32X-2, 39	294.79	1.33	0.55	2.29	75.5	139.3	3.12		
32X-2, 110	295.50							65.29	
32X-3, 39	296.29	1.33	0.54	2.38	77.0	147	3.41		
32X-3, 110	297.00							51.78	
32X-4, 39	297.79	1.39	0.63	2.47	74.1	120.6	2.90		
32X-4, 110	298.50							64.54	
32X-5, 39	299.29	1.32	0.53	2.37	77.4	150.6	3.48		
32X-5, 110	300.00							62.29	
32X-6, 39	300.79	1.32	0.52	2.4	77.8	152.3	3.57		
32X-6, 110	301.50							91.56	
32X-7, 39	302.29	1.39	0.63	2.49	74.4	121.3	2.95		
33X-1, 39	302.89	1.31	0.51	2.34	77.7	155.3	3.54		
33X-1, 110	303.60							51.78	
33X-2, 39	304.39	1.33	0.55	2.33	76.1	142.3	3.23		
33X-2, 110	305.10							69.79	
33X-3, 39	305.89	1.34	0.57	2.36	75.5	135.7	3.13		
34X-1, 39	312.59	1.31	0.54	2.24	75.7	144.2	3.16		
34X-1, 110	313.30							58.54	
34X-2, 39	314.09	1.29	0.47	2.36	79.8	174.9	4.03		
34X-2, 110	314.80							66.04	
34X-3, 39	315.59	1.28	0.48	2.27	78.6	168.6	3.73		
34X-3, 110	316.30							54.78	
34X-4, 39	317.09	1.30	0.49	2.35	78.7	163.3	3.75		
34X-5, 39	318.59	1.27	0.45	2.28	79.7	179.9	4.01		
34X-5, 110	319.30							42.78	
35X-1, 39	322.29	1.29	0.49	2.27	78.3	165.3	3.66		
35X-1, 110	323.00							53.28	
35X-2, 39	323.79	1.30	0.49	2.36	78.8	164.5	3.78		
35X-2, 110	324.50							56.29	
35X-3, 39	325.29	1.35	0.56	2.5	77.1	140.1	3.42		
35X-3, 80	325.70							2032.3	
35X-3, 110	326.00							61.54	
35X-4, 39	326.79	1.30	0.52	2.22	76.2	149.8	3.25		
35X-4, 110	327.5							64.54	
35X-5, 39	328.29	1.32	0.54	2.33	76.6	145.7	3.32		
35X-5, 110	329.00							58.54	
36X-1, 39	331.89	1.28	0.48	2.23	78.1	166.5	3.62		
36X-1, 110	332.60							43.53	

Table 13 (continued).

Core, section, interval (cm)	Depth (mbsf)	Wet-bulk density (g/cm ³)	Dry-bulk density (g/cm ³)	Grain density (g/cm ³)	Wet porosity (%)	Dry water content (%)	Void ratio	Shear strength (kPa)	Compressional wave velocity (m/s)
37X-1, 39	341.59	1.33	0.55	2.3	75.8	141.6	3.18		
37X-1, 110	342.30							48.78	
37X-2, 39	343.09	1.34	0.55	2.39	76.6	142.4	3.32		
37X-2, 110	343.80							53.28	
37X-3, 39	344.59	1.31	0.53	2.31	76.9	149.6	3.38		
37X-3, 80	345.00								1432.9
37X-3, 110	345.30							50.28	
38X-1, 39	351.29	1.31	0.52	2.31	77.0	150.5	3.40		
38X-1, 110	352.00							51.78	
38X-2, 39	352.79	1.35	0.58	2.35	75.0	132.2	3.04		
38X-2, 110	353.50							48.78	
38X-3, 39	354.29	1.27	0.48	2.2	78.0	168.3	3.61		
38X-3, 80	354.70								2029.4
38X-4, 39	355.79	1.24	0.42	2.18	80.5	197.9	4.21		
38X-4, 110	356.50							33.77	
38X-5, 39	357.29	1.29	0.47	2.34	79.3	171.2	3.90		
38X-5, 110	358.00							57.04	
38X-6, 39	358.79	1.28	0.48	2.24	78.0	165.4	3.61		
38X-6, 110	359.50							65.29	
39X-1, 109	361.59	1.3	0.51	2.28	77.4	156.3	3.47		
39X-2, 109	363.09	1.33	0.55	2.34	76.1	141.5	3.23		
39X-2, 110	363.10							64.54	
39X-3, 40	363.90								2150.0
39X-3, 109	364.59	1.29	0.49	2.29	78.2	163.3	3.65		
39X-3, 110	364.60							48.03	
39X-4, 109	366.09	1.31	0.52	2.29	77.1	153.4	3.42		
39X-4, 110	366.10							54.78	
39X-5, 109	367.59	1.33	0.55	2.33	76.1	142.2	3.23		
39X-5, 110	367.60							56.29	
39X-6, 109	369.09	1.35	0.58	2.41	75.6	133.4	3.13		
39X-6, 110	369.10							86.30	
40X-1, 109	371.29	1.42	0.69	2.4	70.9	104.7	2.46		
40X-1, 110	371.30							62.29	
40X-2, 109	372.79	1.36	0.59	2.4	75.2	131.5	3.08		
40X-2, 110	372.80							73.55	
40X-3, 40	373.60								1415.8
40X-3, 109	374.29	1.33	0.56	2.32	75.6	138.9	3.14		
40X-3, 110	374.30							58.54	
40X-4, 109	375.79	1.33	0.56	2.32	75.7	139.3	3.16		
40X-4, 110	375.80							49.53	
40X-5, 109	377.29	1.32	0.53	2.32	76.9	149.5	3.38		
40X-5, 110	377.30							57.04	
40X-6, 109	378.79	1.33	0.56	2.27	74.9	135.9	3.02		
40X-6, 110	378.80							60.79	
41X-1, 109	381.09	1.32	0.52	2.43	78.2	153.7	3.64		
41X-1, 110	381.10							48.78	
41X-2, 109	382.59	1.3	0.50	2.27	77.5	158.3	3.51		
41X-2, 110	382.60							56.29	
41X-3, 40	383.40								1752.8
41X-3, 109	384.09	1.33	0.56	2.32	75.5	138.3	3.13		
41X-3, 110	384.10							57.79	
41X-4, 109	385.59	1.35	0.60	2.27	73.4	126.1	2.79		
41X-4, 110	385.60							57.04	
41X-5, 109	387.09	1.3	0.50	2.3	78.0	160.5	3.61		
41X-5, 110	387.10							48.03	
41X-6, 109	388.59	1.26	0.48	2.02	75.7	160.3	3.16		
41X-6, 110	388.60							66.04	
42X-1, 109	390.79	1.31	0.52	2.33	77.4	152.8	3.47		
42X-2, 109	392.29	1.35	0.59	2.34	74.6	129.8	2.97		
42X-2, 110	392.30							50.28	
42X-3, 40	393.10								1878.8
42X-3, 110	393.80							45.78	
42X-3, 110	393.80	1.31	0.51	2.35	78.0	157.3	3.61		
42X-4, 109	395.29	1.3	0.52	2.25	76.7	152.2	3.35		
42X-4, 110	395.30							54.03	
42X-5, 109	396.79	1.34	0.56	2.38	76.0	138.6	3.22		
42X-5, 110	396.80							57.79	
42X-6, 109	398.29	1.32	0.54	2.26	75.7	143.1	3.16		
42X-6, 110	398.30							60.79	
43X-1, 109	400.59	1.28	0.49	2.19	77.2	161	3.44		
43X-1, 110	400.60							59.29	
43X-2, 109	402.09	1.33	0.56	2.26	74.8	136.2	3.01		
43X-2, 110	402.10							60.79	
43X-3, 40	402.90								1501.8
43X-3, 109	403.59	1.31	0.54	2.24	75.5	142.9	3.13		
43X-3, 110	403.60							65.29	
43X-4, 109	405.09	1.33	0.57	2.21	73.8	132.4	2.85		
43X-4, 110	405.10							58.54	
43X-5, 109	406.59	1.31	0.52	2.35	77.5	153.1	3.51		
43X-5, 110	406.60							57.04	
43X-6, 109	408.09	1.28	0.50	2.15	76.4	156.5	3.29		
43X-6, 110	408.10							54.03	
43X-7, 39	408.89	1.32	0.55	2.28	75.6	141	3.14		
44X-2, 115	411.95							56.29	
44X-3, 109	413.39	1.25	0.42	2.21	80.5	194.9	4.20		

Table 13 (continued).

Core, section, interval (cm)	Depth (mbsf)	Wet-bulk density (g/cm ³)	Dry-bulk density (g/cm ³)	Grain density (g/cm ³)	Wet porosity (%)	Dry water content (%)	Void ratio	Shear strength (kPa)	Compressional wave velocity (m/s)
44X-5, 109	416.39	1.27	0.46	2.2	78.6	173.4	3.73		
45X-1, 109	420.29	1.24	0.42	2.13	79.9	194.3	4.04		
45X-1, 110	420.30							42.03	
45X-2, 109	421.79	1.28	0.48	2.23	77.9	164.7	3.59		
45X-2, 110	421.80							50.28	
45X-3, 109	423.29	1.25	0.45	2.12	78.6	180.6	3.74		
45X-3, 110	423.30							42.03	
45X-4, 109	424.79	1.28	0.49	2.16	77.0	161.7	3.40		
45X-4, 110	424.80							45.78	
45X-5, 109	426.29	1.28	0.49	2.17	77.1	161.7	3.42		
45X-5, 110	426.30							40.53	
45X-6, 109	427.79	1.34	0.56	2.36	75.8	138.4	3.18		
45X-6, 110	427.80							96.81	
48H-1, 109	449.79	1.32	0.53	2.36	77.2	149.2	3.44		
48H-1, 110	449.80							90.81	
48H-2, 109	451.29	1.35	0.57	2.41	76.1	137.4	3.23		
48H-2, 110	451.30							85.55	
48H-3, 45	452.15								1413.0
48H-3, 109	452.79	1.29	0.49	2.24	77.6	161	3.52		
48H-3, 110	452.80							78.05	
48H-4, 109	454.29	1.3	0.52	2.24	76.5	150.6	3.30		
48H-4, 110	454.30							102.06	
48H-5, 109	455.79	1.32	0.54	2.26	75.7	143.3	3.16		
48H-5, 110	455.80							184.62	
48H-6, 79	456.99	1.34	0.59	2.23	73.4	128.2	2.80		
48H-7, 39	457.59	1.30	0.50	2.3	77.9	159.7	3.59		
49X-1, 109	459.29	1.26	0.45	2.2	79.2	180.2	3.87		
49X-1, 110	459.30							15.76	
49X-2, 109	460.79	1.25	0.45	2.15	78.8	180.2	3.77		
49X-2, 110	460.80							17.26	
49X-3, 75	461.95								2158.3
49X-3, 109	462.29	1.26	0.46	2.12	77.8	172.7	3.57		
49X-3, 110	462.30							44.28	
49X-4, 109	463.79	1.26	0.45	2.21	79.3	180.4	3.89		
49X-4, 110	463.80							38.27	
49X-5, 109	465.29	1.35	0.58	2.4	75.6	133.8	3.13		
49X-5, 110	465.30							61.54	
49X-6, 109	466.79	1.3	0.50	2.29	77.8	159.4	3.56		
49X-6, 110	466.80							39.78	
49X-7, 39	467.59	1.44	0.70	2.55	72.1	105	2.62		
50X-1, 109	469.19	1.37	0.63	2.35	73.1	119.5	2.75		
50X-1, 110	469.20							62.29	
50X-2, 109	470.69	1.45	0.74	2.41	69.1	95.9	2.26		
50X-2, 110	470.70							61.54	
50X-3, 109	472.19	1.35	0.59	2.29	73.9	128.3	2.87		
50X-3, 110	472.20							55.54	
50X-4, 109	473.69	1.32	0.55	2.27	75.4	140.7	3.11		
50X-4, 110	473.70							53.28	
50X-5, 109	475.19	1.32	0.54	2.27	76.0	145	3.22		
50X-5, 110	475.20							48.03	
50X-6, 109	476.69	1.43	0.70	2.47	71.4	104.8	2.53		
50X-6, 110	476.70							64.54	
50X-7, 19	477.29	1.37	0.63	2.24	71.4	115.5	2.53		
51X-1, 109	478.99	1.37	0.59	2.46	75.7	131	3.15		
51X-1, 110	479.00							43.53	
51X-2, 109	480.49	1.32	0.54	2.32	76.2	143.4	3.24		
51X-2, 110	480.50							36.77	
51X-3, 75	481.65								2170.7
51X-3, 109	481.99	1.4	0.67	2.34	71.2	109.5	2.50		
51X-3, 110	482.00							39.78	
51X-4, 109	483.49	1.4	0.68	2.35	70.8	107	2.45		
51X-4, 110	483.50							55.54	
51X-5, 109	484.99	1.4	0.66	2.37	71.9	111.6	2.58		
51X-5, 110	485.00							39.02	
51X-6, 109	486.49	1.43	0.72	2.39	69.6	98.9	2.31		
51X-6, 110	486.50							34.52	
51X-6, 110	486.50							51.78	
51X-7, 19	487.09	1.27	0.51	2.01	74.1	148.4	2.90		
53X-1, 109	498.79	1.39	0.61	2.58	76.1	128.6	3.24		
53X-2, 109	500.29	1.44	0.71	2.48	71.0	102.1	2.47		
53X-3, 75	501.45								2072.0
53X-3, 109	501.79	1.31	0.52	2.35	77.7	154.4	3.54		
53X-3, 110	501.80							30.77	
53X-4, 109	503.29	1.38	0.63	2.41	73.5	119	2.80		
53X-4, 110	503.30							36.02	
53X-5, 109	504.79	1.34	0.58	2.31	74.7	133	3.00		
53X-5, 110	504.80							33.02	
53X-6, 109	506.29	1.31	0.55	2.21	75.0	140.9	3.05		
53X-6, 110	506.30							36.77	
53X-7, 39	507.09	1.29	0.50	2.18	76.6	156.4	3.33		
54X-1, 109	508.69	1.35	0.60	2.29	73.6	126.3	2.82		
54X-1, 110	508.70							7.50	
54X-2, 109	510.19	1.37	0.61	2.38	73.9	123.5	2.87		
54X-2, 110	510.20							47.28	
54X-3, 109	511.69	1.44	0.74	2.39	68.8	95.4	2.23		

Table 13 (continued).

Core, section, interval (cm)	Depth (mbsf)	Wet-bulk density (g/cm ³)	Dry-bulk density (g/cm ³)	Grain density (g/cm ³)	Wet porosity (%)	Dry water content (%)	Void ratio	Shear strength (kPa)	Compressional wave velocity (m/s)
54X-3, 110	511.70							16.51	
54X-4, 109	513.19	1.47	0.76	2.51	69.4	93.5	2.29		
54X-4, 110	513.20							35.27	
54X-5, 109	514.69	1.38	0.64	2.38	72.9	117.2	2.72		
54X-5, 110	514.70							33.02	
54X-6, 109	516.19	1.34	0.59	2.26	73.5	127.5	2.81		
54X-6, 110	516.20							47.28	
54X-7, 39	516.99	1.41	0.69	2.38	70.9	105.8	2.46		
55X-1, 109	518.49	1.31	0.53	2.29	76.5	147.8	3.30		
55X-1, 110	518.50							23.26	
55X-2, 109	519.99	1.39	0.64	2.37	72.4	115.1	2.66		
55X-2, 110	520.00							39.02	
55X-3, 75	521.15								1455.8
55X-3, 109	521.49	1.53	0.86	2.49	65.2	78	1.89		
55X-3, 110	521.50							54.78	
55X-4, 109	522.99	1.46	0.74	2.5	70.0	96.8	2.36		
55X-4, 110	523.00							45.78	
55X-5, 109	524.49	1.46	0.75	2.47	69.4	95.3	2.29		
55X-5, 110	524.50							45.78	
55X-6, 18	525.08	1.43	0.72	2.38	69.4	98.9	2.29		
55X-6, 110	526.00							42.03	
55X-7, 44	526.84	1.34	0.58	2.29	74.5	132.7	2.97		
57X-1, 109	538.19	1.35	0.57	2.41	75.8	135.3	3.18		
57X-1, 110	538.20							51.78	
57X-2, 109	539.69	1.33	0.56	2.35	75.9	139.8	3.20		
57X-2, 110	539.70							49.53	
57X-3, 109	541.19	1.3	0.53	2.16	75.2	146	3.08		
57X-3, 110	541.20							47.28	
57X-4, 109	542.69	1.34	0.57	2.33	75.1	134.3	3.05		
57X-4, 110	542.70							51.78	
57X-5, 109	544.19	1.32	0.57	2.14	73.0	131.1	2.74		
57X-5, 110	544.20							176.36	
57X-6, 109	545.69	1.39	0.65	2.36	72.3	114.3	2.64		
57X-6, 110	545.70							197.38	
57X-7, 39	546.49	1.35	0.60	2.28	73.5	126.3	2.82		
58X-1, 44	547.54	1.57	0.89	2.69	66.8	77.3	2.03		
58X-1, 45	547.55							9.01	
59X-1, 109	558.09	1.55	0.86	2.63	67.0	80	2.05		
59X-1, 110	558.10							36.77	
59X-2, 109	559.59	1.62	0.98	2.63	62.5	65.6	1.68		
59X-2, 110	559.60							81.05	
59X-3, 75	560.75								1417.6
59X-3, 109	561.09	1.54	0.88	2.52	64.8	75.6	1.86		
59X-3, 110	561.10							64.54	
59X-4, 109	562.59	1.51	0.83	2.49	66.5	82.5	2.00		
59X-4, 110	562.60							59.29	
59X-5, 109	564.09	1.47	0.78	2.4	67.3	88.8	2.08		
59X-5, 110	564.10							82.55	
59X-6, 109	565.59	1.34	0.59	2.24	73.2	126.7	2.77		
59X-6, 110	565.60							70.54	
59X-7, 39	566.39	1.41	0.69	2.34	70.2	104.1	2.38		
60X-1, 109	568.09	1.42	0.70	2.43	71.0	104.6	2.48		
60X-1, 110	568.10							29.27	
60X-2, 109	569.59	1.28	0.49	2.21	77.3	161	3.47		
60X-2, 110	569.60							19.51	
60X-3, 75	570.75								1439.5
60X-3, 109	571.09	1.25	0.45	2.05	77.7	177.3	3.55		
60X-3, 110	571.10							9.76	
60X-4, 109	572.59	1.31	0.53	2.26	76.1	146.6	3.23		
60X-4, 110	572.60							20.26	
60X-5, 109	574.09	1.27	0.48	2.14	77.0	163.3	3.40		
60X-5, 110	574.10							37.52	
60X-6, 109	575.59	1.31	0.55	2.19	74.6	139	2.97		
60X-6, 110	575.60							150.85	
61X-1, 109	578.09	1.33	0.56	2.32	75.6	138.7	3.14		
61X-1, 110	578.10							24.77	
61X-2, 109	579.59	1.33	0.55	2.35	76.2	141.8	3.26		
61X-2, 110	579.60							33.77	
61X-3, 109	581.09	1.29	0.50	2.24	77.5	159.6	3.49		
61X-3, 110	581.10							25.52	
61X-4, 109	582.59	1.34	0.58	2.29	74.4	131.8	2.95		
61X-4, 110	582.60							33.02	
61X-5, 109	584.09	1.3	0.50	2.3	77.9	159.5	3.58		
61X-5, 110	584.10							30.77	
61X-6, 109	585.59	1.36	0.61	2.33	73.5	123.5	2.81		
61X-6, 110	585.60							86.30	
61X-7, 39	586.39	1.33	0.56	2.26	75.0	137.9	3.04		
62X-1, 109	588.09	1.29	0.50	2.28	77.8	160.6	3.57		
62X-1, 110	588.10							26.27	
62X-2, 109	589.59	1.26	0.47	2.12	77.3	167.6	3.46		
62X-2, 110	589.60							24.77	
62X-3, 109	591.09	1.29	0.49	2.24	77.6	160.8	3.51		
62X-3, 110	591.10							19.51	
62X-4, 109	592.59	1.28	0.48	2.2	78.0	167.7	3.60		
62X-4, 110	592.60							22.51	

Table 13 (continued).

Core, section, interval (cm)	Depth (mbsf)	Wet-bulk density (g/cm ³)	Dry-bulk density (g/cm ³)	Grain density (g/cm ³)	Wet porosity (%)	Dry water content (%)	Void ratio	Shear strength (kPa)	Compressional wave velocity (m/s)
62X-5, 109	594.09	1.39	0.64	2.44	73.5	117.9	2.81		
62X-5, 110	594.10							48.03	
62X-6, 109	595.59	1.32	0.56	2.19	74.0	134.5	2.88		
62X-6, 110	595.60							47.28	
62X-7, 39	596.39	1.37	0.64	2.29	71.9	115.4	2.58		
63X-1, 109	598.09	1.43	0.70	2.41	70.4	102.3	2.40		
63X-2, 109	599.59	1.34	0.56	2.43	76.8	141.8	3.36		
63X-3, 109	601.09	1.6	0.95	2.62	63.3	68	1.74		
63X-4, 109	602.59	1.69	1.11	2.59	56.9	52.5	1.33		
63X-5, 109	604.09	1.36	0.61	2.31	73.4	124	2.80		
63X-6, 109	605.59	1.58	0.92	2.61	64.5	71.8	1.83		
63X-7, 39	606.39	1.49	0.80	2.5	67.9	87.3	2.13		
64X-1, 99	607.99	1.33	0.54	2.35	76.5	144.3	3.31		
64X-2, 59	609.09	1.66	1.05	2.58	58.9	57.3	1.44		
65X-1, 109	617.79	1.74	1.16	2.7	56.7	50.1	1.32		
65X-2, 109	619.29	1.62	1.02	2.5	59.0	59.4	1.45		
65X-3, 109	620.79	1.66	1.07	2.54	57.8	55.5	1.38		
65X-4, 109	622.29	1.67	1.05	2.69	60.6	59.1	1.55		
65X-5, 109	623.79	1.52	0.82	2.63	68.6	86.1	2.21		
66X-1, 109	627.39	1.59	0.94	2.58	63.5	69.4	1.75		
66X-2, 109	628.89	1.61	0.96	2.63	63.2	67.4	1.73		
66X-3, 109	630.39	1.66	1.04	2.68	61.0	60.3	1.58		
66X-4, 109	631.89	1.69	1.08	2.68	59.5	56.7	1.48		
66X-5, 106	633.36	1.72	1.12	2.73	58.8	53.9	1.43		
66X-6, 109	634.89	1.67	1.05	2.67	60.3	58.6	1.53		
67X-1, 109	637.09	1.48	0.76	2.6	70.7	95.8	2.44		
67X-2, 108	638.58	1.72	1.11	2.73	58.9	54.1	1.44		
67X-3, 113	640.13	1.68	1.05	2.72	61.1	59.7	1.58		
67X-4, 109	641.59	1.73	1.15	2.65	56.1	49.8	1.29		
67X-5, 117	643.17	1.69	1.09	2.66	59.0	55.7	1.45		
67X-6, 109	644.59	1.63	0.99	2.67	62.7	64.8	1.69		
67X-7, 39	645.39	1.74	1.17	2.65	55.7	48.9	1.26		
68X-4, 109	650.69	1.43	0.68	2.53	72.6	108.7	2.68		
68X-5, 39	651.49	1.42	0.68	2.49	72.2	108.2	2.63		
69X-1, 105	655.85	1.62	0.99	2.6	61.8	64.0	1.63		
69X-2, 114	657.44	1.46	0.73	2.53	70.8	99.3	2.45		
69X-3, 110	658.90	1.67	1.03	2.78	62.8	62.8	1.70		
69X-4, 112	660.42	1.69	1.06	2.77	61.4	59.4	1.60		
69X-5, 112	661.92	1.63	1.01	2.59	60.9	62.1	1.57		
69X-6, 111	663.41	1.77	1.22	2.65	53.8	45.2	1.17		
70X-1, 109	665.49	1.74	1.16	2.67	56.2	49.6	1.29		
70X-2, 109	666.99	1.67	1.05	2.66	60.1	58.5	1.52		
70X-3, 110	668.50	1.68	1.05	2.73	61.1	59.5	1.58		
70X-4, 113	670.03	1.69	1.09	2.67	58.8	55.2	1.44		
70X-5, 124	671.64	1.8	1.24	2.75	54.7	45.1	1.21		
70X-6, 114	673.04	1.71	1.10	2.73	59.6	55.7	1.49		
71X-1, 113	675.23	1.79	1.23	2.77	55.5	46.4	1.25		
71X-2, 108	676.68	1.67	1.04	2.74	61.9	61.2	1.64		
71X-3, 108	678.18	1.77	1.20	2.73	55.8	47.7	1.27		
71X-4, 114	679.74	1.72	1.14	2.62	56.1	50.2	1.29		
71X-5, 109	681.19	1.65	1.01	2.72	62.7	63.8	1.69		
71X-6, 109	682.69	1.67	1.05	2.71	61.1	59.6	1.58		
71X-7, 39	683.49	1.69	1.10	2.61	57.6	53.7	1.37		
72X-1, 108	684.78	1.62	0.98	2.61	62.2	65.0	1.66		
72X-2, 108	686.28	1.62	0.96	2.69	64.0	68.2	1.79		
72X-3, 108	687.78	1.72	1.14	2.64	56.5	50.7	1.31		
72X-4, 108	689.28	1.68	1.08	2.63	58.7	55.8	1.43		
72X-5, 108	690.78	1.74	1.15	2.75	57.9	51.6	1.38		
72X-6, 39	691.59	1.72	1.11	2.75	59.2	54.5	1.46		
72X-7, 39	692.59	1.76	1.15	2.82	58.9	52.3	1.44		
73X-1, 109	694.39	1.73	1.14	2.73	58.1	52.4	1.40		
73X-2, 109	695.89	1.74	1.15	2.72	57.4	51.0	1.36		
73X-3, 109	697.39	1.72	1.12	2.75	58.9	53.9	1.44		
73X-4, 109	698.89	1.75	1.18	2.68	55.8	48.7	1.27		
73X-5, 109	700.39	1.86	1.32	2.77	51.9	40.1	1.08		
73X-6, 109	701.89	1.75	1.16	2.74	57.2	50.4	1.35		
74X-1, 109	704.09	1.8	1.24	2.75	54.6	45.0	1.21		
74X-2, 106	705.56	1.79	1.25	2.64	52.4	43.0	1.11		
77X-1, 109	730.99	1.8	1.25	2.73	54.1	44.4	1.18		
77X-2, 22	731.62	1.73	1.16	2.61	55.3	48.8	1.24		
77X-3, 54	733.44	1.69	1.07	2.72	60.5	58.2	1.54		
77X-3, 55	733.45								
77X-4, 21	734.61	1.75	1.16	2.74	57.3	50.5	1.35		1914.1
77X-5, 39	736.29	1.82	1.27	2.77	53.9	43.5	1.18		
78X-1, 99	740.69	1.80	1.24	2.72	54.2	44.8	1.19		
78X-2, 72	741.92	1.86	1.3	2.88	54.8	43.2	1.22		
78X-3, 130	744.00	1.72	1.21	2.42	49.9	42.3	1.00		
78X-3, 131	744.01								1999.8
78X-4, 23	744.43	1.84	1.27	2.85	55.0	44.3	1.23		
78X-5, 102	746.72	1.65	1.01	2.7	62.1	62.8	1.65		
78X-6, 78	747.98	1.73	1.13	2.7	57.7	52.1	1.37		
79X-1, 73	750.23	1.81	1.29	2.64	51.0	40.6	1.05		
79X-2, 23	751.23	1.64	1.00	2.68	62.3	63.6	1.66		
79X-3, 89	753.39	1.76	1.17	2.8	58.0	50.9	1.39		
79X-3, 90	753.40								1919.6

Table 13 (continued).

Core, section, interval (cm)	Depth (mbsf)	Wet-bulk density (g/cm ³)	Dry-bulk density (g/cm ³)	Grain density (g/cm ³)	Wet porosity (%)	Dry water content (%)	Void ratio	Shear strength (kPa)	Compressional wave velocity (m/s)
82X-1, 108	780.28	1.89	1.39	2.72	48.6	35.8	0.95		
82X-2, 76	781.46	1.97	1.51	2.74	44.9	30.5	0.82		
82X-3, 83	783.03	1.98	1.51	2.78	45.5	30.9	0.84		
82X-3, 83	783.03								2118.5
82X-4, 58	784.28	1.97	1.52	2.69	43.3	29.1	0.76		
82X-5, 74	785.94	2.00	1.55	2.76	43.7	28.9	0.78		
82X-6, 89	787.59	2.12	1.76	2.73	35.4	20.6	0.55		
83X-1, 97	790.17	1.60	0.93	2.68	64.9	71.2	1.86		
83X-2, 94	791.64	1.95	1.49	2.74	45.5	31.4	0.84		
83X-3, 32	792.52								2637.9
83X-3, 51	792.71	1.62	0.99	2.6	61.5	63.4	1.61		
83X-4, 14	793.84	2.01	1.51	2.98	49.0	33.2	0.96		
84X-1, 39	799.59	1.96	1.52	2.65	42.6	28.7	0.74		
84X-1, 40	799.60								2147.4
86X-1, 66	819.16	1.58	0.89	2.77	67.5	77.7	2.10		
86X-2, 96	820.96	1.46	0.77	2.34	66.7	88.5	2.02		
86X-3, 13	821.63	1.64	1.03	2.58	59.8	59.4	1.50		
86X-3, 31	821.81								1841.1
86X-4, 3	823.03	1.61	0.94	2.73	65.3	71.3	1.90		
86X-5, 48	824.98	1.61	0.97	2.59	62.3	65.8	1.66		

related to zones of high susceptibility gradient and, thus, to small depth errors. Thermal drift is a function of two temperatures: the external temperature measured at the receiving coil and the temperature difference between the excited coil and the receiving coil. The temperature of the tool decreased during logging operations, but temperature differences between the two runs stayed within 1°C, and the observed discrepancy between the two logs is consistent with the known thermal drift of the tool.

The susceptibility data from Hole 883F are of good quality. No systematic depth or instrumental errors are seen from comparison of the main and repeat logs. Thermal drift is low and is consistent with the changes in the tool temperature during logging. However, the exact calibration coefficient (1 ppm is roughly equivalent to 1×10^{-6} SI) depends on logging speed and hole radius variables. Comparison with the available core susceptibility measurements provides a better estimation of the value of the calibration coefficient.

Comparison of Magnetic Logs with Core Data

Figure 56 shows the comparison of the “local” B field obtained from the first run of the magnetometer (B_{L1} , nT) with the corrected value of susceptibility (k_1 , ppm), and the whole-core susceptibilities measured on cores from Hole 883B and transformed into 10^{-6} SI values. From 200 to 800 mbsf, with the exception of the zone where the effect of the lost magnetic pipe dominates B_{L1} , the anomalies from both logs are strongly anticorrelated. This result is expected for high latitudes. A nearby layer bearing a magnetization with vector components x_1, y_1, z_1 will, in a borehole, produce an induction (or B field) with an $x_1, y_1, -2z_1$ direction (Barthes, 1990). Thus, the projection of the B field arising from the surrounding rock’s susceptibility onto the direction of the ambient earth field will produce an apparent anticorrelation. However, this anticorrelation is a geometrical effect and only results from anomalies arising from the sediments surrounding the borehole, not from regional anomalies. Thus, a given susceptibility will have a variable effect on the magnetometer sensor, depending on the magnetic latitude (as well as the tool’s response and hole diameter): the transfer coefficient between the two tools will depend on the field inclination. In Figure 56, the relative scales for both tools have been chosen for practical presentation purposes. Thus, if variations in the susceptibility log appear higher than those observed in the B field log, this does not mean that surrounding rocks are more susceptible than remanent. The difference is mostly a scale effect. However, the relative variation of susceptibility and of the B field is not always the same. High B anomalies in the 450-mbsf zone indicate more remanent magnetizations.

Comparison with Core Susceptibility Measurements

Several observations can be made by comparing the downhole and laboratory susceptibility data. More sharp and narrow peaks can be seen in the record obtained from laboratory measurements. Which often correlate to lower amplitude and broader ones in the downhole record. One reason for such a difference is the real resolution of the log and core measurements. Core data are taken each 5 cm and correspond to the measure of a small volume of material. Downhole data, in contrast, measure a much larger volume of material so that the tool’s response will tend to broaden the anomalies. Therefore, wider and smoother peaks will be seen in the susceptibility logs; these often correspond to thin ash layers. Some peaks (which may be seen in the logs) do not appear in the shipboard core measurements. This may reflect lateral variation between Holes 883B and 883F and/or discontinuous core recovery. However, the log and core susceptibility data sets can be correlated over some intervals of several meters to tens of meters, more or less peak to peak (e.g., within the 200–240 mbsf interval of Hole 883F). Finally, the correlations between the core and log data imply no significant depth offset between Holes 883B and 883F (Fig. 56), which are 50 m apart.

Comparison with Lithology

From a magnetic standpoint, overall rock magnetization should decrease as the biogenic silica content increases. An increase in clay and ash content should correspond to an increase of rock magnetization. Strictly speaking, the clays themselves are paramagnetic, but often are associated with detrital magnetite. As for the carbonate and nanofossil contents, these can correspond either to an increase of magnetization, if magnetite is associated, or a decrease, if the rocks are pure calcium carbonate.

The top of the basement, Unit VI, was identified in both logs from 823 to 834 mbsf (Figs. 49 and 53). Within the sedimentary section, the susceptibility tool recorded a change in overall values slightly above 648 mbsf (Fig. 53), which coincides roughly with the boundary between lithologic Units III and IV. A similar change also was observed in the detailed portion of the total induction log (Fig. 50). This transition, which corresponds to an increase in carbonate contents, also seems to correspond to an increase in magnetization. A lesser magnitude change also can be seen in both the susceptibility and B field logs (Figs. 50, 53, 56B) at about 440 mbsf, slightly above the top of Unit III. No clear contrast is observed at the boundaries of Subunits IIIA and IIIB at 597 mbsf and of Subunits IVA and IVB at 740 mbsf.

Table 14. Index properties, compressional wave velocity, and shear strength data from Hole 883C.

Core, section, interval (cm)	Depth (mbsf)	Wet-bulk density (g/cm ³)	Dry-bulk density (g/cm ³)	Grain density (g/cm ³)	Wet porosity (%)	Dry water content (%)	Void ratio	Shear strength (kPa)	Compressional wave velocity (m/s)
145-883C-									
1H-1, 114	1.14	1.35	0.53	2.62	79.3	152.6	3.90	8.35	1489.9
1H-1, 115	1.15								
1H-2, 40	1.90								
1H-2, 119	2.69	1.39	0.60	2.66	77.2	132.2	3.43	20.87	
1H-2, 120	2.70								
2H-1, 109	4.09	1.24	0.38	2.39	83.6	224.3	5.23	32.46	
2H-1, 110	4.10								
2H-2, 109	5.59	1.27	0.45	2.35	80.5	184.3	4.22	31.07	
2H-2, 110	5.60								
2H-3, 40	6.40								1497.8
2H-3, 109	7.09	1.40	0.62	2.66	76.2	125.2	3.25	29.68	
2H-3, 110	7.10								
2H-4, 119	8.69	1.45	0.68	2.70	74.3	111.4	2.94	39.88	
2H-4, 120	8.70								
2H-5, 109	10.09	1.28	0.46	2.37	80.1	176.9	4.09	35.25	
2H-5, 110	10.10								
2H-6, 109	11.59	1.26	0.43	2.32	81.0	192.0	4.36	37.10	
2H-6, 110	11.60								
2H-7, 39	12.39	1.41	0.66	2.54	73.8	115.0	2.85	49.16	
3H-1, 109	13.59	1.42	0.67	2.47	72.5	110.5	2.67		
3H-1, 110	13.60								
3H-2, 109	15.09	1.32	0.53	2.29	76.3	146.4	3.27	53.28	
3H-2, 110	15.10								
3H-3, 40	15.90								1512.2
3H-3, 109	16.59	1.36	0.56	2.59	78.1	143.7	3.63	30.77	
3H-3, 110	16.60								
3H-4, 109	18.09	1.40	0.61	2.74	77.5	130.5	3.49	38.27	
3H-4, 110	18.10								
3H-5, 109	19.59	1.48	0.76	2.55	69.9	94.3	2.35	42.78	
3H-5, 110	19.60								
3H-6, 109	21.09	1.30	0.47	2.50	81.0	178.2	4.35	44.28	
3H-6, 110	21.10								
3H-7, 39	21.89	1.44	0.68	2.70	74.5	112.4	2.96	32.27	
4H-1, 109	23.09	1.35	0.57	2.42	76.1	137.0	3.24		
4H-1, 110	23.10								
4H-2, 109	24.59	1.43	0.68	2.54	72.7	108.9	2.70	36.02	
4H-2, 110	24.60								
4H-3, 40	25.40								1507.4
4H-3, 109	26.09	1.41	0.65	2.55	74.2	117.0	2.91	36.77	
4H-3, 110	26.10								
4H-5, 109	29.09	1.49	0.78	2.55	69.1	90.8	2.26	33.02	
4H-5, 110	29.10								
4H-6, 79	30.29	1.43	0.68	2.53	72.6	108.8	2.68	36.77	
5H-1, 114	32.64	1.41	0.66	2.49	73.1	113.1	2.75		
5H-1, 115	32.65								
5H-2, 109	34.09	1.39	0.62	2.53	75.3	125.3	3.10	39.78	
5H-2, 110	34.10								
5H-3, 40	34.90								1494.7
5H-3, 109	35.59	1.42	0.66	2.60	74.3	115.0	2.92	39.02	
5H-3, 110	35.60								
5H-4, 109	37.09	1.40	0.63	2.56	75.0	121.4	3.04	42.03	
5H-4, 110	37.10								
5H-5, 109	38.59	1.47	0.74	2.66	72.0	100.3	2.60	40.53	
5H-5, 110	38.60								
5H-6, 109	40.09	1.47	0.71	2.73	73.5	105.5	2.81	51.03	
5H-6, 110	40.10								
6H-1, 109	42.09	1.27	0.43	2.35	81.3	192.5	4.42	38.27	
6H-1, 110	42.10								
6H-2, 109	43.59	1.17	0.27	2.27	87.9	338.8	7.52	46.53	
6H-2, 110	43.60								
6H-3, 40	44.40								1479.1
6H-3, 109	45.09	1.47	0.73	2.59	71.3	99.4	2.51	43.53	
6H-3, 110	45.10								
6H-4, 109	46.59	1.25	0.40	2.38	83.0	214.9	5.00	51.03	
6H-4, 110	46.60								
6H-5, 109	48.09	1.41	0.64	2.59	74.8	118.9	3.01	51.78	
6H-5, 110	48.10								
6H-6, 109	49.59	1.41	0.65	2.54	74.1	116.8	2.89	46.53	
6H-6, 110	49.60								
7H-1, 109	51.59	1.24	0.40	2.24	81.9	211.7	4.62	40.53	
7H-1, 110	51.60								
7H-2, 109	53.09	1.21	0.34	2.26	84.4	252.3	5.56	42.03	
7H-2, 110	53.10								
7H-3, 40	53.90								1469.9
7H-3, 109	54.59	1.52	0.80	2.68	69.8	89.4	2.34	43.53	
7H-3, 110	54.60								
7H-4, 109	56.09	1.43	0.68	2.57	73.1	109.4	2.75	49.53	
7H-4, 110	56.10								
7H-5, 109	57.59	1.48	0.74	2.74	72.8	101.1	2.70	51.03	
7H-5, 110	57.60								
7H-6, 109	59.09	1.51	0.80	2.63	69.4	89.3	2.29	58.54	
7H-6, 110	59.10								
7H-7, 29	59.79	1.33	0.53	2.39	77.3	148.0	3.45		

Table 14 (continued).

Core, section, interval (cm)	Depth (mbsf)	Wet-bulk density (g/cm ³)	Dry-bulk density (g/cm ³)	Grain density (g/cm ³)	Wet porosity (%)	Dry water content (%)	Void ratio	Shear strength (kPa)	Compressional wave velocity (m/s)
8H-1, 109	61.09	1.40	0.65	2.50	73.8	117.1	2.86		
8H-1, 115	61.15							54.78	
8H-2, 109	62.59	1.39	0.61	2.55	75.8	127.5	3.17		
8H-2, 110	62.60							46.53	
8H-3, 40	63.40								1505.8
8H-3, 109	64.09	1.39	0.60	2.59	76.3	129.5	3.27		
8H-3, 110	64.10							36.77	
8H-4, 109	65.59	1.41	0.65	2.53	73.9	116.6	2.87		
8H-4, 110	65.60							57.04	
8H-5, 109	67.09	1.45	0.70	2.64	73.0	106.5	2.74		
8H-5, 110	67.10							61.54	
8H-6, 109	68.59	1.41	0.65	2.55	74.2	116.9	2.91		
8H-6, 110	68.60							66.79	
8H-7, 39	69.39	1.41	0.65	2.59	74.5	117.2	2.96		
9H-1, 114	70.64	1.40	0.63	2.62	75.7	123.3	3.16		
9H-1, 115	70.65							76.55	
9H-2, 109	72.09	1.39	0.63	2.48	74.2	120.2	2.91		
9H-2, 110	72.10							49.53	
9H-3, 109	73.59	1.34	0.54	2.43	77.2	145.3	3.44		
9H-3, 110	73.60							54.03	
9H-4, 11	74.11							55.54	
9H-4, 109	75.09	1.33	0.53	2.46	78.1	150.9	3.62		
9H-5, 109	76.59	1.18	0.30	2.22	86.1	294.9	6.40		
9H-5, 110	76.60							36.77	
9H-6, 109	78.09	1.41	0.64	2.61	75.0	119.3	3.04		
9H-6, 110	78.10							45.03	
9H-7, 39	78.89	1.45	0.73	2.51	70.6	99.0	2.42		
10H-1, 109	80.09	1.40	0.64	2.50	74.0	117.7	2.88		
10H-1, 110	80.10							64.54	
10H-2, 109	81.59	1.38	0.61	2.49	75.3	127.3	3.09		
10H-2, 109	81.59							64.54	
10H-3, 40	82.40								1505.8
10H-3, 109	83.09	1.35	0.57	2.47	76.8	139.3	3.36		
10H-3, 110	83.10							65.29	
10H-4, 109	84.59	1.27	0.46	2.24	79.0	175.6	3.83		
10H-4, 110	84.60							69.04	
10H-5, 109	86.09	1.37	0.61	2.42	74.6	126.0	2.98		
10H-5, 110	86.10							68.29	
10H-6, 109	87.59	1.31	0.51	2.32	77.5	154.8	3.51		
10H-6, 110	87.60							59.29	
10H-7, 39	88.39	1.23	0.38	2.34	83.4	224.8	5.13		
11H-1, 109	89.59	1.20	0.35	2.12	83.4	247.6	5.13		
11H-1, 110	89.60							43.53	
11H-2, 109	91.09	1.21	0.36	2.17	83.1	237.2	5.03		
11H-2, 110	91.10							37.52	
11H-3, 40	91.90								1538.5
11H-3, 109	92.59	1.24	0.40	2.20	81.4	208.1	4.48		
11H-3, 110	92.60							31.52	
11H-4, 109	94.09	1.23	0.38	2.24	82.7	222.7	4.88		
11H-4, 110	94.10							32.27	
11H-5, 109	95.59	1.22	0.36	2.39	84.7	243.3	5.67		
11H-5, 110	95.60							39.78	
11H-6, 104	97.04	1.21	0.36	2.13	82.6	233.6	4.86		
11H-6, 105	97.05							34.52	
11H-7, 39	97.89	1.24	0.41	2.18	80.9	203.5	4.32		
12H-1, 109	99.09	1.23	0.39	2.16	81.7	215.3	4.54		
12H-1, 110	99.10							34.52	
12H-2, 109	100.59	1.21	0.36	2.21	83.3	237.4	5.12		
12H-2, 110	100.60							33.02	
12H-3, 40	101.40								1499.4
12H-3, 109	102.09	1.29	0.48	2.30	78.6	166.8	3.74		
12H-3, 110	102.10							35.27	
12H-4, 109	103.59	1.25	0.42	2.29	81.2	197.1	4.40		
12H-4, 110	103.60							48.03	
12H-5, 109	105.09	1.29	0.49	2.26	77.9	162.3	3.58		
12H-5, 110	105.10							49.53	
12H-6, 109	106.59	1.26	0.41	2.40	82.4	204.4	4.78		
12H-7, 39	107.39	1.27	0.45	2.26	79.8	182.5	4.03		
13H-2, 109	108.73	1.22	0.37	2.27	83.3	231.2	5.12		
13H-2, 110	108.74							33.02	
13H-3, 119	110.33	1.23	0.39	2.15	81.3	211.9	4.44		
13H-3, 120	110.34							31.52	
13H-4, 40	111.04								1438.5
13H-4, 119	111.83	1.22	0.38	2.20	82.4	223.3	4.79		
13H-4, 120	111.84							35.27	
13H-5, 109	113.23	1.33	0.55	2.35	76.1	140.7	3.22		
13H-5, 110	113.24							45.78	
13H-6, 109	114.73	1.33	0.53	2.43	77.8	150.3	3.56		
13H-6, 110	114.74							57.04	
13H-7, 109	116.23	1.24	0.40	2.28	82.0	208.7	4.64		
13H-7, 110	116.24							51.78	
13H-8, 39	117.03	1.27	0.47	2.24	78.8	173.1	3.79		
14H-1, 109	118.09	1.22	0.38	2.14	81.7	218.2	4.55		
14H-1, 120	118.20							30.77	

Table 14 (continued).

Core, section, interval (cm)	Depth (mbsf)	Wet-bulk density (g/cm ³)	Dry-bulk density (g/cm ³)	Grain density (g/cm ³)	Wet porosity (%)	Dry water content (%)	Void ratio	Shear strength (kPa)	Compressional wave velocity (m/s)
14H-2, 109	119.59	1.25	0.40	2.35	82.4	208.7	4.79		
14H-2, 110	119.60							29.27	
14H-3, 109	121.09	1.24	0.41	2.23	81.2	202.6	4.41		
14H-3, 110	121.10							14.26	
14H-4, 109	122.59	1.25	0.42	2.18	80.2	194.3	4.14		
14H-4, 110	122.60							36.02	
14H-5, 109	124.09	1.25	0.43	2.22	80.5	194.0	4.21		
14H-5, 110	124.10							36.02	
14H-6, 109	125.59	1.23	0.39	2.17	81.8	216.9	4.60		
14H-6, 110	125.60							35.27	
14H-7, 19	126.19	1.25	0.41	2.34	82.2	207.6	4.73		
15H-1, 109	127.59	1.27	0.45	2.33	80.5	184.4	4.19		
15H-1, 110	127.60							27.77	
15H-2, 109	129.09	1.32	0.54	2.29	76.0	143.7	3.21		
15H-2, 110	129.10							38.27	
15H-3, 75	130.25								1456.2
15H-3, 109	130.59	1.31	0.51	2.38	78.3	157.6	3.67		
15H-3, 110	130.60							34.52	
15H-4, 109	132.09	1.27	0.46	2.24	79.2	177.5	3.87		
15H-4, 110	132.10							39.78	
15H-5, 109	133.59	1.24	0.42	2.16	80.3	196.4	4.14		
15H-5, 110	133.60							38.27	
15H-6, 109	135.09	1.30	0.51	2.33	77.9	157.5	3.58		
15H-6, 110	135.10							42.78	
15H-7, 39	135.89	1.34	0.55	2.38	76.3	140.9	3.27		
16H-1, 39	136.39	1.26	0.45	2.18	79.2	182.0	3.87		
16H-1, 110	137.10							35.27	
16H-2, 39	137.89	1.27	0.45	2.27	79.9	183.3	4.06		
16H-2, 110	138.60							30.77	
16H-3, 39	139.39	1.30	0.50	2.28	77.6	158.2	3.51		1426.3
16H-3, 75	139.75								
16H-3, 110	140.10							31.52	
16H-4, 39	140.89	1.29	0.49	2.27	77.8	161.1	3.57		
16H-4, 110	141.60							33.77	
16H-5, 39	142.39	1.27	0.45	2.26	79.8	182.3	4.03		
16H-5, 110	143.10							36.02	
16H-6, 39	143.89	1.25	0.46	2.03	77.2	173.4	3.44		
16H-6, 110	144.60							41.28	
16H-7, 39	145.39	1.35	0.58	2.34	74.7	130.8	2.99		
17H-1, 39	145.89	1.34	0.56	2.42	76.4	139.3	3.28		
17H-1, 110	146.60							21.76	
17H-2, 39	147.39	1.27	0.46	2.22	78.8	174.0	3.77		
17H-2, 110	148.10							26.27	
17H-3, 39	148.89	1.24	0.40	2.21	81.5	207.4	4.48		
17H-3, 75	149.25								1414.9
17H-3, 110	149.60							18.76	
17H-4, 39	150.39	1.21	0.36	2.14	82.8	235.4	4.91		
17H-4, 120	151.20							33.77	
17H-5, 39	151.89	1.21	0.37	2.11	81.9	223.9	4.62		
17H-5, 110	152.60							29.27	
17H-6, 39	153.39	1.23	0.41	2.08	79.8	198.2	4.02		
17H-6, 110	154.10							31.52	
17H-7, 39	154.89	1.33	0.55	2.31	75.6	139.7	3.15		
18H-1, 39	155.39	1.26	0.45	2.13	78.4	178.0	3.70		
18H-1, 110	156.10							33.02	
18H-2, 39	156.89	1.28	0.47	2.31	79.1	170.9	3.85		
18H-2, 110	157.60							30.77	
18H-3, 39	158.39	1.25	0.43	2.24	80.4	191.7	4.19		
18H-3, 75	158.75								1462.8
18H-3, 110	159.10							33.77	
18H-4, 39	159.89	1.29	0.49	2.26	78.1	164.3	3.63		
18H-4, 110	160.60							42.03	
18H-5, 39	161.39	1.44	0.77	2.25	65.2	86.3	1.89		
18H-5, 110	162.10							48.03	
18H-6, 39	162.89	1.43	0.68	2.57	73.2	110.0	2.76		
18H-6, 110	163.60							48.78	
18H-7, 39	164.39	1.36	0.60	2.31	73.6	125.5	2.83		
19H-1, 39	164.89	1.39	0.67	2.31	70.6	107.6	2.42		
19H-1, 110	165.60							33.77	
19H-2, 39	166.39	1.32	0.53	2.36	77.1	148.2	3.41		
19H-2, 110	167.10							30.02	
19H-3, 39	167.89	1.31	0.53	2.28	76.3	147.4	3.28		
19H-3, 110	168.60							22.51	
19H-4, 39	169.39	1.43	0.71	2.45	70.7	102.3	2.44		
19H-4, 110	170.10							34.52	
19H-5, 39	170.89	1.40	0.65	2.48	73.3	115.1	2.79		
19H-5, 110	171.60							30.02	
19H-6, 39	172.39	1.30	0.51	2.28	77.3	155.9	3.46		
19H-6, 80	172.80							30.77	
20H-1, 39	174.39	1.28	0.47	2.26	79.0	173.6	3.84		
20H-1, 110	175.10							21.76	
20H-2, 39	175.89	1.23	0.40	2.18	81.2	207.7	4.41		
20H-2, 110	176.60							12.01	
20H-3, 39	177.39	1.22	0.39	2.08	80.9	213.6	4.33		

Table 14 (continued).

Core, section, interval (cm)	Depth (mbsf)	Wet-bulk density (g/cm ³)	Dry-bulk density (g/cm ³)	Grain density (g/cm ³)	Wet porosity (%)	Dry water content (%)	Void ratio	Shear strength (kPa)	Compressional wave velocity (m/s)
20H-3, 75	177.75								1424.0
20H-3, 110	178.10							11.26	
20H-4, 39	178.89	1.28	0.48	2.20	78.0	167.3	3.60		
20H-5, 39	180.39	1.25	0.44	2.19	79.7	187.3	4.01		
20H-6, 39	181.89	1.25	0.45	2.11	78.3	177.9	3.66		
20H-7, 39	183.39	1.27	0.46	2.23	79.0	175.2	3.82		
21H-1, 39	183.89	1.26	0.45	2.18	79.2	182.3	3.88		
21H-1, 110	184.60							39.02	
21H-2, 39	185.39	1.25	0.43	2.17	80.0	192.3	4.08		
21H-2, 110	186.10							39.78	
21H-3, 39	186.89	1.28	0.47	2.30	79.2	173.1	3.88		
21H-3, 110	187.60							25.52	
21H-4, 39	188.39	1.23	0.40	2.21	81.6	209.2	4.51		
21H-4, 110	189.10							32.27	
21H-5, 39	189.89	1.25	0.42	2.24	80.9	198.0	4.33		
21H-5, 110	190.60							27.77	
21H-6, 39	191.39	1.26	0.45	2.18	79.1	180.6	3.85		
21H-6, 110	192.10							36.02	
21H-7, 39	192.89	1.31	0.52	2.30	77.2	152.7	3.43		
22H-1, 39	193.39	1.27	0.46	2.25	79.4	178.7	3.92		
22H-1, 110	194.10							51.03	
22H-2, 39	194.89	1.35	0.59	2.36	74.8	130.9	3.02		
22H-2, 110	195.60							66.79	
22H-3, 39	196.39	1.25	0.42	2.25	80.9	196.5	4.31		
22H-3, 110	197.10							42.78	
22H-4, 39	197.89	1.24	0.43	2.16	79.9	191.8	4.04		
22H-4, 110	198.60							46.53	
22H-5, 110	200.10							47.28	
22H-6, 39	200.89	1.27	0.46	2.20	78.7	175.1	3.76		
22H-6, 110	201.60							63.04	
22H-7, 39	202.39	1.25	0.42	2.20	80.4	194.3	4.18		
23H-1, 39	202.89	1.21	0.37	2.10	82.1	228.3	4.68		
23H-1, 110	203.60							39.78	
23H-2, 39	204.39	1.22	0.37	2.17	82.6	229.5	4.86		
23H-2, 110	205.10							37.52	
23H-3, 39	205.89	1.24	0.40	2.21	81.5	208.6	4.50		
23H-3, 110	206.60							58.54	
23H-4, 39	207.39	1.19	0.36	2.00	81.7	234.6	4.57		
23H-4, 110	208.10							51.03	
23H-5, 39	208.89	1.23	0.40	2.18	81.4	210.4	4.47		
23H-5, 110	209.60							47.28	
23H-6, 39	210.39	1.30	0.50	2.28	77.7	159.4	3.54		
23H-6, 110	211.10							76.55	
23H-7, 39	211.89	1.27	0.45	2.22	79.2	178.4	3.87		
24H-1, 39	212.39	1.29	0.50	2.19	76.8	156.7	3.35		
24H-1, 110	213.10							72.05	
24H-2, 39	213.89	1.25	0.42	2.29	81.3	199	4.45		
24H-2, 110	214.60							36.02	
24H-3, 39	215.39	1.24	0.41	2.19	80.8	200.8	4.29		
24H-3, 110	216.10							39.02	
24H-4, 39	216.89	1.26	0.45	2.25	79.8	183.4	4.03		
24H-4, 110	217.60							40.53	
24H-5, 39	218.39	1.25	0.42	2.22	80.8	197.2	4.28		
24H-5, 110	219.10							40.53	
24H-6, 39	219.89	1.24	0.41	2.18	81.0	205.0	4.35		
24H-6, 110	220.60							52.53	
24H-7, 39	221.39	1.24	0.41	2.18	80.9	203.4	4.33		
25H-1, 39	221.89	1.25	0.43	2.15	79.5	187.9	3.94		
25H-1, 110	222.60							51.78	
25H-2, 39	223.39	1.25	0.43	2.19	80.2	192.7	4.12		
25H-2, 110	224.10							30.77	
25H-3, 39	224.89	1.25	0.44	2.14	79.2	185.9	3.88		
25H-3, 75	225.25								1455.4
25H-3, 110	225.60							51.03	
25H-4, 39	226.39	1.27	0.46	2.21	78.9	176.1	3.80		
25H-4, 110	227.10							66.79	
25H-5, 39	227.89	1.28	0.49	2.19	77.4	162.5	3.47		
25H-5, 110	228.60							72.05	
25H-6, 39	229.39	1.28	0.48	2.24	78.3	167.9	3.67		
25H-6, 110	230.10							86.30	
25H-7, 39	230.89	1.26	0.46	2.14	78.3	175.8	3.68		
26H-1, 39	231.39	1.30	0.49	2.37	79.2	166.9	3.86		
26H-1, 110	232.10							58.54	
26H-2, 39	232.89	1.30	0.51	2.33	77.9	157.5	3.58		
26H-2, 110	233.60							66.79	
26H-3, 39	234.39	1.27	0.47	2.21	78.4	170.3	3.68		
26H-3, 75	234.75								1345.9
26H-3, 110	235.10							55.54	
26H-4, 39	235.89	1.30	0.51	2.28	77.1	153.7	3.43		
26H-4, 110	236.60							86.30	
26H-5, 39	237.39	1.26	0.42	2.32	81.5	197.5	4.48		
26H-5, 110	238.10							99.81	
26H-6, 39	238.89	1.37	0.60	2.42	74.9	128.4	3.03		
26H-6, 110	239.60							91.56	

Table 14 (continued).

Core, section, interval (cm)	Depth (mbsf)	Wet-bulk density (g/cm ³)	Dry-bulk density (g/cm ³)	Grain density (g/cm ³)	Wet porosity (%)	Dry water content (%)	Void ratio	Shear strength (kPa)	Compressional wave velocity (m/s)
26H-7, 39	240.39	1.27	0.45	2.33	80.4	183.5	4.18		
27H-1, 39	240.89	1.23	0.39	2.22	81.9	213.3	4.62		
27H-1, 110	241.60							141.09	
27H-2, 39	242.39	1.26	0.44	2.26	80.0	185.3	4.09		
27H-2, 110	243.10							111.82	
27H-3, 39	243.89	1.23	0.39	2.20	81.9	215.5	4.63		
27H-3, 110	244.60							108.07	
27H-4, 39	245.39	1.24	0.44	2.09	78.8	185.0	3.78		
27H-4, 110	246.10							99.06	
27H-5, 39	246.89	1.27	0.45	2.26	79.6	180.1	3.98		
27H-5, 75	247.25								1427.1
27H-5, 110	247.60							75.05	
27H-6, 39	248.39	1.27	0.46	2.22	78.7	173.5	3.77		
27H-6, 110	249.10							107.32	
27H-7, 39	249.89	1.27	0.46	2.23	79.2	177.6	3.86		
29X-1, 39	259.99	1.24	0.42	2.09	79.4	191.7	3.91		
29X-1, 110	260.70							30.02	
29X-2, 39	261.49	1.22	0.37	2.22	82.9	228.5	4.95		
29X-2, 110	262.20							40.53	
29X-3, 39	262.99	1.26	0.43	2.30	80.8	191.1	4.28		
29X-3, 98	263.58							62.29	
29X-4, 39	264.49	1.22	0.40	2.09	80.7	208.9	4.26		
29X-4, 110	265.20							21.76	
29X-5, 39	265.99	1.24	0.41	2.20	81.1	203.7	4.37		
29X-5, 110	266.70							19.51	
29X-6, 13	267.23	1.24	0.41	2.24	81.1	200.9	4.38		
30X-1, 39	269.09	1.22	0.38	2.17	81.9	218.0	4.63		
30X-1, 110	269.80							15.01	
30X-2, 39	270.59	1.23	0.40	2.13	80.7	205.5	4.27		
30X-2, 110	271.30							33.77	
30X-3, 39	272.09	1.27	0.46	2.20	78.5	173.1	3.71		
30X-3, 110	272.80							20.26	
30X-4, 39	273.59	1.27	0.45	2.28	79.8	181.0	4.03		
30X-4, 110	274.30							33.77	
30X-5, 39	275.09	1.28	0.46	2.35	80.0	177.2	4.06		
30X-5, 110	275.80							36.77	
30X-6, 39	276.59	1.27	0.46	2.30	79.8	179.1	4.02		
30X-6, 110	277.30							52.53	
30X-7, 39	278.09	1.42	0.55	3.59	84.2	155.8	5.45		
31X-1, 109	279.39	1.26	0.46	2.15	78.4	175.2	3.68		
31X-1, 110	279.40							35.27	
31X-2, 109	280.89	1.27	0.46	2.20	78.6	173.5	3.73		
31X-2, 110	280.90							58.54	
31X-3, 40	281.70								1700.1
31X-3, 109	282.39	1.26	0.44	2.26	80.0	184.4	4.06		
31X-3, 110	282.40							42.03	
31X-4, 109	283.89	1.28	0.47	2.27	78.8	171.2	3.79		
31X-4, 110	283.90							59.29	
31X-5, 109	285.39	1.26	0.44	2.29	80.6	188.9	4.23		
31X-5, 110	285.40							53.28	
31X-6, 109	286.89	1.27	0.46	2.27	79.4	176.9	3.92		
31X-6, 110	286.90							53.28	
31X-7, 39	287.69	1.27	0.49	2.10	76.5	161.3	3.31		
32X-1, 109	289.09	1.33	0.56	2.33	75.7	139.1	3.16		
32X-1, 110	289.10							54.03	
32X-2, 109	290.59	1.25	0.43	2.18	79.8	188.2	4.01		
32X-2, 110	290.60							50.28	
32X-3, 40	291.40								1672.0
32X-3, 109	292.09	1.28	0.47	2.32	79.5	174.2	3.94		
32X-3, 110	292.10							56.29	
32X-4, 109	293.59	1.31	0.51	2.39	78.5	159.3	3.72		
32X-4, 110	293.60							66.79	
32X-5, 109	295.09	1.29	0.50	2.24	77.3	158.1	3.46		
32X-5, 110	295.10							51.78	
32X-6, 109	296.59	1.35	0.59	2.34	74.3	128.5	2.93		
32X-6, 110	296.60							57.79	
32X-7, 39	297.39	1.45	0.73	2.51	70.7	99.7	2.44		
33X-1, 109	298.69	1.28	0.46	2.34	79.9	177.1	4.05		
33X-1, 110	298.70							38.27	
33X-2, 109	300.19	1.28	0.47	2.23	78.4	169.6	3.69		
33X-2, 110	300.20							48.78	
33X-3, 39	300.99	1.42	0.69	2.40	71.1	106.0	2.48		
34X-1, 109	308.39	1.41	0.69	2.34	70.0	103.3	2.36		
34X-1, 110	308.40							51.03	
34X-2, 109	309.89	1.29	0.48	2.37	79.5	170.5	3.95		
34X-2, 110	309.90							54.78	
34X-3, 40	310.70								1606.1
34X-3, 109	311.39	1.32	0.54	2.27	76.0	145.3	3.22		
34X-3, 110	311.40							63.79	
34X-4, 109	312.90	1.29	0.49	2.24	77.7	162.2	3.55		
34X-4, 110	312.90							45.78	
34X-5, 39	313.69	1.29	0.50	2.22	77.1	157.8	3.43		
35H-1, 109	318.09	1.31	0.52	2.29	76.9	151.0	3.37		
35H-1, 110	318.10							60.79	

Table 14 (continued).

Core, section, interval (cm)	Depth (mbsf)	Wet-bulk density (g/cm ³)	Dry-bulk density (g/cm ³)	Grain density (g/cm ³)	Wet porosity (%)	Dry water content (%)	Void ratio	Shear strength (kPa)	Compressional wave velocity (m/s)
35H-2, 109	319.59	1.28	0.48	2.24	78.0	165.2	3.60		
35H-2, 110	319.60							54.03	
35H-3, 40	320.40								1618.8
35H-3, 109	321.09	1.24	0.42	2.19	80.5	196.2	4.20		
35H-3, 110	321.10							85.55	
35H-4, 109	322.59	1.28	0.49	2.18	77.1	160.9	3.42		
35H-4, 110	322.60							55.54	
35H-5, 109	324.09	1.34	0.57	2.26	74.3	132.5	2.93		
35H-5, 110	324.10							106.57	
35H-6, 109	325.59	1.32	0.53	2.29	76.3	146.2	3.26		
35H-6, 110	325.60							89.31	
36H-1, 109	327.59	1.29	0.50	2.24	77.2	157.0	3.44		
36H-1, 110	327.60							89.31	
36H-2, 109	329.09	1.30	0.51	2.30	77.5	155.2	3.49		
36H-2, 110	329.10							72.05	
36H-3, 40	329.90								1627.8
36H-3, 109	330.59	1.32	0.54	2.25	75.6	143.1	3.15		
36H-4, 100	332							105.82	
36H-4, 109	332.09	1.29	0.50	2.25	77.4	158.4	3.48		
36H-5, 89	333.39	1.40	0.69	2.31	69.8	103.6	2.33		
36H-6, 109	335.09	1.28	0.49	2.19	77.5	163.7	3.50		
36H-6, 110	335.10							75.80	
36H-7, 39	335.89	1.28	0.50	2.13	76.2	155.9	3.24		
37H-1, 109	337.09	1.32	0.52	2.35	77.5	152.3	3.50		
37H-1, 110	337.10							60.79	
37H-2, 109	338.59	1.32	0.54	2.29	75.9	142.9	3.20		
37H-2, 110	338.60							63.04	
37H-3, 40	339.40								1419.5
37H-3, 109	340.09	1.36	0.59	2.38	74.7	129.0	2.99		
37H-3, 110	340.10							59.29	
37H-4, 109	341.59	1.35	0.60	2.29	73.5	125.5	2.81		
37H-4, 110	341.60							89.31	
37H-5, 109	343.09	1.33	0.55	2.33	76.0	141.0	3.21		
37H-5, 110	343.10							96.81	
37H-6, 39	343.89	1.31	0.53	2.29	76.5	147.6	3.30		
37H-7, 39	344.89	1.34	0.57	2.33	75.3	136.2	3.10		
38H-1, 109	346.59	1.30	0.51	2.23	76.6	152.8	3.32		
38H-1, 110	346.60							63.79	
38H-2, 109	348.09	1.34	0.58	2.26	74.0	131.1	2.89		
38H-2, 110	348.10							83.30	
38H-3, 40	348.90								1647.9
38H-3, 109	349.59	1.28	0.48	2.22	77.9	165.5	3.58		
38H-3, 110	349.60							58.54	
38H-4, 109	351.09	1.28	0.49	2.23	77.9	164.3	3.57		
38H-4, 110	351.10							59.29	
38H-5, 109	352.59	1.32	0.54	2.32	76.3	144.7	3.28		
38H-5, 110	352.60							104.32	
38H-6, 109	354.09	1.28	0.47	2.22	78.4	170.1	3.69		
38H-6, 110	354.10							65.29	
38H-7, 39	354.89	1.32	0.54	2.30	76.2	144.2	3.24		

Often, if some overall change of the magnetic signal occurs at lithological boundaries, the correlations with compositional changes are more evident. Unit IV is calcium carbonate with increasing ash content in its lower part (Subunit IVB). An increase of both overall susceptibility and total magnetization (B field) occurs in the 650- to 690-mbsf interval (Figs. 50, 53, 56C, 56F; note change of scale between Figs. 16C and 16D). This anomaly is bimodal in both records, with a first part from 648 to 670 mbsf and a second part between 678 and 690 mbsf. From about 690 to 710 mbsf, no significant anomaly can be seen in either the susceptibility log or the total induction log. A large susceptibility anomaly occurs in the interval from 710 to about 758 mbsf, followed by more moderate anomalies down to about 775 mbsf and then, again by another important anomaly down to slightly above 796 mbsf. Another more "quiet" zone can be found down to 805 mbsf, followed by another huge anomaly between 805 and about 815 mbsf, that corresponds to the ash-derived clay layer of Unit V (see "Lithostratigraphy" section, this chapter). Below this anomaly, susceptibility remains high, but without significant peaks, down to the top basement at 823 mbsf. By analyzing the core lithological data from Hole 883B, a tight correlation can be demonstrated between this entire sequence of anomalies and the composition of the sediments.

Ash occurs at about 190, 240, between 305 and 335, and at 370 mbsf and corresponds to discrete peaks of susceptibility (Fig. 56). The

correlation between the clay occurrences and the susceptibility logs is not so clear. However, positive correlations can be found in the 530- to 560- and 580- to 590-mbsf intervals of Subunit IIIA (Fig. 56C) and possibly at 335 mbsf (Fig. 56A). In the interval from 400 to 450 mbsf, clay content increases (Figs. 3 and 4), but it does not correlate with anomalies in the susceptibility log between 400 and 440 mbsf (Fig. 56B). A sharp change in average susceptibility, which occurs between 440 and 452 mbsf, may be related to a change in the clay composition. In the 445- to 490-mbsf interval, the B field anomaly becomes dominant, compared to the susceptibility data. One may consider a change in the type of magnetization that would become essentially remanent. In such hypothesis, the lowermost clays of Unit II and the uppermost carbonates of Subunit IIIA would be more magnetite-rich.

Conclusions

The data obtained with both susceptibility and total induction logging tools at Hole 883F are of good quality, as deduced from the analysis of the main logs and repeat sections. Both records are consistent, and some correlations can be made between downhole susceptibility and laboratory core susceptibility measurements. Most variations in the magnetic logs can be correlated with changes in

Table 15. Index properties and compressional wave velocity data from Hole 883E.

Core, section, interval (cm)	Depth (mbsf)	Wet-bulk density (g/cm ³)	GRAPE bulk density (g/cm ³)	Dry-bulk density (g/cm ³)	Grain density (g/cm ³)	Dry water content (%)	Wet porosity (%)	Void ratio	Compressional wave velocity (m/s)
145-883E-									
1R-1, 107	548.07	1.96		1.54	2.64	41.9	21.7	0.71	
1R-2, 50	549.00	1.58		0.91	2.69	66.4	42.6	1.95	
1R-3, 79	550.79	1.43		0.67	2.65	75.0	53.4	2.96	
1R-4, 52	552.02	1.59		0.97	2.47	60.9	38.9	1.54	
1R-4, 54	552.04								1712.1
2R-1, 13	640.13	1.67		1.07	2.6	58.9	35.8	1.42	
2R-1, 14	640.14								1751.6
3R-1, 115	650.95	1.49		0.80	2.5	68.3	46.6	2.13	
3R-1, 117	650.97								1784.2
3R-2, 125	652.55	1.48		0.75	2.59	71.2	49.0	2.43	
3R-4, 107	655.37	1.65		1.02	2.64	61.4	37.9	1.57	
3R-6, 15	657.45	1.77		1.17	2.82	58.5	33.7	1.40	
4R-1, 19	659.79	1.77		1.20	2.69	55.5	32.0	1.23	
4R-1, 20	659.80								1823.7
4R-2, 11	661.21	1.71		1.12	2.65	57.8	34.4	1.36	
4R-3, 10	662.40	1.80		1.23	2.76	55.4	31.3	1.23	
5R-1, 31	669.81	1.78		1.23	2.67	54.1	30.9	1.17	
5R-1, 32	669.82								1904.6
5R-2, 125	672.25	1.75		1.19	2.62	54.6	31.8	1.19	
5R-3, 136	673.86	1.73		1.14	2.7	57.9	34.0	1.36	
5R-4, 61	674.61	1.47		0.73	2.62	72.2	50.0	2.56	
6R-1, 59	679.99	1.55		0.85	2.71	68.8	45.1	2.17	
6R-1, 60	680.00								1828.4
6R-2, 16	681.06	1.73		1.14	2.69	58.0	34.2	1.36	
6R-3, 116	683.56	1.69		1.08	2.72	60.5	36.3	1.51	
6R-4, 122	685.12	1.78		1.23	2.66	54.0	30.9	1.16	
6R-5, 64	686.04	1.73		1.12	2.76	59.5	35.0	1.45	
7R-1, 143	690.73	1.81		1.23	2.86	57.2	32.1	1.32	
7R-1, 144	690.74								1527.5
7R-2, 53	691.33	1.72		1.15	2.62	56.2	33.2	1.27	
7R-3, 49	692.79	1.71		1.13	2.62	56.9	33.8	1.30	
7R-4, 98	694.78	1.78		1.20	2.79	57.2	32.7	1.32	
7R-5, 93	696.23	1.77		1.22	2.65	54.1	31.0	1.16	
7R-6, 33	697.13	1.72		1.16	2.58	55.3	32.7	1.22	
8R-1, 14	699.34	1.87		1.34	2.81	52.5	28.5	1.09	
8R-1, 15	699.35								1831.7
8R-2, 12	700.82	1.81		1.29	2.62	50.9	28.7	1.03	
9R-1, 48	709.48	1.79		1.25	2.64	52.9	30.1	1.11	
9R-1, 90	709.90								2408.7
9R-2, 21	710.71	2.06		1.71	2.58	33.6	16.6	0.50	
11R-1, 110	729.90	1.83		1.29	2.74	53.2	29.6	1.13	
11R-2, 110	731.40	1.80		1.23	2.76	55.4	31.4	1.23	
11R-3, 110	732.90	1.83		1.27	2.80	54.7	30.4	1.19	
12R-1, 127	739.87								2100.7
12R-3, 69	742.29	1.81		1.27	2.73	53.8	30.1	1.15	
13R-3, 62	752.02								1846.4
13R-3, 71	752.11	1.78		1.22	2.73	55.4	31.6	1.23	
14R-1, 13	758.43	1.93		1.45	2.74	47.2	24.9	0.89	
14R-1, 72	759.02								1889.8
15R-1, 110	769.20	1.91		1.42	2.74	48.4	25.8	0.93	
15R-3, 123	772.33								2146.1
16R-1, 66	778.66	2.00		1.57	2.69	41.8	21.3	0.71	
16R-1, 70	778.70								2054.4
17R-1, 133	789.23								2233.1
19R-5, 63	814.13	1.61		0.94	2.7	65.3	41.4	1.86	
19R-5, 67	814.17								1545.4
20R-1, 69	818.09	2.39			2.85	25.2	10.7	0.33	
20R-1, 70	818.10								5074.5
20R-2, 70	819.43		2.66						4970.6
20R-2, 89	819.62	2.62			2.88	14.0	5.40	0.16	
20R-3, 99	821.15	2.62			2.82	11.4	4.40	0.13	
20R-4, 84	822.29		2.50						5691.9
20R-6, 95	825.06		2.74						6895.0
21R-2, 67	829.33	2.36			2.67	19.1	8.30	0.23	
21R-2, 67	829.33		2.63						5695.0
21R-2, 85	829.51		2.21						4254.7
21R-2, 89	829.55	2.19			2.73	32.1	14.9	0.47	
21R-3, 109	831.00	2.15			2.73	33.9	16.0	0.51	
21R-3, 110	831.01		2.14						4296.4
21R-5, 78	833.16		2.9						8211.8
21R-5, 84	833.22	2.76		—	2.97	10.7	4.0	0.12	
22R-2, 4	838.00	2.79		—	3.21	19.2	7.0	0.24	
22R-2, 5	838.01		2.68						6814.1
22R-3, 79	840.25	3.10		—	4.19	34.4	11.3	0.52	
22R-3, 80	840.26		2.49						5402.3
22R-6, 59	844.24	2.68		—	2.98	15.2	5.7	0.18	
22R-6, 62	844.27		2.72						6343.7
23R-2, 114	849.54	3.56		—	4.5	27.0	7.7	0.37	
23R-2, 120	849.60		2.66						6115.6

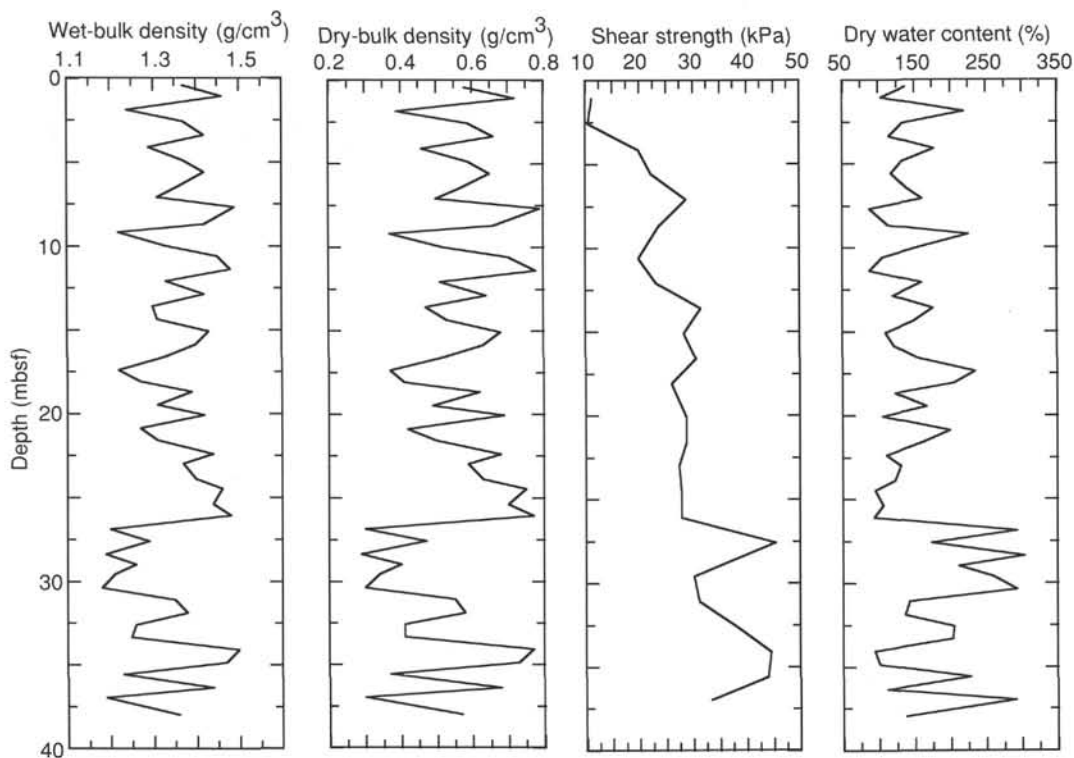


Figure 34. Index property and shear strength data vs. depth below seafloor for Hole 883A.

lithology observed in Hole 883B about 50 m away. Finally, though magnetizations are often low, one can hope that a magnetostratigraphic interpretation of the logs will be possible, at least below 300 mbsf and perhaps down to 700 mbsf.

CORRELATION OF SEISMIC WITH LITHOLOGIC DATA

All the Leg 145 drilling locations were surveyed in order to drop the beacon at the proper pre-selected location. In every case, the surveys were run in the figure of the number 4, with the long leg duplicating the site-survey track line used to select the site and the cross-leg being as nearly orthogonal as practical. The shipboard air-gun seismic reflection profiling system was used for all the surveys except for Site 883, when it was inoperable; the 3.5-kHz profiling system was used to locate that drill site. Details of the survey and seismic processing techniques are given in the "Site 881" chapter ("Seismic-Lithologic Correlation" section, this volume).

The seismic reflection record taken from the 1988 site-survey cruise aboard the *Thomas Washington* crossing the location of Site 883 (Fig. 57) shows at least 0.9 s (two-way traveltime) of sediment overlying basement. The sedimentary section here conforms to the regional topography of Detroit Seamount (Fig. 2). The lower lithologic units are difficult to resolve on this profile. Carbonate-rich Unit III is highly reflective, in marked contrast to Unit II, the more nearly pure diatom ooze. Lithologic Unit I, the upper 87 m, is characterized by silty diatom ooze with ash layers and dropstones and is more highly reflective in character.

SUMMARY AND CONCLUSIONS

Geologic Record

Drilling at Site 883 penetrated about 830 m of uppermost Cretaceous and Cenozoic sediments atop Detroit Seamount and 37.5 m into the underlying basalts. The sedimentary section can be divided into five lithologic units. Unit I (0–86.9 mbsf) is a Quaternary to upper

Pliocene dark gray clay with quartz and diatoms. Vitric ash layers are common, and dropstones are more rare as accessory lithologies. The ash layers are usually light brown or gray, but a few are black. Thicker ashes have sharp lower boundaries, show size grading, and have burrowed upper boundaries. The unit is bioturbated and shows the resultant color mottling and burrow fillings. Unit I corresponds in age almost exactly with the Brunhes and Matuyama chrons. Unit II (86.9–458 mbsf) is an upper Pliocene to upper Miocene, grayish-green diatom ooze. Calcium carbonate is an accessory component in this unit, and clay occurs in minor amounts. Ash layers are present, but in much lower abundances than in Unit I; pumice fragments occur at 131.26 to 131.46 mbsf. Unit II is moderately bioturbated and mottled. Unit III is a biogenic ooze that can be divided into an upper more siliceous portion and a lower, more calcareous portion. Lithologic Subunit IIIA (458–597 mbsf) is an upper Miocene to middle Miocene, light gray calcareous diatom ooze that forms a transitional unit from the more siliceous units above and the more calcareous sequence below. Subunit IIIA displays moderate bioturbation. Lithologic Subunit IIIB (597–652.2 mbsf) is a middle Miocene to lower Miocene, light greenish-gray diatomaceous chalk. The subunit is characterized by subhorizontal *Zoophycos* burrows, a few of which are rimmed by pyrite crystals. Unit IV is a Paleogene chalk that can be divided into two subunits. Lithologic Subunit IVA (652.2–740 mbsf) is an upper Oligocene to middle Eocene, very light brown nannofossil chalk. The boundary with the overlying ooze is marked by a pronounced color change from greenish-grays above, to the creamy tans of Unit IV below (Fig. 8) and a lacuna of several million years. Some dark-colored vitric ash occurs in Subunit IVA. The entire subunit is extensively bioturbated. Subunit IVB (740–814 mbsf) is a middle Eocene to lower Eocene or perhaps Paleocene nannofossil chalk with ash that becomes more abundant downhole so that the lower part of the unit becomes a nannofossil ash. The unit is bioturbated in the upper portion and displays mottling and *Zoophycos* traces. Current-related sedimentary structures are common (such as lenticular microlamination, small-scale cross lamination, load casts, convolute laminations, scoured surfaces, and burrowed hardgrounds).

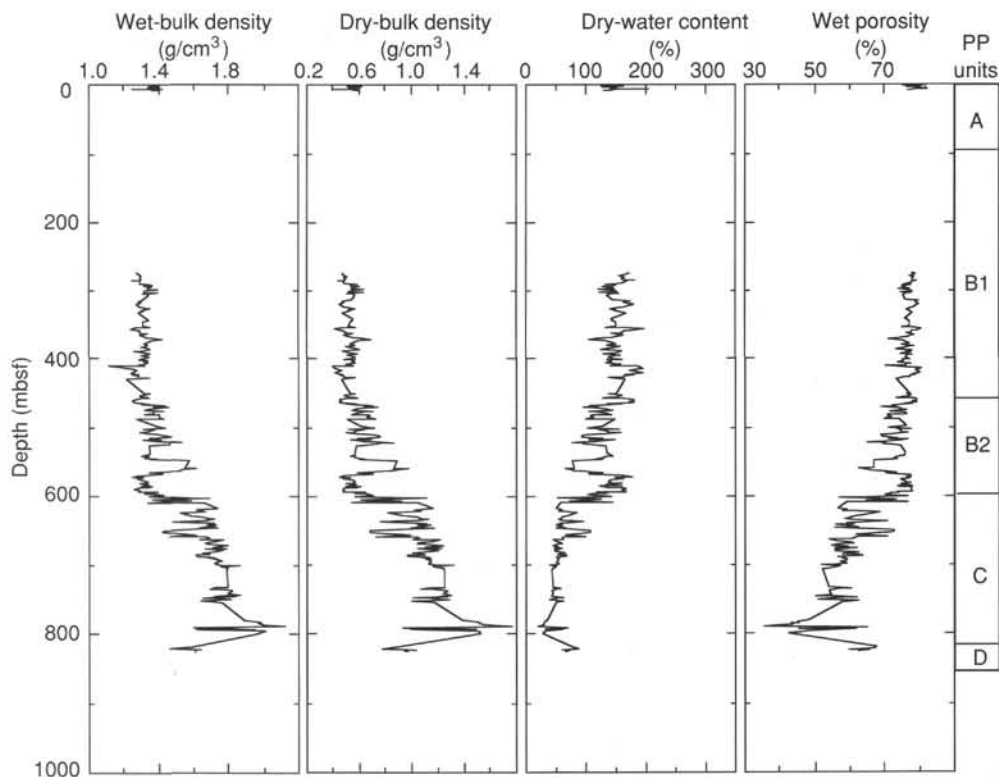


Figure 35. Index property data vs. depth below seafloor for Hole 883B. The physical properties (PP) Units A, B, C, and D are shown (center) and are discussed in the text.

Microfaulting and soft-sediment deformation, including centimeter to decimeter-scale recumbent folding, can be observed. Subunit IVB in both Holes 883B and 883E displays considerable evidence for downslope displacement of sedimentary material, a process that is more important lower in the section. Debris flows, seen as matrix-supported diamictites having angular clasts of brown altered ash in a light tan chalk matrix, are common and carbonate turbidites also occur. Unit V, (814–830 mbsf) in Hole 883B, but much thinner in Holes 883E and 883F) consists of Paleocene to Campanian(?) yellow green to yellow brown altered ashes that are speckled with iron and manganese oxides. These palagonite clays have been now converted to smectites with minor amounts of illite, chlorite, quartz and feldspar. Lithologic Unit VI (819–856.5 mbsf in Hole 883E and 822.6–849.4 mbsf in Hole 883F) consists of a series of pillow basalts. These basalts contain 10% to 15% plagioclase microphenocrysts and iddingsite pseudomorphous after olivine in a fine-grained groundmass. Clinopyroxene occurs rarely. The bulk chemistry of the basalts places them in the Ocean-Island Basalt (OIB) category. Numerous lithologic or flow units can be recognized, commonly on the basis of the glassy margins of the pillows, now altered to a brown color. Vesicles and small fractures are common and are usually filled with calcite. Calcite, limestone, and palagonite sediments fill the interpillow voids.

Shipboard measurements of the physical properties show changes in accord with the major lithologies. Unit I is characterized by dry-bulk densities (DBD) of 0.59 g/cm^3 and porosities of 76%. Diatom-rich Unit II is more porous and correspondingly less dense, with DBD values that average 0.49 g/cm^3 . Porosity decreases slightly in Unit III, where DBD values increase to 0.61 g/cm^3 in Subunit IIIA and increase sharply in the chalks of Subunit IIIB to 1.10 g/cm^3 , with a corresponding decrease in porosity to 59%. Bulk densities are slightly higher in Unit IV.

Biostratigraphic control was provided by siliceous microfossils in Units I, II, and III, with some assistance from calcareous nannofossils

in Quaternary sediments. Nannofossil zonation provides the age control in the Paleogene sediments of Units IV and V. Magnetic reversal stratigraphy is well constrained in the upper, clay-rich portion of the core. Reversals related to the Brunhes/Matuyama boundary, Jaramillo, Olduvai, and Reunion events, and the Matuyama/Gauss boundary are clear. The Matuyama/Gauss reversal boundary occurs at essentially the same position in the core as the boundary between lithologic Units I and II. Overall sedimentation rates for the various lithologic units show moderate deposition rates (for the Northwest Pacific) for Unit I, approximately 47 m/m.y. for the past 1 m.y. and lower rates of 23 m/m.y. for the interval between about 1.0 and 2.6 Ma. The phenomenon of enhanced sedimentation rates during the past 1.0 m.y. is seen in all four of the Leg 145 Northwest Pacific Ocean drill sites. Unit II has accumulated the most rapidly, with an overall rate in excess of 90 m/m.y. Slower rates are found deeper in the section, at 23 m/m.y. in Subunit IIIA, 10 m/m.y. in Subunit IIIB, and about the same down through Subunit IVA. We did not determine meaningful pelagic sedimentation rates for the lower portion of Unit IV, which has been subjected to extensive downslope re-depositional processes.

Fluxes of the sedimentary components within the various units can be determined by combining the lithology, sedimentation rate, and DBD information for the intervals of interest. In late Pliocene and Quaternary age Unit I, diatoms have mass accumulation rates (MAR) of 0.6 to $0.7 \text{ g}(\text{cm}^2 \cdot \text{k.y.})^{-1}$, and terrigenous materials, clay and quartz, accumulated at higher rates, a total of approximately $1.0 \text{ g}(\text{cm}^2 \cdot \text{k.y.})^{-1}$. In lithologic Unit II, clays and quartz accumulated at somewhat lower rates, about $0.3 \text{ g}(\text{cm}^2 \cdot \text{k.y.})^{-1}$, but the rate of silica accumulation increased five-fold to values in excess of $3.0 \text{ g}(\text{cm}^2 \cdot \text{k.y.})^{-1}$. In the upper portion of Unit III, silica accumulated at a rate similar to that in Unit I, about $0.6 \text{ g}(\text{cm}^2 \cdot \text{k.y.})^{-1}$. This opal flux rate declines further in older sediments. The MAR of calcium carbonate is 0.3 to $0.4 \text{ g}(\text{cm}^2 \cdot \text{k.y.})^{-1}$ in Units II and III; the calcite MAR doubles in the upper nannofossil chalks of Unit IV to $0.7 \text{ g}(\text{cm}^2 \cdot \text{k.y.})^{-1}$.

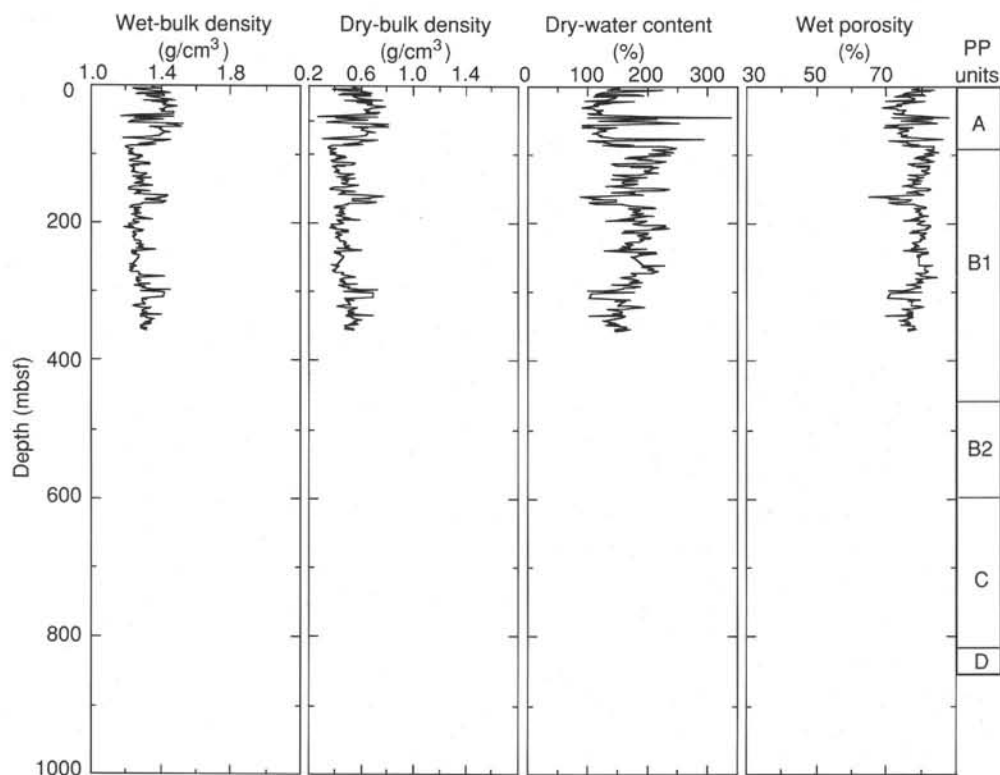


Figure 36. Index property data vs. depth below seafloor for Hole 883C. The PP Units A, B, C, and D are shown (right) and are discussed in the text.

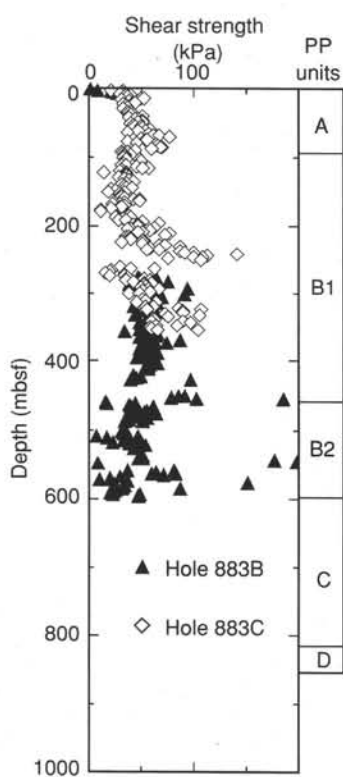


Figure 37. Shear strength data vs. depth below seafloor for Holes 883B and 883C. The PP Units A, B, C, and D are shown (to the right) and are discussed in the text.

Paleoceanography and Paleoclimatology

The basalts of Detroit Seamount were erupted during latest Cretaceous time, presumably at the Hawaiian hot spot in the subtropical North Pacific Ocean. The seafloor at the location of Site 883 apparently never reached sea level, as suggested by the complete lack of shallow-water or reefal materials in the lowest portion of the sedimentary section. Presumably, nearby volcanic eruptions provided volcanic ash to the region, ash now seen as the altered palagonites and smectites of lithologic Unit V. Carbonate and ash deposits on the slopes of Detroit Seamount occasionally reached positions of instability during early Eocene and probably Paleocene time and moved rapidly downslope as turbidites, slumps, or debris flows. Physical indications of bottom-water activity remain in the sediment column as sedimentary structures. Significant amounts of Paleocene and Eocene reworking and downslope sediment redistribution have been documented elsewhere in the central and northern Pacific Ocean (Schlanger and Premoli Silva, 1981; Rea and Thiede, 1981; Vallier et al., 1983) and the information from Detroit Seamount significantly broadens the known region of that activity. During Eocene time, the influx of ash declined and the more normal nannofossil chalk of middle Eocene- to early Oligocene-aged Subunit IVA was deposited at rates of between 0.5 and $1.0 \text{ g}(\text{cm}^2 \cdot \text{k.y.})^{-1}$, rates that fall into the low-to-normal range for carbonate deposition beneath oligotrophic subtropical gyres (Rea et al., 1990).

Above the late Oligocene to early Miocene hiatus, the siliceous component of the sediment becomes important. The MAR of calcite declines to 0.3 to $0.4 \text{ g}(\text{cm}^2 \cdot \text{k.y.})^{-1}$ in the chalk and oozes of Units III and II, and the flux of silica increases from $0.2 \text{ g}(\text{cm}^2 \cdot \text{k.y.})^{-1}$ in the more carbonate-rich lower portion of Unit III to $0.6 \text{ g}(\text{cm}^2 \cdot \text{k.y.})^{-1}$ in the upper, middle, and lower Miocene, portion of the unit. The diatom ooze of Unit II defines a time of extreme silica deposition in the northwestern Pacific Ocean. Silica flux average $3.0 \text{ g}(\text{cm}^2 \cdot \text{k.y.})^{-1}$

during the time between 2.6 and 6.8 Ma and may have been much higher than that during the early Pliocene. This latest Miocene and early Pliocene episode of silica deposition was observed at the other Leg 145 drill sites in the Northwest Pacific Ocean and represents a short period of extreme productivity in high latitudes, associated with the warm interval of the same age.

Important changes in sediment accumulation occurred in conjunction with the onset of Northern Hemisphere glaciation at 2.6 Ma. The flux of terrigenous clays and quartz to the sediments at Site 883 more than triples, to values of $1.0 \text{ g}(\text{cm}^2 \cdot \text{k.y.})^{-1}$, and the flux of opal returns to its pre-uppermost Miocene levels of approximately $0.6 \text{ g}(\text{cm}^2 \cdot \text{k.y.})^{-1}$. This same enhanced influx of terrigenous materials was found at Site 881, where the increase was greater than an order of magnitude and has been associated with the onset of bottom-current activity, and at Site 882 where the increase in the flux of terrigenous material was by a factor of 4 Ma. Enhanced flux of hemipelagic materials at the time of onset of significant continental glaciation has been recorded commonly in the North Atlantic and North Pacific oceans.

At Site 883, dropstones occur in Unit I in slightly lower abundances than those encountered at Site 882, 90 km to the south, and in much lower abundances than those at Site 881, about 455 km to the south, again emphasizing the northward decline in ice-rafted debris. Taken together, the Leg 145 drill sites and the Leg 86 drill sites (Krissek et al., 1985; Heath, Burckle, et al., 1985) neatly define the source of the Northwest Pacific Ocean dropstones to be the Sea of Okhotsk, or possibly the Kamchatka Peninsula, a fact first suspected by Conolly and Ewing (1970). Dropstones appear in the section at the time of the Matuyama/Gauss reversal boundary at 2.6 Ma and thus herald the onset of major glaciation in the Northern Hemisphere (Rea and Schrader, 1985). In contrast to more southerly locations, no dropstones were found in Site 883 sediments older than late Pliocene.

Ash layers are common to abundant in sediments younger than 2.6 Ma, and occur again in the Eocene portion of the section. At 2.6 Ma, the deposition of volcanogenic material increase by more than an order of magnitude. This increase in ash deposition, which began during the latest Pliocene in the North Pacific Ocean, has been known for many years (Kennett and Thunell, 1975; Kennett et al., 1977), however, the Leg 145 sites provide much better-dated sequences for determining timing of onset of the northwestern Pacific Ocean portion of this oceanwide volcanic episode than has been available previously. Examination of the individual ash layers should reveal geochemical trends in Kuril-Kamchatka volcanism. The lower occurrence of ash layers provides one of the first good definitions of a period of Eocene volcanism, which has been suggested by various data from scattered locations, such as Hess Rise (Vallier et al., 1983) and the Central Pacific basins (Rea and Thiede, 1981).

The upper Unit I, a gray clay with quartz and diatoms, contains up to 5% calcium carbonate; most samples contain a few foraminifers. Nannofossil zonations are possible in the Pleistocene sections but not below. From these bits of evidence, we may conclude that Site 883, at its depth of 2385 m, lies near the present Northwest Pacific Ocean calcite compensation depth (CCD). The nearest drill sites, Site 192 at a depth of 3014 m and Site 882 at a depth of 3244 m, clearly are located below the CCD (Creager, Scholl, et al., 1973; this volume). This observation means that the CCD is significantly shallower in the far northwestern Pacific than it is in the central gyre region. Both Shatsky Rise (Site 306) at 3399 m and Hess Rise (Site 310) at 3516 m are characterized by silica-bearing nannofossil ooze of 60% to 70% CaCO_3 (Larson, Moberly, et al., 1975). The northernmost site on Hess Rise, Site 464 at 39.9°N and a water depth of 4670 m, contains 11% CaCO_3 in its uppermost siliceous ooze unit (Thiede, Vallier, et al., 1981; Dean, 1981), twice as much as occurs at Site 883 at 51.2°N , almost 2300 m shallower.

Shoaling of the CCD toward highly productive polar regions and coastal upwelling zones, such as those off the west coasts of South America and Africa, is a well-known phenomenon in the modern ocean (Berger, 1974, 1989). It occurs because much of the biological productivity in these regions is in siliceous material, which results in

the biogeneration of opal and organic carbon. The ensuing breakdown of the organic carbon enhances the rate of dissolution of whatever calcite is produced in these regions, serving to raise the CCD to shallow depths. The northward-shoaling of the CCD by more than 2 km, observed in the North Pacific Ocean between about 40° to 50°N , appears to be a classic example of this productivity/dissolution control of carbonate preservation on the seafloor.

REFERENCES*

- Akiba, F., Hiramatsu, C., and Yanagisawa, Y., in press. A Cenozoic diatom genus *Cavitatus* Williams; an emended description and two new biostratigraphically useful species, *C. lanceolatus* and *C. rectus* from Japan. *Bull. Nat. Sci. Mus. (Tokyo)*.
- Aubry, M.-P., 1992. Paleogene calcareous nannofossils from the Kerguelen Plateau, Leg 120. In Wise, S.W., Jr., Schlich, R., et al., *Proc. ODP, Sci. Results*, 120: College Station, TX (Ocean Drilling Program), 471–491.
- Barron, J.A., 1989. The late Cenozoic stratigraphic record and hiatuses of the northeast Pacific: results from the Deep Sea Drilling Project. In Winterer, E.L., Hussong, D.M., and Decker, R.W. (Eds.), *The Geology of North America (Vol. N): The Eastern Pacific Ocean and Hawaii*. Geol. Soc. Am., Geol. of North America Ser., 311–322.
- Barthes, V., 1990. Modelisation magnetique en forage. *Rap. CEA/LETI/DSYS/SETIA*, 90–59.
- Beaufort, L., and Aubry, M.-P., 1990. Fluctuations in the composition of late Miocene calcareous nannofossil assemblages as a response to orbital forcing. *Paleoceanography*, 5:845–865.
- Berger, W.H., 1974. Deep-sea sedimentation. In Burk, C.A., and Drake, C.L. (Eds.), *The Geology of Continental Margins*: New York (Springer-Verlag), 213–241.
- , 1989. Global maps of ocean productivity. In Berger, W.H., Smetacek, V.S., and Wefer, G. (Eds.), *Productivity of the Oceans: Present and Past*: New York (Wiley), 429–455.
- Bischoff, J.L., Greer, R.E., and Luistro, A.O., 1970. Composition of interstitial waters of marine sediments: temperature of squeezing effect. *Science*, 167:1245–1246.
- Broecker, W.S., and Peng, T.-H., 1982. *Tracers in the Sea*: Palisades, NY (Eldigio Press).
- Cande, S.C., and Kent, D.V., 1992. A new geomagnetic polarity timescale for the Late Cretaceous and Cenozoic. *J. Geophys. Res.*, 97:13917–13951.
- Conolly, J.R., and Ewing, M., 1970. Ice-rafted detritus in Northwest Pacific deep-sea sediments. In Hays, J.D. (Ed.), *Geological Investigations of the North Pacific*. Mem.—Geol. Soc. Am., 12:219–231.
- Creager, J.S., Scholl, D.W., et al., 1973. *Init. Repts. DSDP*, 19: Washington (U.S. Govt. Printing Office).
- Dean, W.E., 1981. Calcium carbonate and organic carbon in samples from Deep Sea Drilling Project Sites 463, 464, 465, and 466. In Thiede, J., Vallier, T.L., et al., *Init. Repts. DSDP*, 62: Washington (U.S. Govt. Printing Office), 869–876.
- Deer, W.A., Howie, R.A., and Zussman, J., 1966. *An Introduction to the Rock-Forming Minerals*: London (Longman Group).
- Foreman, H.P., 1975. Radiolaria from the North Pacific, Deep Sea Drilling Project, Leg 32. In Larson, R.L., Moberly, R., et al., *Init. Repts. DSDP*, 32: Washington (U.S. Govt. Printing Office), 579–676.
- Hays, J.D., 1970. Stratigraphy and evolutionary trends of radiolaria in North Pacific deep sea sediments. In Hays, J.D. (Ed.), *Geological Investigations of the North Pacific*. Mem.—Geol. Soc. Am., 126:185–218.
- Heath, G.R., Burckle, L.H., et al., 1985. *Init. Repts. DSDP*, 86: Washington (U.S. Govt. Printing Office).
- Keller, G., and Barron, J.A., 1987. Paleodepth distribution of Neogene deep-sea hiatuses. *Paleoceanography*, 2:697–713.
- Kennett, J.P., McBirney, A.R., and Thunell, R.C., 1977. Episodes of Cenozoic volcanism in the circum-Pacific region. *J. Volcanol. Geotherm. Res.*, 2:145–163.
- Kennett, J.P., and Thunell, R.C., 1975. Global increase in Quaternary explosive volcanism. *Science*, 187:497–503.
- Krissek, L.A., Morley, J.J., and Lofland, D.K., 1985. The occurrence, abundance, and composition of ice-rafted debris in sediments from Deep Sea

* Abbreviations for names of organizations and publication titles in ODP reference lists follow the style given in *Chemical Abstracts Service Source Index* (published by American Chemical Society).

- Drilling Project Sites 579 and 580, northwest Pacific. In Heath, G.R., Burckle, L.H., et al., *Init. Repts. DSDP*, 86: Washington (U.S. Govt. Printing Office), 647–655.
- Landing, W.M., and Bruland, K.W., 1980. Manganese in the North Pacific. *Earth Planet. Sci. Lett.*, 49:45–46.
- Larson, R.L., Moberly, R., et al., 1975. *Init. Repts. DSDP*, 32: Washington (U.S. Govt. Printing Office).
- Ling, H.Y., 1973. Radiolaria: Leg 19 of the Deep Sea Drilling Project. In Creager, J.S., Scholl, D.W., et al., *Init. Repts. DSDP*, 19: Washington (U.S. Govt. Printing Office), 777–797.
- McDuff, R.E., 1985. The chemistry of interstitial waters, Deep Sea Drilling Project, Leg 86. In Heath, G.R., Burckle, L.H., et al., *Init. Repts. DSDP*, 86: Washington (U.S. Govt. Printing Office), 675–687.
- Müller, D.W., Hodell, D.A., and Ciesielski, P.F., 1991. Late Miocene to earliest Pliocene (9.8–4.5 Ma) Paleoceanography of the subantarctic Southeast Atlantic: stable isotopic, sedimentologic, and microfossil evidence. In Ciesielski, P.F., Kristoffersen, Y., et al., *Proc. ODP, Sci. Results*, 114: College Station, TX (Ocean Drilling Program), 459–474.
- Rea, D.K., Dehn, J., Driscoll, N., Farrell, J., Janeczek, T., Owen, R.M., Pospichal, J.J., Resiwati, P., and the ODP Leg 121 Scientific Party, 1990. Paleoceanography of the Eastern Indian Ocean from ODP Leg 121 drilling on Broken Ridge. *Geol. Soc. Am. Bull.*, 102:679–690.
- Rea, D.K., and Schrader, H., 1985. Late Pliocene onset of glaciation: ice rafting and diatom stratigraphy of North Pacific DSDP cores. *Palaeogeogr. Palaeoclimatol., Palaeoecol.*, 49:313–325.
- Rea, D.K., and Thiede, J., 1981. Mesozoic and Cenozoic mass accumulation rates of the major sediment components in the Nauru Basin, Western Equatorial Pacific. In Larson, R.L., Schlanger, S.O., et al., *Init. Repts. DSDP*, 61: Washington (U.S. Govt. Printing Office), 549–555.
- Riedel, W.R., and Sanfilippo, A., 1970. Radiolaria, Leg 4, Deep Sea Drilling Project. In Bader, R.G., Gerard, R.D., et al., *Init. Repts. DSDP*, 4: Washington (U.S. Govt. Printing Office), 503–575.
- , 1978. Stratigraphy and evolution of tropical Cenozoic radiolarians. *Micropaleontology*, 24:61–96.
- Sayles, F.L., Manheim, F.T., and Waterman, L.S., 1973. Interstitial water studies on small core samples, Leg 20. In Heezen, B.C., MacGregor, I.D., et al., *Init. Repts. DSDP*, 20: Washington (U.S. Govt. Printing Office), 871–874.
- Schlanger, S.O., and Premoli Silva, I., 1981. Tectonic, volcanic, and paleogeographic implications of redeposited reef faunas of Late Cretaceous and Tertiary age from the Nauru Basin and the Line Islands. In Larson, R.L., Schlanger, S.O., et al., *Init. Repts. DSDP*, 61: Washington (U.S. Govt. Printing Office), 817–827.
- Scholl, D.W., and Creager, J.S., 1973. Geologic synthesis of Leg 19 (DSDP) results: far North Pacific and Aleutian Ridge, and Bering Sea. In Creager, J.S., Scholl, D.W., et al., *Init. Repts. DSDP*, 19: Washington (U.S. Govt. Printing Office), 897–913.
- Shackleton, N.J., Backman, J., Zimmerman, H., Kent, D.V., Hall, M.A., Roberts, D.G., Schnitker, D., Baldauf, J.G., Desprairies, A., Homrighausen, R., Huddleston, P., Keene, J.B., Kaltenback, A.J., Krumstiek, K.A.O., Morton, A.C., Murray, J.W., and Westberg-Smith, J., 1984. Oxygen isotope calibration of the onset of ice-rafting and history of glaciation in the North Atlantic region. *Nature*, 307:620–623.
- Thiede, J., and Rea, D.K., 1981. Mass accumulation rates of Barremian to Recent biogenic sediments from the Mid-Pacific Mountains (Deep Sea Drilling Project Site 463) and Hess Rise (Sites 464, 465, 466) central North Pacific Ocean. In Thiede, J., Vallier, T.L., et al., *Init. Repts. DSDP*, 62: Washington (U.S. Govt. Printing Office), 637–651.
- Thiede, J., Vallier, T.L., et al., 1981. *Init. Repts. DSDP*, 62: Washington (U.S. Govt. Printing Office).
- Vallier, T.L., Dean, W.E., Rea, D.K., and Thiede, J., 1983. Geologic evolution of Hess Rise, central North Pacific Ocean. *Geol. Soc. Am. Bull.*, 94:1289–1307.
- van Morkhoven, F.P.C.M., Berggren, W.A., and Edwards, A.S., 1986. Cenozoic cosmopolitan deep-water benthic foraminifera. *Bull. Cent. Rech. Explor.-Prod. Elf-Aquitaine*, Mem. 11.
- Woodruff, F., 1985. Changes in Miocene deep-sea benthic foraminiferal distribution in the Pacific Ocean: relationship to paleoceanography. In Kennett, J.P. (Ed.), *The Miocene Ocean: Paleoceanography and Biogeography*. Mem.—*Geol. Soc. Am.*, 163:131–175.

Ms 145IR-107

NOTE: For all sites drilled, core-description forms (“barrel sheets”) and core photographs can be found in Section 3, beginning on page 395. Forms containing smear-slide data can be found in Section 4, beginning on page 985. Thin-section data are given in Section 5, beginning on page 1013. Conventional- log, FMS, dipmeter, and geochemical log (element and oxide weight %) data can be found in CD-ROM form (back pocket).

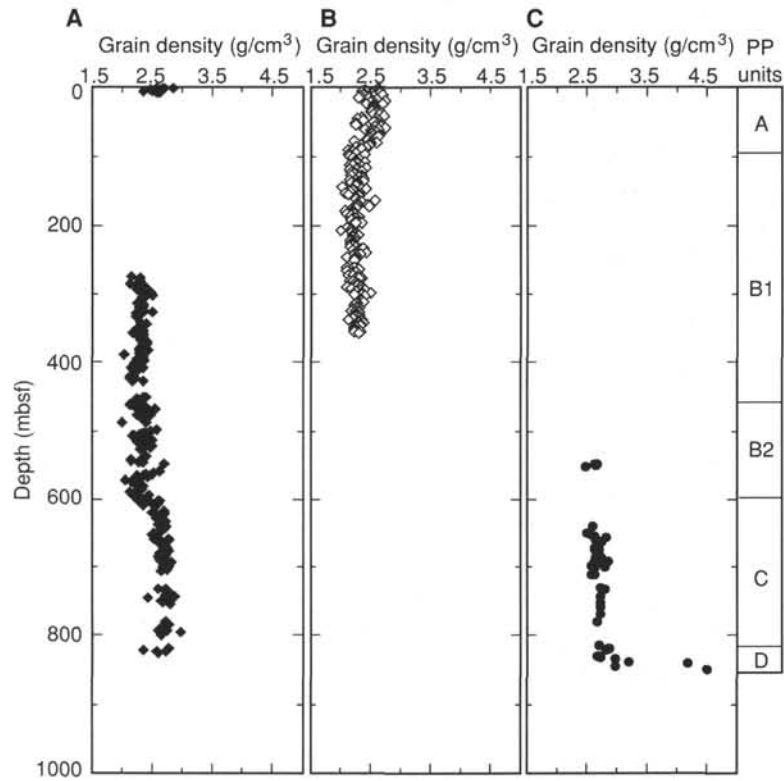


Figure 38. Grain density data vs. depth below seafloor for Holes 883B, 883C, and 883E. The PP Units A, B, C, and D are shown (to the right) and are discussed in the text.

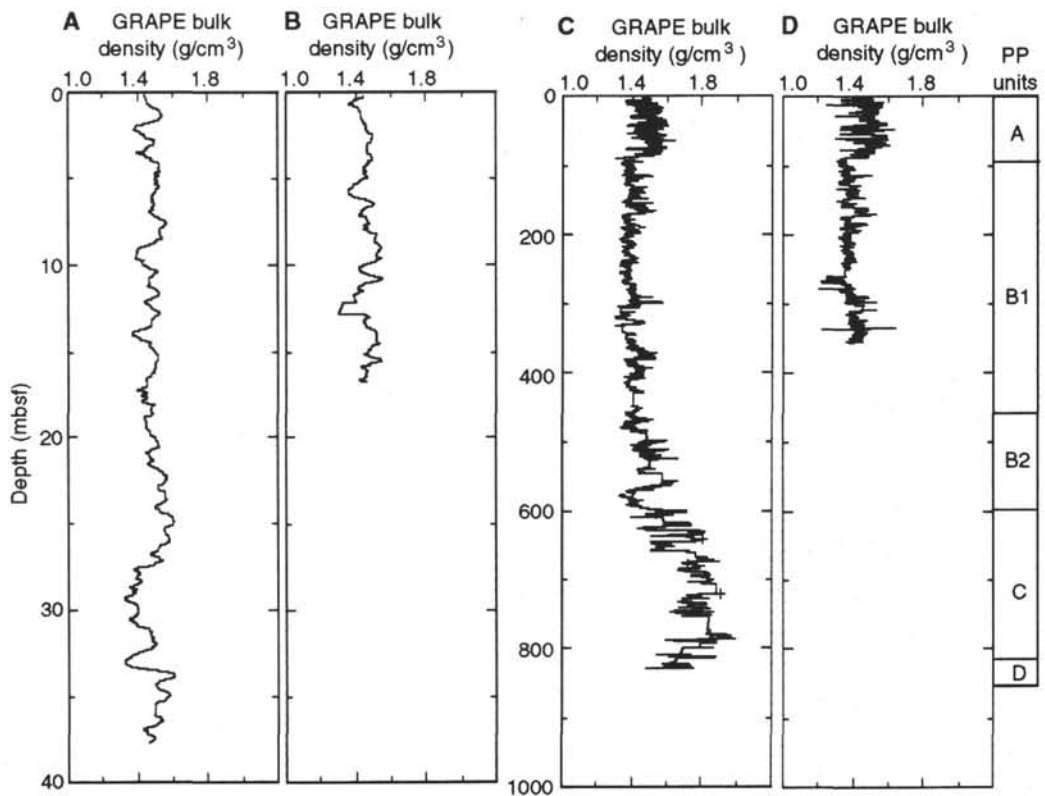


Figure 39. GRAPE bulk density data vs. depth below seafloor for Holes 883A, 883B, 883C, and 883D (note the change in depth scale). The PP Units A, B, C, and D are shown among profiles for Holes 883B and 883C (to the right) and are discussed in the text.

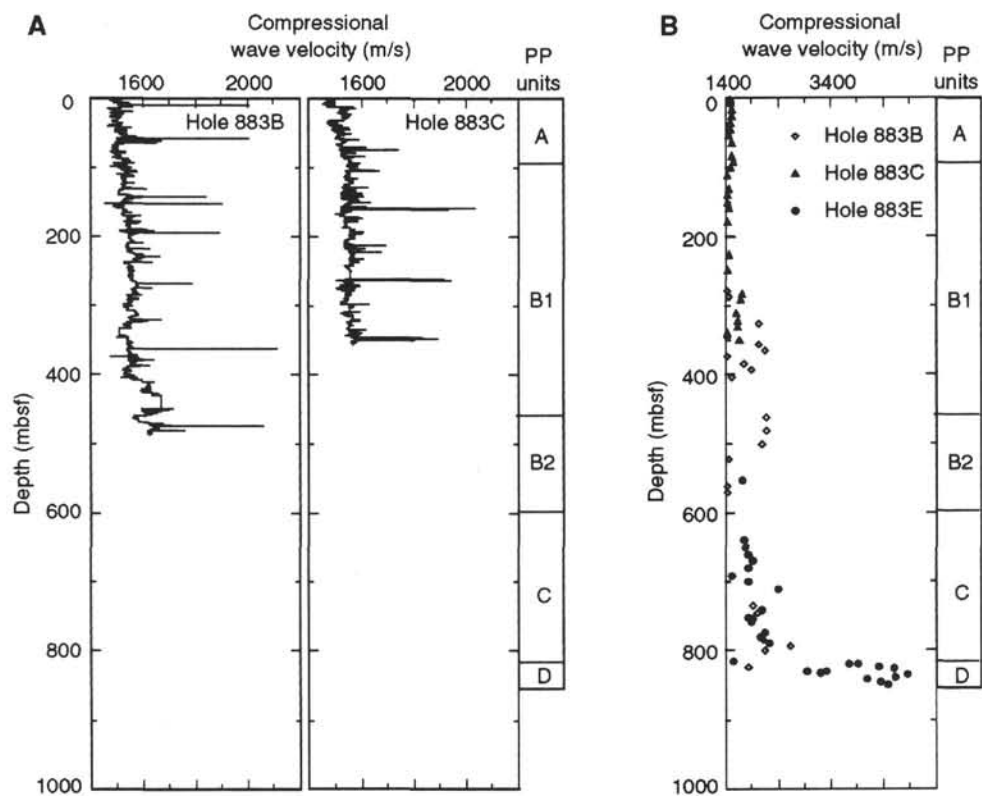


Figure 40. Compressional wave velocity data vs. depth below seafloor. **A.** P-wave logger data from Holes 883B and 883C. The PP Units A, B, C, and D are shown (center) and are discussed in the text. **B.** Hamilton Frame and DSV data from Holes 883B, 883C, and 883E. The PP Units A, B, C, and D are shown (to the right) and are discussed in the text.

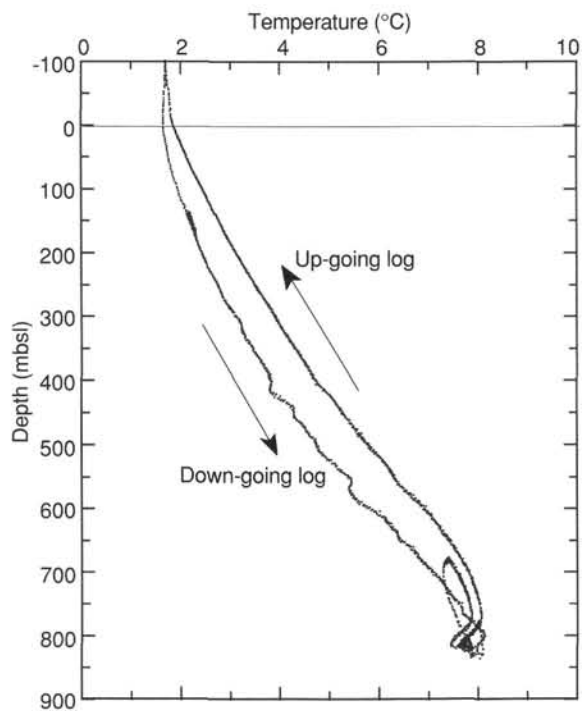


Figure 41. Temperature data recorded by the Lamont temperature logging tool located at the base of the Quad combination tool string.

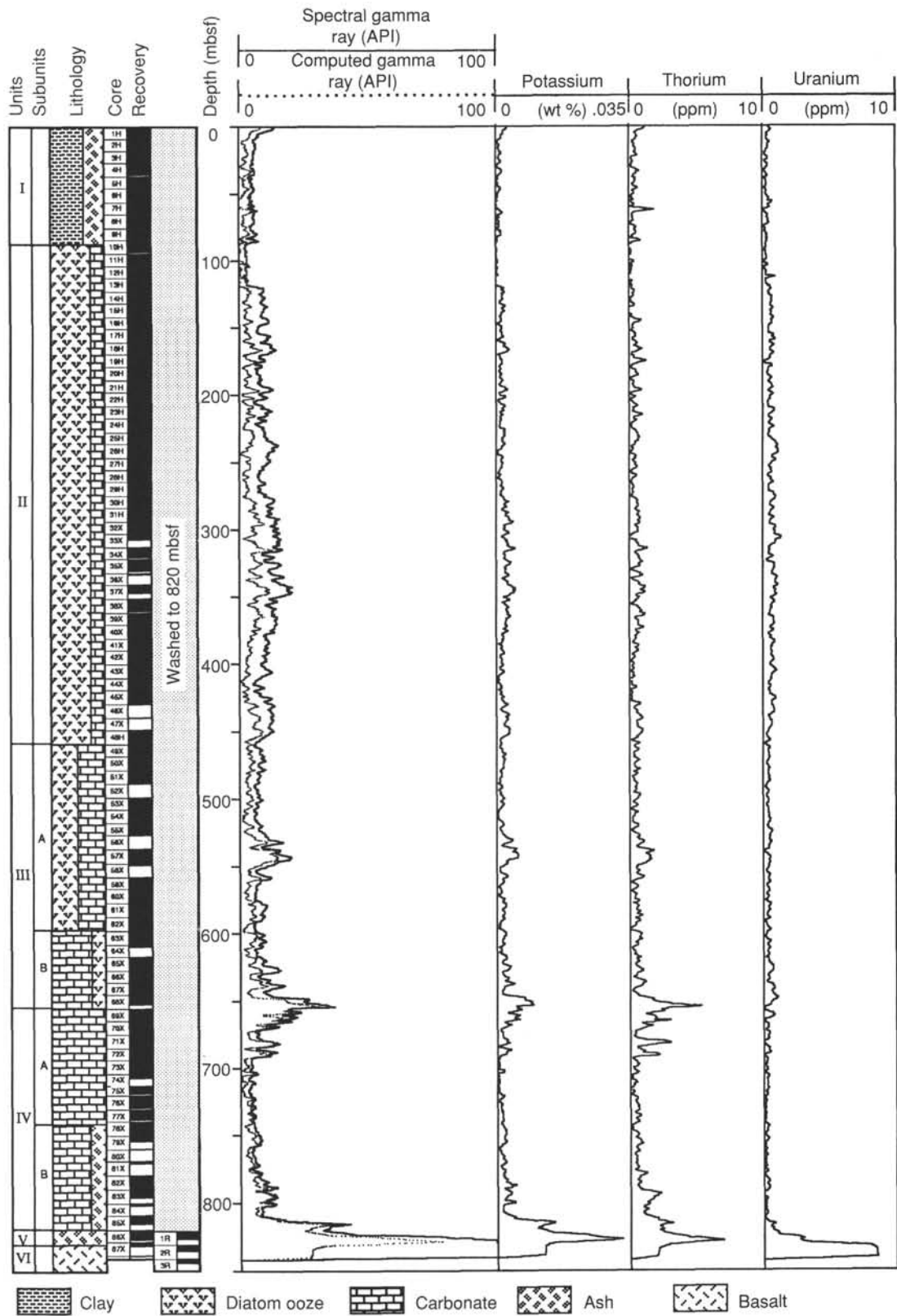


Figure 42. Data from the natural gamma-ray spectrometry tool, recorded on the geochemical tool string.

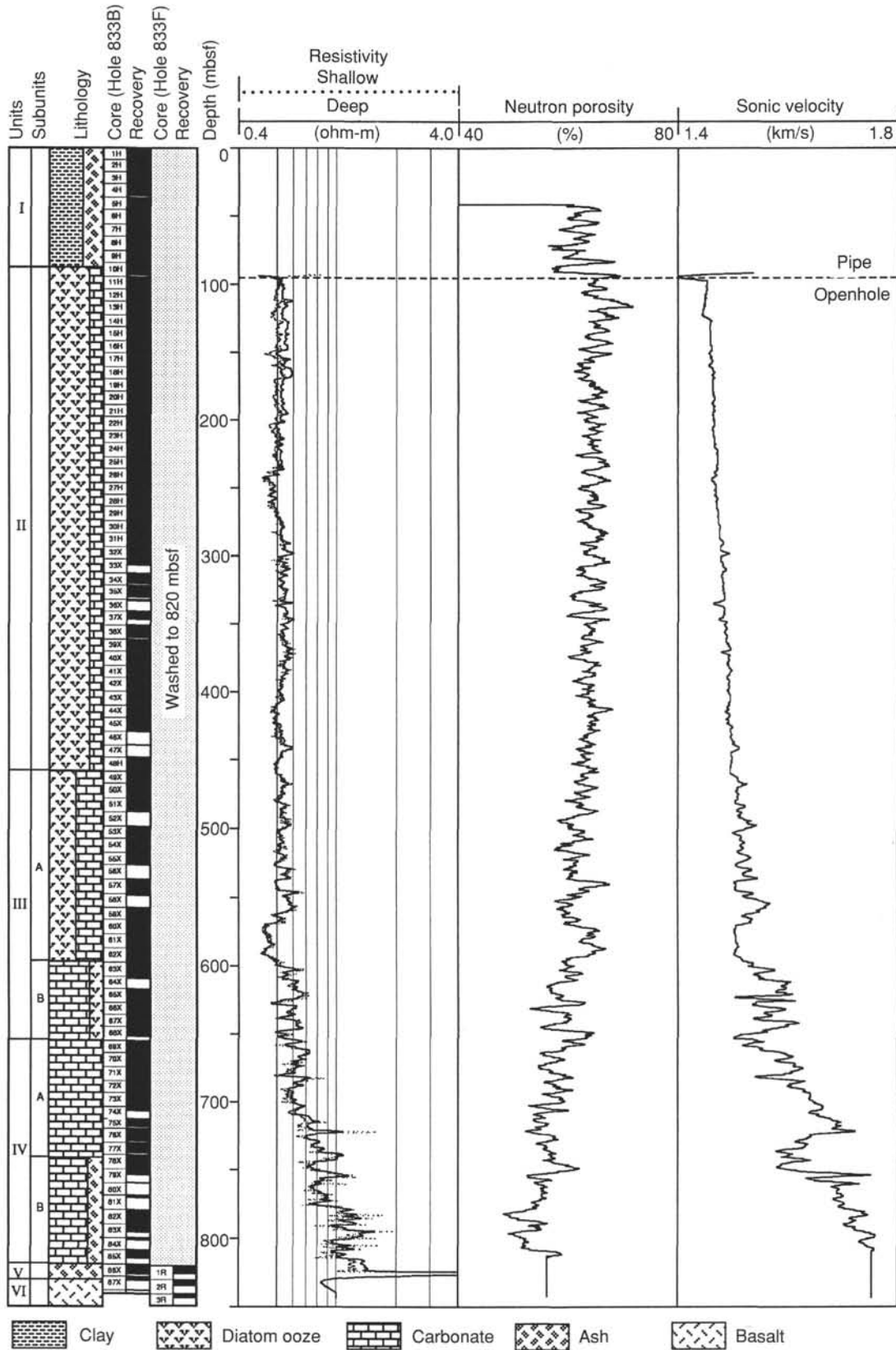


Figure 43. Data from the dual induction, compensated neutron porosity, and sonic velocity tools, recorded on the Quad combination tool string.

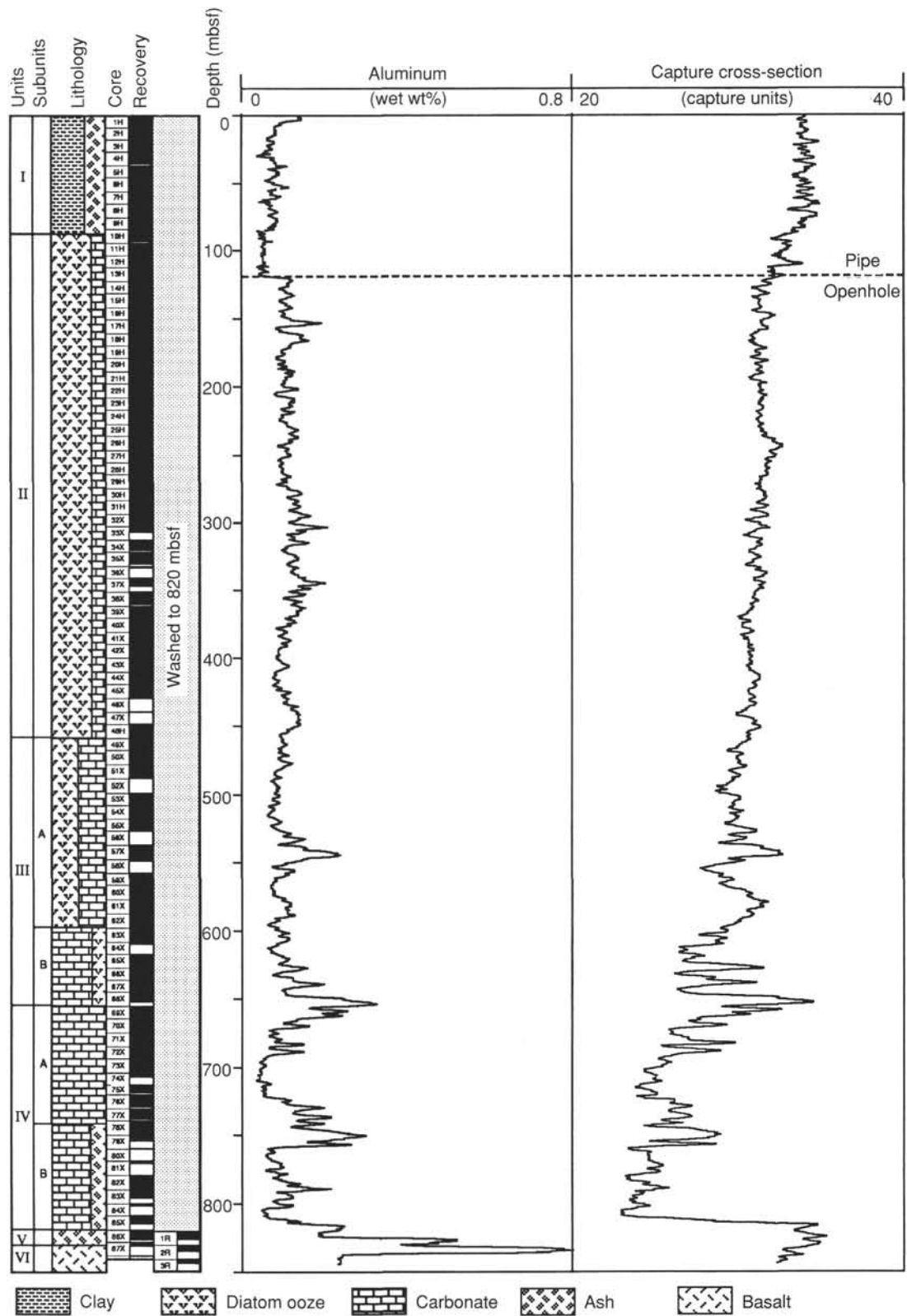


Figure 44. Data from the geochemical tool combination, aluminum yield from the aluminum activation clay tool and neutron capture cross section from the gamma-ray spectrometry tool.

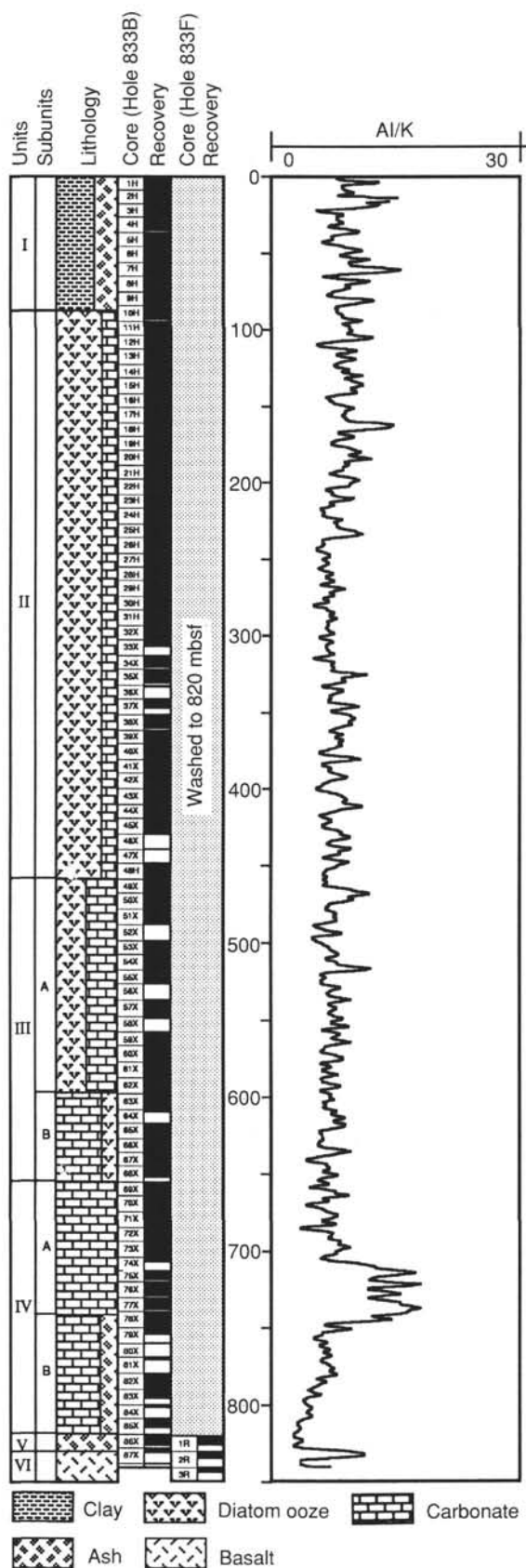


Figure 45. Log of Al/K ratio in the openhole section.

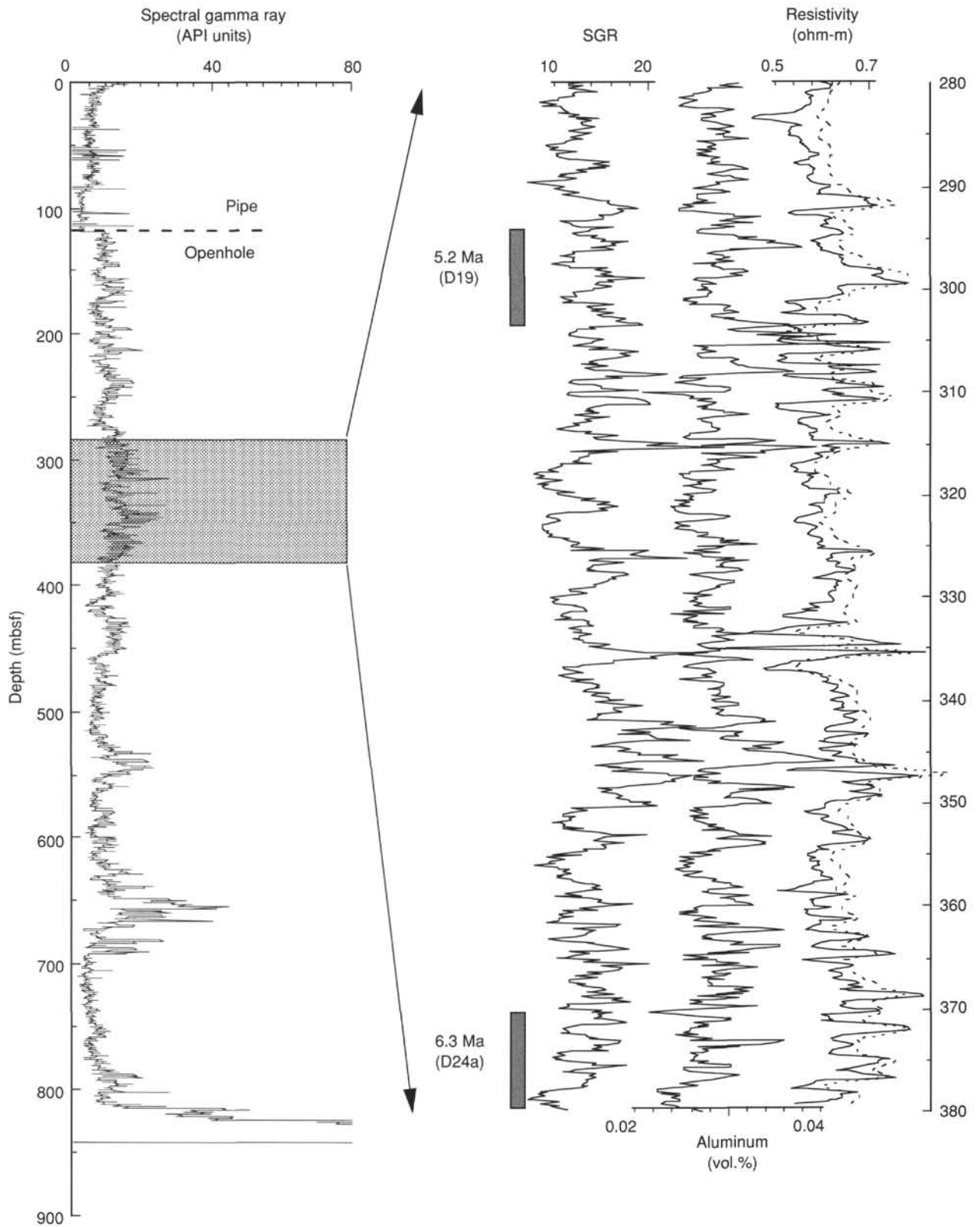


Figure 46. Correlation of total gamma-ray, Al, and resistivity logs.

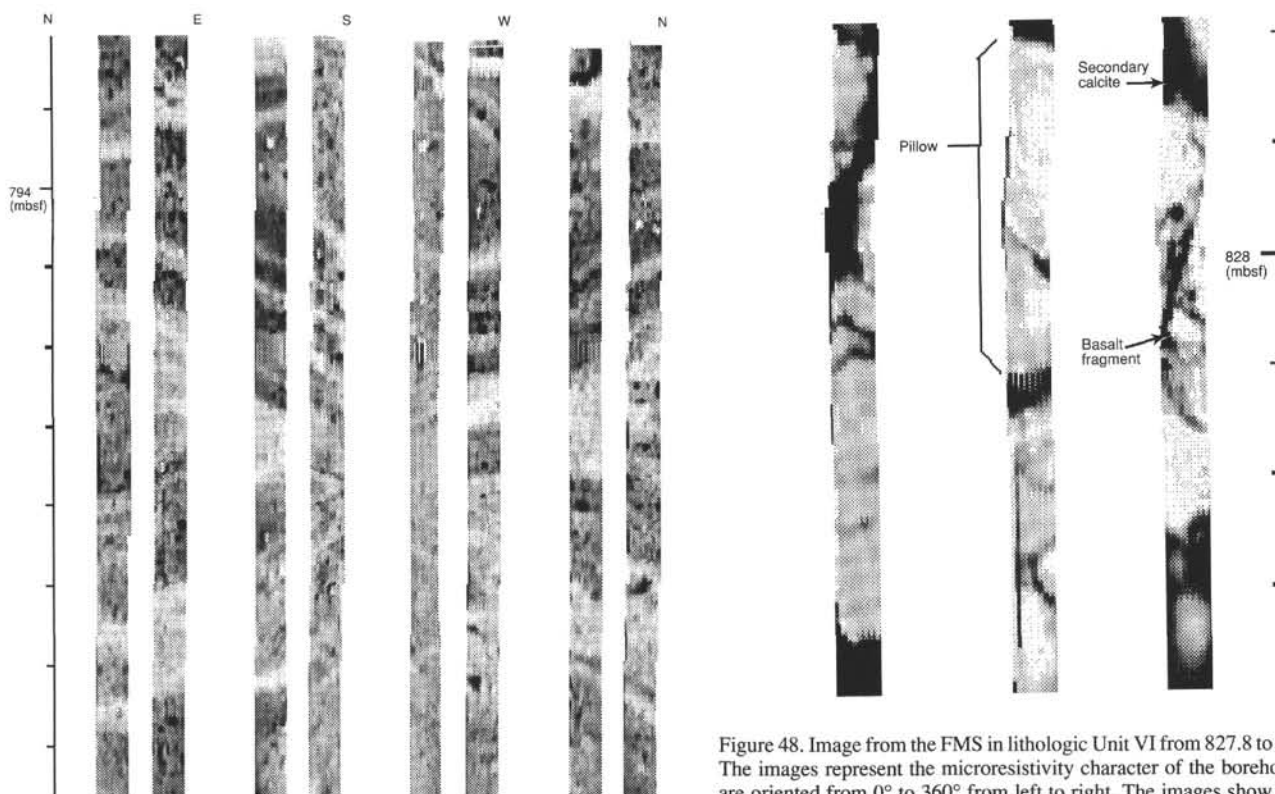


Figure 47. Merged image from the FMS from repeat Passes 2 and 3 over the interval from 793.8 to 794.75 mbsf. The images represent the microresistivity character of the borehole wall and are oriented from 0° to 360° from left to right. This image has been interpreted as representing slump structures within the sediments of lithologic Unit IV.

Figure 48. Image from the FMS in lithologic Unit VI from 827.8 to 828.4 mbsf. The images represent the microresistivity character of the borehole wall and are oriented from 0° to 360° from left to right. The images show dark pillow basalt structures and the more resistive secondary calcite (white) filling in the voids and fractures.

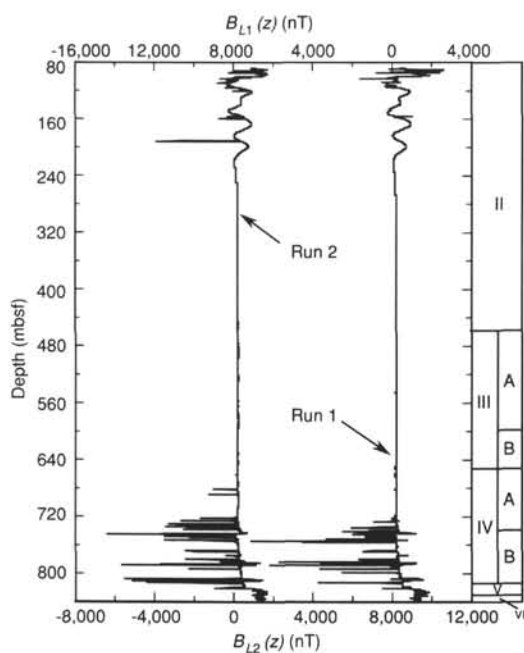


Figure 49. Plot of "local" total induction B_L ("B field", see text) vs. depth in Hole 883F for Runs 1 and 2. As a reference, the boundaries between the main lithologic units (II through VI), as defined from Hole 883B, are shown on the right. The local part of the total induction was obtained by correcting the total induction for the main dipolar field; scale shift between runs is 9000 nT.

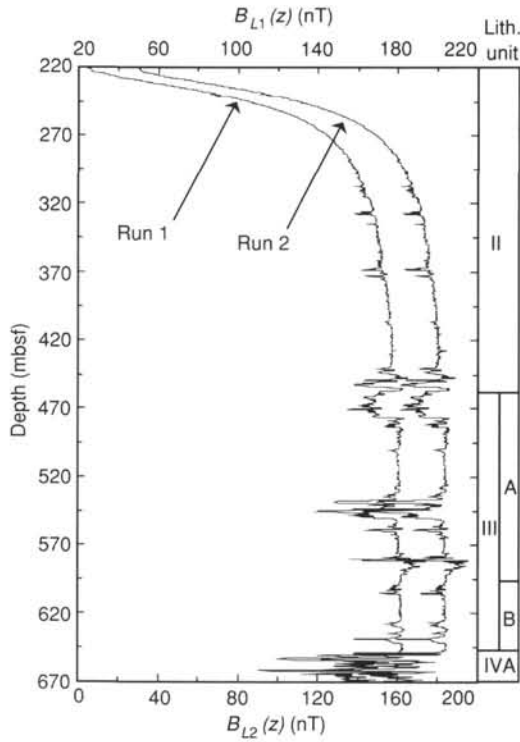


Figure 50: Detailed view of the "local" B field (B_L) between 220 and 670 mbsf in Hole 883F for Runs 1 and 2; scale shift between runs is 20 nT. As a reference, the boundaries between the main lithologic units (II through IV), as defined from Hole 883B, are shown on the right.

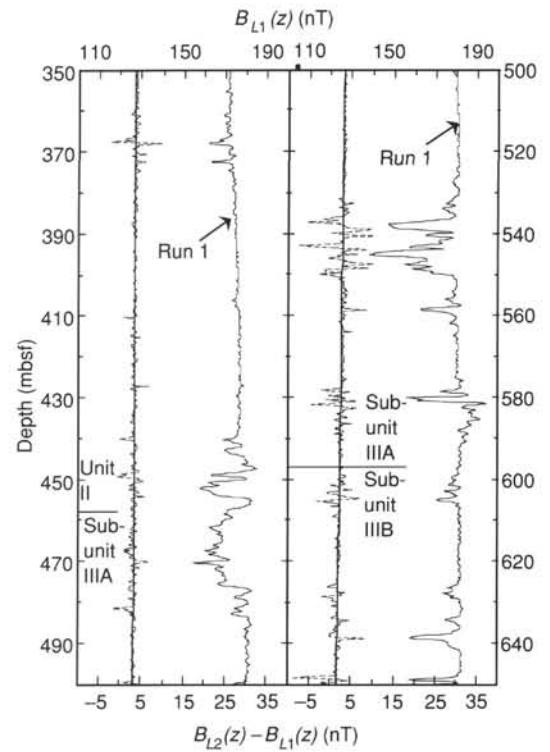


Figure 52: Close up of the "local" B field (B_L) between 350 and 650 mbsf in Hole 883F for Run 1 and the difference ($B_{L2} - B_{L1}$) between the two runs, with location of the boundaries between the main lithologic units (II through III), as

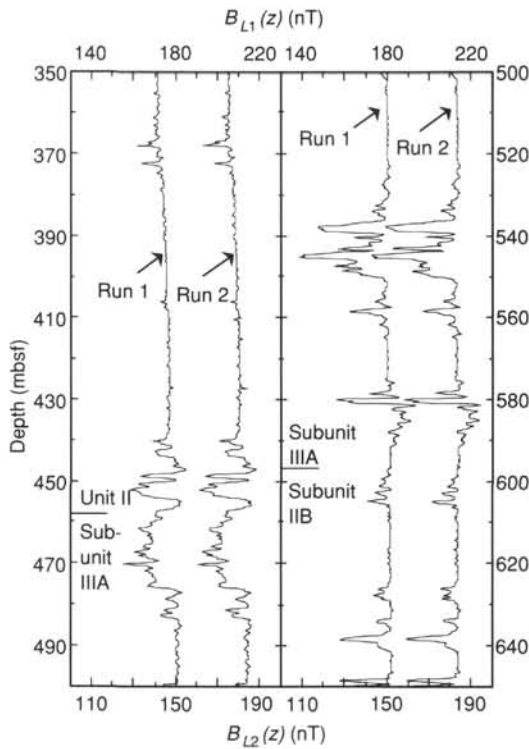


Figure 51: Close-up of the "local" B field (B_L) between 350 and 650 mbsf in Hole 883F for Runs 1 and 2, with location of the boundaries between the main lithologic units (II through III), as defined from Hole 883B; scale shift between runs is 30 nT.

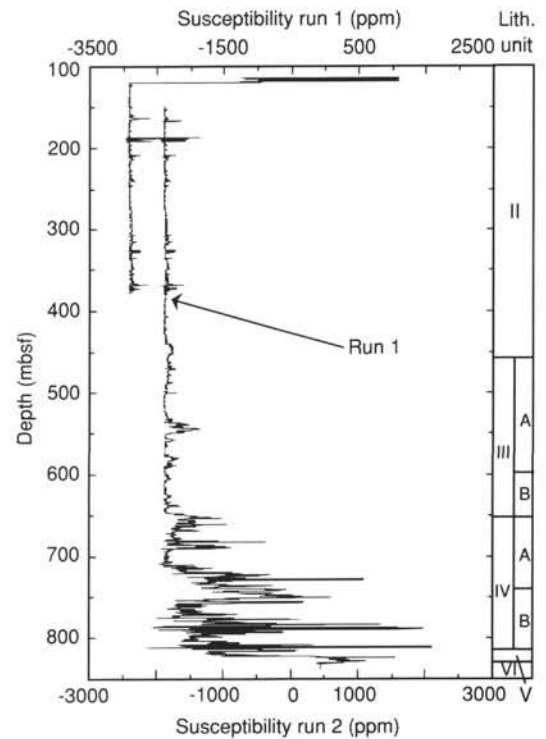


Figure 53: Plot of susceptibility vs. depth in Hole 883F for the main log and the partial repeat section; scale shift between runs is 500 ppm. As a reference, the boundaries between the main lithologic units (II through VI), as defined from Hole 883B, are shown on the right.

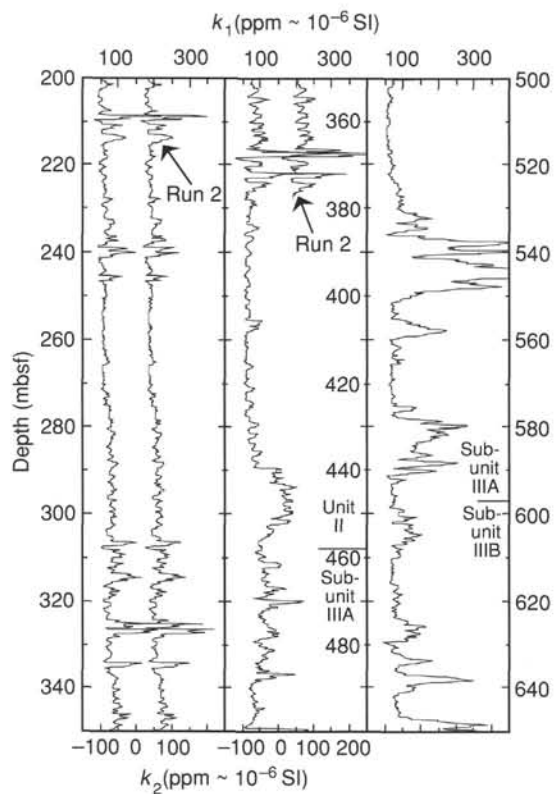


Figure 54. Detailed evolution between 200 and 650 mbsf of susceptibility for the main log and the partial repeat section (corrected for a -2450 ppm offset) in Hole 883F, with location of the boundaries between the main lithologic units (II through III), as defined from Hole 883B; scale shift between runs is 50 ppm.

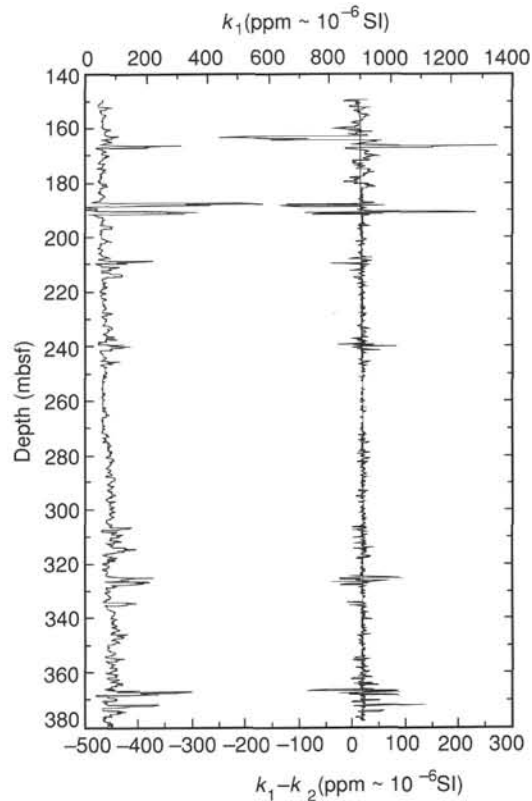


Figure 55. Detailed evolution in Hole 883F between 140 and 380 mbsf of susceptibility for the main log (corrected for a -2450 ppm offset) and difference $k_1 - k_2$, with the partial repeat section.

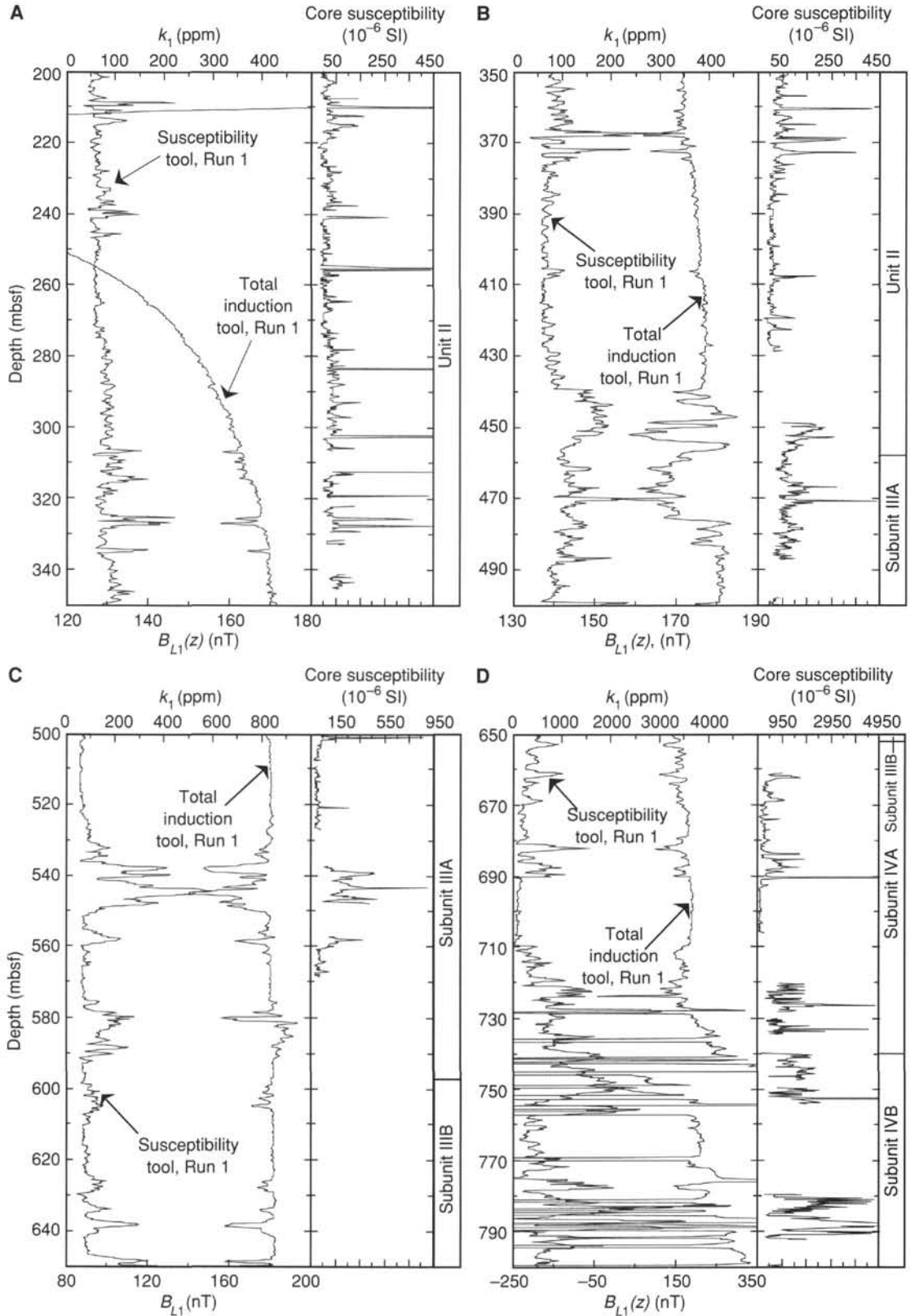


Figure 56. Detailed comparative evolution of susceptibility (corrected for a -2450 ppm offset), "local" B field B_{L1} (Run 1) in Hole 883F and susceptibility values obtained from core measurements in Hole 883B with location of the boundaries between the main lithologic units (II through IV), as defined from Hole 883B. In all plots, the relative full scales are preserved, while the width for logging data full scale is double of the one for core measurements. **A.** 200–350 mbsf; full-scale is 500 ppm, 60 nT, and 500 10^{-6} SI units. **B.** 350–500 mbsf; full-scale is 500 ppm, 60 nT, and 500 10^{-6} SI units. **C.** 500–650 mbsf; full-scale is 1000 ppm, 120 nT, and 1000 10^{-6} SI units. **D.** 650–800 mbsf; full-scale is 5000 ppm, 600 nT, and 5000 10^{-6} SI units.

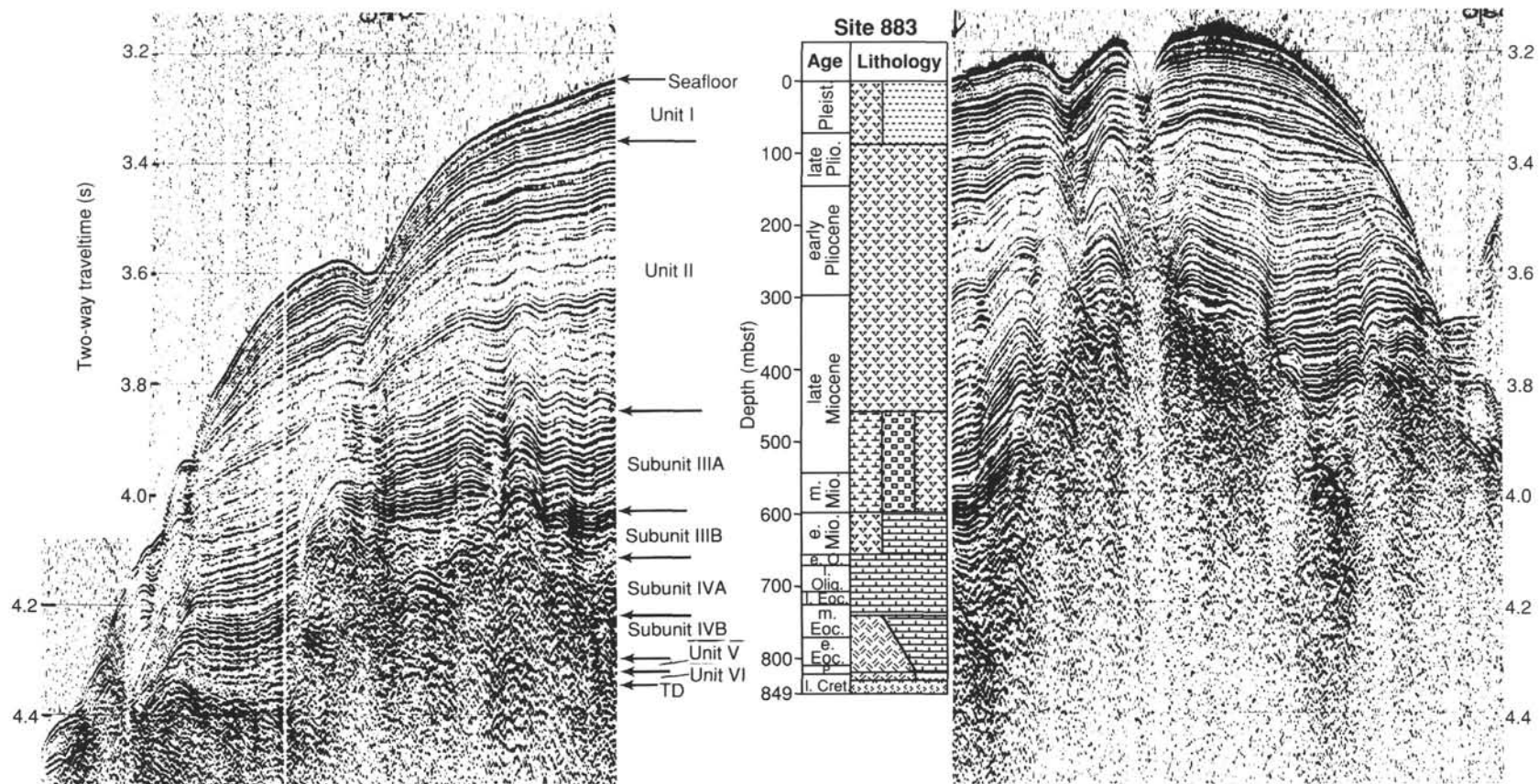
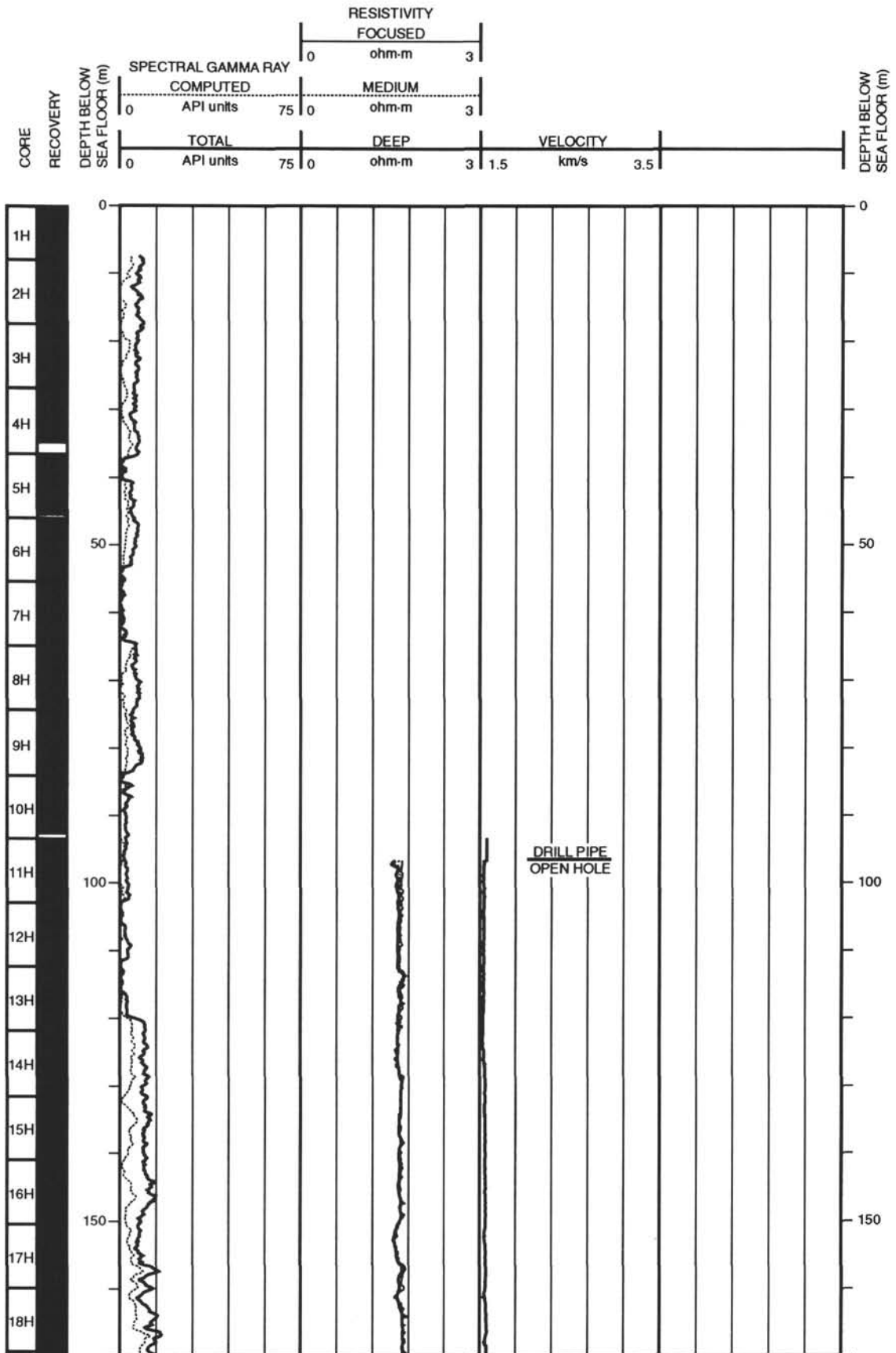
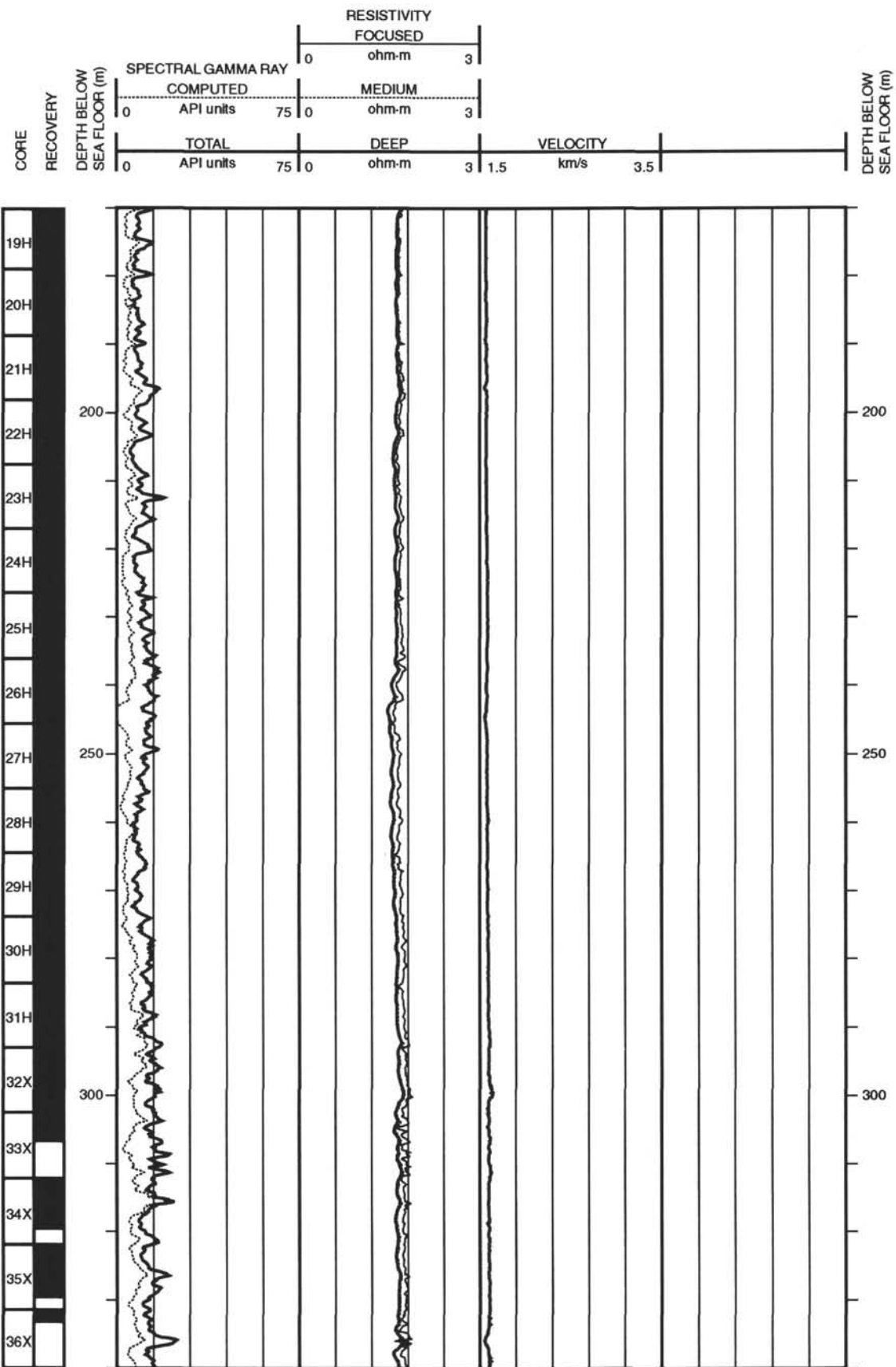


Figure 57. Seismic reflection profile from the site-survey, 1988 Roundabout cruise of the *Thomas Washington* crossing the location of Site 883. Line trends east-westerly; west is to the right. The depth ranges of lithologic Units I through V are indicated on the profile inset. Lithologic Unit VI is basaltic basement.

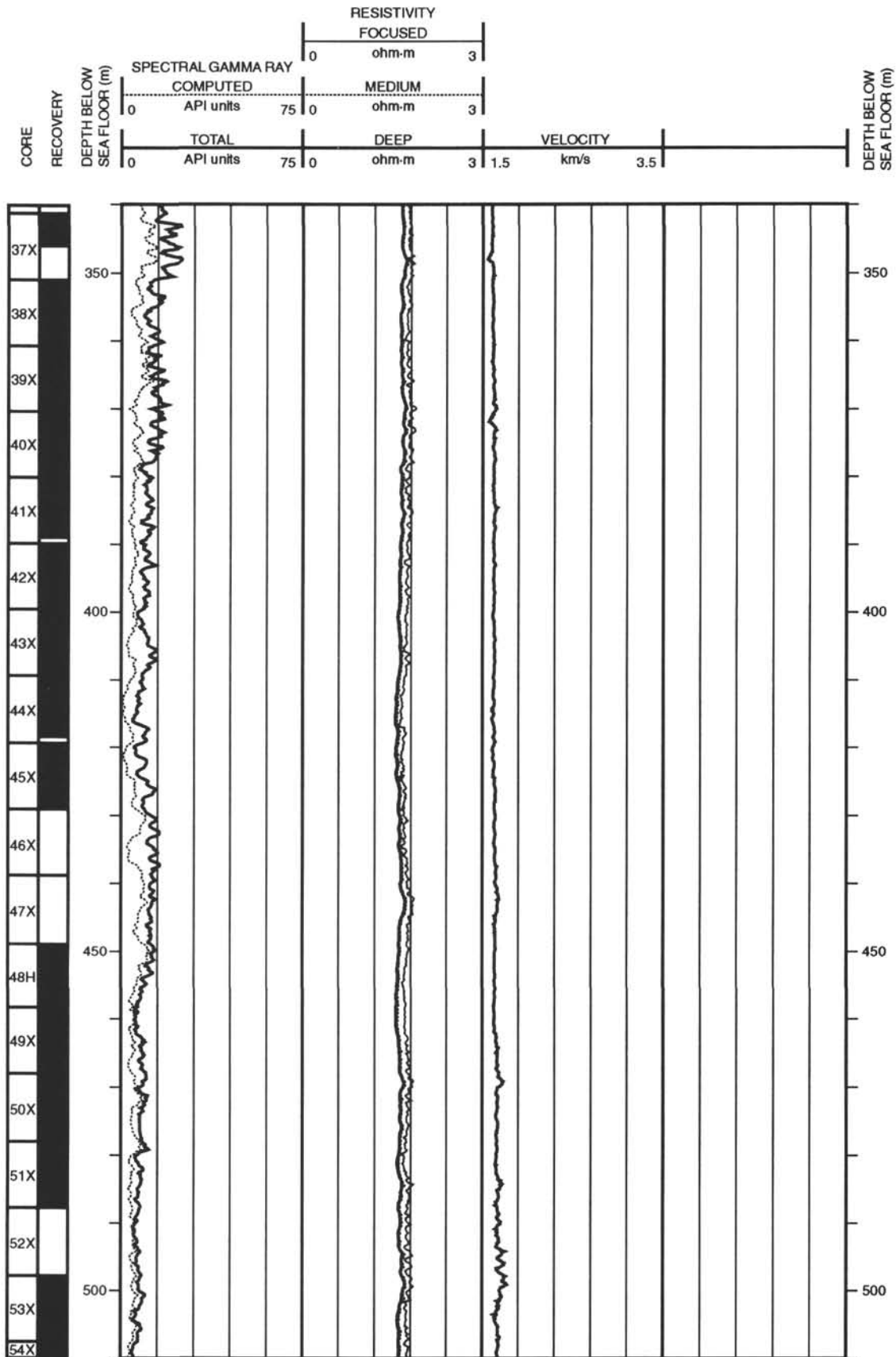
Hole 883F: Resistivity-Velocity-Natural Gamma Ray Log Summary



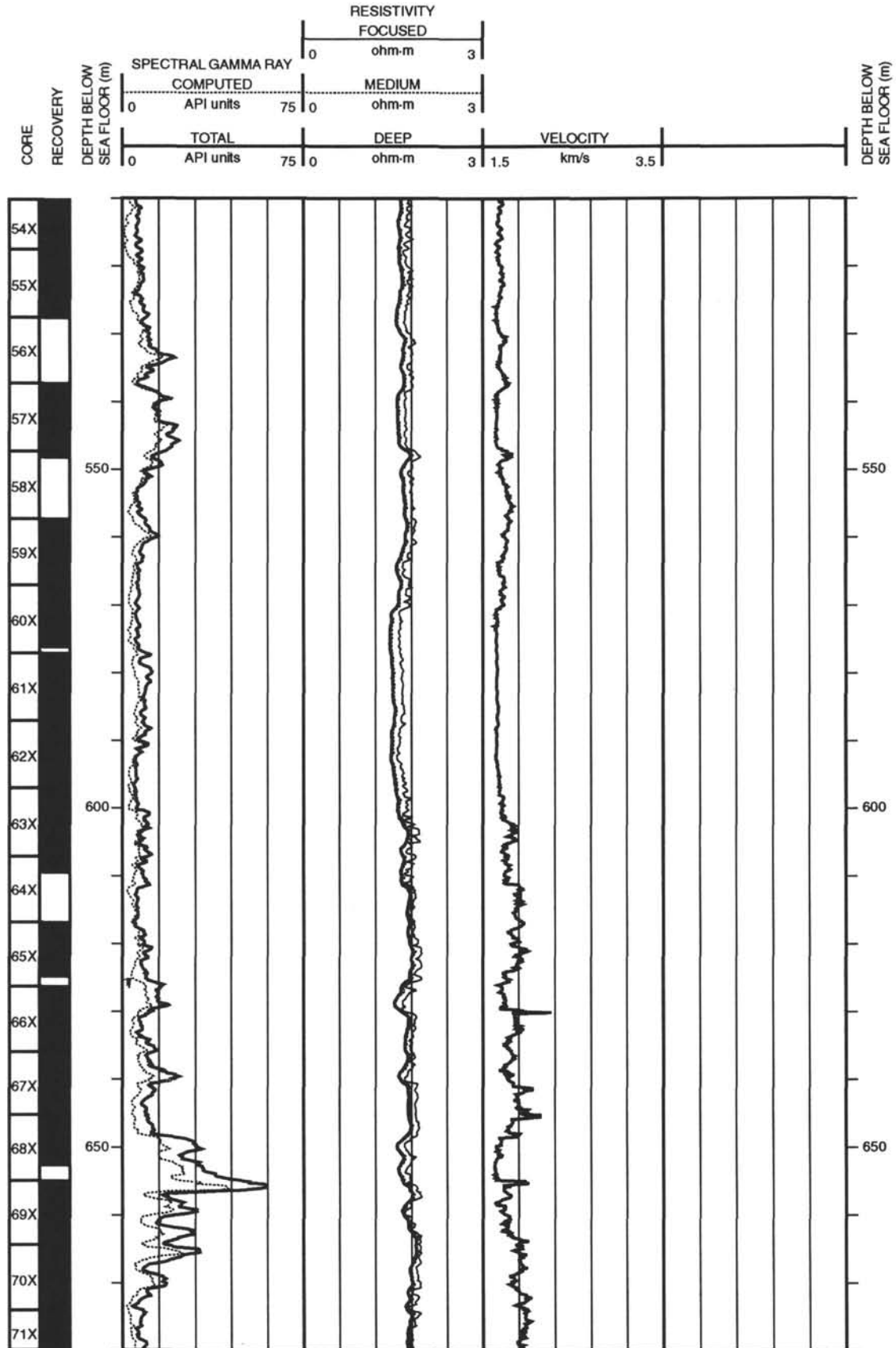
Hole 883F: Resistivity-Velocity-Natural Gamma Ray Log Summary (continued)



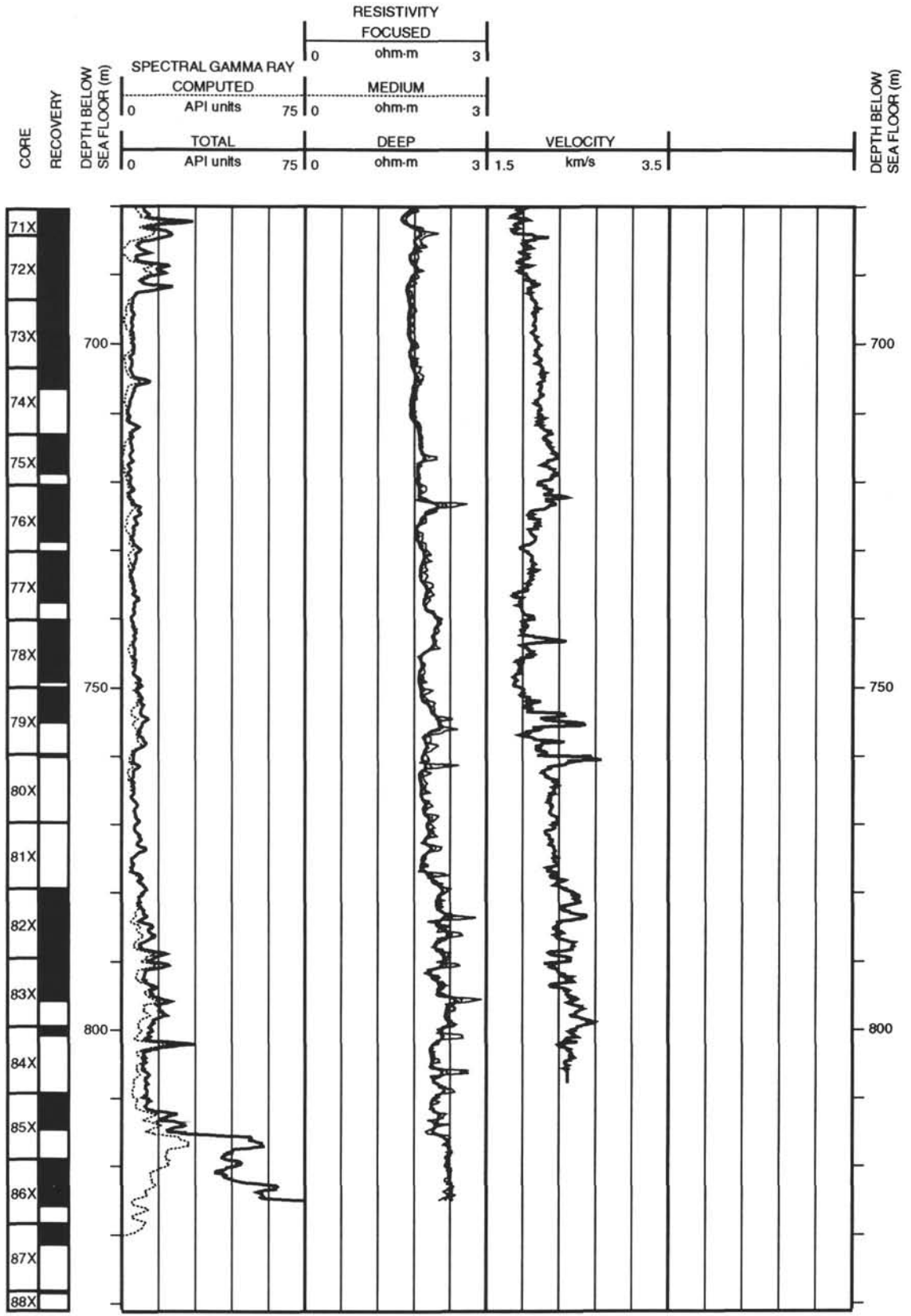
Hole 883F: Resistivity-Velocity-Natural Gamma Ray Log Summary (continued)



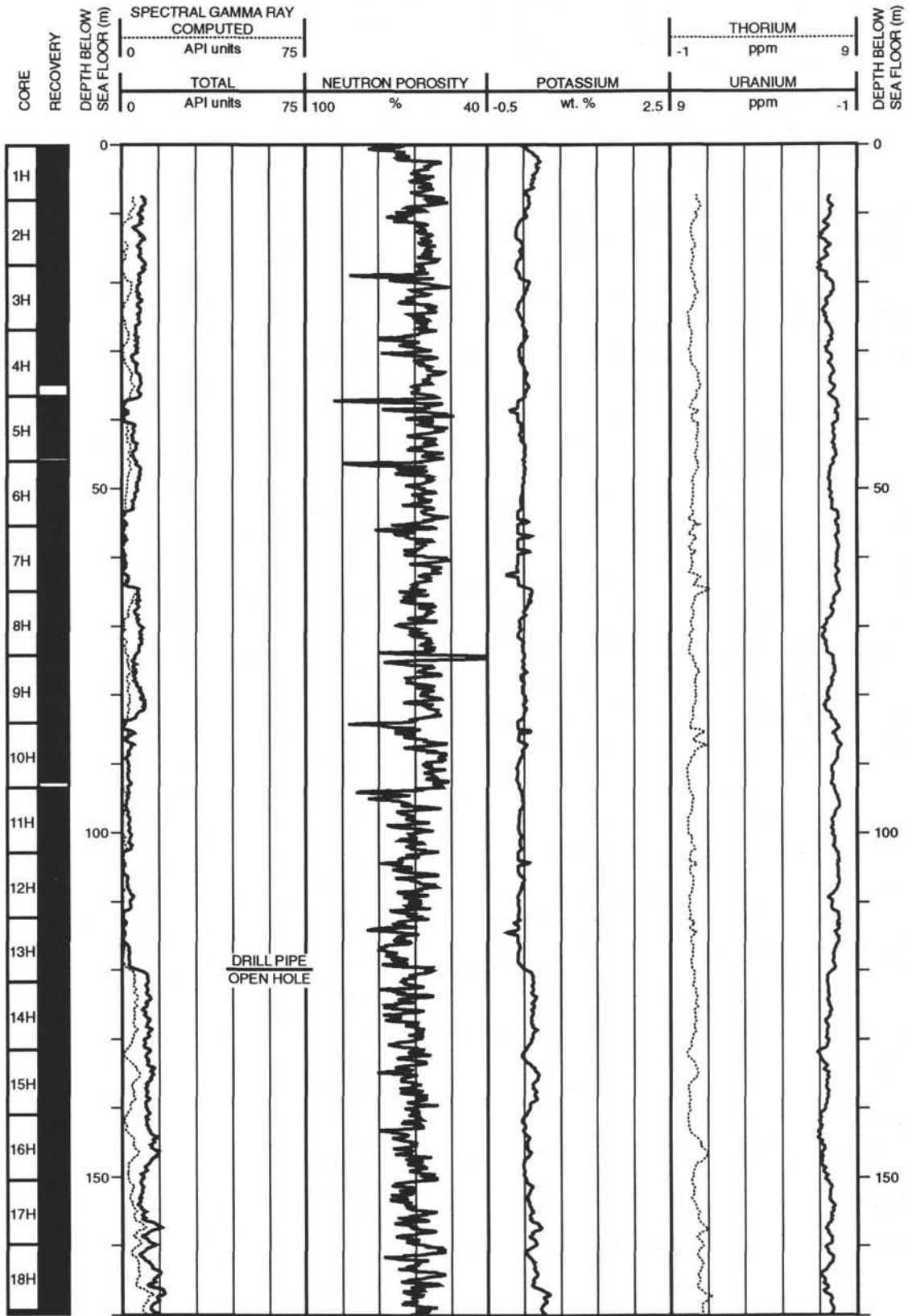
Hole 883F: Resistivity-Velocity-Natural Gamma Ray Log Summary (continued)



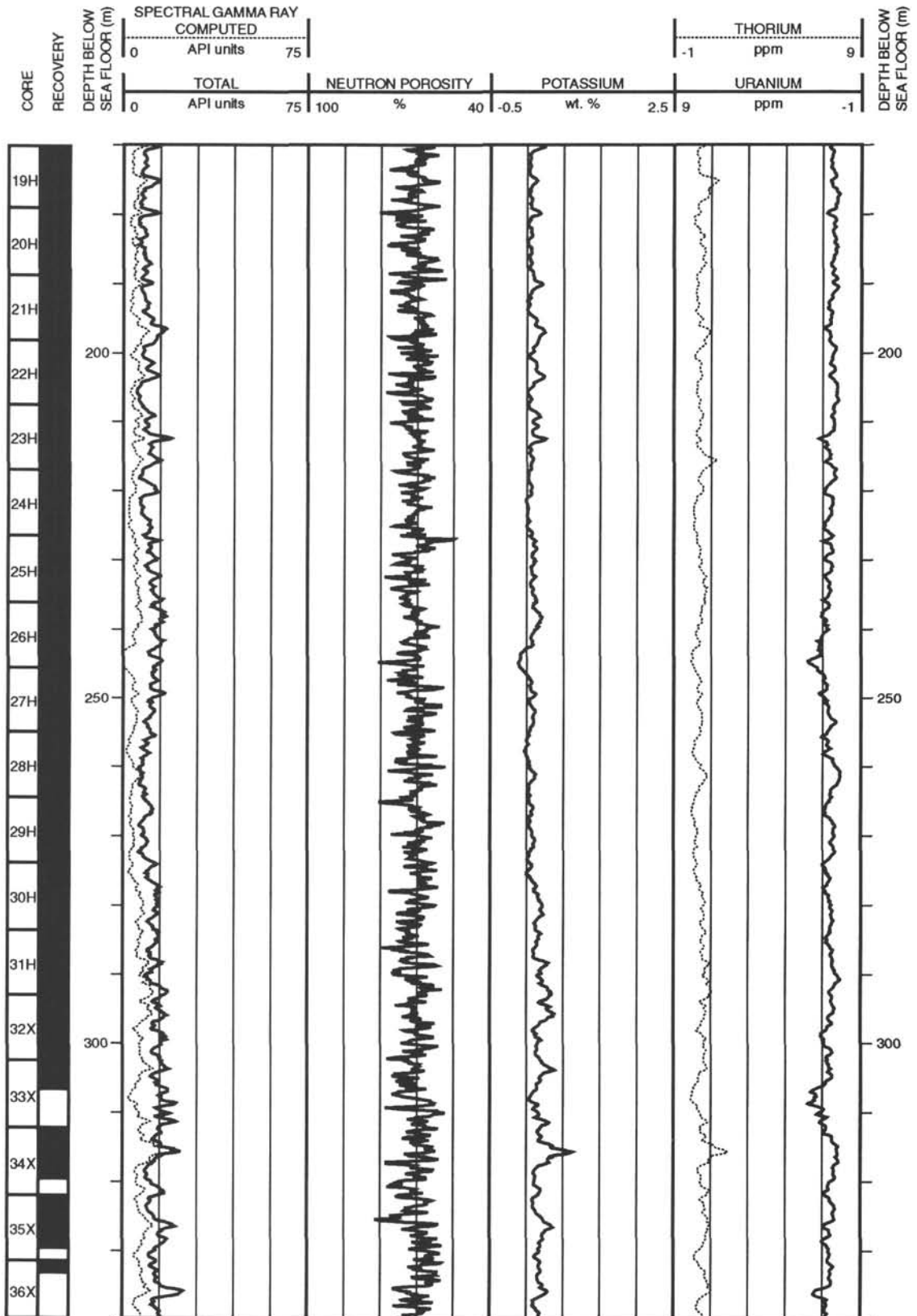
Hole 883F: Resistivity-Velocity-Natural Gamma Ray Log Summary (continued)



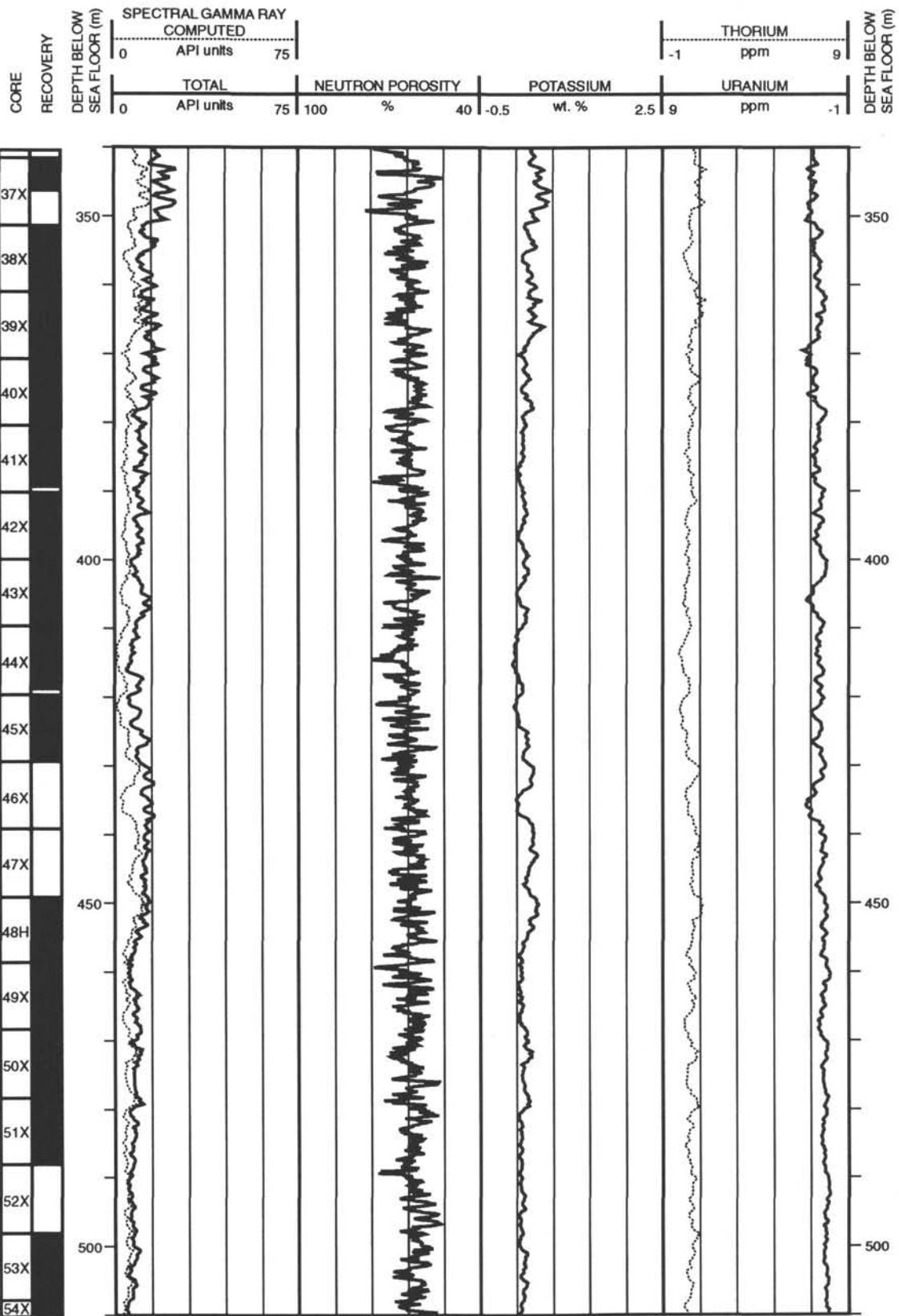
Hole 883F: Porosity-Natural Gamma Ray Log Summary



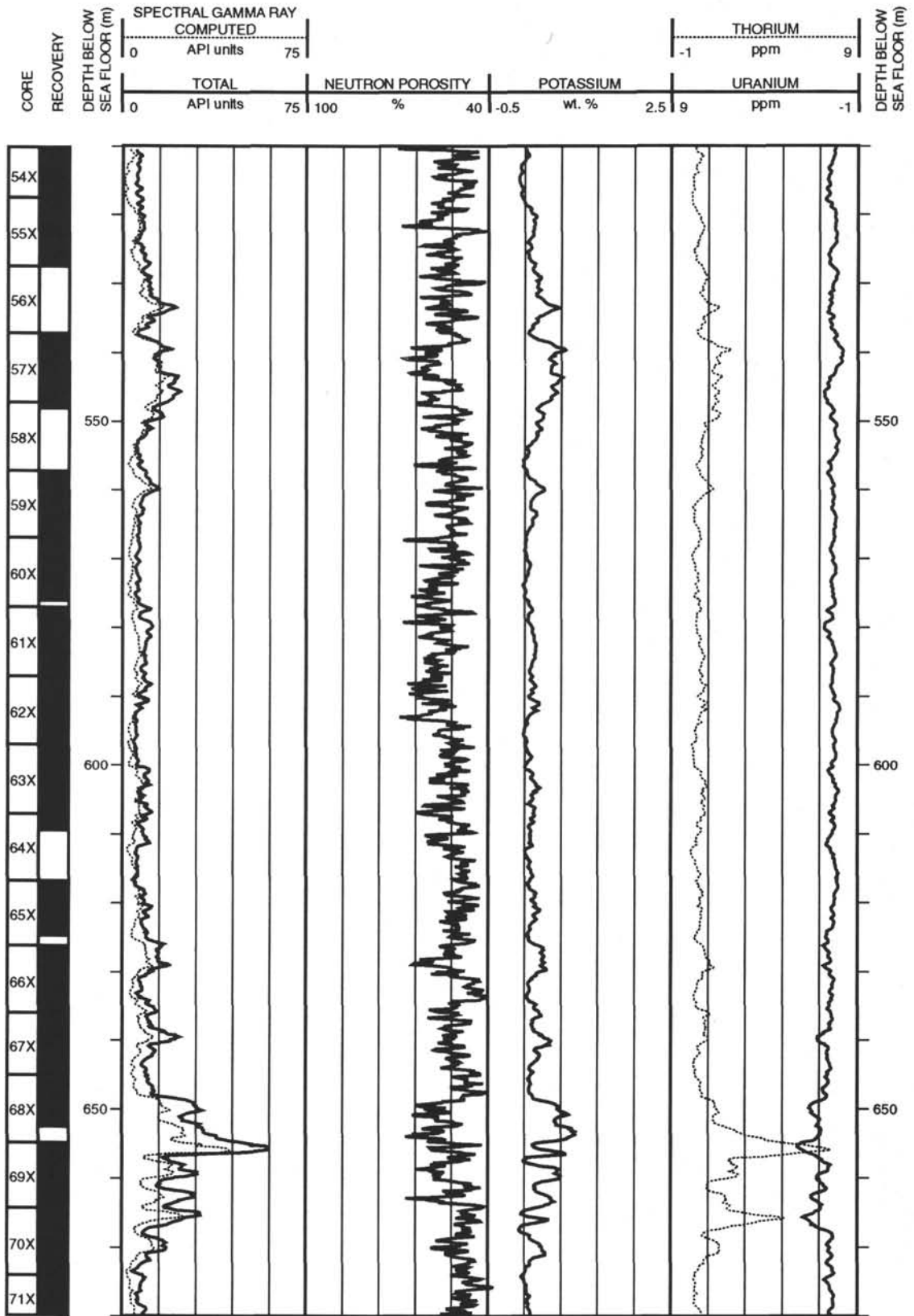
Hole 883F: Porosity-Natural Gamma Ray Log Summary (continued)



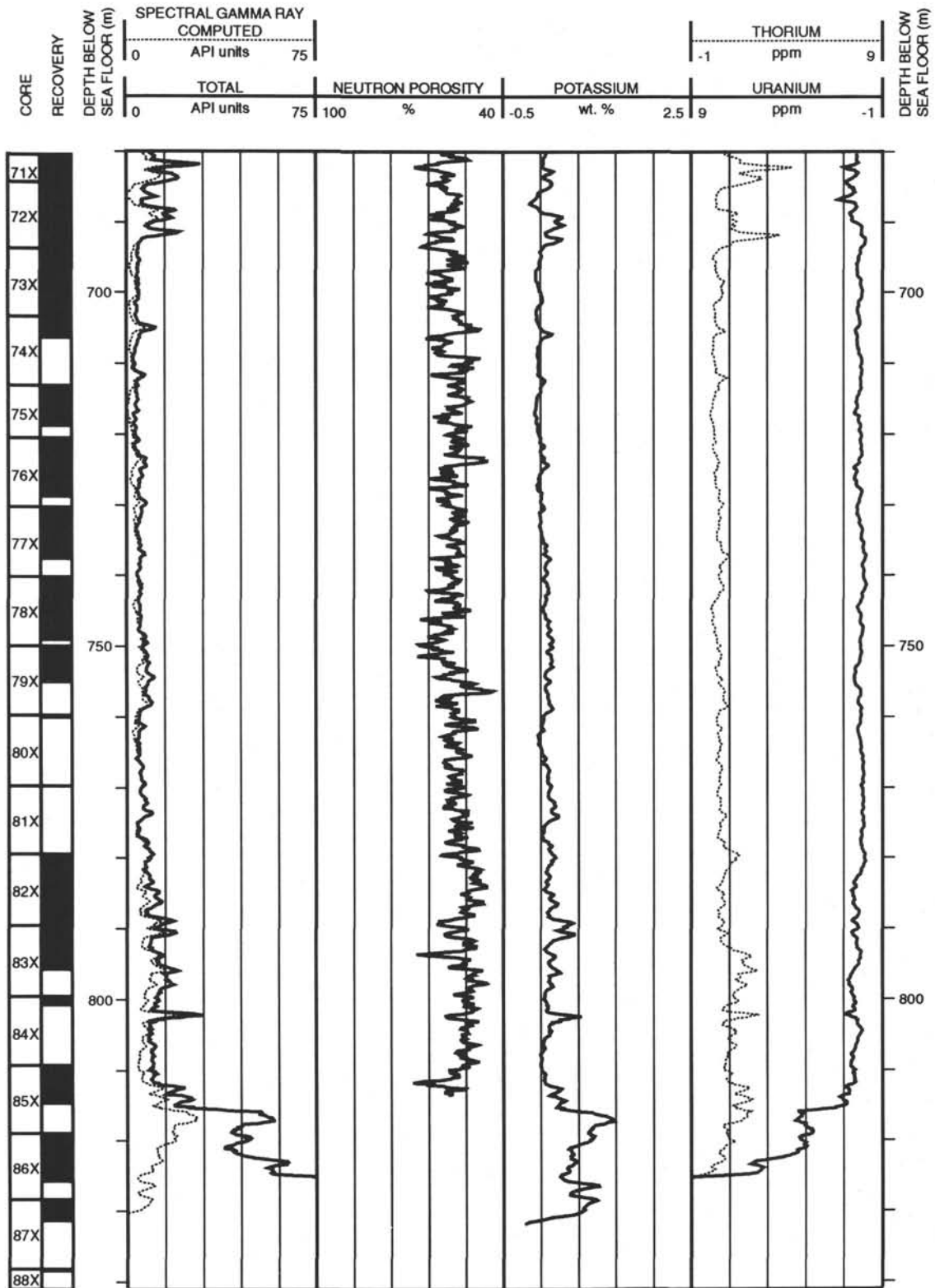
Hole 883F: Porosity-Natural Gamma Ray Log Summary (continued)



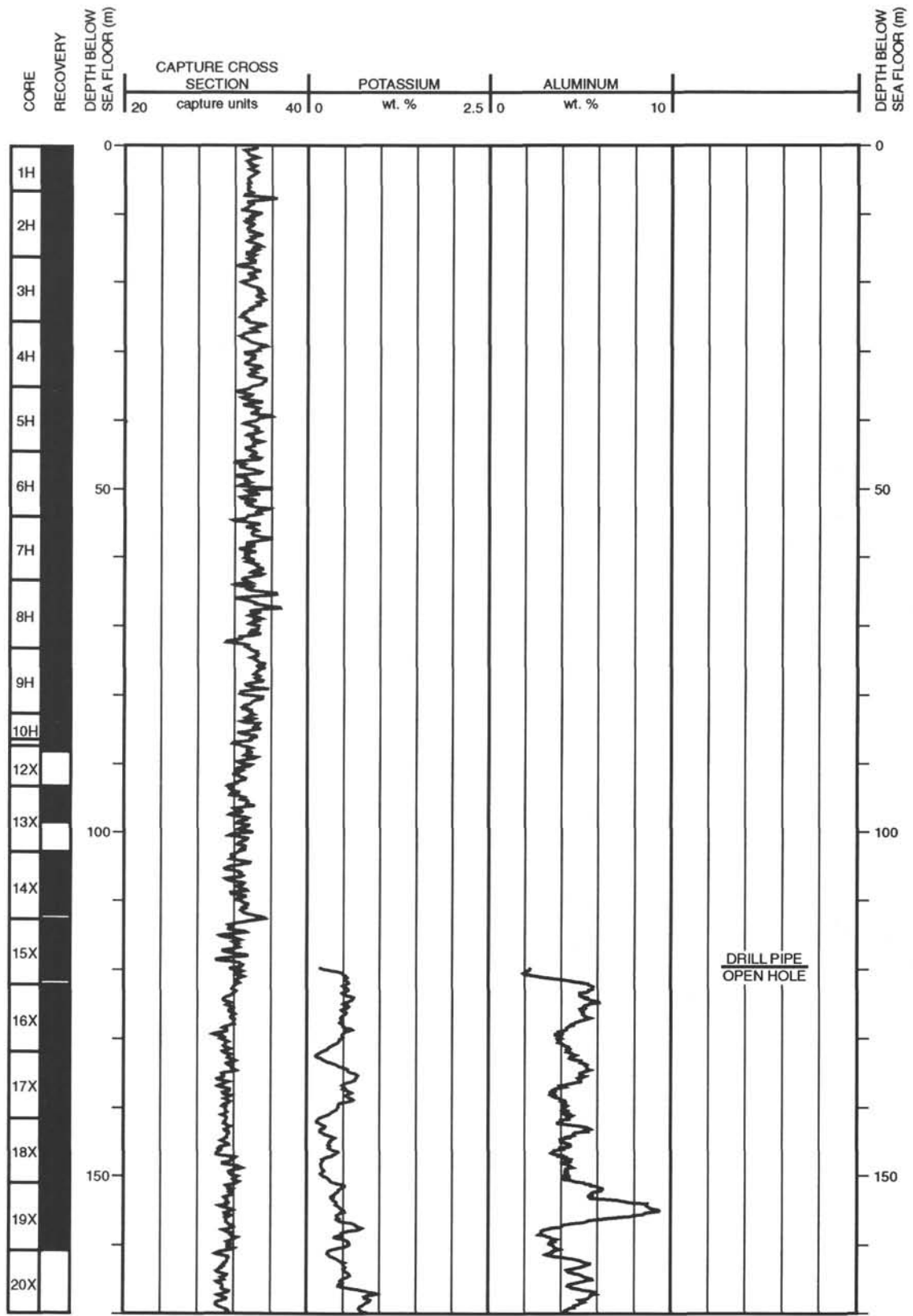
Hole 883F: Porosity-Natural Gamma Ray Log Summary (continued)



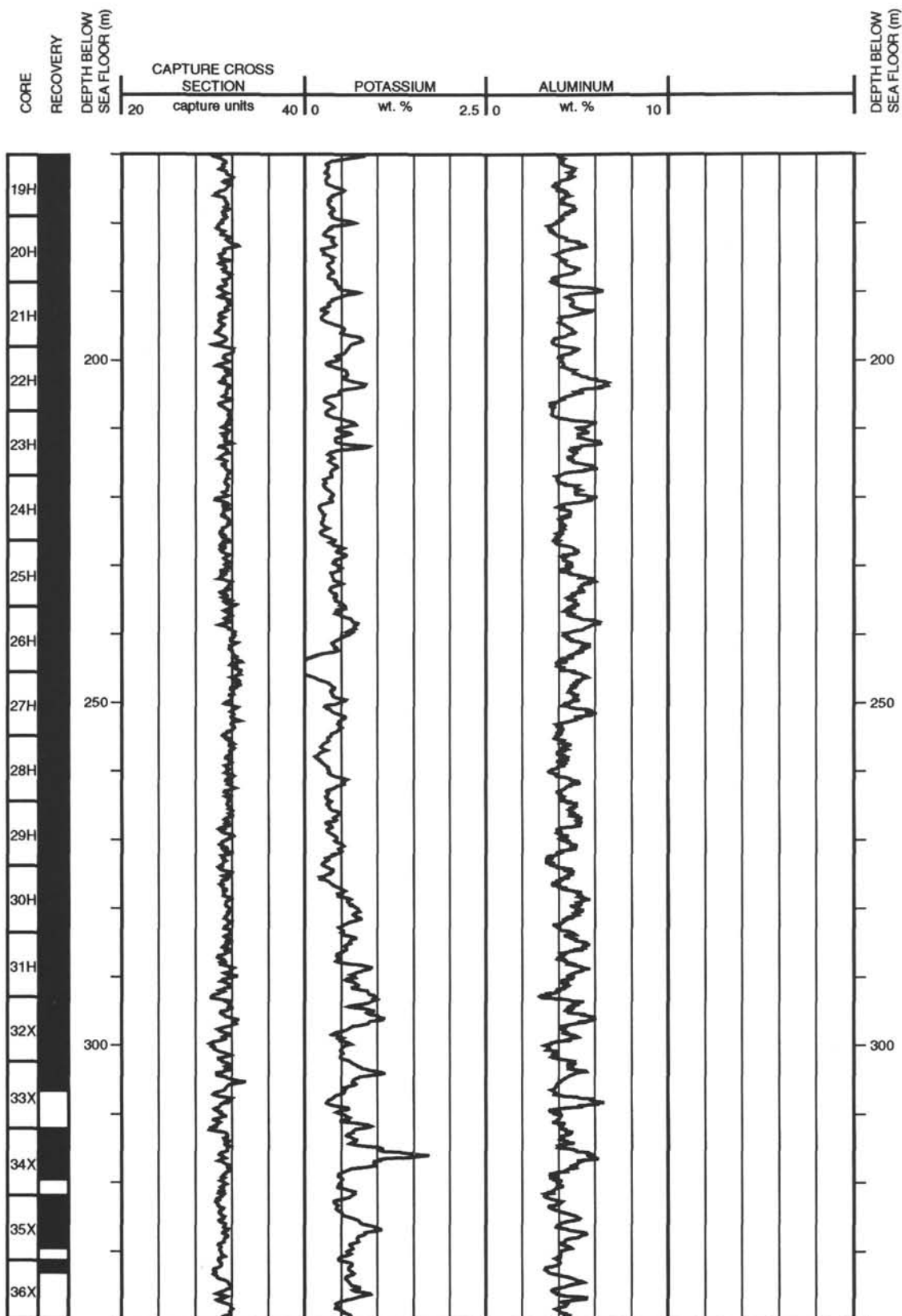
Hole 883F: Porosity-Natural Gamma Ray Log Summary (continued)



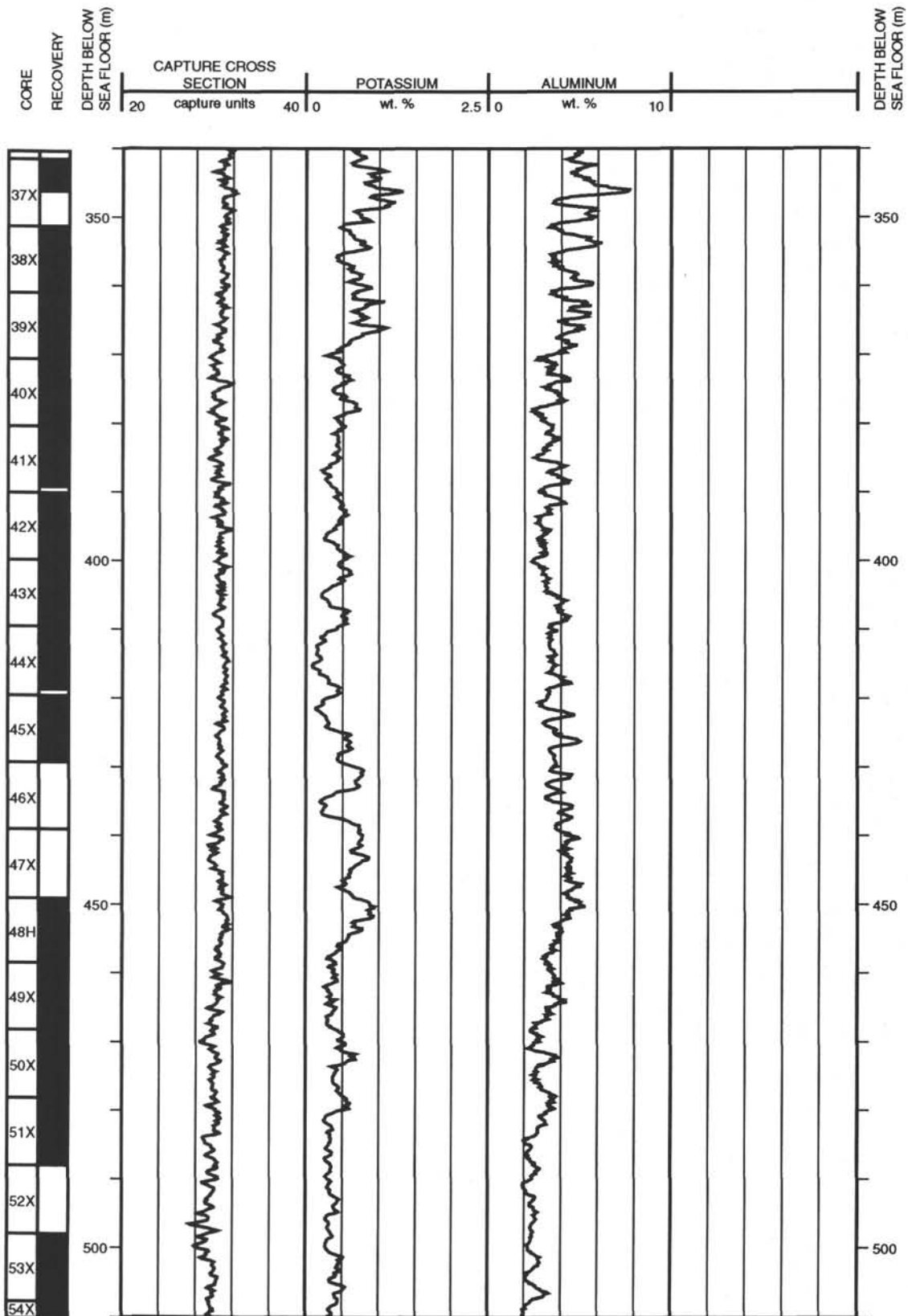
Hole 883F: Geochemical Log Summary



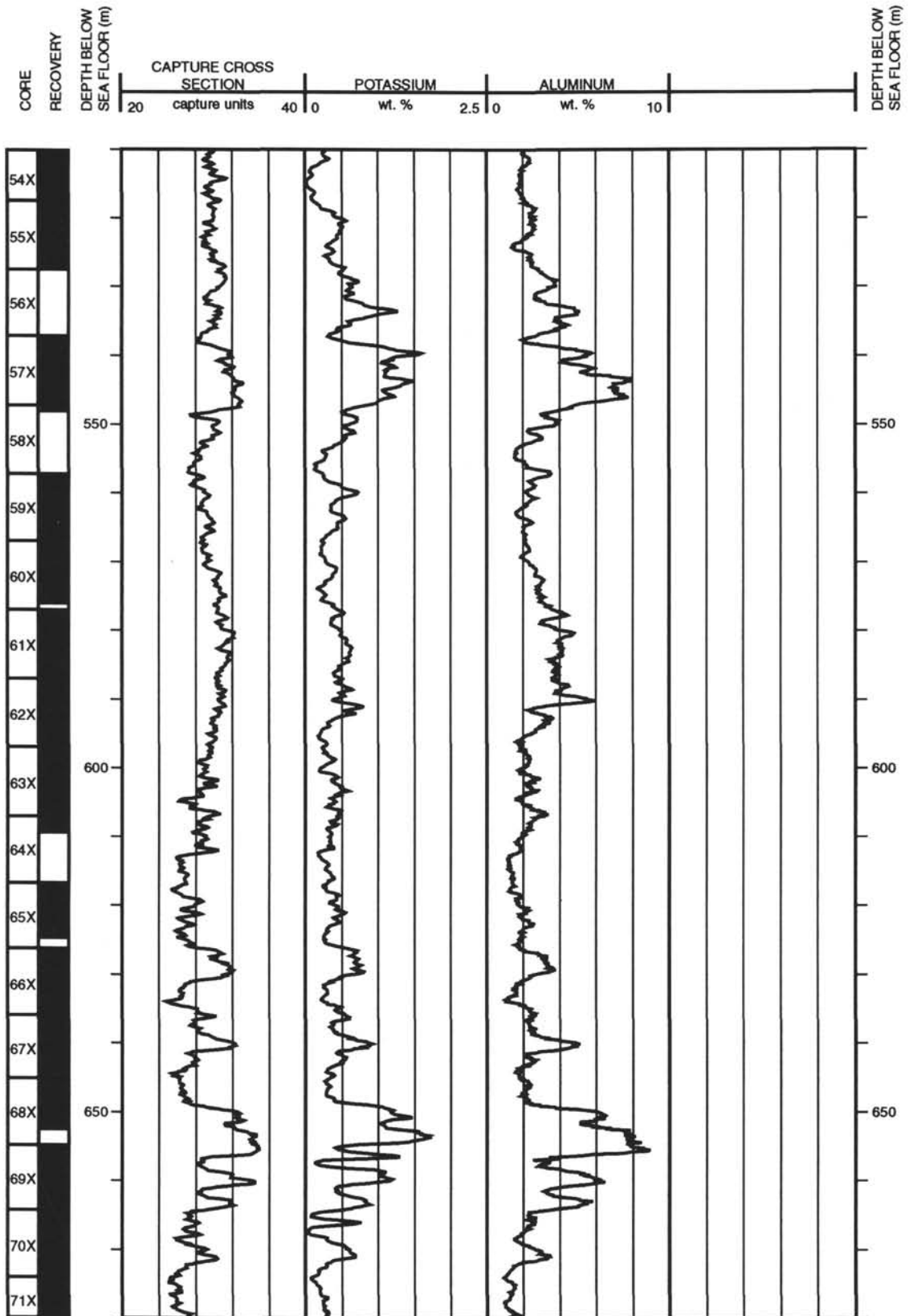
Hole 883F: Geochemical Log Summary (continued)



Hole 883F: Geochemical Log Summary (continued)



Hole 883F: Geochemical Log Summary (continued)



Hole 883F: Geochemical Log Summary (continued)

